THE UNIVERSITY *of* EDINBURGH

Spatial and Temporal Control of Regulated Exocytosis by Protein and Lipid Interactions

Alison Dun
PhD

The University of Edinburgh

2013

Abstract

Cellular communication requires the transport of chemical messengers between intracellular compartments and from cell to cell. The regulated exocytosis of a secretory vesicle at the plasma membrane involves the merger of two bilayers, with markedly different lipid composition, within a millisecond time scale. The spatial and temporal control of the protein and lipid complement at these fusion sites is essential. A highly conserved family of proteins are known to drive this fusion event; SNAP-25 and syntaxin-1 (t-SNAREs) associate at the plasma membrane in a 1:1 stoichiometry to provide a binding site for the vesicle-membrane protein synaptobrevin (v-SNARE). The formation of this complex and subsequent fusion requires accessory proteins for efficient calcium-triggered exocytosis; which of these proteins facilitate the initial attachment of vesicle to the plasma membrane prior to fusion is still under debate. Specific sites for vesicle fusion have been proposed and the organisation of lipids and proteins at these fusion sites has been extensively investigated with limited spatial and temporal resolution; however the presence of raft-forming lipids at these sites as well as the arrangement of SNARE proteins at the molecular level is still under contention. The data presented within this thesis aims to elucidate the protein and lipid environment at the fusion site using super-resolution microscopy and advanced vesicle tracking. Under diffraction-limited microscopy the t-SNAREs are visualised as 200 nm homogenous clusters; however I have used single molecule localisation microscopy to reveal a more complex heterogeneous molecular arrangement. Quantification of lipid order exclusively at the plasma membrane provided insight into the influence of cholesterol-induced lipid arrangement on SNAP-25 localisation. In addition the t-SNARE interaction was investigated using TCSPC-FLIM identifying two lipid-order-dependent conformations in distinct clusters at the plasma membrane. Extensive vesicle tracking at optimum sampling rates demonstrated the ‘sampling’ behaviour of LDCVs and allowed characterisation of vesicle fusion sites. In summary I find that vesicles exhibit preference for residence and probably fusion at regions of plasma membrane with a low t-SNARE density; these proteins appear to exert control over exocytosis by adopting alternative conformations that are under cholesterol-induced regulation.

Declaration

This thesis is a result of my own work with the exception of that done in collaboration. These sections have been indicated in the acknowledgments. All other portions of this thesis are the result of my own work.

Signed Date

List of figures

Figure 1.1	Secretory proteins undergo exocytosis at the plasma membrane	5
Figure 1.2	A diagrammatic representation of the SNARE complex	11
Figure 1.3	The limit of resolution	20
Figure 1.4	Photoactivatable GFP is activated with UV light	23
Figure 1.5	Imaging single vesicle fusion at the plasma membrane	26
Figure 2.1	Laurdan reports on lipid order in membranes	48
Figure 2.2	Imaging using total internal reflection fluorescence	51
Figure 2.3	TCSPC-FLIM	53
Figure 2.4	FRET between Cerulean and EYFP	55
Figure 2.5	FRET between the SNAREs	56
Figure 2.6	PALM below the "limit of resolution"	58
Figure 3.1	Laurdan reports on lipid order throughout the cell	66
Figure 3.2	Membrane sheets can be distinguished in widefield illumination	68
Figure 3.3	FLIM reports on temperature-dependent lipid reorganisation in isolated membranes	70
Figure 3.4	Cholesterol depletion from both layers abolishes lipid phase heterogeneities	71
Figure 3.5	Fixation consistently alters lipid ordering	72
Figure 3.6	Laurdan-stained intracellular structures are visible under TIRFM	74
Figure 3.7	Laurdan GP in PC12 cell membrane sheets fit to a single distribution	75
Figure 3.8	Lipids in isolated plasma membranes are dynamic	77
Figure 3.9	Cholesterol depletion in HEK-293 membrane sheets reduces lipid ordering	78
Figure 4.1	Movement of vesicles at the plasma membrane	87
Figure 4.2	Vesicle localisation at the plasma membrane is not uniform	88
Figure 4.3	Vesicle mobility can be described by a Brownian model	90
Figure 4.4	Vesicles are restricted in their freedom of movement	91
Figure 4.5	Distribution of vesicle track parameters	93
Figure 4.6	The majority of vesicles have a caged mobility	94
Figure 4.7	Vesicles can be categorised dependent on their track length and displacement	95
Figure 4.8	Vesicle behaviour in MβCD-treated PC12 cells	97
Figure 4.9	Cholesterol depletion significantly alters vesicle mobility	98
Figure 4.10	Calcium concentration after ATP addition	100
Figure 4.11	Vesicle behaviour in stimulated PC12 cells	101
Figure 4.12	Cell stimulation significantly alters vesicle mobility	102
Figure 4.13	Vesicles 'scanning' the plasma membrane are dynamic in their behaviour	104
Figure 4.14	Cell stimulation reduces the mobility of 'scanning' vesicles	105
Figure 4.15	'Scanning' vesicles slow down and become more caged upon cell stimulation	106
Figure 4.16	'Scanning' vesicles that fuse have reduced mobility compared to non-fusers	108
Figure 4.17	Resident vesicles do not significantly change their mobility	

	after cell stimulation	110
Figure 4.18	Newly recruited vesicles display a different mobility to resident vesicles	111
Figure 4.19	Newly recruited vesicles 'jump' considerably in the final step to fuse	112
Figure 4.20	Vesicle mobility correlates with phases of secretion	114
Figure 4.21	Vesicle fusion can occur in the same region more than once	115
Figure 4.22	Sites of vesicle fusion correlate with regions of high density	116
Figure 5.1	Single molecule distribution of SNAP-25 at the plasma membrane	127
Figure 5.2	Analysis of the spatial organisation of single molecules	128
Figure 5.3	SNAP-25 is clustered at the plasma membrane	129
Figure 5.4	SNAP-25 remains clustered at the plasma membrane after cholesterol depletion	131
Figure 5.5	Single molecules of SNAP-25 reside proximal to lipids of varying order	133
Figure 5.6	mCer-syntaxin-1 at the plasma membrane has a mean fluorescent lifetime of 2288 $\pm$ 40 ps	134
Figure 5.7	SNAP-25 and syntaxin-1 interaction within one pixel of an image	136
Figure 5.8	Calculating the mean lifetime of mCer-syntaxin-1 at the plasma membrane	137
Figure 5.9	Heterogeneous interaction states of syntaxin-1 and SNAP-25 are spatially distinct	138
Figure 5.10	SNAP-25 mutations on the second SNARE helix	140
Figure 5.11	Two t-SNARE conformations are a result of differential SNAP-25 engagement	141
Figure 5.12	Cholesterol depletion influences the t-SNARE interaction	143
Figure 6.1	Spatial and temporal control on exocytosis by protein and lipid interactions	158

Abbreviations

a-FRET	FRET amplitude (see also FRET)
ADC	Analogue digital convertor
ATP	Adenosine triphosphate
BoNT/A	Botulinum toxin serotype A
BoNT/E	Botulinum toxin serotype E
BSA	Bovine serum albumin
CFD	Constant fraction discriminator
CLSM	Confocal laser scanning microscopy
COP	Coat protein
d-STORM	Direct- stochastic optical reconstruction microscopy
DMEM	Dulbecco's modified Eagle's medium
DD	Deionised water
DNA	Deoxyribonucleic acid
DMSO	Dimethyl sulfoxide
DRM	Detergent resistant membrane
DTT	Dithriothreitol
E.Coli	Escherichia coli
EB	Elution buffer
ECFP	Enhanced cerulean fluorescent protein
EGFP	Enhanced green fluorescent protein
EDTA	Ethylenediaminetetraacetic acid
EGTA	Ethylene glycol-bis(2-aminoethylether)-N,N,N',N'-tetraacetic acid
EM	Electron-multiplying
ER	Endoplasmic reticulum
EYFP	Enhanced yellow fluorescent protein
FBS	Foetal bovine serum
FCS	Fluorescence correlation spectroscopy
FLIM	Fluorescence lifetime imaging microscopy
FRAP	Fluorescence recovery after photobleaching
FRET	Förster resonance energy transfer
FSG	Fish skin gelatine
GTP	Guanosine triphosphate
GFP	Green fluorescent protein
GP	Generalised Polarisation
GUV	Giant unilamellar vesicles
HEK-293	Human embryonic kidney 293
HEPES	N-(2-Hydroxyethyl)piperazine-N'-(2-ethanesulfonic acid)
HSCP	High sensitivity calcium pool
IRP	Immediate releasable pool
kDa	kilo Daltons
LB	Lysogeny broth
LDCV	Large dense core vesicles
mCherry	monomeric Cherry

MβCD	Methyl β cyclodextrin
N2a	Neuroblastoma 2a
NPY	Neuropeptide-Y
NSF	N-ethylmaleimide-sensitive factor
PA-FP	Photoactivatable – fluorescent protein
PAINT	Points accumulation for imaging in nanoscale topography
PALM	Photoactivatable localisation microscopy
PBS	Phosphate buffered saline
PC12	Pheochromocytoma-12
PCR	Polymerase chain reaction
PDL	Poly-D-lysine
PFA	Paraformaldehyde
PIP_2	Phosphatidylinositol 4,5-bisphosphate
PMT	Photon multiplier tube
POC	Perfusion Opened-Closed
PS	Phosphatdylserine
PSF	Point spread function
RI	Refractive index
RRP	Readily releasable pool
RSP	Regulatory secretory proteins
SEM	Standard error of the mean
SDS	Sodium dodecyl sulfate
SMLM	Single molecule localisation microscopy
SN1	First SNARE helix
SN2	Second SNARE helix
SNAP	Soluble NSF attachment protein (see also NSF)
SNAP-25	Synaptosomal-associated protein of 25 kDa
SNARE	SNAP receptor (see also *SNAP*)
SRP	Slowly releasable pool
STED	Stimulated emission depletion microscopy
STORM	Stochastic optical reconstruction microscopy
t-FRET	FRET lifetime (see also FRET)
t-SNARE	Target SNARE (see also SNARE)
TBE	Tris/Borate/EDTA
TCSPC	Time correlated single photon counting
TeNT	Tetanus toxin
TGN	Trans-Golgi network
TIRFM	Total internal reflection fluorescence microscopy
TMD	Transmembrane domain
TPE	Two photon excitation
UV	Ultraviolet
v-SNARE	Vesicular SNARE (see also SNARE)
VAMP	Vesicle associated membrane protein
Wt	Wild type

Acknowledgements

I need to start with an apology for the length of these acknowledgements; I could not have completed this thesis without the support from so many people.

Firstly to Rory for your unwavering support and guidance throughout the last four years; you have been so generous with your time. Thank you for a great project, for your enthusiasm and your patience. Thank you to Colin for the many many hours you have given teaching me in both the lab and sat in front of analysis computers; your input into my project has been invaluable. I have thoroughly enjoyed working with you both and I cannot thank you enough.

A big thank you to people who have helped with the production of the thesis in formatting or analysis; Chris Martin, Lei Yang and Rory Duncan. Data in the following figures were in collaboration with colleagues: 5.6, 5.9, 5.11 and 5.12. Analysis was performed in collaboration with Lei Yang in Figures: 4.2, 4.3, 4.4, 4.5, 4.6, 4.8, 4.9, 4.11, 4.12 and 4.22. The construct NPY-GFP was a kind gift from Guy Rutter.

Thank you to Annya who has helped me out in so many ways throughout the last four years both in and out of work; thank you for your friendship. To all the girls at Heriot Watt thank you for making my move over there so easy by being so welcoming and making me laugh at points where I wanted to scream!

I wouldn't have been able to finish this thesis without the amazing friends who put a roof over my head when I was penniless; Katia, Kirsty, Susannah and Iain. Thank you to James for letting me stay; for listening to me moan over the last couple of thesis-writing months and for providing the motivational speeches I badly needed. Jess and Alex you took me in (and all my worldly belongings) without question and provided support at a time I most needed it. And to Amy, thank you for letting me stay again and again, for the beer and the honest and refreshing advice on the bad days.

Lastly I would never have reached this point without the unbelievable support from my family; Mum, Jess, Alex, Nana, Bob, Steve, Mad and Laura thank you for the countless phone calls, invaluable advice and for always being there for me.

I dedicate this thesis to my wonderful Mum; you are my inspiration in everything I do, thank you for your continuous support and belief in me.

Publications

Rickman, C., Medine, C. N., Dun, A. R., Moulton, D. J., Mandula, O., Halemani, N. D., Rizzoli, S. O., et al. (2010). t-SNARE protein conformations patterned by the lipid microenvironment. The Journal of Biological Chemistry, *285*(18), 13535–41.

Dun, A. R., Rickman, C., Duncan, R. R. (2010). The t-SNARE complex: a close up. Cellular and Molecular Neurobiology*, 30(8). 1321-6.*

Yang, L., Dun, A. R., Martin, K. J., Qiu, Z., Dunn, A., Lord, G. J., Lu, W., Duncan, R. R., and Rickman, C. (2012). Secretory Vesicles Are Preferentially Targeted to Areas of Low Molecular SNARE Density. PLoS ONE *7 (11), e49514.*

Table of Contents

Preliminaries

Abstract i
Declaration ii
List of figures iii
Abbreviations v
Acknowledgements vii
Publications viii
Table of Contents ix

Chapter One: Introduction

1.0 The Foundations of Cell Communication 1
1.1 The Secretory Pathway 2
1.1.1 Proteins through the secretory pathway 3
1.1.2 Lipids through the secretory pathway 4
1.1.3 Packaging of the secretory cargo 4
1.1.4 Lipid organisation at the plasma membrane 6
1.2 Vesicles at the Plasma Membrane 8
1.2.1 The tethering of vesicles to the plasma membrane 8
1.2.2 The vesicle pools 9
1.3 The SNARE Proteins 10
1.3.1 The identification of the SNARE proteins 10
1.3.2 SNAP-25 12
1.3.3 Syntaxin 1 14
1.3.4 Synaptobrevin 15
1.4 Regulated Exocytosis through the SNARE Complex 16
1.4.1 The t-SNARE complex 16
1.4.2 The ternary complex 17
1.4.3 Regulation of SNARE-mediated fusion 18
1.5 Imaging the Exocytotic Machinery 19
1.5.1 Microscopy in brief 19
1.5.2 The fluorescent proteins 21
1.5.3 Imaging vesicles at the plasma membrane 24
1.5.4 Imaging proteins past the limit of resolution 25
1.5.5 Fluorescence imaging of lipid dynamics at the plasma membrane 28
1.5.6 Visualising the proteins, lipids and vesicles 29
1.6 Aims 31

Chapter Two: Materials and Methods

2.0 Materials and Solutions 33
2.0.1 Buffers and growth solutions 33
2.0.2 Antibodies 34
2.1 Molecular Techniques 34
2.1.1 Polymerase-chain-reaction 34
2.1.2 Site directed mutagenesis 34
2.1.3 Expand high fidelity PCR 36
2.1.4 Restriction digests 37
2.1.5 Ligation of insert DNA into vector DNA 38
2.1.6 Gel electrophoresis 38
2.1.7 DNA extraction from agarose gel 39
2.1.8 DNA purification 39
2.1.9 Large scale DNA purification 40
2.1.10 DNA quantification 41
2.1.11 Transformation 41
2.1.12 Agar plates 41
2.1.13 Immunostaining 42
2.2 Cell Culture 42
2.2.1 Cell storage and reuse 42
2.2.2 Cell maintenance 43
2.2.3 Cell culture media 44
2.2.4 Preparation of coverslips 44
2.2.5 Cell transfections 45
2.3 Experimental Cell Conditions 45
2.3.1 Cell stimulation 45
2.3.2 Cholesterol depletion 46
2.3.3 Cell fixation 46
2.3.4 Cell unroofing 46
2.3.5 Laurdan staining 46
2.3.6 Calcium dye loading 47
2.4 Imaging Techniques 49
2.4.1 Confocal laser scanning microscopy (CLSM) 49
2.4.2 Widefield fluorescence microscopy 49
2.4.3 Total internal fluorescence microscopy (TIRFM) 50
2.4.4 Time correlated single photon counting – fluorescence lifetime imaging microscopy (TCSPC-FLIM) 52
2.4.5 Photoactivated localisation microscopy (PALM) 57
2.4.6 Direct-stochastic optical reconstruction microscopy (dSTORM) 57
2.5 Analysis and Data Processing 55
2.5.1 Deconvolution and Niquist sampling 59
2.5.2 Vesicle mobility analysis 60
2.5.3 PALM and dSTORM data analysis 60
2.5.4 TCSPC-FLIM analysis 61
2.5.5 Laurdan staining analysis 61
2.5.6 Statistical analysis 62

Chapter Three: Quantification of Lipid Order at the Plasma Membrane

3.0 Introduction 63
3.1 Materials and Methods 65
3.2 Results 65
3.2.1 Lipid order in whole cells can be detected using Laurdan 65
3.2.2 Quantitative analysis of lipid order in membrane sheets using FLIM 67
3.2.3 Imaging of the plasma membrane under TIRF 73
3.2.4 Membrane sheets as a model for lipid behaviour quantified by the GP of Laurdan 76
3.3 Conclusions 79

Chapter Four: Large Dense Core Vesicle Dynamics

4.0 Introduction 82
4.1 Materials and Methods 85
4.2 Results 86
4.2.1 Vesicles at the plasma membrane display heterogeneous behaviour and are restricted to domains 86
4.2.2 Vesicles display a restricted motion 89
4.2.3 Categorisation of vesicles by their mobility 92
4.2.4 Examining the influence of cholesterol on vesicle behaviour 96
4.2.5 Calcium fluctuations under continuous stimulus 99
4.2.6 Vesicles become more mobile after cell stimulation 99
4.2.7 Examination of vesicles that scan the membrane 103
4.2.8 Resident vesicles behave differently to newly recruited vesicles 107
4.2.9 Vesicle fusion at the plasma membrane is temporally and spatially controlled 109
4.3 Conclusions 117

Chapter Five: t-SNARE Organisation at the Plasma Membrane

5.0 Introduction 123
5.1 Materials and Methods 125
5.2 Results 126
5.2.1 Clustering of single molecules of SNAP-25 at the plasma membrane 126
5.2.2 SNAP-25 molecules remain clustered after cholesterol depletion 130
5.2.3 The t-SNARE interaction at intermolecular distances 132
5.2.4 Identification of two conformations of t-SNARE interaction at the plasma membrane 135
5.2.5 SNAP-25 engagement is the determining factor in t-SNARE conformation states 139
5.2.6 The interaction status of the t-SNAREs is dependent on lipid order 142
5.3 Conclusions 144

Chapter Six: Discussion

6.0 Summary of Results 149
6.1 Interpretation of Findings 151
6.1.1 SNAP-25 imposes temporal and spatial control over exocytosis through single molecule distribution and the zippering of the second SNARE helix 151
6.1.2 SNAP-25 clusters are regulated by the cholesterol-induced lipid order at the level of t-SNARE interaction 153
6.1.3 LDCVs prefer regions of plasma membrane with low SNARE density 155
6.2 The Significance of my Findings in Regulated Exocytosis 157
6.3 Summary 159

Bibliography xiii

Publications xxxvii

Chapter One:

Introduction

1.0 The Foundations of Cell Communication

The transfer of information from cell to cell is fundamental in multicellular life and the study of this communication has provided insight into a plethora of cellular functions. The requirement of efficient cell communication led to the specialisation of certain cells designed to fulfil this purpose, for example neurons. These cells enable fast transmission of information through the cellular network within the peripheral and central nervous system to the effecter cells throughout the body (Cowan et al., 2001). The efficiency of this communication was found to rely on synapses, extracellular spaces between presynaptic and postsynaptic cells where information was transmitted either chemically or electrically (Dale, 1936; Eccles, 1948; Cowan et al., 2001). The majority of synapses have been found to be chemical, utilising chemical messengers such as acetylcholine or noradrenaline (Valenstein, 2002). Electron microscopy allowed for the visualisation of synapses and revealed a multitude of vesicular-like structures within the presynaptic cleft proximal to the plasma membrane (Palay and Palade, 1955). Isolation of single nerve fibres enabled the analysis of the end plate potential and led to the discovery of mini end plate potentials at cellular junctions (Graham and Gerard, 1946; Fatt and Katz, 1950). Further investigation revealed these mini end plate potentials were quantal and led to the vesicle hypothesis; transmitter is released in small discrete vesicular packets (Fatt and Katz, 1951; Castillo and Katz, 1954).

The exocytotic process of vesicle and plasma membrane bilayer merging to allow fusion was first suggested in 1965 (Katz and Miledi, 1965) and since then there has been extensive research into the exact mechanisms controlling this event. The transmission of signals at the synapse is rapid and undertaken by synaptic vesicles which are ~ 35 nm in diameter (Palay and Palade, 1955). The limitations in visualising these fusion events in real time under microscope systems has led to the use of neuroendocrine cells as a model system for neurotransmission and has been widely used within the field in either primary culture or cell lines (Heinemann et al., 1993; Zucker, 1996; Westerink and Ewing, 2009; Warashina and Ogura, 2004).

Cell to cell communication requires tight regulation to ensure that chemical messengers are transmitted at the right time, at the right concentration and that the signal is correctly interpreted at its target cell (Alberts et al., 2002). This allows for vital cellular processes in human biology to occur such as cell growth and survival, which when perturbed form the basis for the development of cancerous cells and tumours as well as neurodegenerative pathologies (Gschwind et al., 2001; Garden & La Spada, 2012). Cell to cell communication can fail through a number of pathways; in type II diabetes mellitus there is an inability to read the signal as there is an impaired response to the hormone insulin whereas in multiple sclerosis the propagation of the signal is disrupted due to the destruction of the myelin sheath along neurons (Alberts et al., 2002).

Regulated exocytosis is the process of secreting a chemical signal into the extracellular space, either into the bloodstream by neuroendocrine cells or into the synaptic cleft by neurons. The proteins involved in the facilitation of this process are known targets for Botulinum toxins (Schiavo et al., 1993; Chapman et al., 1994; Bajohrs et al., 2004) and a reduction in the expression of these proteins has been associated with type II diabetes and schizophrenia (Thompson et al., 2003; Ostenson et al., 2006). The diseases associated with disruptions in cell communication pathways make the process of regulated exocytosis an important area of research.

1.1 The Secretory Pathway

The viability of a eukaryotic cell relies on communication between intracellular compartments as well as from cell to cell which, with a high flux of cargo being exchanged, requires tight regulation and precise balance. Membrane trafficking ensures organelles are equipped with their functional complement of proteins and lipids and that efficient signalling from cell to cell can occur (Van Meer, 1989; Simons and Ikonen, 1997).

1.1.1 Proteins through the secretory pathway

A secretory molecule is synthesised in the endoplasmic reticulum (ER), modified in the Golgi and trafficked to the plasma membrane for release via the trans-Golgi network (TGN) (Novick et al., 1981). Secretory proteins undergo folding within the ER; a lace-like structure adjacent to the cell nucleus. Release is regulated through addition of glucose after complete folding, without which proteins cannot leave (Porter et al., 1945). The transport of these secretory molecules relies on the ability of organelles to create sharp curved buds within their membrane, which encapsulate the cargo and can exit as vesicular structures. Specific proteins at budding sites are required to physically deform the membrane and can assist in the selection of the proteins, dependent on their destination within the cell (Schekman and Orci, 1996). At the ER membrane the coat protein, COPII, mediates this process and is associated until the vesicle begins to move along microtubules towards the cis-Golgi (Barlowe, 1998).

The Golgi is a lipid and protein processing system consisting of parallel stacks of flattened cisternae which has a polarised structure with secretory vesicles packaged into the dilated rims of the transmost-Golgi (Dalton et al., 1956; Farquhar and Palade, 1981; Ladinsky et al., 1999). Early studies suggested that proteins and lipids move through cisternal progression to the trans network (Bergmann et al., 1981); however recent work proposes that there is not a defined lag time at the cis-Golgi and that proteins are processed at an exponential rate proportional to the Golgi abundance (Patterson et al., 2008). Transport of secretory molecules from this structure is mediated through COPI, a coat protein also responsible for recycling proteins and lipids back to the ER (Letourneur et al., 1994; Orci et al., 1997).

The TGN is the final station in the Golgi complex and controls the transport of secretory proteins to the plasma membrane (Matlin and Simons, 1983). Additionally the TGN can recycle proteins back through the endosomal pathway, a process involving the third coat protein, clathrin (Griffiths and Simons, 1986; Traub and Kornfeld, 1997).

1.1.2 Lipids through the secretory pathway

The labelling of lipids in live cells is relatively primitive (compared to protein studies) and so less is known about their distribution throughout the secretory pathway. Glycosphingolipids and sterols are key functional lipids in the vesicular and plasma membrane and their sorting is believed to be connected with that of secretory proteins (Cross, 1987; Simons and Van Meers, 1988; Patterson et al., 2008). It is believed that these lipids are at a low concentration at the ER and accumulate toward the plasma membrane (Van Meer and Simons, 1988). Sorting occurs within the Golgi where glycosphingolipids and sterols are segregated from glycerolipids, which are retrieved by recycling vesicles rather than being transported to the TGN (Holthuis et al., 2001). At the TGN sphingolipids and sterols form vesicles using the lipid raft clustering method, enabling raft proteins inclusion and trafficking to the plasma membrane (Wang et al., 2000; Klemm et al., 2009).

1.1.3 Packaging of secretory cargo

Secretory proteins are released at the plasma membrane by one of two mechanisms, regulated or constitutive exocytosis (Burgess and Kelly, 1987) (Figure 1.1). Both these pathways originate from the TGN, where the cargo is segregated dependent on their route. Constitutive cargo is transported in post-Golgi vesicles and is mediated by endocytotic components such as dynamin and actin (Jaiswal et al., 2009). This cargo is released very soon after it reaches the plasma membrane and the triggers for this are not known. Regulatory secretory proteins (RSPs) undergo regulated exocytosis; a tightly controlled pathway triggered by an increase in intracellular calcium and facilitated through complex protein-protein and protein-lipid interactions (Dunn and Holz, 1983; Burgoyne and Morgan, 1993). In neuroendocrine cells RSPs such as neuropeptides accumulate in the TGN where they are packaged into large dense core vesicles (LDCVs) (Plattner et al., 1997). Formation involves homotypic fusion between two immature LDCVs, which allows removal of unwanted material, this concentrates the RSP inside the vesicle

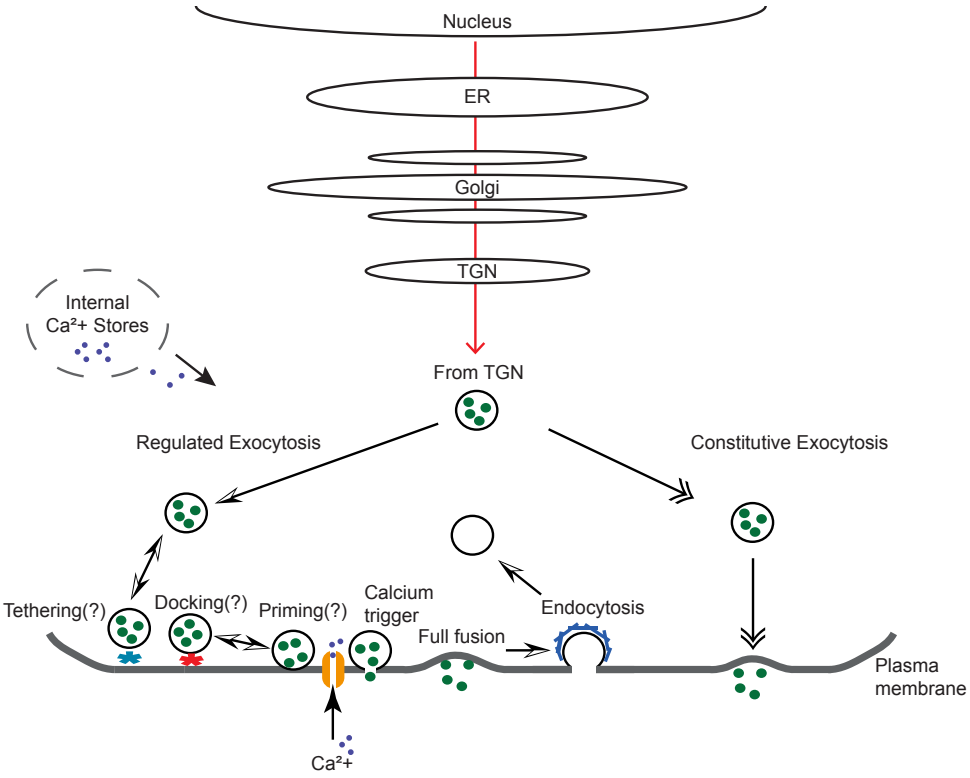

Figure 1.1 Secretory proteins undergo exocytosis at the plasma membrane. Proteins and lipids traffic through the secretory pathway (red arrow). Secretory proteins (green filled circles) are packaged into vesicles (black circles) and trafficked to the plasma membrane. In regulated exocytosis vesicles can tether (blue asterix) and then dock (red asterix) via protein-protein and protein-lipid interactions. Cell stimulation triggers calcium (purple filled circles) influx via internal stores and membrane receptors (orange). After release of secretory proteins vesicles are recycled via clathrin-mediated (blue) endocytosis. Constitutive exocytosis is not triggered by calcium.

(Klumperman et al., 1998; Wendler et al., 2001). No protein coat is required for mature LDCV budding, however it is thought aggregates such as chromogranin and Dynamin II may play a part (Kim et al., 2001; Yang et al., 2001). Upon release from the TGN LDCVs are translocated along microtubules to the plasma membrane, a process that may be mediated by Rab proteins (Grosshans et al., 2006).

1.1.4 Lipid organisation at the plasma membrane

The plasma membrane of mammalian cells is abundant in phospholipids, which are interspersed with bulk quantities of sterols and glycosphingolipids that can translocate between the leaflets of the membrane bilayer and create an asymmetrical fluid structure (Edidin, 1974; Van Meer, 1989). A plasma membrane in a mammalian cell is highly complex with a large number of lipids moving in and out of the membrane and a high degree of variation in the acyl chains of the phospholipids (Edidin, 1974). The selective arrangement of lipids with differing properties gives rise to different transitional phases, ordered and disordered, that coexist within the membrane. Lipids are seen to transition from a more ordered phase to a more disordered phase upon a temperature increase (Ipsen et al., 1989). A lipid-ordered region contains cholesterol, a sterol with a bulky rigid structure that can interact with sphingolipids and phospholipids via hydrogen bonding (Simons and Vaz, 2004). There are various models describing the interaction of cholesterol with these lipids, one describes a condensing mechanism where cholesterol reduces the surface area occupied by the phospholipids (McConnell and Radhakrishnan, 2003) while another termed the umbrella model suggest cholesterol relies on the polar head of the phospholipid to protect it from water molecules (Huang and Feigenson, 1999). The importance of cholesterol in lipid-ordering has been demonstrated in many works (Gaus et al., 2003; Eggeling et al., 2009; Zhang et al., 2009) by the transition to more lipid-disordered phases after treatment with Methyl-β-Cyclodextrin (MβCD); a cholesterol chelating agent that acts to remove cholesterol from the external leaflet of the bilayer (Ohtani et al., 1989).

The identification of highly ordered domains within the plasma membrane of mammalian cells led to the lipid raft hypothesis, which describes the functional organisation that these domains give to the membrane (Simons and Ikonen, 1997). These rafts are thought to be dynamic within the plasma membrane and provide a platform for protein attachment. These rafts are suggested to be enriched with cholesterol, sphingomyelin and phosphotidylcholine (a phospholipid) and their identification has led to extensive research into their existence and effect on cellular processes (Simons and Ikonen, 1997; van Meer et al., 2008; Lingwood and Simons, 2010). Lipid rafts were isolated from biological membranes as fragments which were resistant to detergent and so termed detergent resistant membranes (DRMs) (Brown and Rose, 1992) and this method allowed over 200 proteins to be purified and allocated to lipid rafts, including the SNARE (soluble *N*-ethylmaleimide-sensitive-factor attachment protein receptor) proteins (see 1.3.1) (Chamberlain et al., 2001; Foster et al., 2003). This method of solubilisation has been criticised as not being representative of living cells (Lichtenberg et al., 2005) and the lipid raft hypothesis has been replaced with the membrane raft hypothesis, which includes the regulation that proteins exert on these domains. These rafts are now characterised as small (10-200 nm), heterogeneous, highly dynamic, sterol- and sphingolipid-enriched domains that compartmentalise cellular processes (Lang et al., 2001; Pike, 2006).

The plasma membrane is a highly complex structure responsible for the facilitation of a large number of biological processes and the proteins involved in these processes can be spatially controlled through lipid raft formation as described above. Another method of control is described in the picket fence model (Tsuji et al., 1988), whereby the actin meshwork compartmentalises anchored membrane proteins, positioning them dependent on their functional relevance. An association between actin and cholesterol is postulated (Dinic et al., 2013; Tomatis et al., 2013), which may demonstrate another mechanism by which lipid rafts impose spatial control at the plasma membrane.

1.2 Vesicles at the Plasma Membrane

1.2.1 The tethering of vesicles to the plasma membrane

As a secretory vesicle arrives at the plasma membrane it can be seen to lose mobility and transition from a directed motion to a caged motion, which is thought to represent the association with the plasma membrane (Steyer et al., 1997; Oheim and Stühmer, 2000; Karatekin et al., 2008). This association is thought to involve a docking step followed by a priming step before final fusion. The tethering of the vesicle is suggested and is thought to be a transient association that can lead to docking; however these steps remain speculative (Burgoyne and Morgan, 2003). A small selection of protein complexes have been identified which may act in the initial tethering of vesicles to the Golgi or endosomal compartments (Whyte and Munro, 2002), but for secretory vesicles the proteins are not as definitive. It is suggested that the SNAREs (see 1.3.1), a family of proteins essential for regulated exocytosis, are involved in this step (Palfreyman et al., 2006; de Wit et al., 2006; Wu et al., 2012) although it is still debated if they are required this early in the process (Hunt et al., 1994; Broadie et al., 1995; Cao et al., 1998). Proteins that have been implicated include Rab proteins, Munc18-1, GTPases and a protein complex termed the exocyst (Kee et al., 1997; Li and Chin, 2003; de Wit, 2010).

The priming of a vesicle is the final maturation step required to become fusion competent and the mobility of the vesicle just before fusion is thought to represent this (Becherer and Rettig, 2006; Nofal et al., 2007). Some studies have identified a transition from a caged mobility to nearly immobile prior to fusion (Toonen et al., 2006; Nofal et al., 2007) whereas others describe an increase in mobility where the vesicles ‘jump’ to fuse (Degtyar et al., 2007; Karatekin et al., 2008). The vesicle behaviour immediately prior to fusion is still unresolved; however it is well established that the calcium sensor synaptotagmin acts in this step, integrating both calcium and lipids into the fusion reaction (Chapman and Davis, 1998; Wang and Richards, 2011; Rickman and Davletov, 2003). Other suggested priming factors include Munc13 (Augustin et al., 1999), Munc18-1 (Gulyás-Kovács et al., 2007) and complexin (McMahon et al., 1995).

The final step in the regulated exocytosis pathway is the fusion of the vesicle with the plasma membrane. In the classic mode of exocytosis the vesicle fully flattens on the plasma membrane and the lipids in both membranes merge. In this event all of the luminal content is released (Heuser and Reese, 1973). The vesicular components that mix with the plasma membrane in this process are retrieved through clathrin-mediated endocytosis; the budding of the plasma membrane to form endocytotic vesicles (Heuser and Reese, 1973; Granseth et al., 2007). Synaptotagmin is proposed to facilitate both processes (Zhang et al., 1994). An additional mode of exocytosis is hypothesised that combines vesicle fusion and recycling within one process; a vesicle forms a transient fusion pore and partially releases its content, before being recaptured inside the cell. This process is termed 'kiss and run' (Ceccarelli et al., 1973; Taraska et al., 2003). It is believed that both modes can occur during a stimulation, the mode that takes place is suggested to be dependent on the calcium concentrations upon stimulation (Alés et al., 1999; Richards et al., 2005).

1.2.2 The vesicle pools

Vesicles have been previously categorised dependent on a type of behaviour; either directed, caged or nearly immobile motion, and identification of these led to the classification of vesicle pools: groups with varying fusing probability and proximity to the plasma membrane (Augustine and Neher, 1992; Stevens et al., 2011). It is proposed that newly synthesised vesicles are found closest to the membrane (Duncan et al., 2003) and in chromaffin cells these readily releasable vesicles are suggested to reside in four distinct pools: the readily releasable pool (RRP), the slowly releasable pool (SRP), the immediately releasable pool (IRP) and the highly sensitive calcium pool (HSCP) (Voets et al., 1999; Yang and Gillis, 2004). The IRP contains ~35 vesicles and is located closest to calcium channels and so can release in response to moderate stimuli (Voets et al., 1999). It is understood that the RRP represents the fast burst of exocytosis and the SRP the slow burst; these vesicles are already primed at the time of release and so pools are depleted within ~1 second (Voets et al., 1999; Becherer and Rettig, 2006). The reserve pool of vesicles (caged

motion) are docked at the plasma membrane but not primed until required; they are responsible for the sustained release. Vesicles over a 200 nm distance from the cell surface are within a depot pool (directed motion) and are recruited to replenish depleted pools after a stimulus (Rahamimoff and Yaari, 1973; Augustine and Neher, 1992). The works described above are predominantly based on amperometric recordings and behavioural analysis at sub-optimum acquisition times; it has not so far been possible to visualise such pools of vesicles in live cells.

1.3 The SNARE Proteins

1.3.1 The identification of the SNARE proteins

It was postulated as early as 1975 (Palade, 1975) that membrane-vesicle targeting and fusion events were controlled by specific proteins at the plasma membrane and the investigation into this process began by looking further upstream of this event. Work demonstrating the polarity of the Golgi highlighted the importance of intra-cisternal transport, a process when reconstituted *in vitro* marked a significant step in the discovery of the proteins involved in vesicle fusion (Palade, 1975; Fries, 1980; Bergmann et al., 1981). Two proteins, N-ethylmaleimide-sensitive factor (NSF) and α-soluble NSF-attachment protein (SNAP) were found to facilitate fusion in this compartment and are now known to act throughout the cell (Fries, 1980; Block et al., 1988; Clary et al., 1990).

Interaction studies led to the identification of three key proteins which bind NSF and α-SNAP to form one particle; named SNARE proteins. Synaptobrevin 2 is bound to the vesicular membrane and so termed v-SNARE whereas the two target (t)-SNAREs, syntaxin-1a (or 1b) and SNAP-25A (soluble *N*-ethylmaleimide-sensitive-factor attachment protein of 25 kDa), bind at the plasma membrane (Söllner et al., 1993; Ferro-Novick and Jahn, 1994) (Figure 1.2). These proteins are now known to be essential for exocytosis and are conserved across the species (Ferro-Novick and Jahn, 1994); however unlike NSF and α-SNAP each form of intracellular

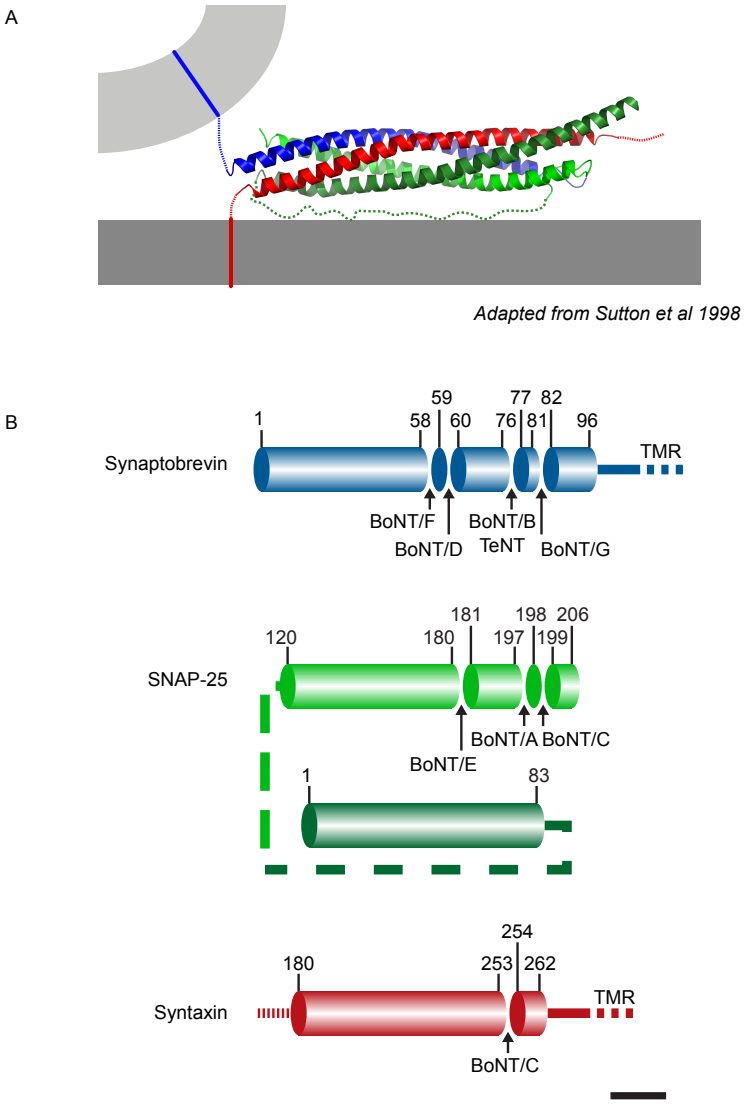

Figure 1.2 A diagramatic representation of the SNARE complex. A) Syntaxin (not including Habc domain) (red) associates with plasma membrane (dark grey) via transmembrane domain. SNAP-25 (1-83 dark green, 83-120 dashed line, 120-206 light green) binds syntaxin. Synaptobrevin (blue) is vesicle membrane (light grey) associated and binds t-SNAREs. Not to scale. B) Cleavage sites for clostridial neuro-toxins in synaptobrevin (blue), SNAP-25 (green) and syntaxin (red). Scale bar 20 amino acids.

fusion has its own specific set of these three SNAREs (Bennett et al., 1993; Rothman and Wieland, 1996; Bock et al., 1997). Within this thesis SNAP-25A and syntaxin-1 (a or b) are investigated and will be referred to as SNAP-25 and syntaxin-1 throughout.

Binary reactions between synaptobrevin 2 and either t-SNARE are weak compared to that between the two t-SNAREs; however the most dramatic change in interaction strength is when all three are bound within one sodium dodecyl sulfate (SDS)- resistant complex (Hayashi et al., 1994). A resounding factor in the requirement of this complex in vesicle fusion is the effect of clostridial neurotoxins on its functions. These toxins are known to inhibit exocytosis in both neurons and neuroendocrine cells and it appears their action is through cleavage of these proteins (Hayashi et al., 1994; Rossetto et al., 1995).

1.3.2 SNAP-25

SNAP-25, a protein composed of two alpha helical SNARE motifs divided by a protease-sensitive linker domain, was first identified in subpopulations of the mammalian nervous system (Oyler et al., 1989). This protein is also found within the neuroendocrine system, at the plasma membrane of chromaffin cells and on the surface of chromaffin granules (Roth and Burgoyne, 1994; Tagaya et al., 1996).

SNAP-25 was initially believed to be trafficked from the Golgi to the plasma membrane in a syntaxin-1-dependent manner, a theory inspired by the ability of syntaxin-1 to enhance SNAP-25 initial association with the plasma membrane (Vogel et al., 2000; Washbourne et al., 2001). It is now known that SNAP-25 traffics independently and that ectopic t-SNARE interactions in the cytosol are detrimental to membrane trafficking (Loranger and Linder, 2002; Medine et al., 2007).

A stretch of 26 amino acids within the linker region of SNAP-25, including 4 closely spaced cysteine residues and five highly conserved amino acids, are required

for membrane association (Gonzalo and Linder, 1998). The formation of a stable union between the membrane and SNAP-25 occurs through palmitoylation; the addition of a C16 saturated fatty acid via a thioester linkage (Gonzalo and Linder, 1998; Gonzalo et al., 1999). There are works which challenge this theory and describe an association dependent on syntaxin-1 (Vogel et al., 2000; Washbourne et al., 2001); however more recent work has identified the enzymes involved in palmitoylation, a family of substrate specific DHHC palmitoylate transferases, and found them to be essential for the association of SNAP-25 with the membrane (Fukata et al., 2004; Roth et al., 2006; Greaves et al., 2010).

At the plasma membrane SNAP-25 is known to initially bind syntaxin-1, forming the t-SNARE complex and create a binding site for the v-SNARE (Söllner et al., 1993a; Ferro-Novick and Jahn, 1994). The role of the two SNARE motifs (SN1 residues 1-80 and SN2 (second SNARE helix) residues 142-206) has been investigated using the *Botulinum* toxins A (BoNT/A) that cleaves 9 and E (BoNT/E) that cleaves 26 amino acids from the C-terminal of SN2 (Schiavo et al., 1993). Such works suggest that synaptobrevin 2 requires the last 26 amino acids of SN2 for association; late post-docking steps depend in particular on residues 181-197 (Hayashi et al., 1994; Chapman et al., 1994; Banerjee et al., 1996). BoNT/E-cleaved SNAP-25 is quickly removed from the membrane whereas BoNT/A-cleaved SNAP-25 remains bound to the core complex and retains the ternary complex in a state with reduced calcium sensitivity, leading to slower fusion kinetics (Keller and Neale, 2001; Bajohrs et al., 2004; Sakaba et al., 2005; Xu et al., 1998). BoNT/E poisoning can be rescued by addition of the cleaved peptide and BoNT/A by high calcium (Banerjee et al., 1996; Chen et al., 2001a). The interaction between syntaxin-1 and SNAP-25 requires both SN1 and the membrane linker; however whether the loss of part or all of SN2 causes the interaction to fail is under debate (Bajohrs et al., 2004; Rickman et al., 2010) (see 1.4.1).

1.3.3 Syntaxin-1

Syntaxins are a family of proteins found in all eukaryotic cells to have a broad tissue distribution; in neuroendocrine cells it is syntaxin-1 that is essential for full fusion of secretory vesicles in calcium-triggered exocytosis (Barnstable et al., 1985; Bennett et al., 1993; Hayashi et al., 1994; Chen and Scheller, 2001). Syntaxin-1 is anchored to the plasma membrane via a hydrophobic 23 amino acid domain; implicated in fusion pore conductance and syntaxin-1 homodimerization (Laage et al., 2000; Han et al., 2004). The cytoplasmic H3 domain, consisting of an α-helical SNARE motif, is cleaved by BoNT/C1 resulting in inhibition of exocytosis (Blasi et al., 1993; Hayashi et al., 1994; O'Connor et al., 1997). Docking of synaptic vesicles was not perturbed in this study; however other works have shown docking phenotypes in the absence of syntaxin-1 (de Wit et al., 2006). The H3 domain has been extensively characterised and appears to form three different conformations: bound to Munc18-1, synaptobrevin and SNAP-25 and in isolation where it may exist as potentially large oligomers (Misura et al., 2000; Rickman et al., 2005). The H3 domain is connected, via a flexible linker region, to the N-terminal Habc domain; a regulatory structure consisting of three α-helices that mediates syntaxin-1-complex configuration (Margittai et al., 2003).

A key stretch of residues between 194 and 288 have been identified as a binding site for SNAP-25, VAMP (vesicle associated membrane protein) and α-SNAP; implicating syntaxin-1 in SNARE complex assembly and disassembly via NSF (Chapman et al., 1994; Calakos et al., 1994; Hanson et al., 1995). In addition strong evidence supports the role of syntaxin-1 in the calcium-trigger for fusion based on the coimmunoprecipitation with N-type calcium channels and the interaction with the calcium sensor, synaptotagmin (Bennett et al., 1992; Inoue et al., 1992; Söllner et al., 1993b). Syntaxin-1 binds synaptotagmin via residues 194-288 in a calcium-sensitive reaction and both form a ternary complex with N-type calcium channels *in vitro* (Lévêque et al., 1994; Chapman et al., 1995). This regulation is thought to influence late fusion steps after the dissociation of α-SNAP and increases the efficiency of calcium-triggered fusion (O'Connor et al., 1994; Rettig et al., 1997).

Conversely syntaxin-1 is believed to negatively regulate activity and expression of sodium and potassium channels (Naren et al., 1998; Chen et al., 2011).

The translocation of syntaxin-1 to the plasma membrane of chromaffin cells is dependent on an interaction with Munc18-1 (Rowe et al., 1999; Medine et al., 2007; Arunachalam et al., 2008). Extensive research into this protein, its homologues and isoforms, describe a family of proteins with a wide tissue distribution (Hata et al., 1993; Tellam et al., 1995) that have both a positive and negative effect on fusion (Hosono et al., 1992; Verhage et al., 1997; Wu et al., 2001). Munc18-1 consists of two β-sheet domains and one α-helical domain that form an arch with a central cavity where syntaxin-1 binds in either an ‘open’ or ‘closed’ form (Dulubova et al., 1999). The 'closed' form, where Munc18-1 binds to the 4-helical bundle created when the Habc domain of syntaxin-1 folds to interact with the H3 domain, is found mostly on intracellular membranes and in the chaperoning of syntaxin-1 to the plasma membrane (Dulubova et al., 1999; Misura et al., 2000; Rickman et al., 2007). Dissociation of the Habc domain from H3 is required for t-SNARE binary interaction and in this rearrangement it is believed that Munc18-1 binds syntaxin-1 via the N-terminal Habc domain and may act as a scaffold for vesicle docking and fusion (Carr et al., 1999; Zilly et al., 2006; Rickman et al., 2007). A number of proteins are proposed to mediate the transition from 'closed' to 'open' formation (Fujita et al., 1998; Gladycheva et al., 2004; Rickman and Davletov, 2005) and may involve phosphorylation of either protein (Sasaki, 1996; Fletcher et al., 1999; Rickman and Duncan, 2010). Munc18-1 is essential in the tight regulation of calcium-triggered exocytosis as a negative regulator of SNARE complex assembly that may also act to facilitate the final fusion step (Carr et al., 1999; Graham et al., 2004; Rickman et al., 2007).

1.3.4 Synaptobrevin

Synaptobrevin 2 resides on the membrane of synaptic vesicles and LDCVs in pheochromocytoma-12 (PC12) cells and provides the third helix in the ternary

SNARE complex prior to fusion (Söllner et al., 1993b; Rothman and Orci, 1992; Fernández-Chacón and Südhof, 1999). Like the t-SNAREs synaptobrevin 2 is a target of neurotoxins, for example Tetanus toxin (TeNT), which cleaves the protein toward its C-terminus (Pellizzari et al., 1996). This activity is believed to effect protein function downstream of docking, resulting in an inactive ternary complex and an accumulation of docked vesicles that are unable to fuse (Schiavo et al., 1992; Hunt et al., 1994).

Synaptobrevin is widely distributed throughout neuronal and neural secretory tissues and has a structured hydrophobic membrane anchor that is highly conserved (Matthew et al., 1981; Elferink et al., 1989). A juxtamembrane linker extends from this anchor into the cytoplasmic space at an angle of 36°, the flexibility and short length of this region accommodates the folding of the t-SNAREs and is necessary for fast fusion at the plasma membrane (Bowen and Brunger, 2006; Ellena et al., 2009). The cytoplasmic domain contains the SNARE motif and is largely unstructured yet two regions with helical propensities have been identified at the beginning and end of this motif (Dascher et al., 1991). The first helix is thought to act as a nucleation site for the t-SNAREs with its C-terminal end producing a “stop signal” as a possible late docking step (Hayashi et al., 1994; Hazzard et al., 1999). The second helix stretches from the last SNARE motif layer into the juxtamembrane layer and may transmit force from SNARE complex assembly into the membrane, leading to membrane bending and subsequent lipid mixing and fusion (Bowen and Brunger, 2006; Ellena et al., 2009).

1.4 Regulated Exocytosis through the SNARE Complex

1.4.1 The t-SNARE complex

The formation of the SNARE complex is strictly sequential and is initiated by the high affinity 1:1 interaction between syntaxin-1 and SNAP-25; a possible rate limiting step in ternary formation (Fasshauer et al., 1997; Fasshauer and Margittai, 2004; Rickman et al., 2004). These proteins colocalise on the plasma membrane in

both chromaffin and beta cells in the absence of synaptobrevin 2 (Rickman et al., 2004; Ohara-Imaizumi et al., 2004a); whether they are preassembled or interact after a prefusion signal is still under debate (Hu et al., 2002a; Lang et al., 2002). Studies applying super-resolution techniques have predominantly focused on syntaxin-1 localisation at the plasma membrane and shown these molecules to reside in clusters 50-60 nm in diameter (Sieber et al., 2006). It has been suggested that the t-SNARE heterodimer forms on these preassembled syntaxin-1 particles (Sieber et al., 2006, 2007); however the homodimerization of syntaxin-1 in vivo remains speculative (Laage et al., 2000; Rickman et al., 2005; Halemani et al., 2010). Early work *in vitro* described an intermediate state in which the SN2 of SNAP-25 (SN2) is not associated with the t-SNARE complex (Hayashi et al., 1994; Fasshauer et al., 1997); this has now been observed in reconstituted bilayers, native membrane sheets and live cells (An and Almers, 2004; Wang et al., 2008; Weninger et al., 2008; Rickman et al., 2010). The functional relevance of this reversible conformation is postulated to be regulatory in recent work from our group (Rickman et al., 2010) (Chapter Five); with the association of SN2 marking a rate limiting step in synaptobrevin 2 binding and the possible involvement of accessory proteins such as complexin (Giraudo et al., 2009) or synaptotagmin (Rickman and Davletov, 2003).

1.4.2 The ternary complex

The t-SNAREs form a nucleation site for synaptobrevin 2 binding; some studies have attributed this to SNAP-25 (Pevsner et al., 1994) while other works implicate syntaxin-1 as the mediator (Bowen et al., 2004; Liu et al., 2005). Once synaptobrevin 2 is associated the ternary complex is observed as a highly twisted and parallel 4-helix bundle, seen to partially assemble and disassemble reversibly during priming (Sutton et al., 1998, Chen et al., 2001b). Formation of both the t-SNARE and the ternary complex relies on heptad repeats; patterns of hydrophilic and hydrophobic residues that give the proteins a high probability of forming coiled coils (Cohen and Parry, 1986; Chapman et al., 1994; Weimbs et al., 1997). The hydrophobic residues within each SNARE motif pack together in the centre of the

ternary complex (Lin and Scheller, 1997; Hanson et al., 1997; Li et al., 2007). In addition the four SNARE helices each contribute a number of ionic residues, which are highly conserved across the SNARE family (Sutton et al., 1998). These residues line up within the hydrophobic core of the ternary SNARE complex, forming a hydrogen bonding network, which gives both strength and registration to the interactions (Sutton et al., 1998; Fasshauer et al., 1998).

1.4.3 Regulation of SNARE-mediated fusion

The SNARE complex is believed to zipper in the N to C-terminal direction (Fiebig et al., 1999; Sørensen et al., 2006); a process that can be interrupted in an effort to control when or how quickly neurotransmitter release will occur (Xu et al., 1999; Melia et al., 2002). It is thought that N-terminal complex formation leads to the priming step with the full zippering of the C-terminal SN2 of SNAP-25 as the final step (Xu et al., 1998; Sakaba et al., 2005; Sørensen et al., 2006). The neuronal protein complexin may act as a clamp on partial SNARE zippering, acting at the N-terminal end proximal to the transmembrane domains (TMD) of both syntaxin-1 and synaptobrevin 2 and controlling the force that the trans-SNAREs apply onto the fusing membranes (Chen et al., 2002; Hu et al., 2002b; Giraudo et al., 2009). This interaction may hold the vesicle in the docked position with the progression to a primed status initiated by the disassociation of complexin by synaptotagmin; although this is still poorly defined (Schaub et al., 2006; Tang et al., 2006; Chicka and Chapman, 2009). Despite their excitatory and inhibitory actions, both complexin and synaptotagmin are promoters of regulated exocytosis and suppress spontaneous release (Voets et al., 2001; Pang et al., 2006; Maximov et al., 2009). Synaptotagmin may exert this regulation through specific lipid interactions (Schiavo et al., 1996; Fernandez et al., 2001; Bai et al., 2004) and is suggested to reduce the energy barrier for fusion through calcium-dependent promotion of positive membrane curvature, bringing the two membranes close together (Rickman and Davletov, 2003; Martens et al., 2007). Energy is also provided via the dramatic structural changes as the SNARE motifs fold and the proteins zipper (Sutton et al., 1998; Weber et al., 1998).

Whether one SNARE complex provides enough energy for fusion of one vesicle is heavily debated with numbers ranging from only 1 to 70 (Mohrmann et al., 2010; Knowles et al., 2010; Sinha et al., 2011). The disassembly of the complex is the final step required to allow full fusion of the vesicle with the membrane, α-SNAP binds directly to syntaxin-1 and allows NSF to bind at the N-terminus; following adenosine-triphosphate (ATP) hydrolysis these two proteins disassociate and the SNARE complex disassembles (Söllner et al., 1993a; Kee et al., 1995; Hanson et al., 1995).

1.5 Imaging the Exocytotic Machinery

1.5.1 Microscopy in brief

The ability to visualise biological processes at a greater magnification than is possible by eye became achievable upon the creation of the first microscopes in the 15th century (Singer, 1914). Microscope systems are limited by the diffraction of light emitted from single molecules through the optics; a single molecule only a few nanometres in diameter will not appear as a single point but as a diffuse circular disk. These disks of diffracted light are termed Airy disks and were discovered by George Airy in 1827. The light is most intense in the central point with decreasing intensity as distance from this point increases. This distribution of diffracted light in 3-dimensions is termed the point spread function (PSF) and it is characterised by the objective lens and the excitation wavelength. The centre of fluorescence emission from a single molecule can be determined through a statistical fit of a theoretical PSF compared to its measured PSF however under excitation illumination all of the fluorescent molecules within the focal plane will fluoresce and the corresponding PSFs will overlap, making them impossible to assign to their original source. This limitation defines the resolution limit of a microscope, the minimum distance two single molecules need to be apart for them to be defined as single molecules (Pawley, 2006) (Figure 1.3).

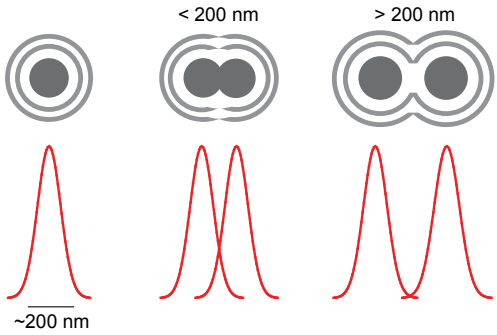

Figure 1.3 The limit of resolution. A single object imaged under light microscopy (left panel) will have a 3D-PSF (red distribution) and be visualised as an Airy pattern (grey cirlces) due to light diffraction and chromatic abberation. Two objects <200 nm apart will be visualised as one object (centre panel) whereas two objects >200 nm apart will be resolved as two (right panel).

Light microscopy has maintained its place at the forefront of biological research through constant improvement on optical aberrations and the resolution at which we can view cellular processes (Abbe, 1873; Denk et al., 1990; Hell and Wichmann, 1994; Hess et al., 2006). Cloning of the green fluorescent protein (GFP) marked a key turning point in fluorescence microscopy, yet still did not allow for the ultra-structural imaging that techniques such as electron microscopy did (Porter et al., 1945). Continued developments have now led to both spatial and temporal observations of single molecules within secretory cells, providing further insight into the intricate process of regulated exocytosis (Patterson and Lippincott-Schwartz, 2002; Betzig et al., 2006; Schermelleh et al., 2010).

1.5.2 The fluorescent proteins

The identification, isolation and cloning of GFP has been a cornerstone in biological imaging and research (Shimomura et al., 1962; Cody et al., 1993). It was identified as a companion protein to Aequorin; a chemiluminescent protein from the Aequorea Victoria jellyfish. Aequorin fluoresces with a blue light (407 nm) and has been shown to efficiently transfer its luminescence energy to GFP causing it to emit light peaking at 508 nm (Morise et al., 1974).

GFP is a 27 kDa protein that after translation folds into an 11-stranded beta-barrel structure with a single alpha-helix running through the centre (Ormo et al., 1996; Zimmer, 2002). This helix is positioned deep within the hydrophobic core of the protein and is where the chromophore, 4-*p*(hydroxybenzylidene)-5-imidazolinone, forms. The chromphore undergoes three steps to become light absorbing: cyclisation, oxidation and dehydration to form a fully conjugated ring structure. This process results in a protein that can fluoresce with a high quantum fluorescence yield and photostability (Morise et al., 1974; Cody et al., 1993; Heim et al., 1994). Wild type (wt)GFP has a minor absorption peak at 475 nm, emitting at 503 nm and the major peak at 395 nm emitting at 508 nm (Heim et al., 1994). wtGFP has been further developed through mutagenesis to produce variants with a

diverse range of properties (Heim et al., 1994; Tsien, 1998). Enhanced GFP (EGFP) is the most commonly used GFP variant in biological applications; it has only one absorption peak at 489 – 490 nm, is 6-fold brighter than wt and matures 4 times faster (Heim et al., 1995; Cheng et al., 1996; Patterson et al., 1997).

GFPs have become a versatile tool in cellular imaging with a range of applications, the most successful being as a fusion tag, which has led to the observation of protein localisation, trafficking and interaction throughout the cell (Marshall et al., 1995; Kaether and Gerdes, 1995; Carey et al., 1996; Presley et al., 1997). GFP has also been utilised as an indicator for calcium increase (Miyawaki et al., 1997; Romoser et al., 1997) and for detecting pH change (Llopis et al., 1998; Miesenbock et al., 1998). The spectral properties of GFP are dependent on the three-dimensional structure of the amino acid residues surrounding the chromophore and specific alterations can produce fluorophores with different excitation/emission spectra (Heim et al., 1994; Heim and Tsien, 1996). The development of variants such as enhanced yellow fluorescent protein (EYFP), enhanced cyan fluorescent protein (ECFP) have allowed for dual colour imaging as well as experiments using Förster resonance energy transfer (FRET) as an indicator of a change in interaction (Tsien, 1998; Patterson et al., 2000; Shaner et al., 2005; Peter et al., 2005). In addition adaptations of GFP have produced photoactivatable (PA-FPs) and photoswitchable (PC-FPs) fluorescent proteins. PA-FPs are ‘switched on’ from a dim to a brighter state after irradiation with UV light (Patterson and Lippincott-Schwartz, 2002; Lukyanov et al., 2005) (Figure 1.4), whereas PC-FPs are photoconverted to emit a different wavelength of light after UV irradiation (Wiedenmann et al., 2004; McKinney et al., 2009).

PA-FPs have revolutionised imaging on conventional microscopes with their application in cellular trafficking, protein interaction and localisation (Patterson and Lippincott-Schwartz, 2002; Giordano et al., 2002; Ando et al., 2004). Photoactivatable (PA)-GFP was the first developed and allowed for the localisation of cellular components below the diffraction limit through photoactivatable localisation microscopy (PALM) (see 2.4.5); a technique that localises single

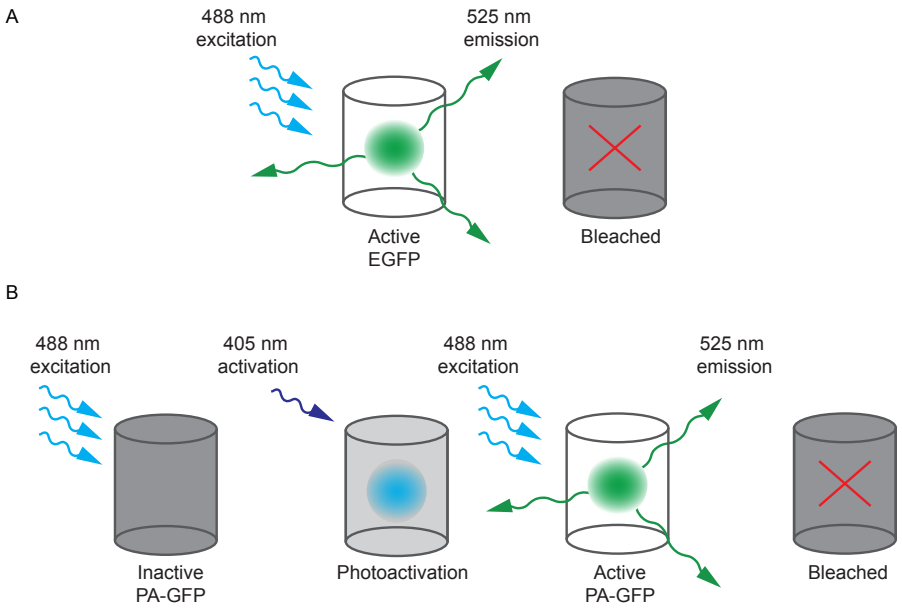

Figure 1.4 Photoactivatable GFP is activated with UV light. A) EGFP is fluorescent under 488 nm light (blue arrows), emiting 525 nm light (green arrows) until it becomes irreversibly bleached (grey cylinder red cross). B) Under 488 nm light PA-GFP is not fluorescent (grey cylinder). After activation with UV light PA-GFP becomes fluorescent under 488 nm light until it becomes irreversible bleached.

molecules by irreversibly ‘switching on’ small subsets of molecules and subsequently bleaching them off (Patterson and Lippincott-Schwartz, 2002; Betzig et al., 2006; Hess et al., 2006). The advancement came from the knowledge that upon activation with UV light wtGFP undergoes photoconversion to a predominantly anionic state with an increase in the minor absorption peak (Chattoraj et al., 1996; Niwa et al., 1996). The mutated variant known as PA-GFP (Thr203H) gave a dramatically reduced minor peak, which upon activation increases in brightness 3-fold (Patterson and Lippincott-Schwartz, 2002). PA-FPs have continued to be developed, the most efficient being PA-mCherry with improved photostability and high single molecule brightness, which has led to dual colour imaging at super-resolution (Subach et al., 2009).

1.5.3 Imaging vesicles at the plasma membrane

It is established that LDCVs in PC12 cells have an average diameter of 365 nm (Plattner et al., 1997) and so are visible under diffraction limited light microscopy systems such as Total Internal Reflection Fluorescence Microscopy (TIRFM) (see 2.4.3) (Rohrbach, 2000; Xia et al., 2004). The ability to image only 100 nm into the base of the cell gives a high signal to noise ratio and has allowed vesicle mobility examination and single fusion event quantification (Steyer and Almers, 1999; Oheim et al., 1999; Johns et al., 2001; Aoki et al., 2010). In addition TIRFM has been successfully combined with capacitance recordings to quantify catecholamine release and investigate fusion (Steyer et al., 1997; Zenisek et al., 2000). Studies using the TIRFM system account for the majority of vesicle behaviour studies; however the recent advances in super-resolution techniques have also been applied to this research area with live stimulated emission depletion microscopy (STED) and use of photoactivatable tags (Willig et al., 2006; Baltrusch and Lenzen, 2008; Westphal et al., 2008).

The most definitive identification of single vesicle fusion under TIRFM is a sudden increase in fluorescence followed by a large freely diffusing cloud, which has

been visualised using acridine orange (Steyer et al., 1997) and EGFP-tagged neuropeptide-Y (NPY) (Lang et al., 1997; Ohara-Imaizumi et al., 2004b; Bai et al., 2007). It has been more recently shown that acridine orange is not suitable in this application as laser illumination of the fluorescent molecule causes vesicles to undergo lysis, causing a flash in fluorescence, which can be mistaken for a fusion event (Jaiswal et al., 2007). In the case of EGFP-tagged proteins the effect is due to the pH-sensitivity of EGFP, which is quenched inside the vesicle lumen at pH 5.5 and upon release into the extracellular space at pH 7.5; the fluorophore increases in brightness before diffusing away (Allersma et al., 2004) (Figure 1.5). This pH sensitivity is due to the protonation and deprotonation of certain residues within the chromophore, which can be mutated to intensify the effect of pH on fluorescence (Palm et al., 1997; Llopis et al., 1998; Miesenbock et al., 1998). The PA-GFP variants have also been applied to vesicle imaging, the most promising being fluorescent timers that have segregated vesicles in relation to age and found this to be a determining factor in vesicle fusion probability (Duncan et al., 2003; Tsuboi et al., 2010).

1.5.4 Imaging proteins past the limit of resolution

It has been established for some time that SNARE proteins at the plasma membrane are not uniformly distributed but are clustered (Lang et al., 2001; Rickman et al., 2004; Low et al., 2006); however the analysis of these clusters has been restricted by the 200 nm resolution limit of conventional microscopes. The introduction of super-resolution techniques has enabled more in-depth probing of these proteins and their partners (Rust et al., 2006; Betzig et al., 2006; Meyer et al., 2009; Lang and Rizzoli, 2010). The most studied until now is syntaxin-1; originally believed to reside in clusters 200 nm in diameter (Lang et al., 2001; Rickman et al., 2004), they were later resolved to 50-60 nm through STED (Sieber et al., 2007). The organisation of the proteins within the clusters has been assessed using direct-stochastic optical reconstruction microscopy (dSTORM) and a gradient that relates to syntaxin-1 reactivity has been suggested (Bar-On et al., 2012). In addition a recent

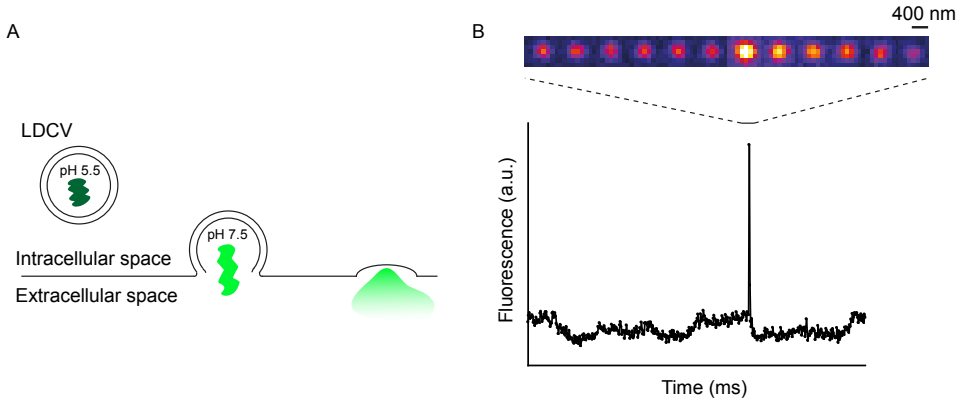

Figure 1.5 Imaging single vesicle fusion at the plasma membrane. A) EGFP is quenched (dark green) at pH 5.5 and upon vesicle fusion is unquenched (light green). EGFP diffuses into the extracellular space. B) A vesicle fusing at the plasma membrane of a PC12 cell (upper panel) and a graph representative of the sharp increase in fluorescence lasting ~50-100 ms upon vesicle fusion (lower panel). Scale bar 400 nm.

study from our group describes a heterogeneous arrangement with drifts of low and high density single syntaxin-1 molecules; clusters of proteins surrounded by more dispersed molecules (Yang et al., 2012). The collection of work described here demonstrates the advantages of using super-resolution imaging to gain insight into molecular localisation; imaging past the limit of resolution reveals highly complex arrangements which are portrayed as large homogeneous clusters in diffraction-limited studies.

It is accepted that the t-SNAREs interact *in vitro* and colocalise at the plasma membrane of live cells under diffraction limited systems (Fasshauer et al., 1997; Ohara-Imaizumi et al., 2004a; Rickman et al., 2004). The visualisation of single molecule interaction in real time may be in the early stages but determining the degree of protein interaction with both temporal and spatial information has been possible for some time by measuring FRET (Förster, 1946). FRET is a measure of energy transfer between two fluorescent probes and is indicative of interaction; this method is described in 2.4.4. This method has been applied to live cell imaging in numerous works looking at the SNARE proteins and have revealed two distinct modes of binding between syntaxin-1 and its chaperone Munc18-1, the trafficking of these proteins and SNAP-25 to the plasma membrane and the transitioning t-SNARE interaction at the plasma membrane (An and Almers, 2004; Rickman et al., 2007; Medine et al., 2007; Rickman et al., 2010).

The application of super-resolution imaging to the study of exocytotic proteins has provided invaluable insight into the mechanism of vesicle fusion but the findings have been limited to a 2-dimensional view. The current challenge for biologists is the examination of single molecules in the x, y and z plane over time in living specimens, which is problematic due to high background noise, the limited speed of acquisition and the high volume of data analysis. Applications are attempting to tackle these; there have been advancements in live cell (Manley et al., 2008) and dual colour (Subach et al., 2009) super-resolution imaging as well as 3D PALM (iPALM) (Shtengel et al., 2009).

1.5.5 Fluorescence imaging of lipid dynamics at the plasma membrane

The application of fluorescence microscopy to the investigation of lipid membranes focused initially on the elucidation of the presence of particular lipid phases (Bagatolli, 2006; Owen et al., 2007). The molecular organisation that these phases could impose on membrane proteins as well as the broader membrane structure has made them an important subject in understanding exocytosis.

Giant unilamellar vesicles (GUVs) have proven an excellent platform for the fluorescence imaging of the lipids as the lipid content can be controlled and the size of the vesicles do not restrict the membrane dynamics (Haverstick and Glaser, 1987; Korlach et al., 1999; Kahya et al., 2003). The synthetic nature of GUV s has attracted criticism however and the use of native membranes and natural lipid extracts has allowed for a more direct comparison to live cells (Dietrich et al., 2001a; Hammond et al., 2005; Lingwood et al., 2008). Laurdan (6-dodecanoyl-2-dimethylamine-naphthalene) (Weber and Farris, 1979), an ampiphillic polarity sensitive dye which inserts into membranes and can label lipid order in cells is the most commonly used fluorescent probe in membrane imaging (described in 2.3.5) (Parasassi et al., 1991; Gaus et al., 2003; Owen et al., 2007). These dyes suffer from rapid bleaching under excitation light and so to minimise this dyes are commonly imaged under two-photon excitation (TPE). TPE reduces the amount of bleaching outside of the focal plane as the wavelength used is of a lower energy (described in 2.4.4), TPE therefore reduces photobleaching throughout the sample and in turn improves the detection of fluorescent signal against background noise (Denk et al., 1990). Imaging of Laurdan by TPE on native GUVs as well as cell membranes has enabled phase separated domain identification and visualisation of the effect that cholesterol and temperature have on these phases (Yu et al., 1996; Parasassi et al., 1997; Bagatolli and Gratton, 1999; Gaus et al., 2003).

Observing the dynamic transitions that lipids undergo at the plasma membrane is a challenge on conventional microscopes as their size is far below that of the resolution limit and they are mobile across the bilayers. Techniques that

attempt to elucidate the mobility of lipids include Fluorescence Recovery after Photobleaching (FRAP) and Fluorescence Correlation Spectroscopy (FCS). These techniques have proven successful and further established the role of cholesterol in raft formation and lipid mobility (Fahey et al., 1977; Dietrich et al., 2001b; Bacia et al., 2004a). Super-resolution techniques, such as STED and Points Accumulation for Imaging in Nanoscale Topography (PAINT) (Eggeling et al., 2009; Kuo and Hochstrasser, 2011) have also been applied to visualise their spatial arrangement in membranes but the visualisation and analysis of membrane lipid dynamics still has far to go.

1.5.6 Visualising the proteins, lipids and vesicles

Currently one of the major questions surrounding the mechanics of exocytosis relates to how the SNARE proteins, the lipids and the vesicles are connected, both temporally and spatially at the site of fusion. The limitations in imaging these components simultaneously lie with the rate at which events can be recorded, the sensitivity of the probes available and the size and dynamic nature of the molecules of interest. These difficulties have been approached through use of amperometric techniques, super-resolution imaging and energy transfer between labelled molecules (Eggeling et al., 2009; Zhang et al., 2009a; Rickman et al., 2010). In addition the application of an “unroofing” method, involving the isolation of native plasma membrane through brief sonication, has provided a useful platform for the study of the SNARE proteins (Avery et al., 2000; Lang et al., 2002). The proteins are more accessible and so more sensitive to analysis and remain within their natural lipid environment.

The localisation of the SNARE proteins in relation to their lipid environment has been extensively studied over the past few decades; however the majority of works have used DRMs or reconstituted bilayers as platforms and these works still debate whether the SNARE proteins prefer more ordered or disordered lipid domains (Chamberlain et al., 2001; Bacia et al., 2004b). Investigation into the importance of

cholesterol in SNARE localisation using microscopy has been minimal and confined to diffraction-limited observations (Lang et al., 2001). More recent work has used FRET to provide access to information beyond the diffraction limit and examine protein-lipid interactions (Zacharias et al., 2002; Silvius and Nabi, 2006), for example between syntaxin-1 and specific phospholipids, such as phosphatidylinositol 4,5-bisphosphate (PIP_2) (Lam et al., 2008; Murray and Tamm, 2011).

One reason for the large volume of research into the localisation of the SNARE proteins is that they are thought to represent the sites for exocytosis (Goda, 1997; Lang et al., 2001). Dual imaging of the SNARE proteins and vesicles under TIRFM revealed a colocalisation between the two components and supports the idea that the t-SNAREs provide the docking and fusion site for exocytosis (Barg et al., 2010; Knowles et al., 2010). Despite the evidence for this spatial arrangement the existence of syntaxin-1 alone in distinct clusters and the apparent transient nature of this protein (Sieber et al., 2007; Bar-On et al., 2009) could suggest the SNARE proteins are not the initial target for vesicles.

The lipid environment at the site of exocytosis is influential over the fusion kinetics and there is accumulating evidence that synaptotagmin mediates this regulation (Schiavo et al., 1996; Bai et al., 2004). Two phospholipids of interest are PIP_2 and phosphatdylserine (PS); both have been shown to interact with synaptotagmin. PIP_2 markedly increases the calcium sensitivity of the protein and increases the fusion efficiency (Gong et al., 2005; Radhakrishnan et al., 2009), in comparison PS is thought to reduce fusion pore dynamics (Domanska et al., 2010). Perturbations in the abundance of these lipids as well as cholesterol have an effect downstream of the fusion site; impairing vesicle docking, vesicle pool size and trafficking (Milosevic et al., 2005; Gong et al., 2005; Zhang et al., 2009a; Koseoglu et al., 2011). The apparent effect of the lipids prior to and upon fusion has suggested that the lipid arrangement is influential over where a vesicle will fuse.

Aims

The extensive research into exocytosis has led to many theories about how the proteins, the lipids and the vesicles behave at the plasma membrane and their spatial and temporal relationship to one another. The majority of this research has been attempting to answer the same question: are there specific sites for vesicle fusion at the plasma membrane and if so how are they determined by the protein and lipid environment? My project aims to further explore this by investigating some specific questions outstanding in the field:

- How does SNAP-25 impose control over exocytosis through its plasma membrane localisation and degree of interaction with syntaxin-1?
- How does the cholesterol content at the plasma membrane influence the t-SNARE interaction, SNAP-25 localisation and vesicle behaviour?
- Is vesicle fusion spatially controlled in specific sites and if so how many SNARE proteins are within these sites?

The fusion event is on a millisecond time scale and the size of the proteins and lipids of interest are below the resolution limit of microscopes, both of these characteristics pose problems in examining the exocytotic event. In addition imaging multiple components simultaneously is problematic as it increases the sampling time when attempting to track an event in real time. Recent advances such as super resolution technologies have bypassed the resolution limit and allowed for the visualisation of single molecules providing a more informative method for SNARE protein localisation. The outstanding questions listed above will be examined within this thesis using the following approaches:

- Lipid order quantification using Laurdan at the plasma membrane of neuroendocrine cells using TIRFM and TCSPC-FLIM
- Characterisation of vesicle mobility in live unstimulated, stimulated and cholesterol depleted cells using TIRFM and the identification of vesicle fusion sites in relation to vesicle mobility.

- Analysis of the single molecule organisation of SNAP-25 and the relationship with cholesterol at the plasma membrane using PALM and dSTORM
- Super-resolution colocalisation of vesicles and single SNARE molecules using PALM
- Quantification of the interaction between the t-SNAREs at intermolecular distances and examination of the importance of cholesterol in this interaction using TCSPC-FLIM.

Chapter Two:

Materials and Methods

2.0 Materials and Solutions

2.0.1 Buffers and growth solutions

Orange G Loading Dye (10x):	50% (v/v) Glycerol
	5 mg/ml Orange G
Sheet Buffer (in deionised (dd) HO):	20 mM HEPEs (pH 7.2)
	120 mM Potassium Glutamate
	20 mM Potassium Acetate
	2 mM EGTA
	2 mM ATP
	0.5 mM DTT
KREBs Buffer (in dd H_2O):	115 mM Sodium Chloride
	5 mM Potassium Chloride
	24 mM Sodium Bicarbonate
	2.5 mM Calcium Chloride
	1 mM Magnesium Chloride
	10 mM HEPEs (pH 7.4)
	0.1% (w/v) BSA
STORM Buffer:	20 mM Cystamine in 1% PBS
	0.5 mg/ml glucose oxidase
	40 µg/ml catalase
	10% (w/v) glucose

2.0.2 Antibodies

Table 2.1 Primary and secondary antibodies for direct immunofluorescence

Antibody	Host	Clone	Dilution for IF	Source
Anti-SNAP25	Mouse	SMI81	1:1000	Sigma Aldrich, UK
Anti-synaptobrevin2	Mouse	69.1	1:500	Synaptic Systems, Germany
Alexa 647	Goat		1:1000	Invitrogen, UK

2.1 Molecular Techniques

2.1.1 Polymerase-chain-reaction (PCR)

The PCR is a molecular biology technique used to amplify DNA using thermal cycling. The Gene Amp PCR System 9700 (Applied Biosystems) was used to carry out PCRs, to either amplify large fragments of DNA (Expand High Fidelity PCR System - Roche, UK) or a few specific nucleotides in oligomer-directed replication (QuikChange Lightning Site-Directed Mutagenesis kit - Stratagene).

2.1.2 Site directed mutagenesis

This process involved the incubation of a supercoiled dsDNA vector, with required insert, and a pair of complimentary oligomers (Sigma Genosys, Sigma-Aldrich, UK) containing the desired mutation and was carried out using QuikChange Lightning Site-Directed Mutagenesis kit (Stratagene).

Table 2.2 Standard PCR reaction

Reagents	**Volume**
10X reaction Buffer	5 µl
DNA template	5 ng/µl of plasmid
Oligomer 1	100 ng/µl
Oligomer 2	100 ng/µl
Nucleotide mix (10 mM of each dNTP)	1 µl
Quiksolution	3 µl
Pfu Ultra DNA polymerase	2.5 U/µl
dd H_2O	Up to final volume of 50 µl

Table 2.3 Standard PCR cycle

Number of cycles	**Temperature** ºC	**Time**
1	95	2 min
18	95	20 sec
	60	10 sec
	68	30 sec/kb
	68	5 min
1	4	∞

The template DNA was initially denatured at 95ºC to give single stranded DNA strands; a drop in temperature then allowed the oligomers to anneal to their complimentary sites within these single strands. The elongation step used *Pfu* Ultra DNA polymerase to drive oligomer-directed replication of DNA at high fidelity, producing strands with staggered nicks at each end. The repetition of this cycle translated to an amplification of DNA to several orders of magnitude. Once complete the amplification reaction was mixed with 1 µl DPNI and incubated for 1 hour at 37ºC. DPNI is an endonuclease which digests only methylated DNA to create blunt ends and allow only newly synthesised DNA to ligate. The resulting sample was run on an agarose gel to confirm the presence of DNA before being transformed into XL-10 Gold ultra-competent *E. coli* cells (Stratagene).

2.1.3 Expand high fidelity PCR

A polymerase enzyme mix (*Taq* DNA polymerase and *Tgo* DNA polymerase) is used in this protocol to extend oligonucleotides, annealed to the DNA plasmid, in a 3' direction. Over multiple temperature cycles this yields a high number of DNA fragments, which can be visualised using gel electrophoresis.

Table 2.4 Standard expand high fidelity PCR reaction

Reagents	**Volume**
10X reaction Buffer (w/ $MgCl_2$)	5 µl
DNA template	5 ng/µl of plasmid
Oligomer 1	100 ng/µl
Oligomer 2	100 ng/µl
Nucleotide mix (10 mM of each dNTP)	1 µl
deionised H_2 O	40 µl
Expand High Fidelity enzyme mix	1 µl

Table 2.5 Standard expand high fidelity PCR cycle

Number of cycles	**Temperature** ℃	**Time**
1	95	2 min
18	94	15 sec
	55	30 sec
	72*	45 sec
20	94	15 sec
	65	30 sec
	72	45 sec
1	72	7 min
1	4	∞

**For DNA fragments < 3kb*

The DNA product was electrophoresed on an agarose gel, removed under UV light and extracted using Qiagen gel extraction protocol (see 2.1.7). This was then ligated into a pGEM-T-EASY vector, transformed and purified using the QIAprep Miniprep Kit (see 2.1.8).

2.1.4 Restriction digests

Restriction digests were performed using Fermentas Fastdigest kits to excise inserts of interest from DNA plasmids.

Table 2.6 Restriction digest reaction

Reagent	**Sample**	**Control**
DNA	3 µl	3 µl
10x *fermentas fastdigest* Buffer	3 µl	-
fermentas fastdigest Enzyme 1	1.5 µl	-
fermentas fastdigest Enzyme 2	1.5 µl	-
dd H_2O	20 µl	27 µl

These reagents were mixed and incubated at 37ºC; after 30 minutes both samples were run on an agarose gel (see 2.1.6) alongside a 1 kb DNA ladder. Once positive samples were clearly separated into insert and vector bands the required DNA bands were cut under UV light and stored separately in eppendorf tubes ready for Qiagen gel extraction protocol (see 2.1.7).

2.1.5 Ligation of insert DNA into vector DNA

After DNA fragments were excised they were ligated to form one plasmid using Fermentas Ligafast kits:

Table 2.7 Ligation reaction

Reagent	Ratio: 1:3	Ratio: 1:1	Ratio: 3:1	Negative control
Vector	1 µl	1 µl	1 µl	1 µl
Insert	0.3 µl	1 µl	3 µl	-
2x t4 ligase buffer	5 µl	5 µl	5 µl	5 µl
deionised H_2 O	2 µl	2 µl	-	3 µl
T4 ligase	1 µl	1 µl	1 µl	1 µl

The above samples were incubated at 4°C overnight or for 20 minutes at room temperature and 5 µl of each was run on a gel to test if the ligation was successful (see 2.1.6). Following this each sample was transformed into E. Coli cells (see 2.1.11). The ligations were performed at varying ratios so that the optimum growth was obtained after transformation.

2.1.6 Gel electrophoresis

To confirm the presence of DNA in a sample we used gel electrophoresis to separate DNA dependent on size and charge, this was achieved by passing an electric current across a gel matrix containing the sample. A 1% (w/v) agarose gel solution in 1 x Tris/Borate/Ethylenediaminetetraacetic acid (TBE) buffer was heated until boiling before SYBR Safe (Invitrogen, UK) was added at a 1:10,000 dilution. This was then poured into a gel tank, with the appropriate gel comb, and allowed to cool.

Once the gel was set it was immersed in TBE 1x buffer and the DNA samples, mixed with equal amounts of Orange G, were added as well as a 1 kb plus DNA marker (Invitrogen, UK). The DNA gels were run at 100 V until the bands were toward the end of the gel and then imaged using a UV light source.

2.1.7 DNA extraction from agarose gel

DNA extraction from agarose gel was performed using the QIAquick gel extraction protocol. The Gel fragment was visualised using a UV light source and excised using a scalpel, the fragment was immersed in 300 µl of QG buffer and heated for 10 minutes at 50ºC until fully dissolved. Isopropanol (100 µl at 100%) was added and mixed; the sample was then applied to a QIAquick spin column and centrifuged for 1 minute. Flow-through was discarded and 0.5 ml QG Buffer was added to the sample, this was then centrifuged for 1 minute, flow-through discarded. To wash 0.75 ml of PE Buffer was added and the sample centrifuged for 1 minute, the flow-through was discarded and the sample centrifuged again to remove any residual buffer. DNA was eluted into a clean 1.5 ml microcentrifuge tube, 50 µl of elution buffer (EB) was added, let stand for 1 minute and then centrifuged for 1 minute.

2.1.8 DNA purification

Small scale DNA purification was performed using a QIAprep Miniprep Kit (Qiagen) according to instructions. A single colony was picked using a sterile pipette tip and placed inside a universal tube containing 5 ml Lysogeny Broth (LB) and the 5 µl of the specific antibiotic (1:1000 dilution). The starter culture was then incubated overnight on the shaker, 200 rpm and 37ºC to allow optimum bacterial growth.

Extraction of bacterial cells from the overnight culture was achieved by centrifugation at 4,500 rpm for 10 minutes in a swinging bucket conventional table

top centrifuge. The resulting pelleted cells were resuspended in 250 µl Buffer P1 and transferred to a microcentrifuge tube. Buffer P2 (250 µl) was added followed by 350 µl Buffer N3; both reagents were mixed by inversion of the tube. The samples were centrifuged for 10 minutes at 13,000 rpm in a table top centrifuge and the resulting supernatant was added to a QIAprep spin column. These columns were spun for 30-60 seconds and the flow-through discarded. The column was then washed with 0.5 ml PB Buffer and centrifuged again for 30-60 seconds, flow-through discarded. A second wash was performed using 0.75 ml PE buffer (ethanol added), centrifuged for 30-60 seconds and flow-through discarded. To elute the DNA the column was placed in a clean microcentrifuge tube and 50 µl EB Buffer was added, let stand for 1 minute and then the tube was centrifuged for 1 minute.

2.1.9 Large scale DNA purification

This was performed using UltraPure Maxi Prep kits (Invitrogen, UK). A single colony was picked using a sterile pipette tip and placed inside a universal tube containing 5 ml LB and the 5 µl of the specific antibiotic (1:1000 dilution). This starter culture was then incubated for 8 hours on the shaker at 200 rpm and 37ºC. The culture was then poured into 250ml of LB media and 250 µl of the appropriate antibiotic (1:1000 dilution) and shaken overnight at 200 rpm and 37ºC to maximise growth.

HiPure Maxi Columns were equilibrated by allowing 30 ml of EQ1 Buffer to flow through. The overnight culture was decanted into 250 ml centrifuge bottles and centrifuged at 5,000 x *g* for 10 min at 4ºC, 10 ml resuspension buffer was added and the cells homogenised using a pastette. The cells were lysed by adding 10 ml L7 Buffer and incubated for 5 minutes; 10 ml precipitation Buffer was then added and the cells mixed. This solution was then added to a filter column and allowed to pass through and the flow through discarded. The column was washed with 60 ml Wash Buffer and the DNA eluted by adding 15 ml E4 Buffer to the washed column. Once eluted, 10.5 ml of 100% v/v isopropanol was added to the tube to precipitate DNA.

This was centrifuged for 30 minutes at 15,000 x *g*, the supernatant discarded and 25ml 70% ethanol was added before further centrifugation for 10 minutes. The remaining pellet was left to dry and then resuspended in 500 µl deionised H_2O.

2.1.10 DNA quantification

In preparation for sequencing by CoGenics, DNA was quantified through spectroscopy at 260 nm absorption. DNA was diluted 1:200 with deionised H_2O and measured using a Thermo Electron Corporation, Biomate 3 UV-Vis Spectrophotometer. Hellma 6040-UV 10 mm Quartz cuvettes were used.

2.1.11 Transformation

DNA was grown in XL-10 Gold ultra-competent *E. coli* cells (Stratgene), which were initially allowed to defrost on ice before being aliquotted into sterile, ice cold, eppendorf tubes. Cells (35 µl) were then mixed with 5 µl of sample (for higher concentrations of DNA this was reduced to 1 µl) and incubated on ice for 10 minutes so the DNA could adhere to the cells. This was followed by heat shock to allow the cells to incorporate the DNA; the cells were incubated for 30 seconds in a 42ºC water bath and then immediately placed back on ice. To rescue the cells from this they were dispensed into 0.5 ml of LB and left for 30 minutes on the shaker, 200 rpm and 37ºC to allow optimum bacterial growth. Under a Bunsen burner 100 µl and 10 µl were then plated onto two separate plates, to optimise the subsequent picking of colonies, and left overnight at 37ºC.

2.1.12 Agar plates

Agar (250 ml) was warmed to the correct temperature and 250 µl of the appropriate antibiotic (1:1000 dilution) was added and mixed in. The agar was then

poured out onto plates; this volume made approximately 12 plates. Whenever the agar was in contact with the air it was underneath a Bunsen burner and therefore sterile.

2.1.13 Immunostaining

Cells were fixed (see 2.3.3) and then incubated on ice with 0.5% (v/v) triton X100 in phosphate buffered saline (PBS) for 4 minutes followed by 1% v/v PBS + 0.5% w/v fish skin gelatine (FSG) for 15 minutes. Cells were removed from ice and the desired antibody was diluted 1:1000 in 1% v/v PBS + 0.5% w/v FSG, added to the fixed cells, and incubated at room temperature for 3 hours in a humidified container. Cells were washed thoroughly with 1% v/v PBS + 0.5% w/v FSG, secondary antibody was added in a 1:1000 dilution and incubated at room temperature for 1 hour. The cells were finally washed extensively with PBS and stored in the dark in PBS at 4ºC.

2.2 Cell Culture

Cell culture reagents were supplied by Gibco (Invitrogen, UK) and all plastic ware by Greiner UK.

2.2.1 Cell storage and reuse

For long-term storage of cells, 1ml of confluent cells in growth media was added to 10% (v/v) dimethyl sulfoxide (DMSO) and aliquoted into 1.5 ml cryotubes (Nunc™). These cells were frozen using dry ice immersed in 100% v/v isopropanol and then stored in liquid nitrogen. To reuse the cells, vials were briefly defrosted, cells added to 50 ml of warm media and centrifuged for 5 minutes at 5,000 x *g* in a

swinging bucket tabletop centrifuge to remove DMSO. The cells were then resuspended, decanted into a 25 cm flask and maintained at the appropriate conditions.

2.2.2 Cell maintenance

All cells were maintained in media containing 5 or 10% v/v of foetal bovine serum (FBS) as well as the supplements described in Table 2.3.3. Mouse Neuroblastoma 2a (N2a) were maintained at 37ºC in 5% (v/v) CO_2, 95% (v/v) air. Cells were passaged by removal of waste media followed by trituration with fresh media, to both wash them off the flask and resuspend them. The cells were then reseeded into sterile T75 cm flasks. PC12 cells were maintained at 37ºC in 7.5% (v/v) CO_2, 92.5% (v/v) air as well as Human Embryonic Kidney (HEK) 293 cells. PC12 cells had to be cultured onto collagen coated T75 cm flasks; the cells therefore required versene to loosen the cells. Once the waste media was removed 5 ml of warm versene was added, washed over the cells and then discarded. Fresh media was then used to wash the cells off the flask, which were then added to a 50 ml Falcon tube and resuspended at 5,000 x *g* for 5 minutes. The pelleted cells were then triturated to split the cells up and reseeded into T75 cm collagen coated flasks, usually in a 1:3 dilution. Flasks were coated with 200 µl collagen and left under UV light overnight in the tissue culture hood.

2.2.3 Cell culture media

Table 2.8 Cell culture media

Cell Line	Growth Medium	Media Supplements	Supplier
N2a	Dulbecco's modified Eagle's medium (D-MEM)	10% (v/v) FBS 10 mM L-Glutamine 50 units penicillin 50 µg/ml streptomycin	ATCC*
HEK 293	DMEM	10% (v/v) FBS 0.1% Glutamax 1% pen-strep	ATCC*
PC12	Advanced RPMI 1640	5% (v/v) FBS 10% Horse serum** 1% Glutamax 50 µg/ml Gentamicin	ATCC*

* American Tissue Culture Company, Middlesex, UK.

** Hyclone, UK.

2.2.4 Preparation of coverslips

Glass coverslips (30 mm) were held for 30 seconds in a sonicator, containing 100 mM Sodium Hydroxide and 0.1% v/v Decon-90, to remove any unwanted material. They were then washed 3 times in deionised water followed by immersion in 100% v/v ethanol. Finally the coverslips were washed in 100% v/v acetone and left to dry.

Coverslips were incubated in Poly-D-lysine (PDL) (0.5 mg/ml) at room temperature for up to an hour to provide an efficient adhesive mesh for the cells. The PDL-coated coverslips were then washed using deionised H_20 in a sterile hood and left to dry under UV light for 1 hour. Unless used immediately the coverslips were stored in the fridge.

2.2.5 Cell transfections

Cells reached 60-70% confluency before being cultured onto PDL-coated glass coverslips at approximately 10^6 cells/ml and were maintained at 37ºC in 5% (v/v) CO_2, 95% (v/v) air. Cells were incubated for 24 hours before being transfected. Transfections into N2a cells were performed using ExGen 500 (Fermentas) and Lipofectamine 2000 (Invitrogen, UK) was used for PC12 cell transfections, both were as per the manufacturer's instructions. Post transfections cells were incubated for 48 hours at 37ºC in 5% (v/v) CO_2, 95% (v/v) air.

2.3 Experimental Cell Conditions

All live cells were imaged within a POC (Perfusion Opened-Closed)-chamber system (La Con, Germany) and maintained on a heated stage (37ºC) in a chamber containing 5% (v/v) CO_2, 95% (v/v) air.

2.3.1 Cell stimulation

Live cells were triggered to undergo exocytosis through cell stimulation experiments in KREBs Buffer adjusted to 290 mOsM. ATP was made up in KREBs Buffer to 600 µM and then 500 µl of this was added to 500 µl KREBs buffer already inside the POC chamber via a syringe, giving a final concentration of 300 µM. ATP is known to propagate a calcium-dependent secretion of catecholamine from PC12 cells (Keath and Westhead, 2004; Pouli et al., 1998). The mechanism involves activation of ionotropic purine receptors, which allow calcium to enter the cell and triggers release from intracellular calcium stores (Nakazawa et al., 1990; Inoue and Nakazawa, 1989).

2.3.2 Cholesterol depletion

Cholesterol was depleted using MβCD a cholesterol chelating agent that sequesters cholesterol from cell membranes (Ohtani et al., 1989). Cells were incubated with 10 mM MβCD in non-phenol red serum-free media for 30 minutes at 37ºC prior to either live cell imaging, fixation or unroofing.

2.3.3 Cell fixation

Live cells were washed twice with PBS then immersed in 4% w/v paraformaldehyde (PFA) and incubated for 20 minutes (1 hour if cells for a PALM experiment). The cells were then incubated for 10 minutes in 50 mM NH_4Cl and stored in PBS at 4°C. This was either at 4°C or 37°C depending on the experiment design.

2.3.4 Cell unroofing

Cells were unroofed to produce plasma membrane sheets (Avery et al., 2000). Cells (pre-plated on coverslips 24 – 48 hours before) were washed in sheet buffer and then immersed in 50 ml sheet buffer in a 500 ml glass beaker. Each coverslip was sonicated once for 10 seconds (PC12 cells) and 5 seconds (HEK 293 cells) at 40% (Lang, 2008).

2.3.5 Laurdan staining

Laurdan (6-dodecanoyl-2-dimethylamine-naphthalene) (Invitrogen, UK) reports on lipid phases by inserting its hydrophobic pole in between the lipids, positioning its fluorescent moiety towards the aqueous environment. The dye can then display shifts in emission spectrum with varying levels of lipid order. In gel-

phase Laurdan emission is centred at 440 nm, whereas when in its liquid-crystalline phase the emission shifts to centre at 490 nm. This can be explained by the increased accessibility of water molecules when Laurdan is within a less ordered region of lipids. The dipole moment possessed by Laurdan is increased when Laurdan is excited and may cause reorientation of the surrounding solvent dipoles, causing a red shift in Laurdan emission (Parasassi et al., 1991; Weber et al., 2010; Weber and Farris, 1979) (Figure 2.1). Laurdan was added to live, unroofed or fixed cells at a concentration of 5 μM in sheet buffer (see 2.0.1) and incubated for 1 hour. A fresh solution of 5 μM Laurdan in sheet buffer was applied for imaging. FLIM experiments were recorded on the CLSM using a multi photon laser set at 780 nm, which excited within the UV range (350-400 nm) under two-photon excitation (described in 2.4.4). Lipid order recorded using TIRFM excited Laurdan with a 405 nm laser and 440/40 nm and 525/50 nm filters with a suitable dichroic mirror. This allowed for the ratiometric analysis of Laurdan emission with signal collected in two channels (described in 2.5.5).

2.3.6 Calcium dye loading

Fluo-3AM dyes are almost non-fluorescent at basal cytosolic calcium concentrations of ~0.1 μM and can increase in fluorescence up to 100 fold by binding calcium ions (Minta et al., 1989). The dye (Invitrogen, UK) was reconstituted with anhydrous DMSO and loaded into cells at 1 μM in KREBs buffer (see 2.0.1) at 37°C with no CO_2 for 30 minutes. Cells were washed with KREBs buffer twice and imaged under a 488 nm laser in KREBs buffer at 37°C with no CO_2. For control experiments ionomycin was added to the stage at a final concentration of 1 μM. ATP was added as in 2.3.1.

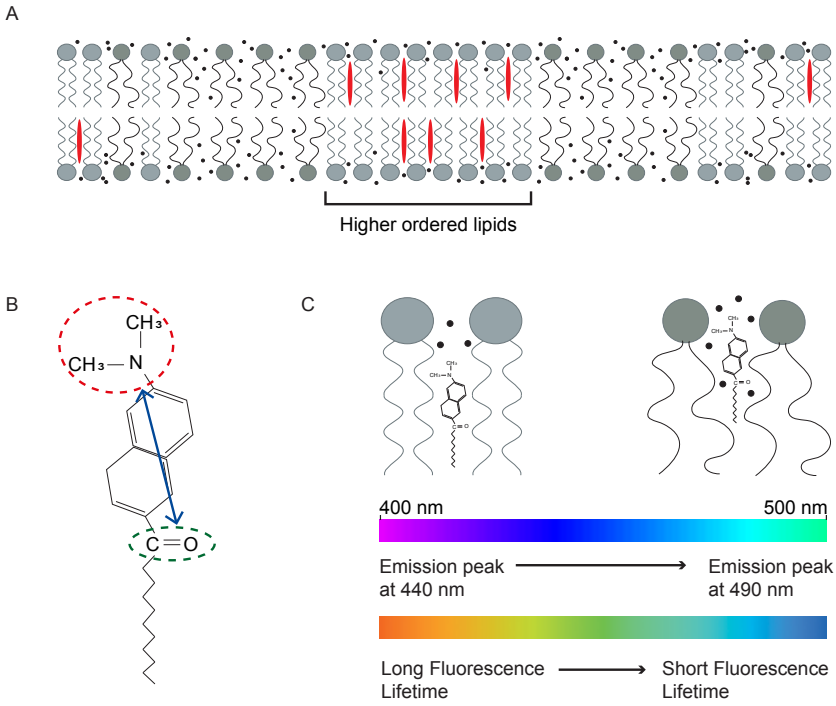

Figure 2.1 Laurdan reports on lipid order in membranes. A) A schematic of the plasma membrane interspersed with phospholipids (dark grey), glycosphingolipids (light grey) and cholesterol (red). Regions of higher order contain cholesterol and sphingolipids (bracket) and water molecules (black circles) penetrate less. B) Chemical structure of Laurdan displaying the dipole moment (blue arrow) between 2-dimethylamino (red dashed) and the 6-carbonyl residues (green dashed). C) Laurdan inserts in between lipids with its fluorescent moiety towards the polar lipid head. In less ordered lipids (right) Laurdan is more accessible to water moleulces and there is a red shift (440 nm to 490 nm) or a decrease in fluorescent lifetime.

2.4 Imaging Techniques

2.4.1 Confocal laser scanning microscopy (CLSM)

Confocal microscopy uses a light source to excite a sample and collects the emitted light using detectors within the system. Light emitted from a sample will include in and out of focus light; the collection of both results in a distorted image. Confocal microscopes use pinholes to reject the out of focus light reaching the detector, providing a more accurate description of the sample (Robinson, 2001). An image is acquired using a confocal laser scanning microscope (CLSM) by scanning every pixel in turn across the x-y coordinates of a sample. By rejecting out of focus light and collecting photons from every pixel a highly informative image can be recorded.

Images were acquired using an LSM510 scan head filtered to a Zeiss Axiovert 100M inverted microscope, which enables point by point illumination of pixels. A Zeiss Plan NeoFLUAR 1.4 NA 63x oil immersion objective lens was used and images were set to contain 1024 X 1024 pixels. Digital zoom was set according to the Nyquist sampling frequency of the system (see 2.5.1) giving a pixel size of 43 nm^2. A MIRA 900 Ti:Sapphire femto-second pulsed laser at 800 nm was used for TCSPC-FLIM experiments (see 2.4.4). The detectors used were photo multiplier tubes (PMTs) (H7422; Hamamatsu Photonics UK), which detect a photon and convert it into a current that can be turned into a digital signal. The PMT detector gain and amplifier offset were adjusted so that voxel intensities were spread over the full dynamic range. The exposure of the specimen to the laser light as well as the laser intensity was limited to minimise phototoxic effects and bleaching.

2.4.2 Widefield fluorescence microscopy

Widefield fluorescence microscopy differs from a confocal microscope as it illuminates the entire sample at once and does not exclude out of focus light as no pinholes are used. A widefield microscope can acquire an image over a much shorter

time frame than a confocal microscope but the resultant image has to be deconvolved to reallocate the light emitted from the sample (see 2.5.1).

Images were obtained on an Olympus IX81 fully motorised microscope controlled by Olympus CellR software. Excitatory light was supplied using a Xenon mercury lamp and subsequent light emitted was detected using an ImageEM EMCCD (Hamamatsu). An Olympus PLAN APO 1.45 NA x150 oil immersion objective was used and images contained 512 x 512 pixels (set by the camera) with a pixel size of 106 nm^2. The electron-multiplying (EM) gain for the camera was set depending on the experimental design.

2.4.3 Total internal reflection microscopy (TIRFM)

Total internal fluorescence microscopy is a technique that allows for high contrast imaging of a thin optical section by selective excitation within an evanescent field (Figure 2.2). When excitatory light passes from a medium of high refractive index (glass RI: 1.518) to a medium of lower refractive index (water RI: 1.33) the light is refracted. If the light hits the interface at or above the critical angle, the angle of incidence that gives an angle of refraction of 90 degrees, then the light is internally reflected. Internal reflection of this light creates an evanescent field within the sample, which subsequently illuminates only a thin layer above the glass interface. This evanescent field decays proportional to the distance from the interface giving a reliable working distance of approximately 100 nm into the sample (Stout and Axelrod, 1989). The selective illumination creates an image with minimal out of focus light and therefore a high signal to noise ratio and minimal bleaching of the sample above the evanescent field.

TIRFM was performed on an Olympus IX81 fully motorised microscope (see 2.4.2), controlled by Olympus CellR software and integrated with a Xenon mercury lamp and 488 and 561 nm diode lasers through independent condensers. An Olympus PLAN APO 1.45 NA x150 oil (RI: 1.515) immersion objective was used as the

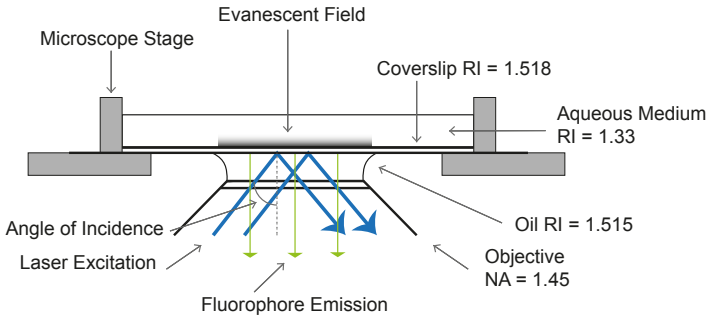

Figure 2.2 Imaging using total internal reflection fluorescence. Laser excitation light (blue arrow) passes from a high refractive index (RI = 1.518) to a low refractive index (RI = 1.33) and undergoes total internal reflection when the angle of incidence is at or above the critical angle.

refractive index of oil is close to that of glass and minimised unwanted light diffraction. Data were acquired on a Hamamatsu Electron Multiplier CCD digital camera. The critical angle was reached and the depth of field adjusted by manual manipulation of a micrometer screw in the illuminator. The system included excitation and emission filters, which allowed for fast sequential acquisition in green and red channels.

2.4.4 Time correlated single photon counting – fluorescence lifetime imaging microscopy (TCSPC-FLIM)

A fluorescent molecule is excited when a photon of specific energy is absorbed and an electron within the molecule moves from the ground state to an excited state; this excitation can occur through single photon excitation or through two-photon excitation (TPE) (Figure 2.3) (Denk et al., 1990). TPE occurs when two photons of lower energy are simultaneously absorbed and their energy combines to excite a fluorophore with a higher energy excitation wavelength. Two photons are most commonly absorbed spontaneously at the focal point and so using TPE reduces out of focus bleaching and provides a high resolution image. TPE requires a pulsed laser with a high repetition rate so that the likelihood of a molecule absorbing two photons at the same time is increased. Within the excited fluorophore the electron at a higher energy state will fall back down to ground state after a certain period of time and emit a photon of lower energy, this time period is known as the fluorescence lifetime (Lakowicz, 1999). To measure the fluorescent lifetime the time at which a fluorophore absorbs a photon and the time at which a photon is emitted needs to be recorded at the level of single photons, this is possible with time correlated single photon counting (TCSPC) (Becker, 2005). Similar to TPE this method uses a pulsed laser with a high repetition rate, for TCSPC this important so that there is short time period over which a photon can be detected thereby increasing the probability of detecting one photon (one event) within a pulse and determining the fluorescence lifetime.

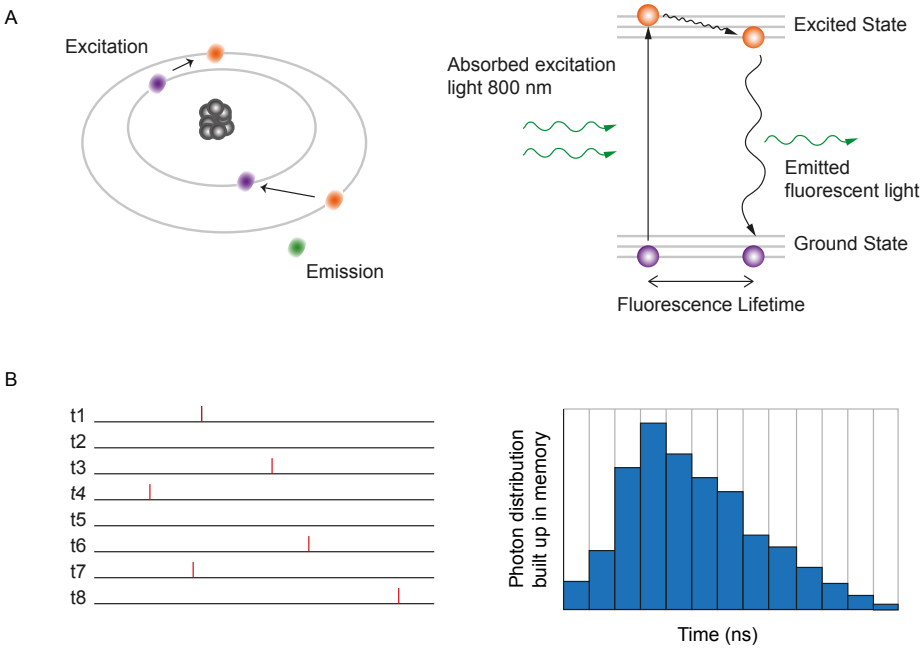

Figure 2.3 TCSPC-FLIM. A) An electron is excited to an excited state (orange) and emits a photon upon its descent back to ground state (purple). The time spent in the excited state is the flourescent liftetime (left panel). Two photons (green arrows) absorbed within 1 attosecond at 800 nm excite a fluorophore with 400 nm energy (two photon excitation) (right panel). B) The time between the detection of a photon (red line) and the start of the laser pulse (ie. t1) is recorded using reverse start-stop. The fluorescent lifetime calculated from this is recorded for every pixel in an image to give a photon distribution (blue bars), which can be fit to an exponential.

TCSPC-FLIM provides highly accurate information about the properties of a fluorophore and can be used to measure interaction between two fluorescent molecules. The light emitted from an excited fluorophore can excite a different fluorophore if the excitation and emission spectra overlap, the molecules are correctly orientated and they are within intermolecular distance (>6 nm) (Figure 2.4). This transfer of energy from a donor to an acceptor fluorophore is known as FRET (Förster, 1946; Morise et al., 1974; Stryer, 1978). The detection of a change in FRET is informative of a change in the interaction status of two fluorescent molecules. FRET can be measured by an increase in acceptor fluorescence intensity, however this does not rule out any changes due to the concentration of the proteins. Fluorescent lifetime on the other hand is not dependent on concentration and so by measuring change in donor fluorescence lifetime using TCSPC-FLIM a direct measure of interaction can be obtained (Lakowicz, 1999).

All imaging experiments were performed on a Zeiss LSM510 Axiovert confocal laser scanning microscope, equipped with a pulsed excitation source (MIRA 900 Ti:Sapphire femto-second pulsed laser coupled with a VERDI 10 W pump laser (Coherent)) capable of delivering pulses of photons at a repetition rate of 80 MHz (every 12.5 ns). A reverse start-stop system was used where the time between a photon being detected and the next laser pulse was recorded. As the time between pulses was known (12.5 ns) then the time between the first laser pulse (photon absorbed) and the photon being emitted was calculated. This time lag (fluorescent lifetime) was recorded within every pixel for every frame of a recording; these values were then displayed as a histogram and fit to an exponential (see Figure 2.3). The half-life time constant of this exponential equated to the average fluorescence lifetime of the fluorophore being measured. The time period between laser pulse and photon release is stochastic so to ensure optimum photon count and therefore an accurate read out images were taken for 60 seconds, with a mean photon count of 10^5 – 10^6 counts per second. For SNARE protein FRET based TCSPC-FLIM experiments EYFP was tagged to the C-terminus of the second SNARE helix of SNAP-25 and mCerulean was tagged to the Habc domain of syntaxin (Figure 2.5).

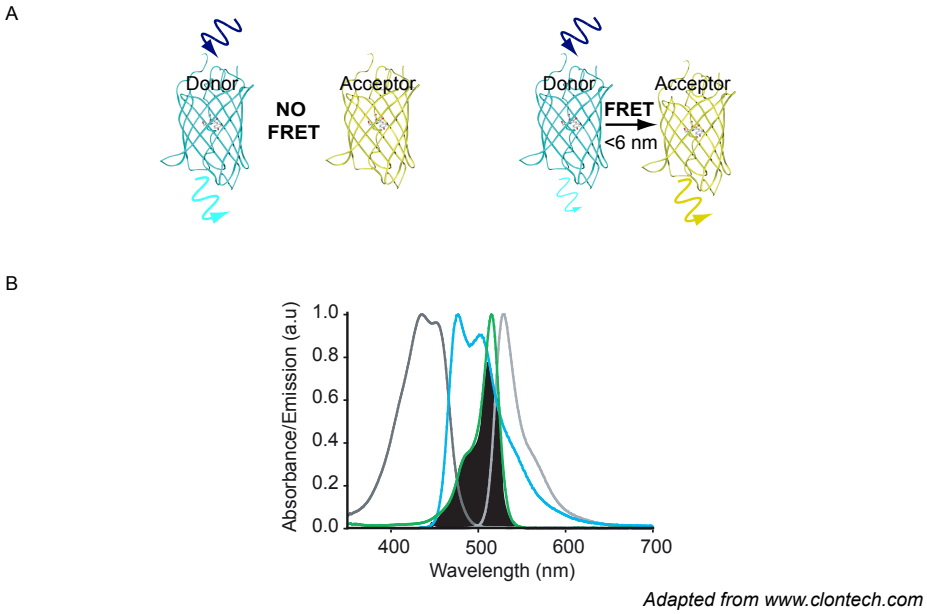

Figure 2.4 FRET between Cerulean and EYFP. A) Cerulean (donor) is excited with ~433 nm light (dark blue arrow) and emits ~ 475 nm light (cyan arrow). When EYFP (acceptor) is within intermolecular distance (<6 nm) FRET occurs and Cerulean excites EYFP, which emits light at ~527 nm (yellow arrow). B) FRET is possible due to overlapping excitation and emission spectra of these fluorophores and a paralell orientation. Cerulean excitation (dark grey), Cerulean emission (cerulean), EYFP excitation (green), EYFP emission (light grey) and overlapping excitation/emission wavelengths (black fill).

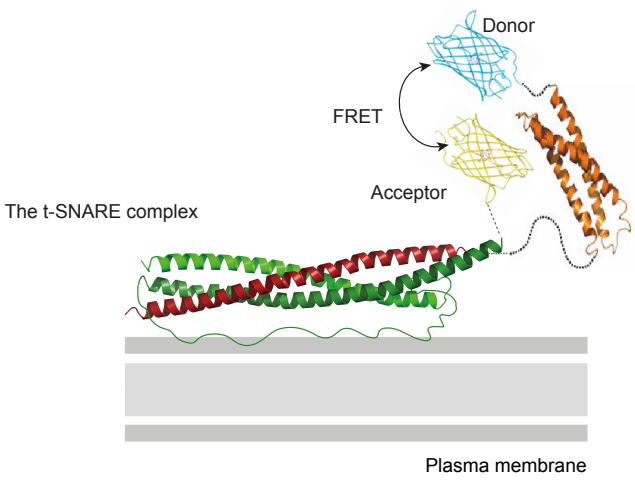

2.5 FRET between the SNAREs. FRET between EYFP-SNAP-25 (green) and mCerulean-Syntaxin (red) indicates change in the t-SNARE conformation. SNAP-25 is tagged with EYFP (yellow ribbon structure) at the C-terminus of SNARE helix 2. Cerulean (cyan ribbon structure) is tagged to the N-terminus of the Habc domain of syntaxin (orange). A change in the interaction between these two proteins evokes a change in distance between the two fluorophores and the change in energy transfer can be detected using FLIM. Not to scale.

2.4.5 Photoactivated localisation microscopy (PALM)

To localise a fluorescent single molecule under diffraction-limited microscope systems the PSF needs to be resolvable, as described in 1.5.1. PALM achieves this by decreasing the density of molecules imaged at one time so there are few enough to be resolved and therefore localised (Patterson and Lippincott-Schwartz, 2002; Hess et al., 2006; Betzig et al., 2006). This occurs through serial photo-activation of a small subset of PA-FPs, which can be switched on and subsequently photo-destroyed in a quantal manner (Figure 2.6). The localisation of these molecules is stored and another subset activated; after adequate rounds of this a localisation map can be extracted, showing single molecules across the base of a cell. The bleaching of a single molecule is permanent which ensures no molecules are mapped twice within a cell (Hess et al., 2006).

This technique was applied using TIRFM; cells were transfected with PA-Cherry (Subach et al., 2009) tagged to the protein of interest and fixed with 4% PFA (see 2.3.3). Cells were then imaged in 1% PBS. PA-Cherry was activated by DAPI epifluorescent light source at 405 nm and then rapidly imaged and bleached off using a 561 nm diode laser set at maximum. Activation and bleaching steps were optimised to ensure a sparse distribution of single molecules were activated and bleached in each cycle. Before each cell experiment the vesicles were imaged in TIRFM using a 488 nm diode laser for nearest neighbour analysis.

2.4.6 Direct - stochastic optical reconstruction microscopy (dSTORM)

dSTORM is a super-resolution technique, which determines the centre of emitted fluorescence from single molecules and therefore localises them in a similar way to PALM through serial activation and photobleaching (van de Linde et al., 2011). Unlike PALM however dSTORM uses conventional fluorescent dyes that can reversibly switch between the fluorescent and the dark state, this means that one

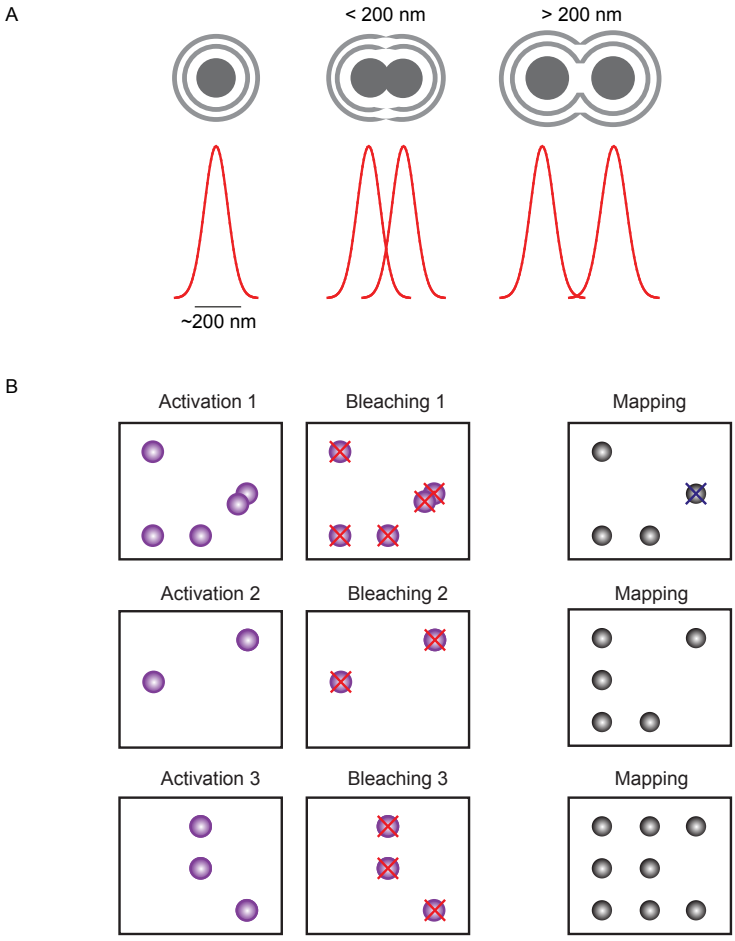

Figure 2.6 PALM below the “limit of resolution”. A) A single object imaged under light microscopy (left panel) will have a PSF (red distribution) and be visualised as an Airy pattern (grey cirlces) due to light diffraction and chromatic abberation. Two objects <200 nm apart will be visualised as one object (centre panel) whereas two objects >200 nm apart will be resolved as two (right panel). B) PALM images a small subset of molecules each activation cycle (purple spheres left panels). These are irreversibly bleached off (red cross - centre panels) and their location recorded (grey spheres right panels). Molecules switched on in one cycle that are >200 nm apart cannot be resolved and are not localised (blue cross).

molecule can be activated more than once but in balance dSTORM provides information on the endogenous proteins rather than the exogenous.

dSTORM experiments were performed in unroofed PC12 cells (see 2.3.4) that were fixed and immunostained with SM18-1 and Alexa-647 for SNAP-25 (see 2.1.13). Imaging was performed on the nose piece stage to minimise lateral drift and this was calibrated to 37°C. Cells were imaged in dSTORM buffer (see 2.0.1) (van de Linde et al., 2011) with Laurdan at a final concentration of 5 μM. Alexa 647 was activated using a 640 nm laser and imaged for approximately 30 minutes.

2.5 Analysis and Data Processing

2.5.1 Deconvolution and Nyquist sampling

A single fluorescent molecule has a PSF determined by the optics of the microscope system, as described in 1.5.1. Under Widefield illumination out of focus emitted light is collected from the sample and degrades the resultant image, deconvolution is a process that reassigns this light and provides a more accurate representation of the sample. Image acquisition can be optimised using Nyquist sampling rates, which describe the required sampling density (size of pixel) to obtain enough information to produce a reliable PSF that best describes the real signal. This rate is dependent on the degree of light diffraction, which is influenced by the numerical aperture of the lens, refractive index of the imaging medium and the wavelength of the excitation and emission light (McNally et al., 1999; Sibarita, 2005).

Images were acquired at Nyquist sampling rates throughout the thesis. Data obtained on the Olympus microscope were deconvolved using Huygens software (Scientific Volume Imaging, The Netherlands), using a theoretical PSF calculated from the microscope parameters, and were analysed using NIH Image J software.

2.5.2 Vesicle mobility analysis

All vesicle experiments were undertaken in PC12 cells expressing EGFP-NPY, acquired at 20 Hz at 37ºC in 5% (v/v) CO_2, 95% (v/v) air and imaged using an Olympus IX81 fully motorised microscope, controlled by Olympus CellR software under TIRFM (see 2.4.3). Vesicles were identified and tracked using either Imaris 7 software (Bitplane) or Matlab (Mathworks), which track the vesicles based on their centroid position. Vesicles that fused were distinguished by a sharp increase in fluorescence, lasting only 50 ms, followed by a rapid decay in fluorescence. This was analysed using Image J to quantify the change in fluorescence over time within the area of the vesicle.

2.5.3 PALM and dSTORM data analysis

Single molecule maps obtained through PALM can be analysed using Ripley's K function, which is a statistic that can be used to summarize a point pattern, test a hypothesis about a pattern, estimate parameters and fit models (Ripley, 1977). Ripley's is concerned with the location of events within a predefined study area and their distribution; whether clustered, regular or random. The pattern of distribution is determined through multi-distance spatial cluster analysis, usually in 2D.

The K function:

$$K(t) = \lambda - 1\ E$$

where E is the number of events within distance t of a randomly chosen event and λ is the density (number per unit area) of event, describes characteristics of the point processes at many distances. It is related to the nearest neighbour function (Bartlett, 1963; Besag, 1972); however the two functions describe different aspects of the point process. Nearest neighbour function is particularly useful in physical and biological sciences and encapsulates approximately six different types of statistical methods. It gives the probability density associated with finding a nearest neighbour at some

given distance from the reference particle within a completely mapped area. This has been applied to previous works in neurons (Jafari-Mamaghani et al., 2010).

PALM and dSTORM data were analysed using Matlab and Image J. Image J software was used for the combining of activation time 1 and 2 for activated molecules and averaging of both these and the vesicles. All the molecules recorded within activation 1 and 2 were localised using a custom localisation script provided by Samuel Hess (Maine) on Matlab, applying thresholding to ensure background noise was not included. These data were then rendered to create a molecular map describing the localised positions of the single molecules at the plasma membrane. The PALM data were then analysed in Matlab using Ripley's K function and nearest neighbour (script designed by Ondřej Mandula (University of Edinburgh)) to quantify single molecule distribution and the relationships with neighbouring vesicles.

2.5.4 TCSPC-FLIM analysis

FLIM data were analysed using pixel-based fitting software (SPCImage, Becker & Hickl). The fit parameters were optimised using the Levenberg-Marquardt algorithm, which minimizes the weighted chi-squared quantity.

2.5.5 Laurdan staining analysis

One method of quantifying the extent of water dipolar relaxation surrounding Laurdan utilises the relationship between the emission intensities obtained on the blue and red side of Laurdan's emission spectrum. This relationship is termed Generalised Polarisation (GP) and directly reports on the phase state of the lipid environment (Parasassi and Gratton, 1995). The calculation for GP is shown below where I_B = intensity of the blue channel and I_R = intensity of the red channel,

$$GP = \frac{I_B - I_R}{I_B + I_R}$$

This calculation was performed in Image J and GP values are presented as an average of the GP for each pixel inside a region of interest inside a cell. Fluorescent lifetime of Laurdan has not previously been recorded but the theory is described in 2.3.5. In these experiments shifts in Laurdan emission were detected using FRET-based FLIM, which calculated a change in fluorescence independent of concentration and scatter in every pixel of the image. These data were analysed using SPCM (Becker & Hickl).

2.5.6 Statistical analysis

In an experiment data were acquired from at least 3 cells from one or more coverslips, data sets shown throughout this thesis combined data taken on different days under the same conditions. The n number describes the number of cells within each data set. The error within these data sets is displayed as the standard error of the mean (SEM), unless otherwise stated, as this reports on how good the estimation of the mean is rather than the variation of the data. The significance of difference between data sets was assessed using either the Mann Whitney rank sum test or the extra sum of squares F-test as these are suitable for data that does not fit a normal distribution. A statistically significant difference was accepted for p values below 0.05. Results for experiments were displayed as either an average or as a distribution dependent on the nature of the data and the question posed.

Chapter Three:

Quantification of Lipid Order at the Plasma Membrane

3.0 Introduction

Cellular membranes are fluid structures with regions displaying varying degrees of lipid order determined predominantly by their cholesterol content. The regions of higher order are suggested to impose functional regulation on cellular processes (Van Meer, 1989; Simons and Ikonen, 1997). The examination of the lipid arrangement at the plasma membrane of secretory cells aims to identify the corresponding protein organisation and interactions to provide insight into the exocytotic event. Although the exact mechanisms are still under debate the lipid composition is believed to influence the kinetics of fusion pore opening (Zhang et al., 2009; Koseoglu et al., 2011) and the organisation of fusion-mediating proteins at the plasma membrane such as synaptotagmin (Schiavo et al., 1996) and the t-SNAREs (Lang et al., 2001; Rickman et al., 2010) (see Chapter Five).

The importance of the lipid organisation has inspired an array of fluorescence-based studies attempting to quantify this organisation within membranes and distinguish between the regions of higher and lower order (Haverstick and Glaser, 1987; Korlach et al., 1999; Bacia et al., 2004). The most commonly used dye is Laurdan, which is advantageous in not requiring polarised filters and provides a quantifiable fluorescent signal (Weber and Farris, 1979). Early studies using this dye assessed its sensitivity and its stability under environmental conditions in reconstituted bilayers and Laurdan was accepted as a suitable dye to report on lipid ordering (Parasassi et al., 1991; Bagatolli and Gratton, 1999). The GP of Laurdan was used as a quantitative measure of lipid order on a scale of -1 to 1 with more positive values relating to more ordered lipid structures (Parasassi et al., 1991).

Laurdan is highly photosensitive and so TPE has been used in past works to minimise photobleaching (Yu et al., 1996; Gaus et al., 2003). In comparison to earlier work in reconstituted bilayers these studies reported on lipid order in fixed or mounted mammalian cells and observed the effect of decreasing lipid order upon temperature increase and cholesterol depletion. GP values were used as a

measurement for lipid order across the mid section of cells in these experiments and so these data relate to both plasma membrane and intracellular membranes.

Fluorescent lifetime imaging has been used to report on the lipid order at intra and extracellular membranes of HEK-293 cells using a different dye; Di-4-ANEPPDHQ, similar to Laurdan this dye demonstrates a blue shift in fluorescence when inside more ordered lipids (Owen et al., 2006). This work has provided an alternative quantifiable method but has not yet been applied to Laurdan imaging.

It is well established that the plasma membrane and intracellular membranes display varying lipid arrangement as they are required to perform different cellular functions (Simons and Van Meer, 1988). Past works predominantly record lipid ordering throughout the entire cell and do not differentiate between the two regions (Yu et al., 1996; Gaus et al., 2003). To investigate the lipids in relation to exocytosis at the cell surface the plasma membrane must be imaged in isolation. In addition lipids are dynamic in their nature (Singer and Nicolson, 1972; Simons and Ikonen, 1997) and it is important when possible to image them in their most natural environment. Past works predominantly use reconstituted bilayers which are not directly comparable to live cells and many apply fixation methods, the effect of which has not been assessed (Parasassi et al., 1991; Yu et al., 1996; Gaus et al., 2003; Owen et al., 2006). To examine the ordering of lipids at the plasma membrane exclusively a brief sonication pulse can be applied to intact cells to obtain sheets of plasma membrane (Avery et al., 2000) (see 2.3.4). This technique has been used in previous works to image protein interactions and vesicle fusion in PC12 cells and is accepted as representative of native plasma membrane (Avery et al., 2000; Lang et al., 2002). The experiments performed within this chapter have attempted to rectify these issues by using this technique and avoiding fixation techniques to accurately report on the lipid order at the plasma membrane.

3.1 Materials and Methods

Cell types used within this chapter include PC12 cells, N2a cells and HEK-293 cells (see 2.2.3). All cells were incubated with 5 μM Laurdan in serum free cell culture media for 1 hour prior to imaging to allow for Laurdan to distribute evenly throughout cell membranes. Unless otherwise stated in all experiments using MβCD cells were incubated for 30 minutes with 10 mM MβCD before being imaged (see 2.3.2). Unroofing has been used within this chapter to attempt to isolate the plasma membrane under the conditions described in 2.3.4. Fluorescent lifetime imaging of Laurdan within cellular membranes can quantifiably report on lipid ordering. The fluorescent lifetime of Laurdan is dependent on its degree of insertion into lipid structures, with Laurdan inside more disordered regions exhibiting a shorter fluorescence lifetime. The fluorescence lifetime of Laurdan was acquired using TCSPC-FLIM on the CLSM under TPE laser illumination as described in 2.4.4 and analysed using FLIM software (SPCM; Becker and Hickl GmbH).Experiments using TIRFM to image at the plasma membrane determine lipid order by calculating the GP of Laurdan fluorescence. Laurdan excitation, emission and detection are described in 2.3.5.

3.2 Results

3.2.1 Lipid order in whole cells can be detected using Laurdan

To observe the ordering of the lipids throughout the N2a cells, neuroendocrine cells derived from a neuroblastoma cell line, were stained with Laurdan and imaged using FLIM. A mid-section of representative N2a cells (Figure 3.1) shows a high degree of lipid order at the plasma membrane, the fluorescent lifetime of Laurdan at these regions are long as Laurdan is inserted further in between the lipids. The lipid structures within intracellular compartments are considerably less ordered and report a shorter fluorescent lifetime. These results were quantified by averaging the frequency of fluorescent lifetime from 7 cells. These data display a bimodal distribution, the most abundant population of lipids are less

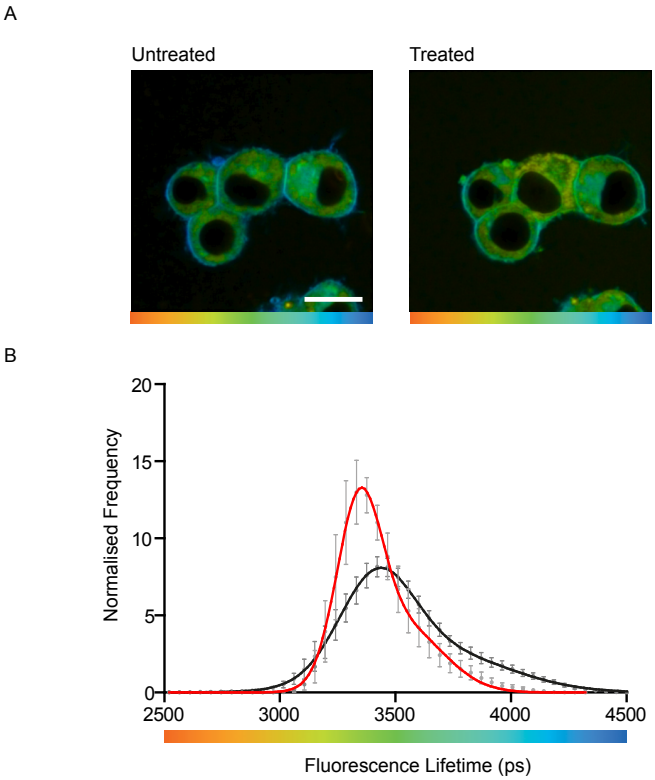

Figure 3.1 Laurdan reports on lipid order throughout the cell. A) Fluorescent lifetime of Laurdan in representative N2a cells: control (left panel) and MβCD-treated cells (right panel). Colour scale represents fluorescence lifetime 2500 ps - 4500 ps. Scale bar 10 μm. B) Fluorescence lifetime in whole cells before (black, n= 7, R^2= 0.9991) and after (red, n= 3, R^2= 0.9981) MβCD is added. Both normalised to pixel number (mean ± SEM) and fit to sum of two Gaussians (two fits compared: Extra sum of F^2= 0.0001).

ordered and may represent the intracellular components with the smaller and more ordered distribution attributed to lipids at the plasma membrane. The same cells represented in Figure 3.1 were treated with MβCD as described previously. The diminished representation of longer fluorescent lifetimes at the plasma membrane within the representative cells could represent the disordering of the lipids within this region. The average fluorescent lifetime values from these treated cells fit to the sum of two Gaussian distributions demonstrating there is still a distinction between lipid ordering at the plasma membrane and the intracellular membranes. The population seen in control cells with longer fluorescent lifetime is markedly reduced in these treated cells as the plasma membrane becomes less ordered and there is an increase in regions with more disordered lipids.

3.2.2 Quantitative analysis of lipid order in membrane sheets using FLIM

To image the plasma membrane in isolation cells were unroofed as described in 2.3.4. Figure 3.2 shows that plasma membrane sheets can be distinguished from intact cells using widefield / TIRFM illumination. An intact cell under widefield illumination will display the mid section of the cell including intracellular components whereas under TIRFM only the basal membrane of the cell will be visualised. An unroofed cell will appear as a sheet of plasma membrane under both widefield and TIRFM illumination.

To quantify modifications in lipid structuring within these membrane sheets upon changes in the cellular environment FLIM was performed. For each condition the fluorescence lifetime of Laurdan was measured per pixel within a PC12 plasma membrane sheet using a confocal laser scanning microscope and the frequency of lifetimes calculated. The unroofing procedure was performed at 22°C and so experiments were conducted at this temperature in this section unless otherwise stated.

The reorganisation of lipids exclusively at the plasma membrane upon temperature change from 22°C to 37°C through a shift in fluorescent lifetime of

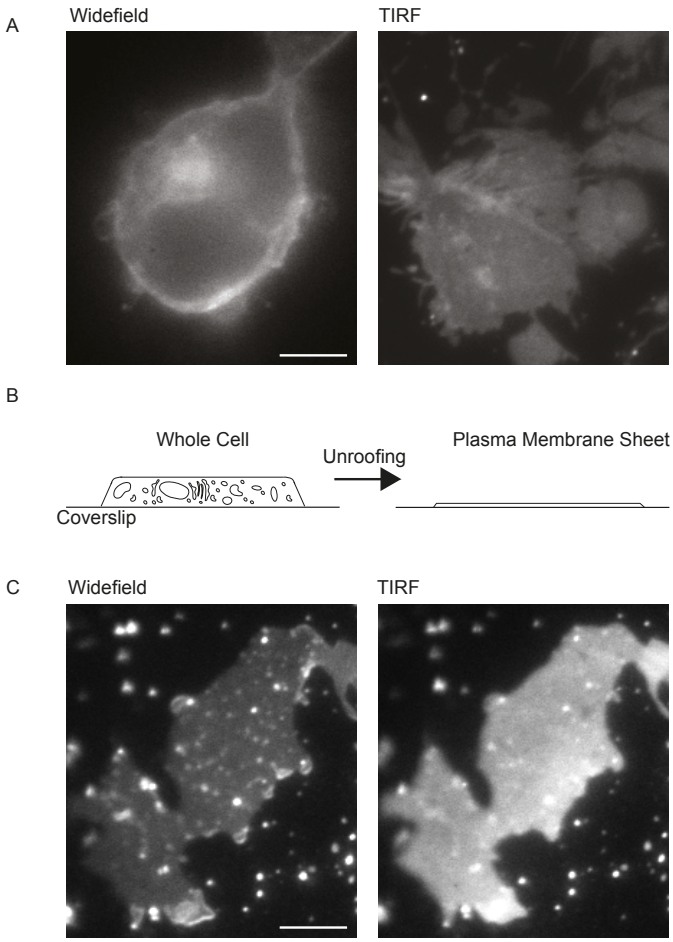

Figure 3.2 Membrane sheets can be distinguished in widefield illumination. A) A representative PC12 cell imaged in Widefield (left panel), the same cell in TIRFM (right panel). B) A schematic of the unroofing procedure. C) A membrane sheet imaged in Widefield (left panel) and in TIRFM (right panel). Scale bar is 5 μm.

Laurdan is shown in Figure 3.3. Representative membrane sheets demonstrate a marked shift in fluorescent lifetimes within the membrane from longer lifetimes at 22°C to shorter lifetimes at 37°C. These reported lifetimes are indicative of more disordered lipids at a higher temperature. Regions of interest were taken from membrane sheets imaged at both temperatures and the mean frequency of fluorescent lifetimes for each was calculated. Laurdan in PC12 membrane sheets at 22°C display fluorescence lifetimes ranging from 3195 ps – 4500 ps which fall within a single distribution. Upon a temperature increase to 37°C there is a marked shortening of fluorescent lifetime with a single distribution ranging from 2550 ps – 4095 ps. This shift in fluorescent lifetime demonstrating the regulation imposed by temperature on the lipid organisation at the plasma membrane validates the use of membrane sheets in lipid imaging as they behave in a predictable way.

To assess the ability for Laurdan to report on this change in membrane sheets Laurdan-stained PC12 cells were unroofed and imaged using FLIM (Figure 3.4). In these experiments MβCD has direct access to both bilayers as it was added after cell unroofing. Treated PC-12 membrane sheets display a considerable decrease in lipid order with fluorescent lifetime values between 2340 ps – 3150 ps. The range of values is markedly reduced in comparison to untreated membrane sheets and this is represented in the lifetime images with treated sheets showing a relatively uniform distribution across the membrane. Although the punctuate regions observed in untreated cells (see also Figure 3.3) cannot be separated into different populations they indicate heterogeneities across the membrane and these data indicate that cholesterol is required for that heterogeneity.

The fixation of cells is a commonly used preparation method and is required for some imaging techniques (Gaus et al., 2003; Sieber et al., 2007; Yang et al., 2012). If fixation is required in some experiments to image the lipids and proteins in combination it is important to first assess the effect fixation may impose on lipid structures. With this in mind Laurdan-stained PC12 plasma membrane sheets were fixed and imaged using FLIM (Figure 3.5). These data demonstrate that fixation imposes a shift to a less ordered lipid arrangement at the plasma membrane. Laurdan

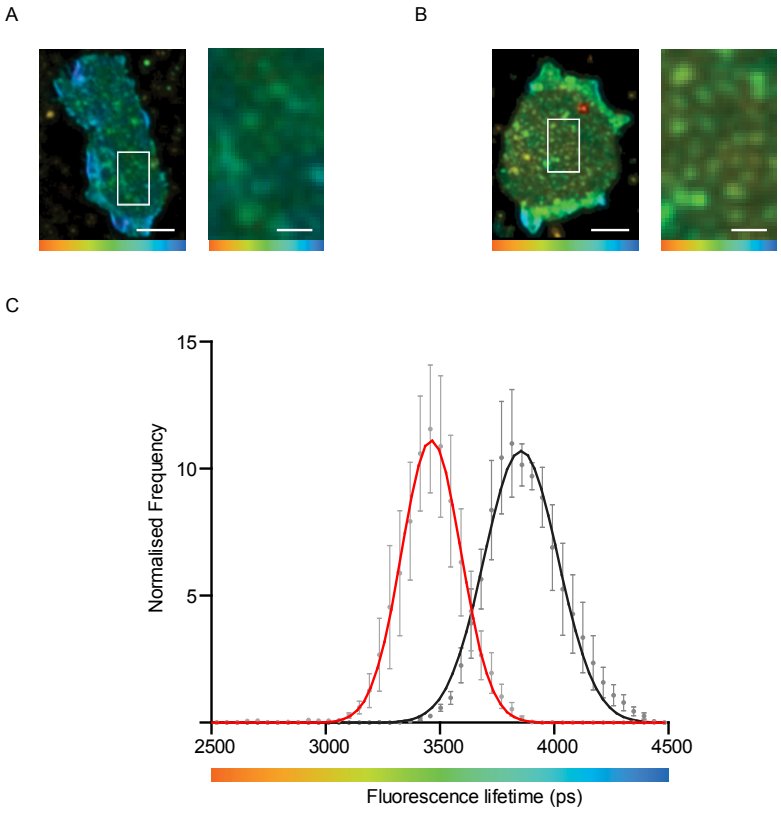

Figure 3.3 FLIM reports on a temperature-dependent lipid reorganisation in isolated membranes. Fluorescence lifetime of Laurdan in representative PC12 membrane sheets. A) At 22°C (left panel). Scale bar 4 µm. Zoom of white box (right panel). Scale bar 1 µm. B) At 37°C (left panel). Scale bar 4 µm. Zoom of white box (right panel). Scale bar 1 µm. Colour scale represents fluorescence lifetime 2500 ps - 4500 ps. C) Fluorescence lifetime in membrane sheets at 22°C (black, n= 4) and at 37°C (red, n= 6). Both normalised to pixel number (mean $\pm$ SEM) and fit to a single Gaussian R^2= 0.9965 (37°C) and R^2= 0.9977 (22°C).

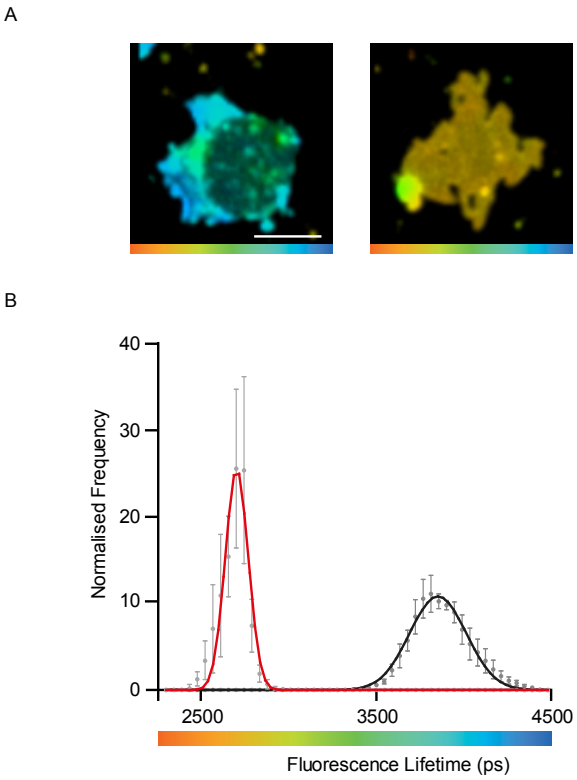

Figure 3.4 Cholesterol depletion from both bilayers abolishes lipid phase heterogeneities. A) Fluorescence lifetime of Laurdan in representative PC12 membrane sheets. Untreated (left panel) and MβCD-treated (right panel). Colour scale represents fluorescence lifetime 2250 ps - 4500 ps. Scale bar 2.5 µm. B) Fluorescence lifetime in membrane sheets in untreated (black, n= 4) and MβCD-treated (red, n= 5). Both normalised to pixel number (mean ± SEM) and fit to a single Gaussian R^2= 0.997 (untreated) and R^2= 0.957 (MβCD-treated).

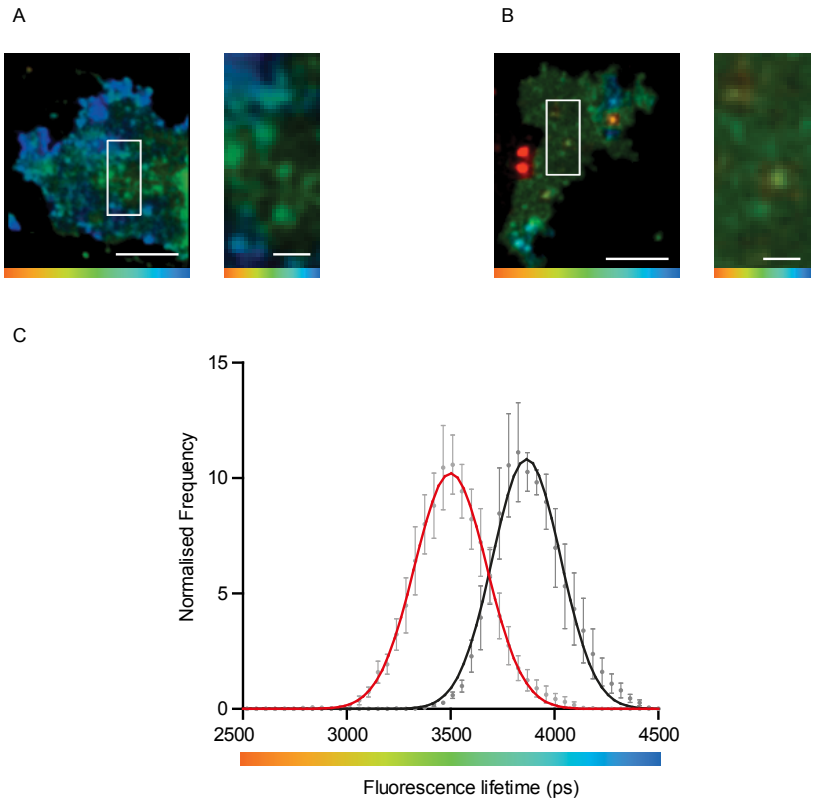

Figure 3.5 Fixation consistently alters lipid ordering. A) Fluorescence lifetime of Laurdan in representative PC12 membrane sheets. A) Unfixed membrane sheets (left panel). Scale bar 5 µm. Zoom of white box (right panel). Scale bar 1 µm. B) Fixed membrane sheets (left panel). Scale bar 5 µm. Zoom of white box (right panel).Scale bar 1 µm. Colour scale represents fluorescence lifetime 2500 ps - 4500 ps. C) Fluorescence lifetime in membrane sheets unfixed (black, n= 4) and at fixed (red, n= 6). Both normalised to pixel number (mean ± SEM) and fit to a single Gaussian R^2= 0.9977 (unfixed) and R^2= 0.989 (fixed).

fluorescent lifetimes within regions of interest from multiple membrane sheets were calculated and averaged to provide a distribution of the frequency of fluorescent lifetimes. Fixed cells exhibited values between 2745 ps – 4185 ps, with considerable overlap with the control distribution. These data show a consistent shift in lipid order upon fixation with a similar width of distribution across lifetime values as controls.

3.2.3 Imaging of the plasma membrane under TIRFM

Confocal microscopy is advantageous in the application of FLIM and TPE, however is limited by a minimal optical thickness of ~500 nm (Robinson, 2001), which is unnecessarily large for a membrane of only 4 nm. To further isolate the plasma membrane TIRFM has been used in the following data to selectively illuminate a thinner section.

Experiments performed on intact Laurdan-stained PC12 cells at 37°C under TIRFM found a GP distribution fit to a sum of two Gaussians (Figure 3.6). FLIM data has shown Laurdan fluorescence follows a single distribution in unroofed cells and one possible explanation is that under TIRFM visible intracellular components remained. The representative cell shown in Figure 3.6 displays punctate regions, which are similar in size to LDCVs (Plattner et al., 1997). These regions display a reduced GP value and therefore a decreased lipid order, which has been previously documented in vesicular membranes (Wang et al., 2000; Klemm et al., 2009). The experiments presented in Figure 3.6 demonstrate that to exclusively image the plasma membrane cells need to be unroofed (Avery et al., 2000). Figure 3.7 shows the GP values within a representative PC12 membrane sheet, imaged at 37°C, to be more uniform. Similar to FLIM data the GP frequency distribution from 10 PC12 membrane sheets are best fit to a single Gaussian distribution; the second distribution seen in intact cells is absent. There are some heterogeneities across the membrane sheets but these are not distinctive enough to divide the lipid order at the plasma membrane into two populations, this is similar to the membrane sheets imaged using

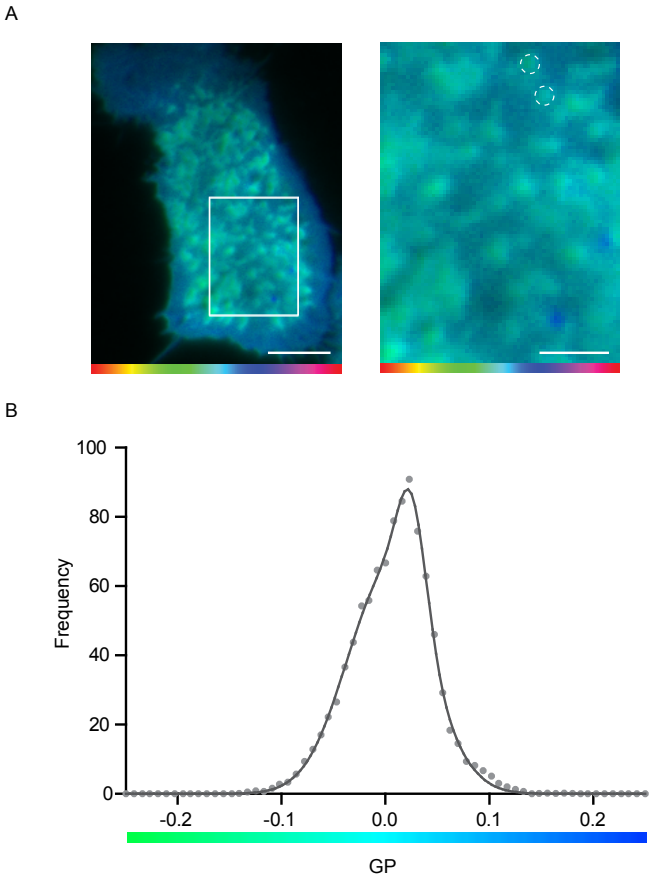

Figure 3.6 Laurdan-stained intracellular structures are visible under TIRF. A) GP values of Laurdan in a representative PC12 cell imaged in TIRFM (left panel). Scale bar 5 µm. A zoom of white box (right panel). Scale bar 2 µm. Example of 400 nm diameter vesicles (dashed white circles). Colour scale represents GP values -1 - 1. B) Frequency of GP within representative PC12 cell fits to a sum of two Gaussians R^2= 0.9762. Colour scale represents GP colour scale -0.25 - 0.25.

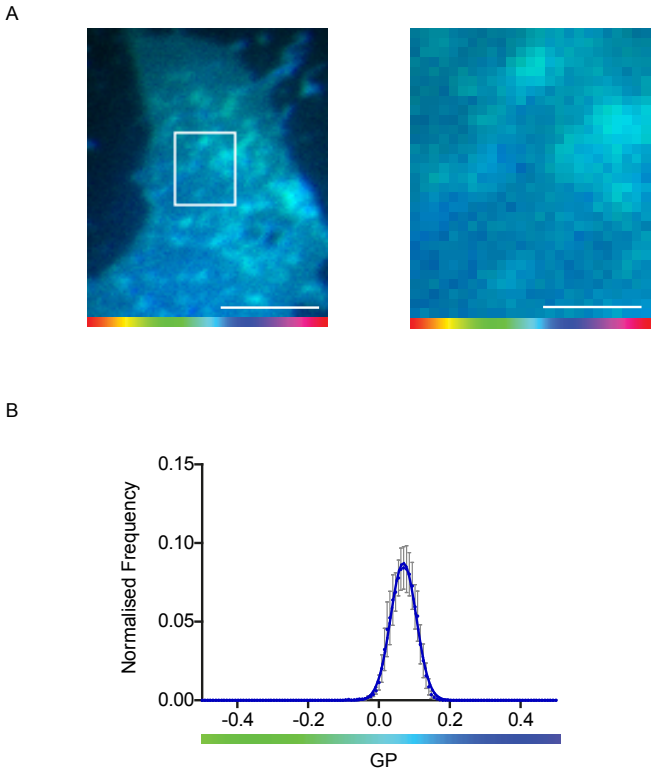

Figure 3.7 Laurdan GP in PC12 cell membrane sheets fits to a single distribution. A) Representative PC12 membrane sheet imaged under TIRF showing GP of Laurdan. Colour scale represents GP from -1 to 1. Region of interest in left panel (scale bar 4 μm) shown as zoom in right panel (scale bar 1 μm). B) Frequency of GP values normalised to number of pixels (mean ± SEM, n= 10) and fit to a single Gaussian R^2= 0.9875. GP colour scale -0.5 - 0.5.

FLIM. These data do not suggest any major modifications on the plasma membrane upon unroofing with peak GP values remaining close to 0 in membrane sheets. These findings unfortunately rule out Laurdan as a tool to image lipids and vesicles in combination as the vesicular membrane is also stained and would not allow differentiation.

3.2.4 Membrane sheets as a model for lipid behaviour quantified by the GP of Laurdan

To investigate the lipid ordering in other cell types and to further examine the suitability of using GP to quantify lipid order within plasma membrane sheets, HEK-293 cells were used. These cells were stained with Laurdan and unroofed as previously described (2.4.4). These sheets were then imaged over time with decreasing temperature from 37°C to 27°C (Figure 3.8). Representative cells at either end of the scale show GP values across the plasma membrane becoming more positive as the temperature decreases; a more positive GP is indicative of an increase in lipid order (Parasassi et al., 1991). These data show that lipids within HEK-293 plasma membrane behave in a similar pattern to those in PC12 cells and that GP is a suitable measure of lipid order.

To further establish the use of membrane sheets as lipid structures representative of intact cells HEK-293 cells were treated with MβCD prior to unroofing and imaged in TIRFM at 37°C (Figure 3.9). Representative cells show the expected shift in lipid order upon treatment with MβCD with GP values becoming more negative. The frequency distributions were quantified by extracting the GP values within each pixel of a region of interest inside untreated and MβCD-treated membrane sheets. These data are displayed as a mean GP distribution from 16 untreated sheets and 15 MβCD-treated sheets, both data sets fit to a single Gaussian distribution, which corresponds with the relatively uniform distribution of GP values within representative images. Treated membrane sheets display a distribution centred over a more negative GP value representing a loss of lipid ordering after cholesterol

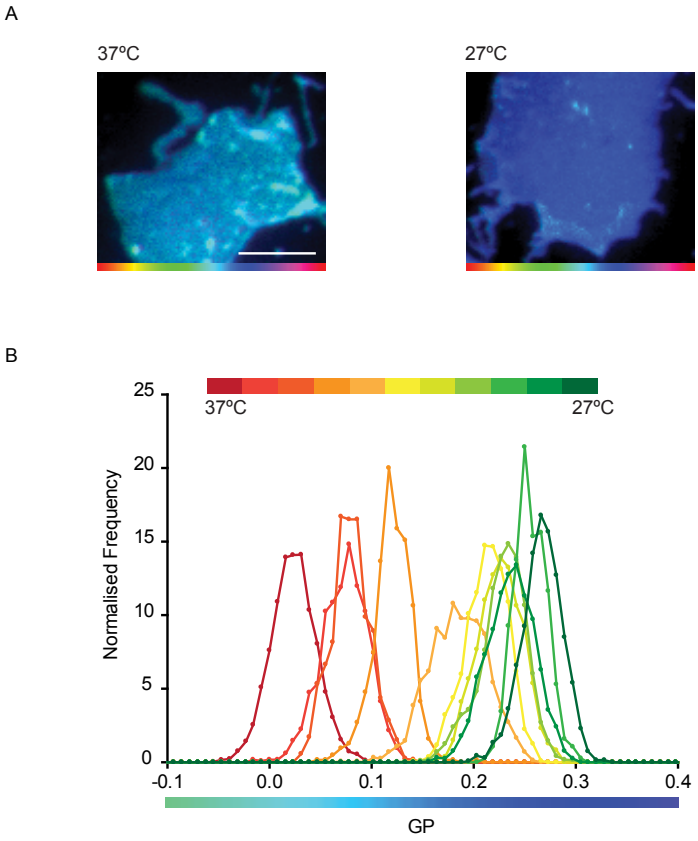

Figure 3.8 Lipids in isolated plasma membranes are dynamic. A) Representative HEK-293 membrane sheets showing the GP of Laurdan at 37°C (left panel) and 27°C (right panel). Colour scale represents GP from -1 to 1. Scale bar 4 µm. B) Frequency of GP values normalised to number of pixels. GP values -0.1 - 0.4 (lower colour bar). Each peak represents GP values from one membrane sheet at temperatures starting at 37°C decreasing by 1°C down to 27°C (upper colour bar).

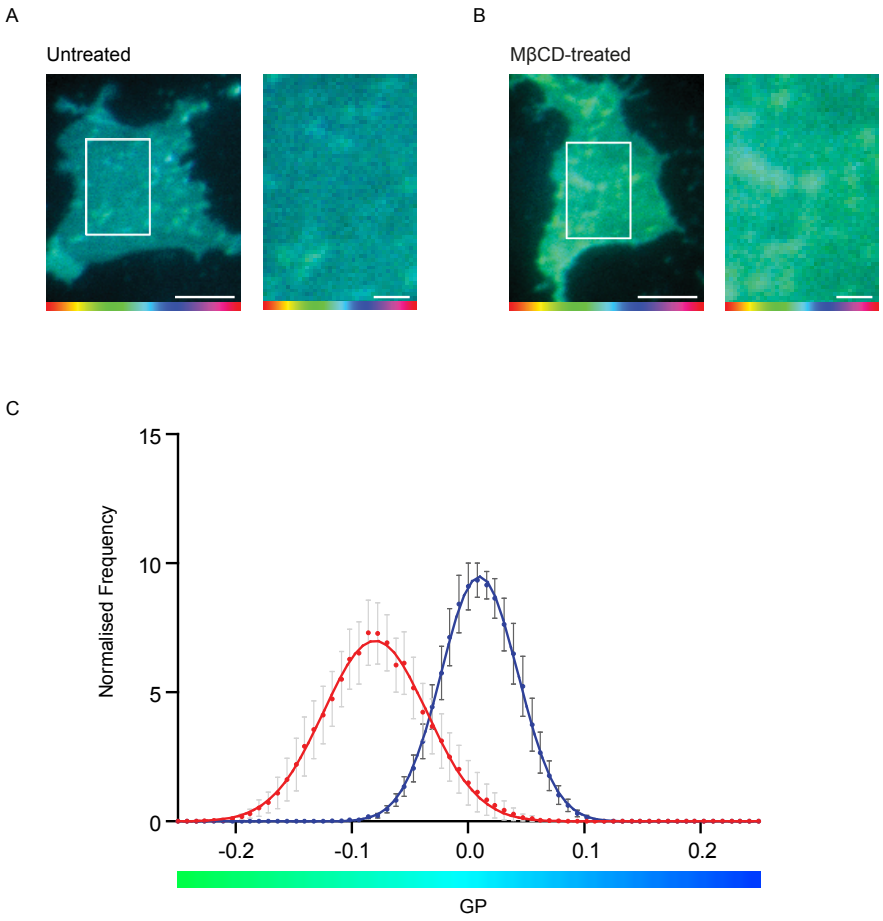

Figure 3.9 Cholesterol depletion in HEK-293 membrane sheets reduces lipid ordering. Representative HEK-293 membrane sheets imaged under TIRF showing GP of Laurdan. Colour scale represents GP from -1 to 1. A) Untreated sheets (left panel). Scale bar 4 μm. Zoom of white box (right panel). Scale bar 1 μm. B) Mβ CD-treated (left panel). Scale bar 4 μm. Zoom of white box (right panel). Scale bar 1 μm. C) Frequency of GP values normalised to number of pixels; mean ± SEM. Both fit to a single Gaussian, untreated in black (n= 16) R^2= 0.9998, MβCD-treated in red (n= 15) R^2= 0.9996. GP colour scale -0.25 - 0.25.

depletion. These data correspond with findings in PC12 cells (Figure 3.4) although the disordering in treated membranes is not as dramatic in HEK-293 membranes. The MβCD was added prior to unroofing in Figure 3.7 and so cholesterol in the inner leaflet is not as markedly reduced.

3.3 Conclusions

It is understood that the lipids at cellular membranes are arranged into regions of higher or lower order and within these regions the lipids are dynamic (Van Meer, 1989; Simons and Ikonen, 1997). To date the examination of this arrangement has been performed in *in vitro* model membranes and there is a lack of studies into lipid organisation in unfixed cells (Bagatolli and Gratton, 1999; Korlach et al., 1999; Gaus et al., 2003).

Fluorescent lifetime and GP of Laurdan were successfully used to quantify lipid order in live neuroendocrine cells in this chapter and findings agree with the theory that lipid order increases from inside the cell to the plasma membrane (Simons and Van Meer, 1988). Intracellular compartments were visualised under TIRFM at a higher resolution than used in previous works (Gaus et al., 2003).

The unroofing of live cells to leave native sheets of plasma membrane is an accepted procedure and has been used to assess protein interaction in a number of studies (Avery et al., 2000; Sieber et al., 2007). There has been minimal work to date investigating the lipid arrangement within these plasma membrane sheets. My data have characterised the effect of increasing temperature and cholesterol depletion within these sheets and shown that the effect mimics that seen in intact cells; a decrease in the ordering of the lipids (Parasassi et al., 1991; Gaus et al., 2003). Whether or not the sheets imaged are plasma membrane alone cannot be assumed however as it has been shown in past works that vesicular structures can remain after unroofing procedures (Avery et al., 2000). The reorganisation of lipids within cellular membranes upon temperature change has been verified in past works (Parasassis et

al., 1984; Bagatolli and Gratton, 1999; Gaus et al., 2003). Experiments imaging these sheets over a range of temperatures (Figure 3.8) could suggest that the lipids remain dynamic within the membrane as they transition into different phases. These findings provide validation to this technique and present membrane sheets as representative platforms for lipid investigation. In addition this method has been shown to be applicable to different cells types; PC12 cells and HEK-293 cells.

It is known that cholesterol imposes structure to phospholipids at the plasma membrane and that depletion of this sterol results in a disordering of the lipid arrangement (Simons and Ikonen, 1997; Dietrich et al., 2001; Gaus et al., 2003). MβCD has been widely used for the depletetion of cholesterol from cellular membranes in past works (Varma and Mayor, 1998; Foster et al., 2003; Eggeling et al., 2009). In untreated membrane sheets FLIM imaging shows punctuate regions of lifetime at the membrane (Figure 3.3), however the fluorescence lifetimes fit to a single distribution, which suggests some segregation exists but it is not resolvable using confocal imaging. This seems highly probable as single lipids are < 1 nm in diameter the raft-like structures they form are likely to vary in size and are thought not to exceed 200 nm (Lang, 2007); the limit of resolution. The uniformity observed in MβCD-treated membrane sheets (Figure 3.4) supports the idea that these punctuate regions visualised under FLIM are representative of raft organisation as they appear to rely on cholesterol.

Experiments within this chapter were performed to investigate whether Laurdan can be imaged alongside the vesicles and the proteins. Dual imaging of vesicles and lipids using Laurdan is not possible as the plasma membrane cannot be visualised without the Laurdan-stained vesicles, which leaves no differentiation between the two components. Previous work demonstrated the ability to image mCherry at 561 nm excitation in combination with Laurdan imaging (Gaus et al., 2003), suggesting live cell imaging of fluorescently tagged proteins at the plasma membrane was possible. Experiments performed on the Olympus microscope using Laurdan and mCherry-SNAP-25 showed considerable bleed through into the red shift of Laurdan fluorescence, making dual imaging in live cells unattainable. The

only available fluorescent marker which does not overlap is the antibody tagged Alexa-647, which required fixation of the cells (see Chapter Five). For this the effect of fixation on the membrane sheets was examined (Figure 3.5) and found to make the lipids less ordered; although this effect was seen consistently it has to be taken into consideration when using fixation techniques in later experiments.

The data presented in this chapter demonstrate the challenges posed by lipids in fluorescent imaging; their nanometre size is limiting for conventional microscopy and their dynamic nature within the membrane requires a fast acquisition time not yet possible with super-resolution techniques. Despite these problems it has been possible to develop two quantifiable methods of lipid imaging, which can be applied to both intact and unroofed cells. In addition the lipid order at the plasma membrane has been successfully examined while maintaining the characteristic lipid behaviour, supporting the use of membrane sheets as representative membrane platforms.

Chapter Four:

Secretory Vesicle Dynamics

4.0 Introduction

The mobility of LDCVs at the plasma membrane has been extensively researched in neuroendocrine cells and cell lines, the most common being PC12 cells (Lang et al., 1997; Xia et al., 2004; Tsuboi and Fukuda, 2007). This cell line is derived from a pheochromocytoma of the rat adrenal medulla (Greene and Tischler, 1976) and has proven a versatile model for neurosecretion (Greene and Tischler, 1976; Westerink and Ewing, 2009). Dopamine is the predominant catecholamine, which is packaged into LDCVs and secreted at the plasma membrane upon calcium-dependent depolarisation (Thureson-Klein, 1983; Shafer and Atchison, 1991). The size of LDCVs (approximately 350 nm) means that they can be tracked under diffraction-limited illumination, allowing for fast tracking of the vesicle as well as the visualisation of the fusion event at the plasma membrane under TIRFM. Quantifying the behaviour of LDCVs can provide insight into the mechanisms behind exocytosis; such as the involvement of accessory proteins in docking and priming steps, the positioning of the SNARE proteins and the kinetics of fusion (Oheim et al., 1998; Duncan et al., 2003; de Wit et al., 2006; Nofal et al., 2007; Yang et al., 2012a).

To understand how vesicles behave upon a secretory signal, and at the point of fusion, their mobility in unstimulated cells needs to first be examined. Vesicles have been segregated in the past dependent on their age (Duncan et al., 2003) and on their mobility (Steyer and Almers, 1999; Nofal et al., 2007); with the two appearing to be closely linked. Newly synthesised vesicles are seen to be nearly immobile and reside closest to the plasma membrane, suggesting a ‘docked’ status. A small population of vesicles display a directed motion; these are hypothesised to represent vesicles from the reserve pool as they approach the plasma membrane from within the cell and are also the oldest vesicles. A third group are caged in their mobility and appear to be docked at the plasma membrane as part of the RRP. These mobility types have been categorised into distinct groups; however it is suggested that the vesicles are more dynamic than implied by this segregation and may transition between mobility types throughout their lifetime at the plasma membrane (Steyer

and Almers, 1999; Nofal et al., 2007). Interestingly these works have been selective in their analysis; excluding those vesicles that cross the same path as well as those vesicles moving a greater distance across the membrane, which may provide insight into organisation at the plasma membrane. In addition a number of works were performed at non-physiological temperatures, which when investigating movement of biological components may have a marked effect.

The various mobilities displayed by vesicles may be related to the lipid environment at the plasma membrane, which in itself is thought to be closely related to the protein organisation (Lang et al, 2001; Milosevic et al, 2005). Cholesterol at the plasma membrane of cells is integral in the maintenance of lipid rafts (see Chapter Three), which provide a functional organisation to the plasma membrane (Simons and Ikonen, 1997). The sequestering of cholesterol using MβCD has been shown to cause a reorganisation of the actin cytoskeleton and alter fusion pore kinetics (Kwik et al, 2003; Chamberlain et al, 2001). High concentrations have been shown to disperse clusters of t-SNAREs at the plasma membrane (Lang et al., 2001), however more recent findings from our group show clustering is not cholesterol-dependent (see Chapter Five) (Rickman et al., 2010). One study has briefly examined the mobility of vesicles after cholesterol depletion however the acquisition time is only 2 Hz and the tracking software used only reported on area covered by vesicles (Zhang et al., 2009). The majority of studies of vesicle secretion have used amperometric or biochemical methods and findings relate to a slowing in release kinetics and reductions in the size of vesicle pools; there has been minimal work to date looking at vesicle mobility at the plasma membrane after cholesterol depletion (Zhang et al., 2009; Koseoglu et al., 2011).

The examination of vesicle behaviour at the plasma membrane in neuroendocrine cells after stimulation examines fusing and non-fusing vesicles and elucidates the requirements for vesicle fusion to take place. The trigger for exocytosis is an increase in intracellular calcium and this has been elicited in previous works by different mechanisms dependent on the experimental set up. High potassium is used in many works and is well established (Steyer et al., 1997; Oheim

et al., 1998). Addition of ATP to the external medium is not as commonly used as it is not a stimulus that occurs in physiological conditions; however the increase in calcium at the membrane after this treatment has been shown (Pouli et al., 1998). Previous works have focused predominantly on the depletion of vesicle pools and the decreased mobility of vesicles on arrival at the plasma membrane (Steyer et al., 1997; Oheim et al., 1999; Johns et al., 2001). Many of these works have attempted to quantify mobility in the z axis, perpendicular to the membrane but fewer studies have examined vesicle mobility lateral to the membrane after cell stimulation Those that have demonstrate a slight increase in lateral mobility after stimulation in some vesicles but not all vesicles (Steyer and Almers, 1999).

Analysing all vesicles at the membrane of stimulated cells shows the reaction to increases in calcium but does not exclusively comment on the behaviour of fusing vesicles. Vesicles within the RRP are thought to have a caged or nearly immobile motion as they are tethered to the plasma membrane; the newly synthesised vesicles have been reported to reside here and to fuse within the fast exocytotic burst in the first few seconds of stimulation (Voets et al., 1999; Zenisek et al., 2000; Duncan et al., 2003). Vesicles with a more directed motion are believed to account for the sustained release as they approach the membrane from the reserve pool, typically after the stimulation has been evoked (Augustine and Neher, 1992; Zenisek et al., 2000; Allersma et al., 2004). The mobility of vesicles within the final stages of fusion is under contention; a decrease in mobility from caged to nearly immobile has been reported (Toonen et al., 2006; Nofal et al., 2007) as well as an increase in vesicle mobility perpendicular (Degtyar et al., 2007; Karatekin et al., 2008) and lateral (Yang et al., 2012a) to the membrane immediately prior to fusion.

It is well established that the localisation of vesicles at the plasma membrane is not uniform and is subject to tight regulation (Steyer et al., 1997; Oheim et al., 1999). In addition the existence of specific sites for exocytosis has been suggested through investigation of t-SNARE dynamics and spatial organisation (Lang et al., 2001; Barg et al., 2010). Whether the regions over which vesicles are reported to reside correspond to these exocytotic sites is still under debate and there has been

minimal work comparing whole cell vesicle tracking with exocytotic events. The presence of these sites at the plasma membrane has been strengthened by the observation of multiple fusion events in the same area in ribbon synapses (Zenisek et al., 2000). Similar studies have been performed in neuroendocrine cells, showing multiple events within a 1 μm square region (Oheim et al., 1999).

A model surrounding vesicle mobility prior to and immediately before exocytosis is beginning to emerge; however there are still unanswered questions and experimental limitations. This chapter aims to characterise vesicle mobility at the plasma membrane of neuroendocrine cells at physiological conditions with a high degree of accuracy using a range of analytical approaches. These data aim to further our understanding as to which vesicles preferentially fuse and where they do so.

4.1 Materials and Methods

All experiments within this chapter were performed in live PC12 cells expressing EGFP-NPY imaged under TIRFM. The EM gain was set to 230 and images were acquired at a frame rate of 50 ms. Stimulation experiments involved the addition of 300 μM ATP to the imaging medium 500 frames (10 seconds) after the start of the image acquisition. Vesicles were tracked and analysed using Imaris or Matlab software and the exocytotic flash was clarified using Image J to quantify change in fluorescence (2.5.2). Single vesicles were tracked in Imaris up until and inclusive of the first frame displaying the flash in intensity to define the final fusion step.

4.2 Results

4.2.1 Vesicles at the plasma membrane display heterogeneous behaviour and are restricted to domains

To examine the localisation and behaviour of vesicles at the plasma membrane over time vesicles were tracked using Imaris over a 2 minute period (Figure 4.1). The initial experiments on resting (unstimulated) cells demonstrated that vesicles at the base of the plasma membrane exhibit various mobilities. The distribution of the tracks seems restricted to areas across the plasma membrane; however within these domains the vesicles appear to be quite mobile.

Tracking vesicles using Imaris software is advantageous in examining the different types of vesicle mobility within a cell however the number of vesicles tracked is restricted because the commercial software has limited abilities to deal with poor signal to noise data. To display the optimum number of tracks and supply an unbiased view of the spatial organisation across the membrane a custom tracking algorithm was used in Matlab on TIRFM recordings of vesicles at the base of PC12 cells. This software is written to deal well with noisy data, delivering accurate, validated tracking data that could not be acquired using any commercial package (Yang et al., 2012b). Cells were imaged at 20 Hz as before and 900 frames were extracted from the recording for analysis; the results are displayed in a contour map (Figure 4.2). The number of times a track crossed each pixel was quantified and these data reconstructed into a spatial ‘contour’ map displaying the density tracks. These results for unstimulated cells imply that there are preferred regions of the plasma membrane that the vesicles will pass through, the punctuate nature of mapped density suggests these regions are relatively small and distinct. There are regions surrounding these discrete sites of high density that are larger in area and display a low density of tracks. These observations could be explained by the existence of different mobility types within cells, regions where a vesicle with directed motion has moved across will have a low density as it will typically only cross that pixel once. When a vesicle is caged its tracks will often cover the same pixel many times as it is very mobile but within a small area; these vesicles could account for the spots

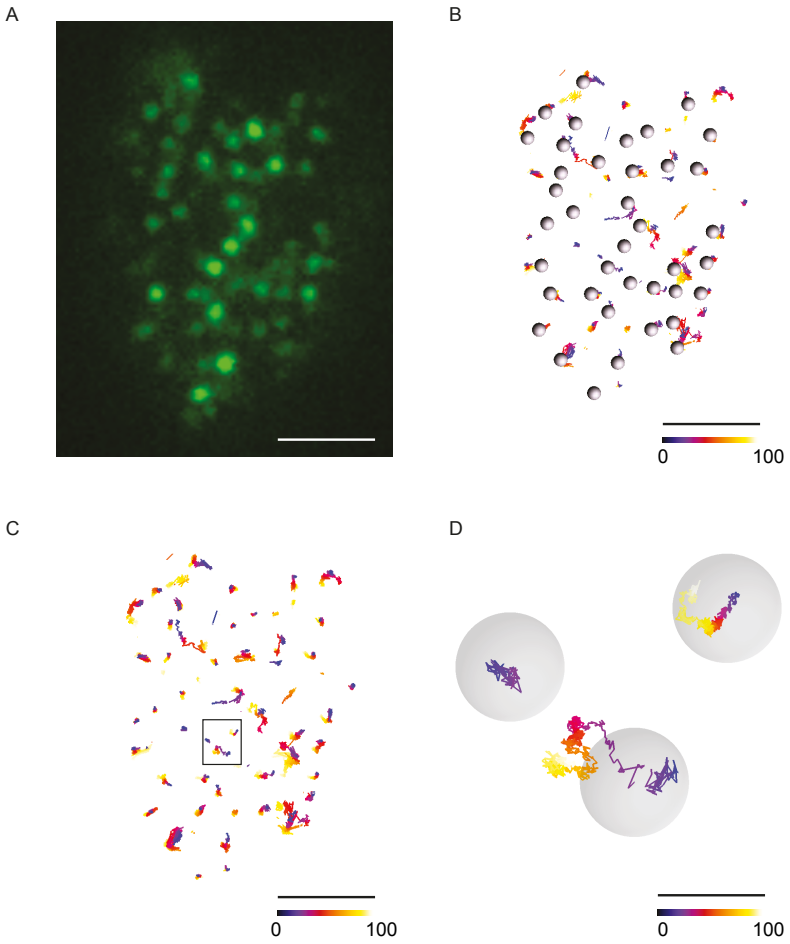

Figure 4.1 Movement of vesicles at the plasma membrane. A) EGFP-NPY-filled vesicles at the plasma membrane of a representative PC12 cell from a single frame within the recording are shown in green. B) Vesicles from the cell in A are tracked over 100 seconds at 20 Hz. Grey spheres represent vesicles present at start of recording and tracks displayed from all vesicles in recording. C) Same tracks as shown in B with region of interest highlighted. D) Enlarged region of interest from C displaying vesicles with different mobilities. Colour of tracks and colour bar represents time in seconds. All scale bars 0.4 μm.

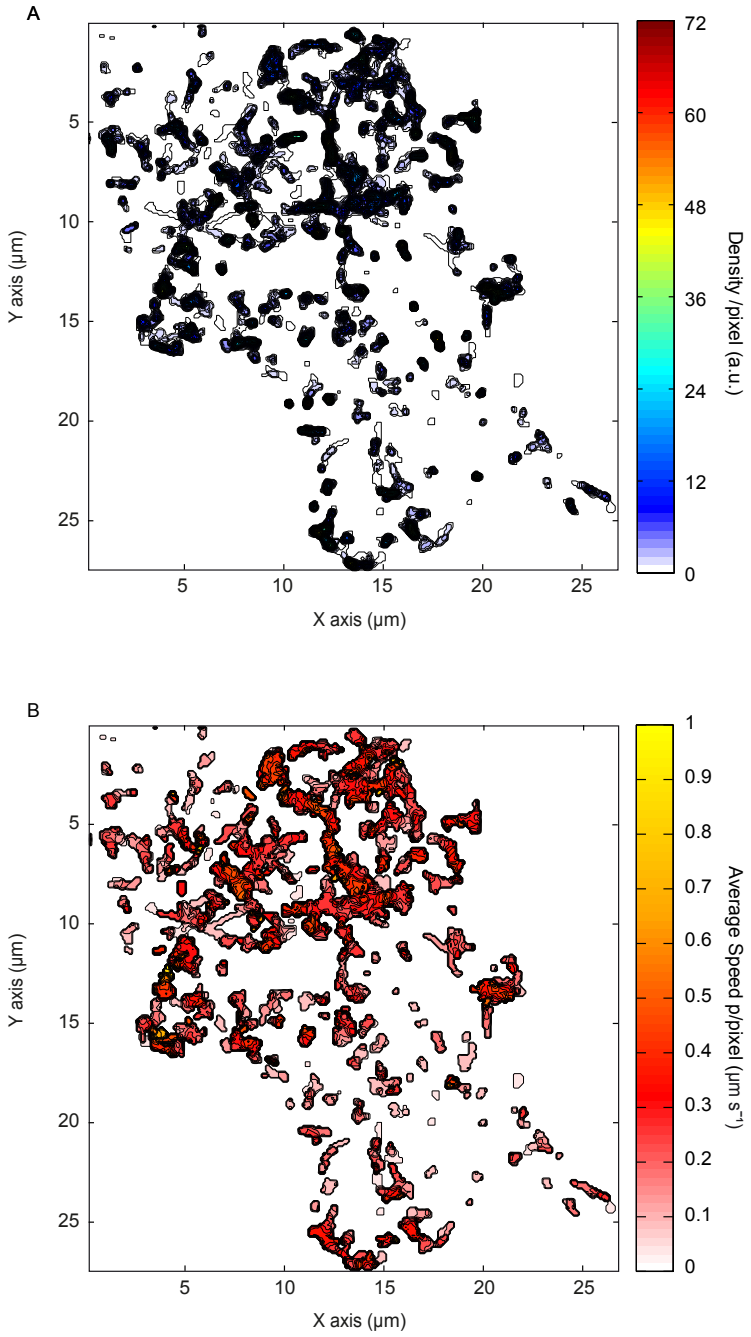

Figure 4.2 Vesicle localisation at the plasma membrane is not uniform. A) Density 'contour' map of a representative PC12 cell over a 45 second recording showing number of tracks within each pixel. B) Speed 'contour' map of cell from A showing average speed of tracks per pixel in µm s^{-1}. n= 2,976 tracks.

of high density in the map. The average track speed in each pixel was also quantified in the same representative cell used for the density contour map. These data show that the majority of vesicles move at average speeds ranging between 0.2 μm s^{-} – 0.4 μm s^{-} . The cell does exhibit vesicles moving at speeds at either end of the scale and these seem to be spatially distinct from one another.

4.2.2 Vesicles display a restricted motion

The behaviour exhibited by vesicles within their tracks can provide insight into the membrane arrangement they are moving over and potentially their protein-lipid interaction status. To investigate the directionality of the vesicles at the plasma membrane all vesicles within a recording were tracked and transformed to begin in the same place (Figure 4.3). These data show that vesicles can move in any direction within their time at the plasma membrane. Whether vesicles move in a selective or random direction from one frame to another (a step) has been quantified for 16,944 LDCV tracks from 5 PC12 cells. The angle at which a vesicle moves within a step is measured for each track and plotted as a histogram, depicting angle, frequency and speed. These data show that with no prior track knowledge the vesicles can move in any direction and that approximately 50 % of vesicles travel at a speed between 0.1 μm s^{-1} and 0.2 μm s^{-1} within one step. There are movements of up to 1 μm s^{-} but these are less frequently observed within the sample. To investigate whether given a forward motion the vesicle mobility was random the same tracks were analysed and each step made within each track was measured relative to its previous movement. These data were reconstructed into a histogram displaying speed, frequency and angle (Figure 4.4). There are a small proportion of vesicles moving forward; however predominantly given a forward motion the vesicles tend to reverse, which is indicative of a restricted caged behaviour.

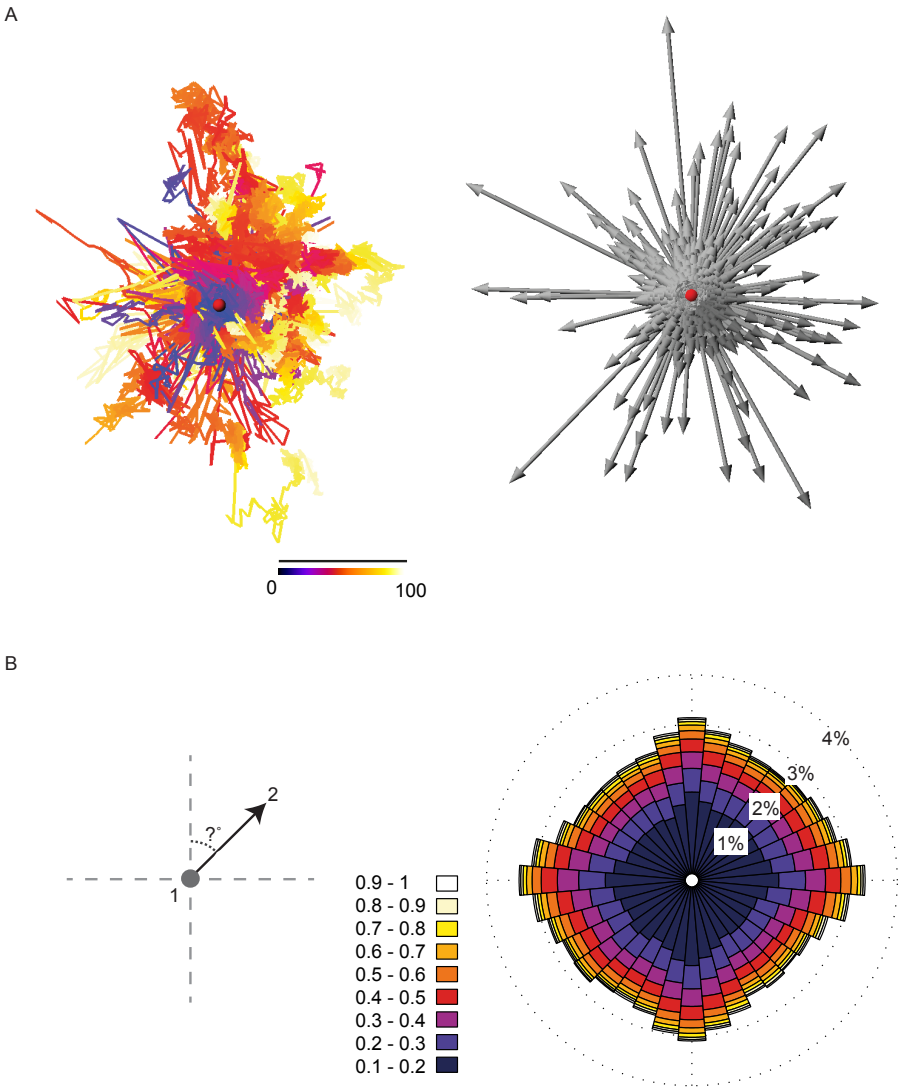

Figure 4.3 Vesicle mobility can be described by a Brownian model. A) 829 tracks from a representative PC12 cell are shown and the tracks are translated to start at the same xy coordinate. The track from each vesicle with colour representing time in seconds (left panel), the vesicle displacement from start to finish by grey arrows (right panel). Scale bar 1 µm. B) The angle and speed of the first movement taken by a vesicle is extracted (left panel) and displayed as a histogram where colour represents speed (µm s^{-1}) and length of a bin represents frequency (right panel). n= 16,944 tracks from 5 PC12 cells.

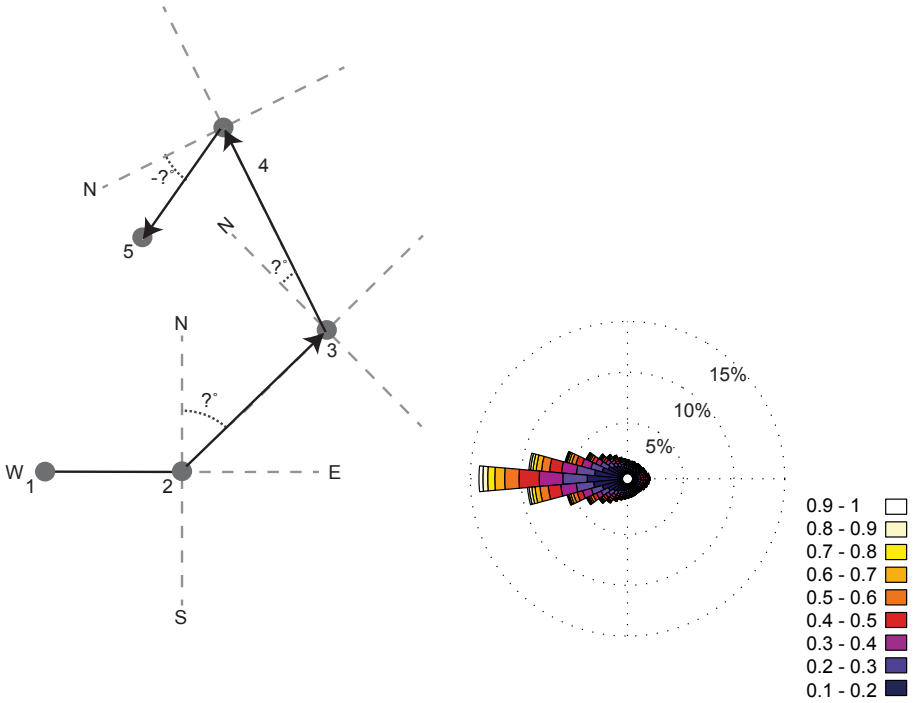

Figure 4.4 Vesicles are restricted in their freedom of movement. The angle and speed of the subsequent movements a vesicle makes in relation to its previous movement is extracted (left panel: vesicles (grey circles), movement (black arrow), angle (dashed line)) and displayed as a histogram where colour represents speed (μm s^{-1}) and length of a bin represents frequency (right panel). n= 16,944 tracks from 5 PC12 cells.

4.2.3 Categorisation of vesicles by their mobility

To further examine the type of mobility undertaken by the vesicles selected parameters were measured for 16,944 LDCV tracks from 5 PC12 cells (Figure 4.5). Within these data the maximum displacement is discussed, which is the furthest distance a vesicle displaces within its track. Vesicles can be categorised into at least two populations dependent on their track displacement and maximum displacement; with the highest frequency of vesicles displaying shorter displacement and maximum displacement. Vesicle speed is bimodal with the majority under 0.25 μm s^{-} , however tracks can reach speeds of 1 μm s^{-} but these are very rare, as mentioned above. The majority of vesicles display track lengths measured up to 4 μm that fit within a single distribution, with some tracks with values as high as 50 μm; however they are rare in comparison. The track length in these data corresponds with duration at the plasma membrane. These data are insufficient to determine the degree of caged mobility, for this the track length was plotted against the track displacement and maximum displacement for the same 16,944 tracks (Figure 4.6). A caged vesicle will display a long track length compared to a short displacement. These data show the majority of vesicles display a caged motion with varying degrees of displacement and maximum displacement, with the highest proportion having the lowest mobility. By comparing data from Figure 4.5 to individual tracks from Imaris analysis it is possible to hypothesis which vesicle mobility types are represented within the histogram (Figure 4.7). Vesicles with a displacement between 0 μm - 0.3 μm (0.3 μm taken as the intersect between the two curves) remain within the vesicle diameter as they track and the majority are dynamic in their mobility, which mean they are not definitively caged or nearly immobile. The vesicles that fall within the second population between 0.3 μm – 0.68 μm (0.68 μm taken as the 95% confidence interval) move outside of the vesicle diameter and appear untethered. Both groups are still caged in their mobility and will be referred to as caged vesicles for simplicity. The third population is small and apparent between 0.68 μm – 3 μm, these are those vesicles which move a greater distance in a more directed manner. These two vesicle types can be distinguished more clearly by comparing their track length and displacement,

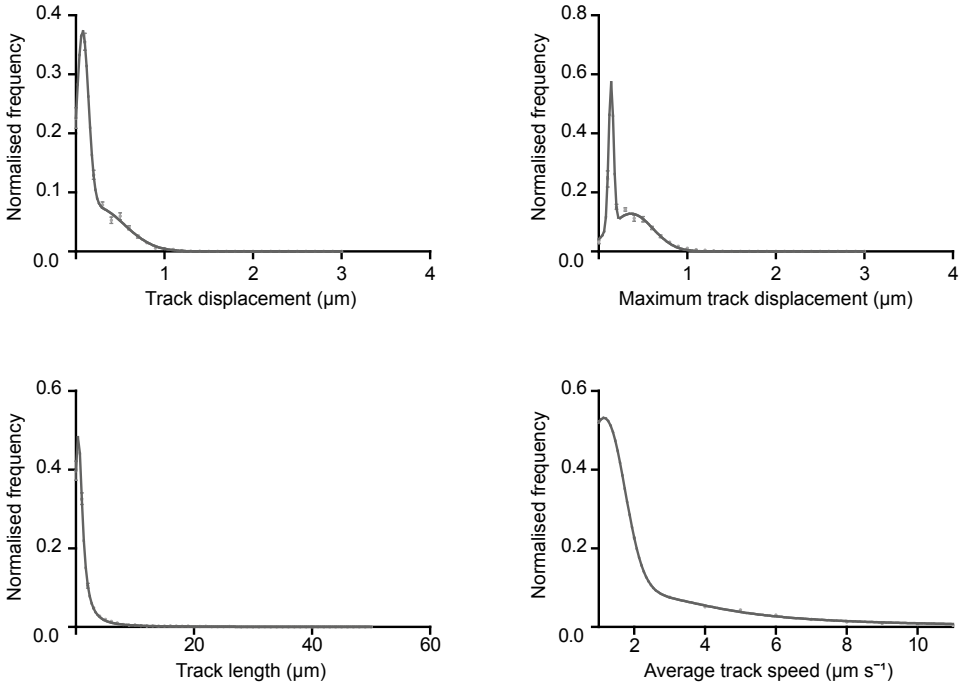

Figure 4.5 Distribution of vesicle track parameters. Track displacement, maximum displacement and average speed can be fit to a bimodal distribution. Track length is best fit to a single distribution. Data normalised to number of tracks per cell (mean ± SEM for 16,944 tracks from 5 PC12 cells). R^2=0.99 for all.

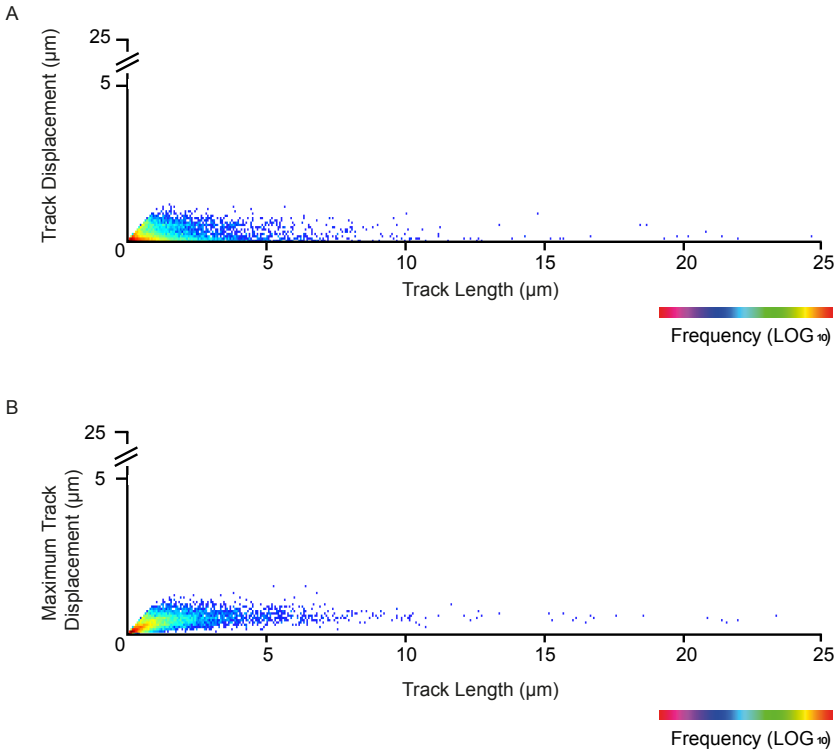

Figure 4.6 The majority of vesicles have a caged mobility. A) The length of vesicle tracks against their track displacement is displayed in a cloud histogram. B) The length of the same vesicle tracks from A are plotted against their maximum displacement and displayed in a cloud histogram. The frequency of tracks is represented by colour in a logarithmic scale from low to high. n= 16,944 tracks from 5 PC12 cells.

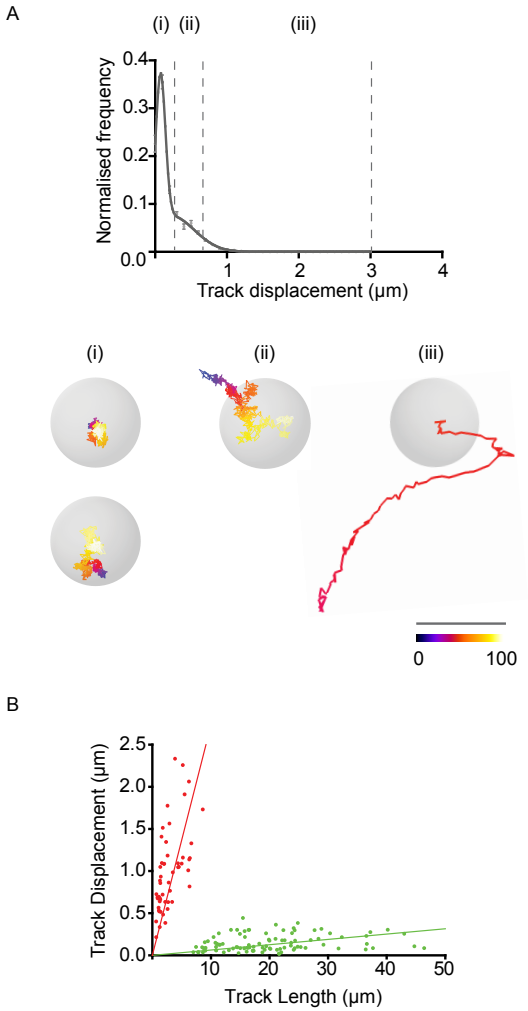

Figure 4.7 Vesicles can be categorised dependent on their track length and displacement. A) The histogram from Figure 4.5 showing displacement of 16,944 tracks from 5 PC12 cells (mean ± SEM). 3 populations of vesicles (dashed lines). Examples of caged/nearly immobile vesicles with displacement below 0.3 µm (set i), example of caged vesicles with displacement above 0.3 µm (set ii), example of vesicle with displacement between 0.68 µm and 3 µm (set iii). Scale bar 0.4 µm. Colour of the track is time in seconds. B) Track length and displacement of selected directed (red n= 52) and caged (green n= 97) vesicle tracks.

directed vesicles have a longer track displacement compared to track length and caged vesicles the opposite.

4.2.4 Examining the influence of lipid order on vesicle behaviour

To investigate whether vesicle mobility is related to the lipid environment at the plasma membrane MβCD was used to deplete cholesterol from the plasma membrane, which quantitatively reduces lipid order as shown in Chapter Three. Vesicles from MβCD-treated cells were tracked using Matlab as seen in Figure 4.2 and a region of interest within a representative cell is shown against a control untreated cell as a contour map (Figure 4.8). Vesicles in MβCD-treated cells appear to follow a similar pattern to controls, with defined regions of high density suggesting preferred areas of plasma membrane. There is a similar distribution of speeds but there is a larger proportion of vesicles undergoing faster speeds (up to 0.6 $\mu m\ s^{-1}$.) There is no detectable correlation between the density and the speed with the contour maps suggesting that in less dense regions the vesicles move more slowly; however, this is a developing trend and not statistically conclusive. To examine any alterations in vesicle behaviour after cholesterol depletion more closely the parameters for 12,541 LDCV tracks from 6 MβCD-treated cells were compared to control cells (Figure 4.9). These data show that vesicles become significantly ($p= 0.0001$) more mobile in MβCD-treated cells. This is most apparent in vesicle displacement, showing a shift to more mobile populations with vesicles moving a greater distance from their starting point. This effect is seen in track length and maximum displacement although it is marginal. The average speed undergone by each vesicle within these data is fit to a single rather than double Gaussian distribution when cholesterol is depleted. There is a loss of vesicles moving at the slowest speeds and an increase in those moving at speeds above 0.25 $\mu m\ s^{-1}$, which the previous findings described in Figure 4.8.

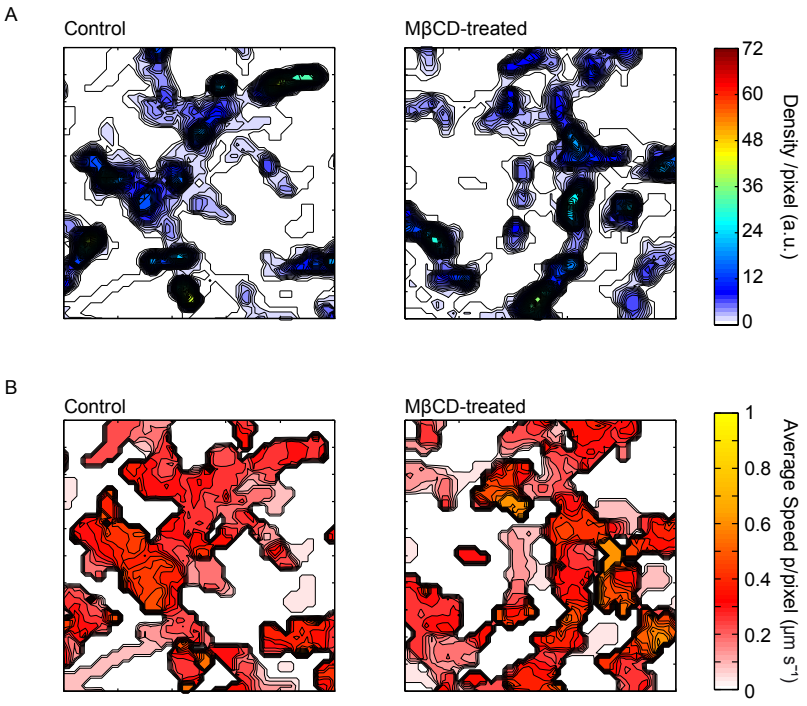

Figure 4.8 Vesicle behaviour in MβCD-treated PC12 cells. 'Contour' maps of vesicle tracking in a representative PC12 cell over a 45 second recording for control cells (n= 2,976 tracks in whole cell) (left panels) and MβCD-treated cells (n= 3,334 in whole cell) (right panels). Tickmarks 1.06 μm. A) Density 'contour' map showing number of tracks within each pixel. B) Speed 'contour' map showing average speed of tracks per pixel in μm s^{-1}.

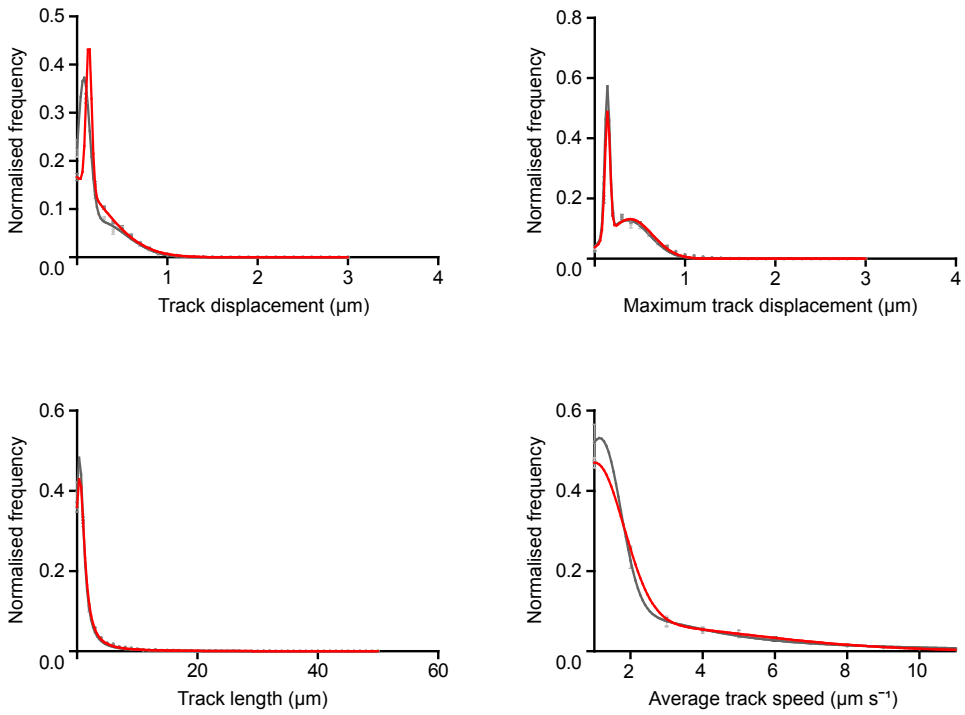

Figure 4.9 Cholesterol depletion significantly alters vesicle mobility. Track parameters displayed for 16,944 tracks from 5 PC12 cells (grey) and 12,541 tracks from 6 Mβ CD-treated PC12 cells (red). Data normalised to number of tracks per cell (mean ± SEM). Track displacement and maximum displacement fit to a double Gaussian R^2= 0.99 (Extra sum of squares F-test test p= 0.0001). Track length fits to a single Gaussian R^2= 0.99 (Extra sum of squares F-test p= 0.0001). Average speed for control fits to a double Gaussian (R^2= 0.99) and +MβCD fits to a single Gaussian (R^2= 0.99).

4.2.5 Calcium fluctuations under continuous stimulus

To observe how vesicles behave upon the triggering of secretory signals ATP was used to stimulate cells (see 4.0). To validate this stimulation method the increase in intracellular calcium upon stimulation was quantified using a Fluo3AM dye (see 2.3.6). Figure 4.10 shows that upon ATP addition cytosolic calcium increases rapidly and remains significantly above basal level for ~45 seconds after stimulation. Previous works have shown that the cytosolic calcium increase seen after ATP in PC12 cells is similar to that measured near the plasma membrane (Pouli et al., 1998).

4.2.6 Vesicles become more mobile after cell stimulation

To investigate whether the vesicles alter their mobility after calcium increase and secretory signalling the 900 frames following cell stimulation were extracted and vesicles tracked using Matlab to produce contour maps displaying spatial information for all vesicles at the plasma membrane within that time. A region of interest within control and stimulated representative cells are shown in Figure 4.11. The 'hotspot' regions observed within control cells appear more frequent and of larger size in stimulated cells. There are a similar number of tracks between the two conditions and so there is not an apparent increase in the number of vesicles present at the membrane. There is a loss of slower vesicles within the stimulated cell and a slight increase in values closer to 0.6 μm s^{-1}, with 'hotspots' of very high speeds close to 0.9 μm s^{-} . These data provide insightful spatial information; however a quantitative approach is required to assess whether the implied increase in mobility is significant within this data set. The parameters of 11,608 vesicle tracks from 4 stimulated PC12 cells were compared to those exhibited by controls (Figure 4.12). There are significant ($p= 0.0001$) differences in vesicle displacement and maximum displacement with a shift to more mobile pools. An increase in both maximum displacement and displacement is indicative of more directed vesicle motion, vesicles move a further distance from where they begin and a further distance within their track, compared to unstimulated cells. The track lengths of the vesicles remain

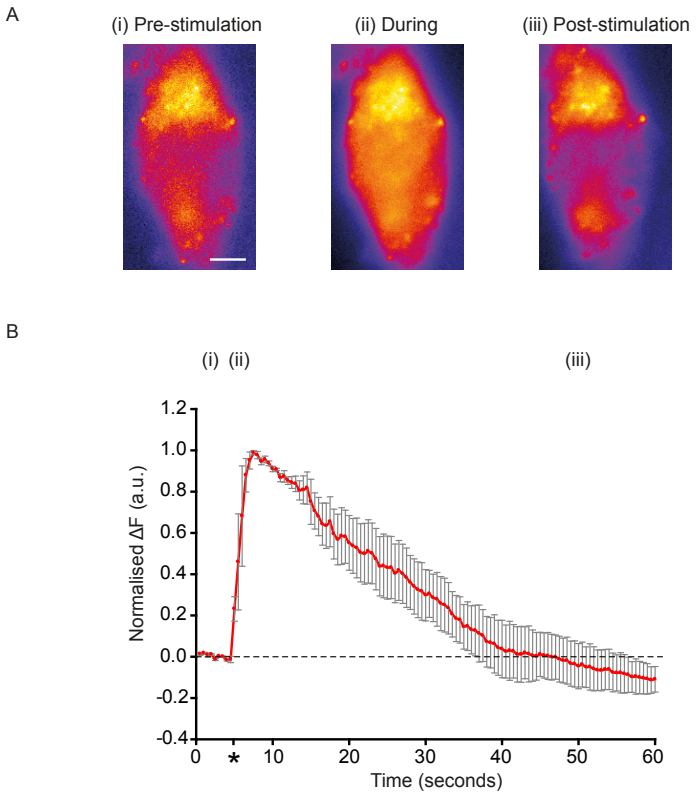

Figure 4.10 Calcium concentration after ATP addition. A) The mid-section of a representative PC12 cell loaded with Fluo 3AM dye. Average of 10 frames at 2 Hz prior to stimulation with ATP shows baseline Fluo 3AM fluorescence (i). Average fluorescence of 10 frames immediately after ATP addition (ii). Average fluorescence of 10 frames after 50 seconds (iii). Scale bar 4 μm. B) Time point depicted in A shown by (i,ii,iii). Change in fluorescence over time (mean ± SEM, n= 3). ATP added at 5 seconds (asterix).

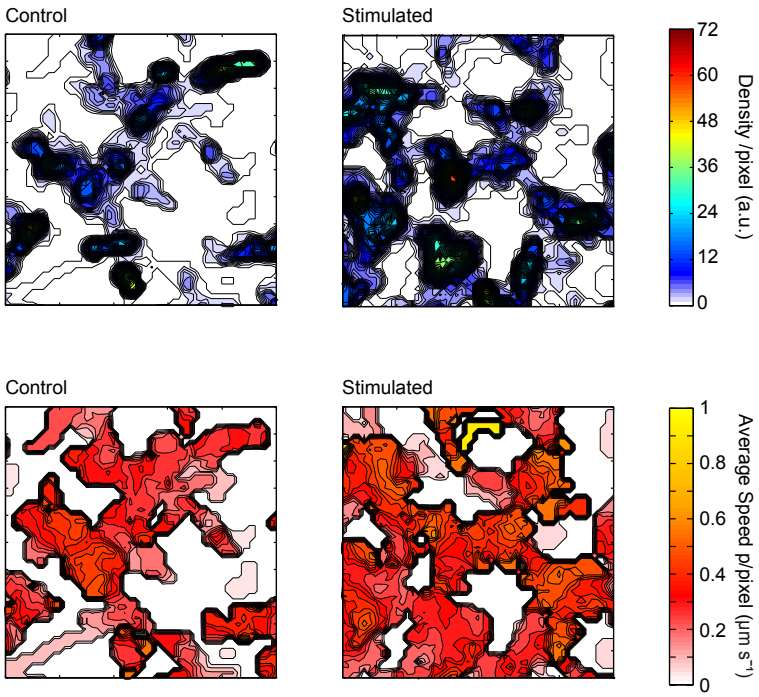

Figure 4.11 Vesicle behaviour in stimulated PC12 cells. 'Contour' maps of vesicle tracking in a representative PC12 cell over a 45 second recording for control cells (n= 2,976 tracks in whole cell) (left panels) and stimulated cells (n= 2,773 in whole cell) (right panels). Tickmarks 1.06 µm. A) Density 'contour' map showing number of tracks within each pixel. B) Speed 'contour' map showing average speed of tracks per pixel in µm s^{-1}.

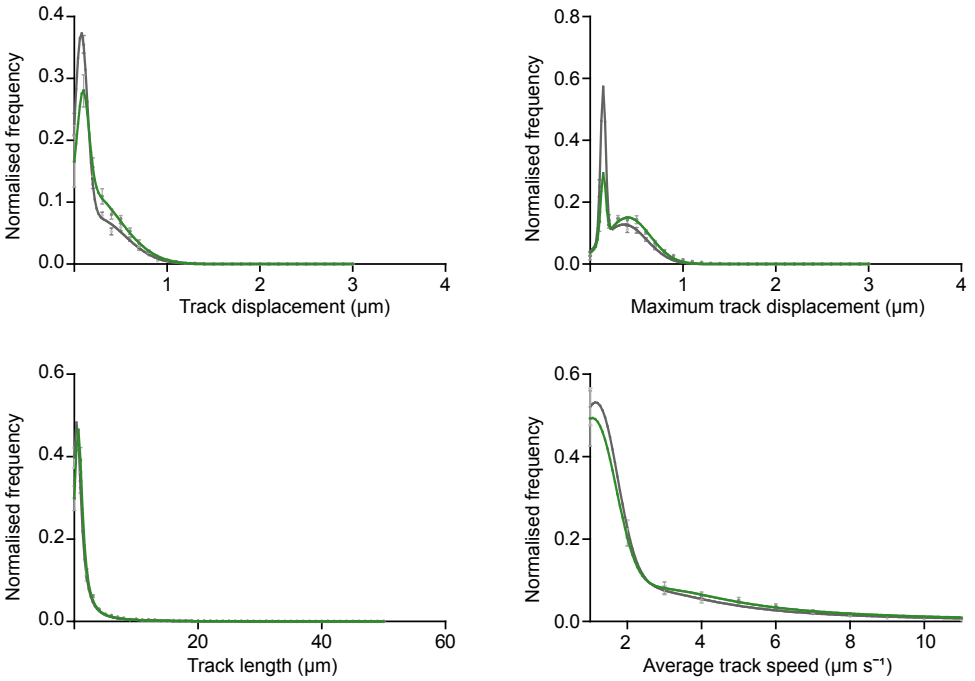

Figure 4.12 Cell stimulation significantly alters vesicle mobility. Track parameters displayed for 16,944 tracks from 5 PC12 cells (grey) and 11,608 tracks from 4 stimulated PC12 cells (red). Data normalised to number of tracks per cell (mean ± SEM). Track displacement and maximum displacement fit to a double Gaussian R^2= 0.99 (Extra sum of squares F-test p= 0.0001). Track length fits to a single Gaussian R^2= 0.99 (Extra sum of squares F-test p= 0.0001). Average speed fits to a single Gaussian (R^2= 0.99) (Extra sum of squares F-test p= 0.0009).

within a single distribution; the curves are significantly (p= 0.0001) different from one another. The average speed of the vesicles is significantly (p= 0.0009) increased with a decrease in the frequency of speeds under 0.2 μm s^{-} and an increase in the faster moving vesicles. These data strongly suggest an increase in the mobility of vesicles upon cell stimulation, whether this increase is isolated within a certain vesicle type requires analysis of individual vesicle tracks.

4.2.7 Examination of vesicles that scan the membrane

The distinct regions of plasma membrane sampled by vesicles imply strongly that there are preferred regions of plasma membrane and these may represent specific sites for vesicle docking and fusion. A subset of vesicles were observed at the plasma membrane of unstimulated cells that appear to be searching for these sites; moving in a caged manner before directly moving to the next site of interest (Figure 4.13). These vesicles were also present in stimulated cells and often exhibit this sampling behaviour over areas previously visited by other vesicles. To investigate whether the mobility of this group of vesicles in particular is affected by stimulation selected vesicle tracks were analysed from unstimulated and stimulated cells (Figure 4.14). The vesicle mobility is dynamic and cannot be defined as either directed or caged when plotting track displacement against track length. When comparing unstimulated to stimulated scanning tracks there is a suggestion that the vesicles within stimulated cells exhibit a more caged behaviour than unstimulated. The average track lengths of both data sets are not significantly different from one another; however both track displacement and average track speed are reduced for these vesicles when a cell is stimulated. It is apparent from these data that the increase in vesicle displacement seen in Figure 4.12 is not caused by this vesicle group. To further examine the behaviour of these vesicles each step (from one frame to the next) from 4 individual tracks in unstimulated cells and 3 tracks in stimulated cells were broken down into either caged or directed motion (Figure 4.15). This criterion was based on the angle of the step relative to the previous; for example a reversal is noted as caged and a forward trajectory as directed. Initial analysis examined the average speed of caged

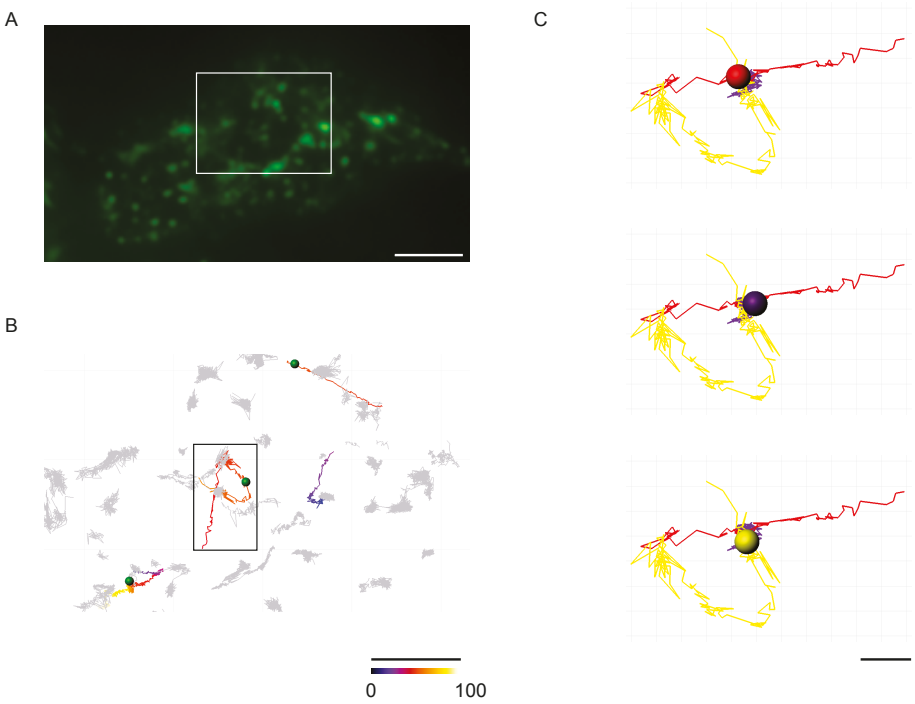

Figure 4.13 Vesicles ‘scanning’ the plasma membrane are dynamic in their behaviour. A) All EGFP-NPY vesicles present at the plasma membrane of a representative PC12 cell over a 45 second TIRFM recording. Scale bar is 4 μm. B) Enlarged region of interest from A (white box). Grey tracks are all vesicles tracked within the recording and coloured tracks are ‘scanning’ vesicle tracks. Scale bar is 2 μm and colour represents time in seconds. C) Enlarged region from B showing 1 caged track (purple) and two ‘scanning’ vesicles (red and yellow) covering similar regions of plasma membrane. Scale bar is 4 μm.

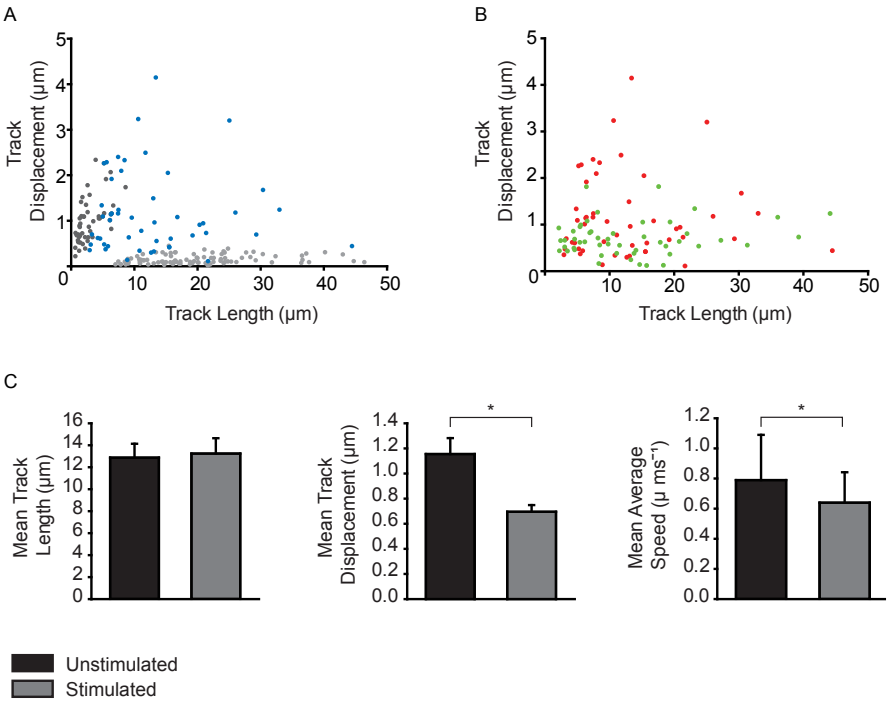

Figure 4.14 Cell stimulation reduces the mobility of 'scanning' vesicles. A) The track length and displacement of 'scanning' vesicles (blue) are compared against directed (dark grey) and caged tracks (light grey). B) The track length and displacement of 'scanning' vesicles in unstimulated cells (red) is compared to 'scanning' vesicles in stimulated cells (green). C) The mean track length (mean ± SEM, n.s), displacement (mean ± SEM, Mann Whitney p= 0.015) and speed (mean ± SEM, Mann Whitney p= 0.006) are displayed for 'scanning' vesicles in unstimulated cells (black) and stimulated cells (grey). n= 50 tracks for unstimulated and stimulated data sets.

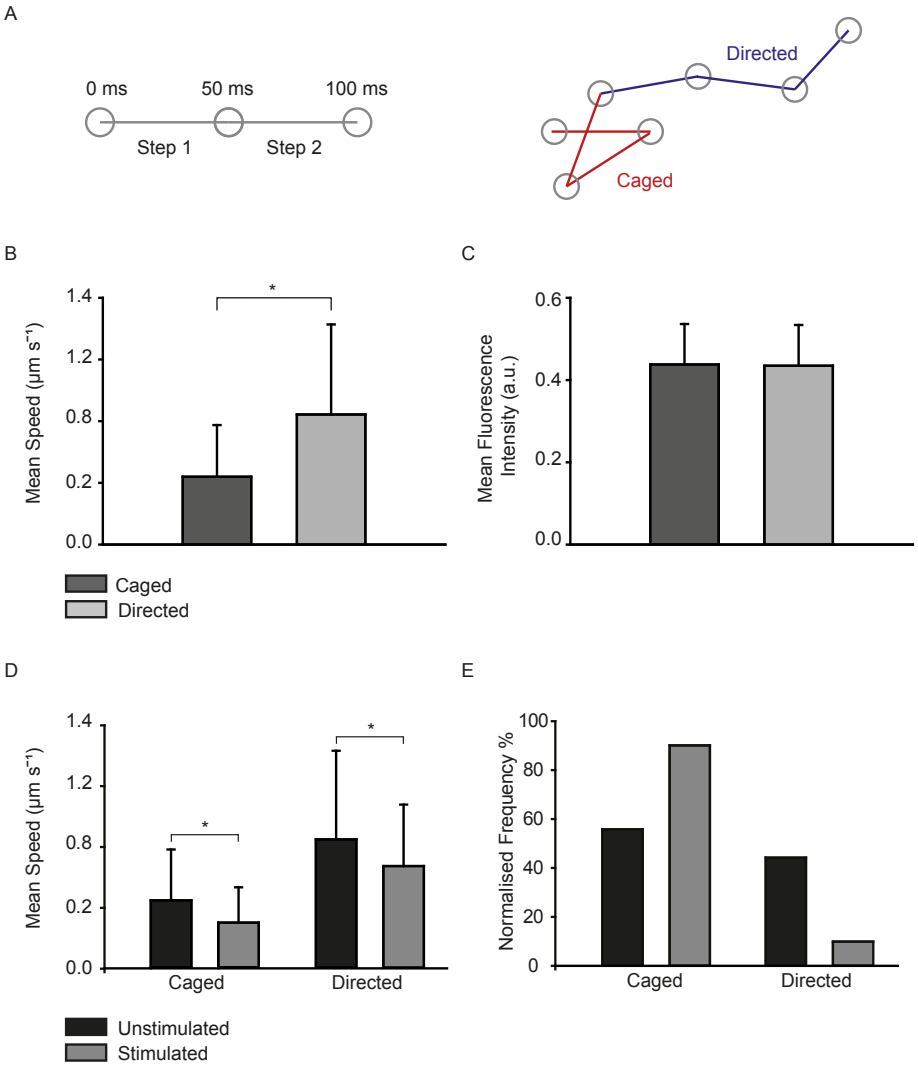

Figure 4.15 'Scanning' vesicles slow down and become more caged upon cell stimulation. A) The movement (grey line) a vesicle (grey circle) makes from one frame to the next (in 50 ms) is one step and can be caged (red) or directed (blue). B) The speed of caged steps (dark grey) within 'scanning' vesicle tracks are compared to directed (light grey) (mean ± SEM, Mann Whitney p= 0.001). C) The fluorescence intensity for caged and directed steps within 'scanning' vesicle tracks (mean ± SEM, n.s). D) The speed of caged steps (mean ± SEM, Mann Whitney p= 0.001) and directed steps (mean ± SEM, Mann Whitney p= 0.016) within 'scanning' vesicle tracks from unstimulated (black) and stimulated (dark grey) cells are compared. E) The frequency, normalised to number of steps, of either caged or directed steps within each track is shown for 'scanning' vesicle tracks from unstimulated (black) and stimulated (dark grey) cells. n= 4 tracks (unstimulated) n= 3 tracks (stimulated).

steps compared to directed in unstimulated cells; caged motions were significantly ($p= 0.001$) slower than directed tracks. Whether the scanning vesicles came closer to the plasma membrane when caged was investigated by measuring fluorescence intensity; the centroid intensity of the vesicle within each frame displaying caged or directed motion was reported. These data demonstrate no significant change in the intensity between these two behaviours. The intensity of these vesicles does fluctuate over time but quantification of these oscillations was not possible due to the possible effect of drift and the non-uniform distribution of EGFP-NPY within the vesicles. Extracting the caged and directed steps within scanning vesicle tracks in stimulated cells further demonstrates the decrease in speed exhibited by these types of vesicles as mentioned in Figure 4.14. Both caged ($p= 0.001$) and directed ($p= 0.016$) steps in stimulated cells are significantly slower than those reported in unstimulated cells. Scanning vesicles in unstimulated cells show a similar proportion of caged tracks to directed tracks whereas in stimulated cells there is a dramatic loss in the proportion of vesicles undergoing directed motion and a marked increase in caged motion.

The change in mobility seen after cell stimulation further supports the functional relevance of these scanning vesicles; however these scanning tracks are not made by vesicle that fuse. Analysis of all fusing vesicles at the plasma membrane reveals a group of vesicles that have a similar scanning behaviour to those discussed so far but on a considerably smaller scale. Figure 4.16 compares vesicles that have been identified as scanning vesicles in stimulated cells and those vesicles that fuse with a dynamic behaviour ranging between caged and directed. There is a significant decrease in track length ($p= 0.03$) and displacement ($p= 0.001$) of those that fuse.

4.2.8 Resident vesicles behave differently to newly recruited vesicles

Analysis of the vesicles that fuse at the plasma membrane reveals two distinct groups, those that are present at the membrane prior to cell stimulation and those that arrive after, termed resident vesicles and newly recruited vesicles. To assess whether fusing vesicles are responsible for the increase in vesicle mobility the resident fusing

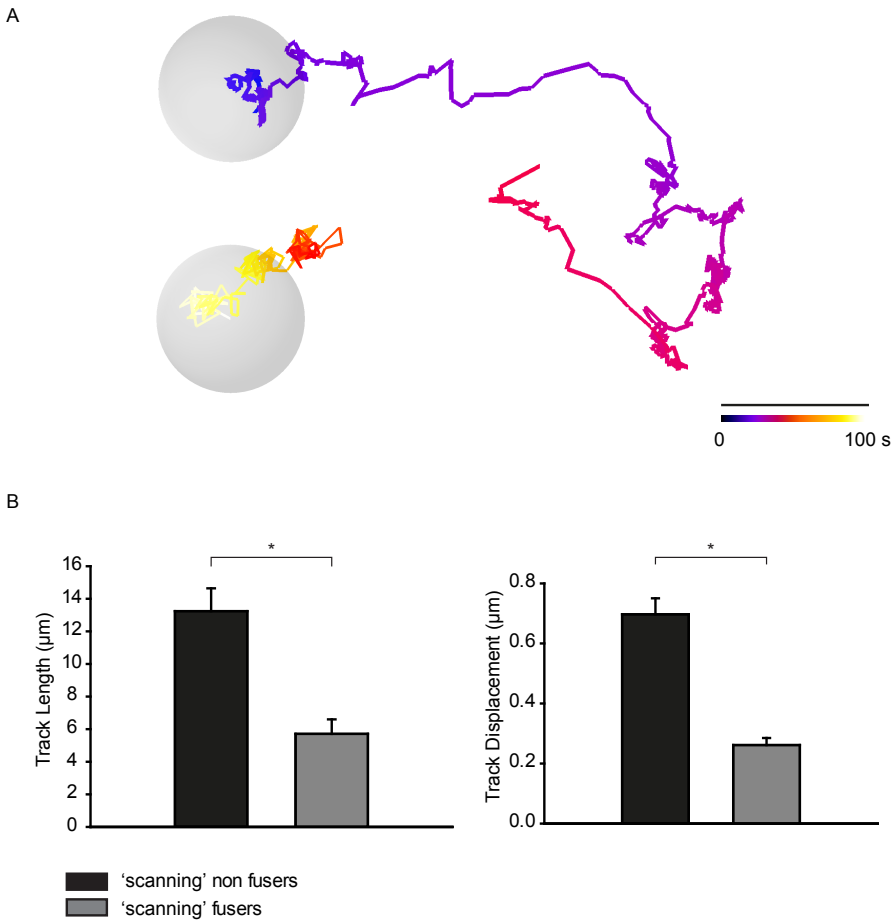

Figure 4.16 'Scanning' vesicles that fuse have reduced mobility compared to non fusers. A) Examples of a 'scanning' vesicle (grey sphere) track at the plasma membrane after stimulation (non-fuser= upper, fuser= lower). Scale bar 0.4 µm. Colour represents time in seconds. B) The track length and displacement for 'scanning' vesicles that do not fuse (black, n= 50) and 'scanning' vesicles that fuse (grey, n= 7) from stimulated PC12 cells. Mean ± SEM, Mann Whitney p= 0.03 (track length), p= 0.001 (track displacement).

vesicles were analysed before and after fusion (Figure 4.17). These vesicles move in a caged manner both before and after fusion and there is no significant change in their track length, displacement or speed upon stimulation. Analysis of newly recruited fusing vesicles shows three different types of mobility; immediate, caged and scanning (Figure 4.18). The scanning vesicles have been discussed previously and move with both caged and directed motion (4.16), immediate fusers have a track length close to 0 and so must fuse within milliseconds of reaching the membrane and the third group are caged/nearly immobile within the diameter of the vesicle. Recruited vesicles display a significant decrease in track length ($p= 0.013$) compared to resident vesicles but an increase in both speed ($p= 0.001$) and displacement ($p= 0.011$). The mean speed of the recruited vesicles is 1.2 $\mu m\ s^{-1}$, which is higher than that seen in vesicles under resting conditions. The faster vesicles are predominantly the immediate fusers and the slower represent the caged/nearly immobile vesicles.

To further investigate this behaviour the speed of vesicles leading up to fusion was examined for residents and newly recruited vesicles (Figure 4.19). The average speed of resident vesicles in these last 60 frames barely fluctuates with a small increase in speed at the last step. Newly recruited vesicles fluctuate more at a slightly increased speed and the average speed undertaken on the last step to fuse is dramatically increased. Some vesicles were present for fewer than 3 seconds prior to fusion and for this reason they were not included in these data. To examine the final fusion step in all tracked resident and newly recruited vesicles this step was isolated and transformed to begin at the same xy coordinate. These data further demonstrate the jump to fuse that the recruited vesicles can undertake and show this displacement can exceed the radius of the vesicle within this frame.

4.2.9 Vesicle fusion at the plasma membrane is temporally and spatially controlled

The majority of fusion events occur within the first 10 seconds post-stimulation, this is followed by a second burst of fusion which peaks at ~20 seconds

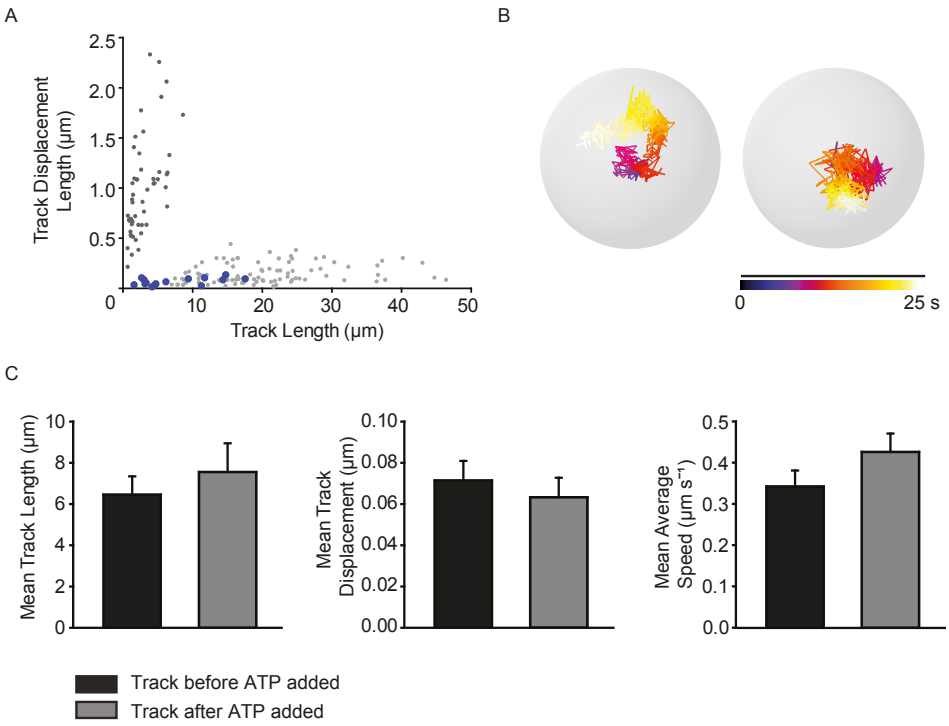

Figure 4.17 Resident vesicles do not significantly change their mobility after cell stimulation. A) Resident vesicle (n= 14, blue) track length and displacement after ATP added are plotted amongst directed (n= 52, dark grey) and 'caged' tracks (n= 97, light grey). B) A representative track before (left) and after (right) stimulation up until fusion. Colour of track represents time in seconds. Scale bar 0.4 µm. C) The mean track length, track displacement and mean average speed of resident tracks before (black) and after (grey) ATP addition (mean ± SEM, n= 14 tracks, Mann Whitney = n.s).

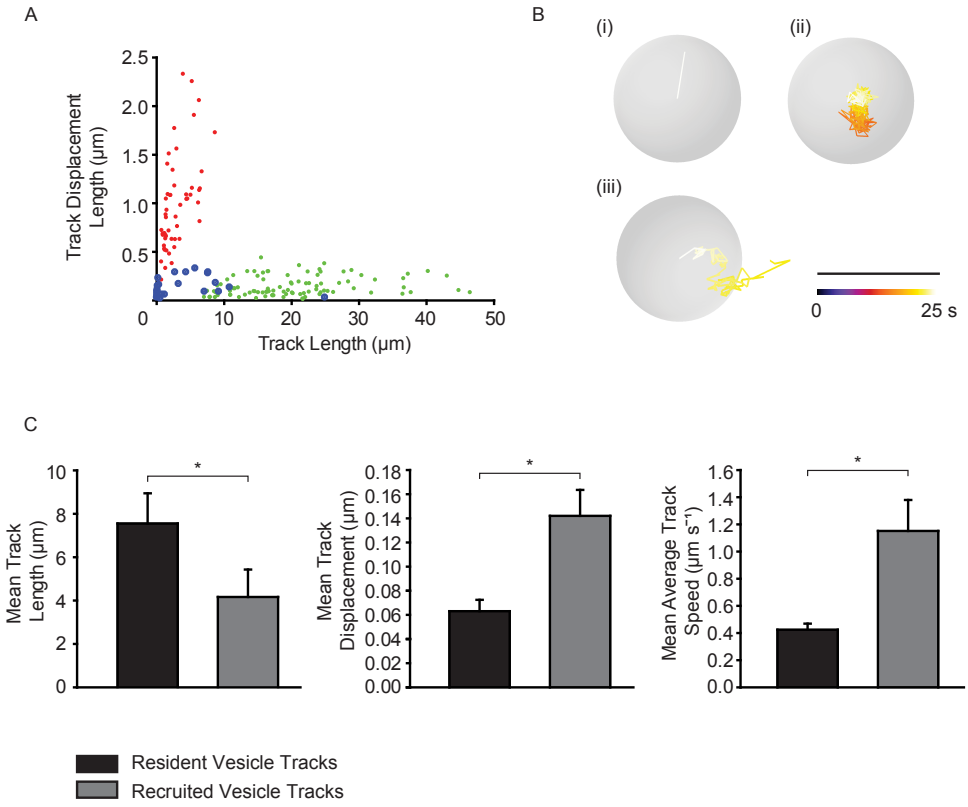

Figure 4.18 Newly recruited vesicles display a different mobility to resident vesicles. A) Recruited vesicle (blue) track length and displacement are plotted amongst directed (n= 52, red) and caged tracks (n= 97, green). B) Representative tracks showing immediate (i), caged (ii) and 'scanning' (iii) up until point of fusion. Colour of track represents time in seconds. Scale bar 0.4 µm. C) Resident vesicle tracks (n= 14, black), recruited vesicle tracks (n= 23, grey). Track length (mean ± SEM. Mann Whitney p= 0.013), track displacement (mean ± SEM. Mann Whitney p= 0.011), Track speed (mean ± SEM. Mann Whitney p= 0.001).

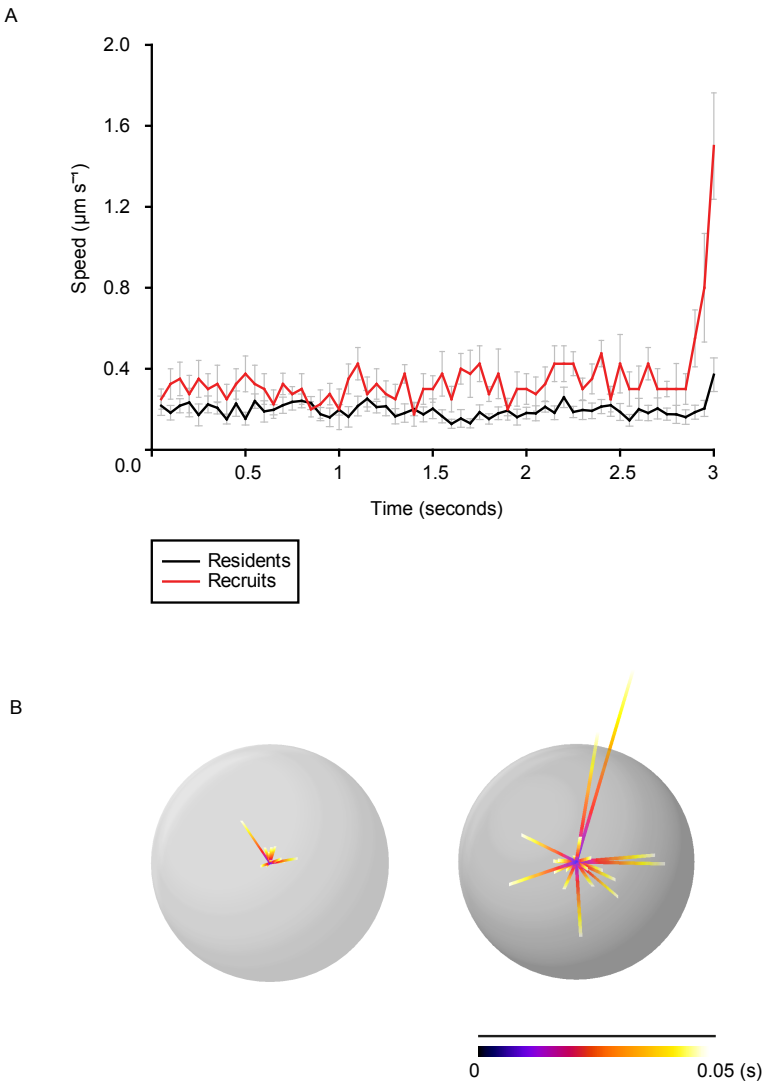

Figure 4.19 Newly recruited vesicles 'jump' considerably in the final step to fuse. A) The last 3 seconds prior to fusion including the final jump (mean ± SEM. Mann Whitney p= 0.001. Residents (black) n= 3. Recruits (red) n= 4). B) The final track before fusion for resident vesicles n= 14 (left panel) and newly recruited vesicles n= 23 (right panel). Tracks are translated to start at the same xy coordinate. Colour track represents time in seconds. Scale bar 0.4 µm.

post-stimulus (Figure 4.20). The resident vesicles fuse within the initial exocytotic burst along with the immediate and caged fusers that are recruited to the plasma membrane. All vesicle types contribute to the sustained release however only the newly recruited scanning vesicles are specific to this phase.

Examination of vesicle fusion at the plasma membrane revealed sites where multiple fusion events occurred (Figure 4.21). To establish fusion within the same vesicle site only events occurring within the radius of a vesicle (200 nm) were selected for analysis. The most common sub-class of vesicles to fuse were those that almost immediately fused upon arrival at the plasma membrane. Vesicles with a caged motion were also seen to fuse within the same 400 nm region and interestingly the minimum refractory period was 1.5 second between the first to second fusion event. In addition vesicles with different mobilities were able to fuse in the same place.

With evidence indicating specific vesicle sites for fusion the xy coordinates of exocytosis from a PC12 cell over 45 seconds were labelled within 400 nm x 400 nm boxes and merged with vesicle contour maps (Figure 4.22) to assess the typical vesicle behaviour at these sites. A representative cell is shown in Figure 4.22; a total of 4 cells containing 11,608 tracks were analysed and displayed a similar pattern. With the exception of a few, vesicles tend to fuse in regions that are frequently populated by other vesicles at the plasma membrane. The ‘contour’ map displaying average vesicle speed shows speeds up to 1 $\mu m\ s^{-}$; however there are no fusion events in areas displaying average speeds > 0.6 $\mu m\ s^{-}$. Fusion events are most commonly seen over areas visited by vesicles displaying speeds between 0.1 $\mu m\ s^{-}$ and 0.5 $\mu m\ s^{-}$.

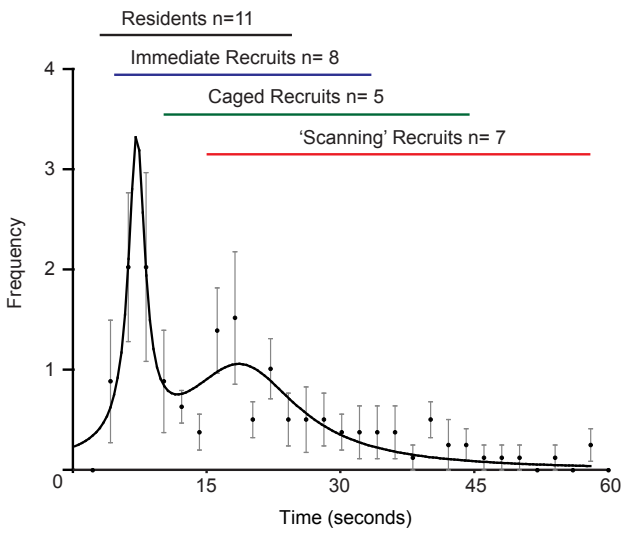

Figure 4.20 Vesicle mobility correlates with phases of secretion. The elapsed time after ATP addition before a vesicle fuses is plotted as a histogram in 2 second bins over 60 seconds (mean ± SEM. n= 31 vesicles in 7 PC12 cells). Data fits to a double Gaussian (Extra sum of squares F-test p= 0.001, R^2= 0.85). Vesicles grouped by mobility fuse within different phases of secretion.

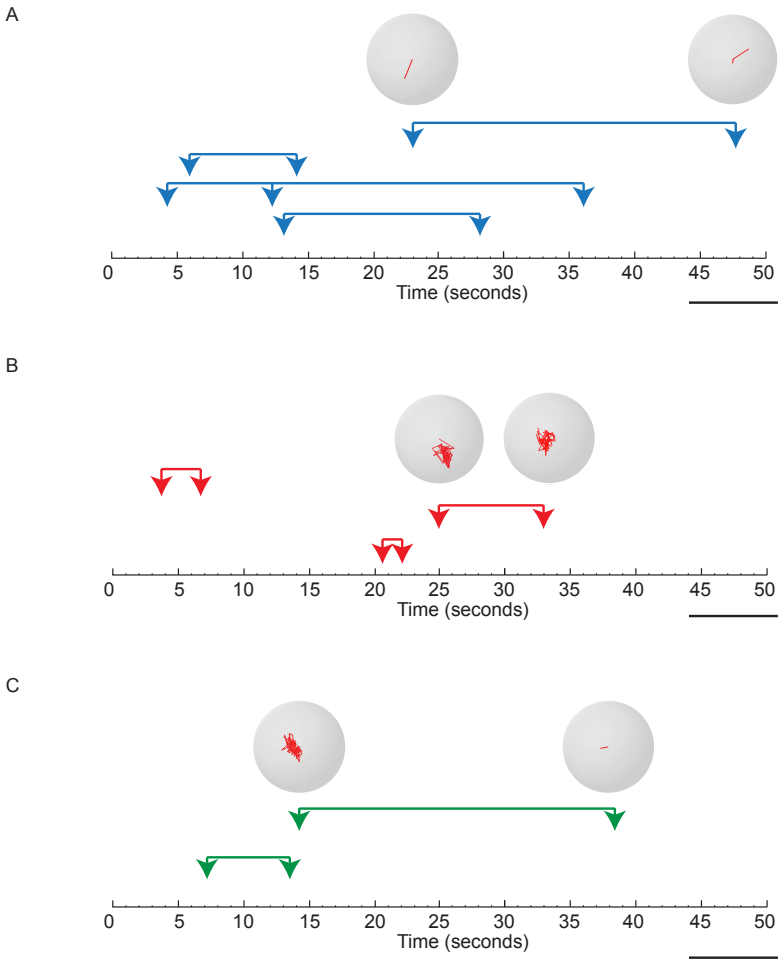

Figure 4.21 Vesicle fusion can occur in the same region more than once. Arrow heads represent point of fusion along the scale with ATP addition at 0. Line shows refractory period until subsequent fusion in same 400 nm² square region of membrane. Example tracks (red) within vesicles (grey spheres) at point of fusion. A) Vesicles which fuse almost immediately. B) Vesicles that are caged before fusion. C) The first vesicle is caged the second is almost immediate. All scale bars 0.4 μm.

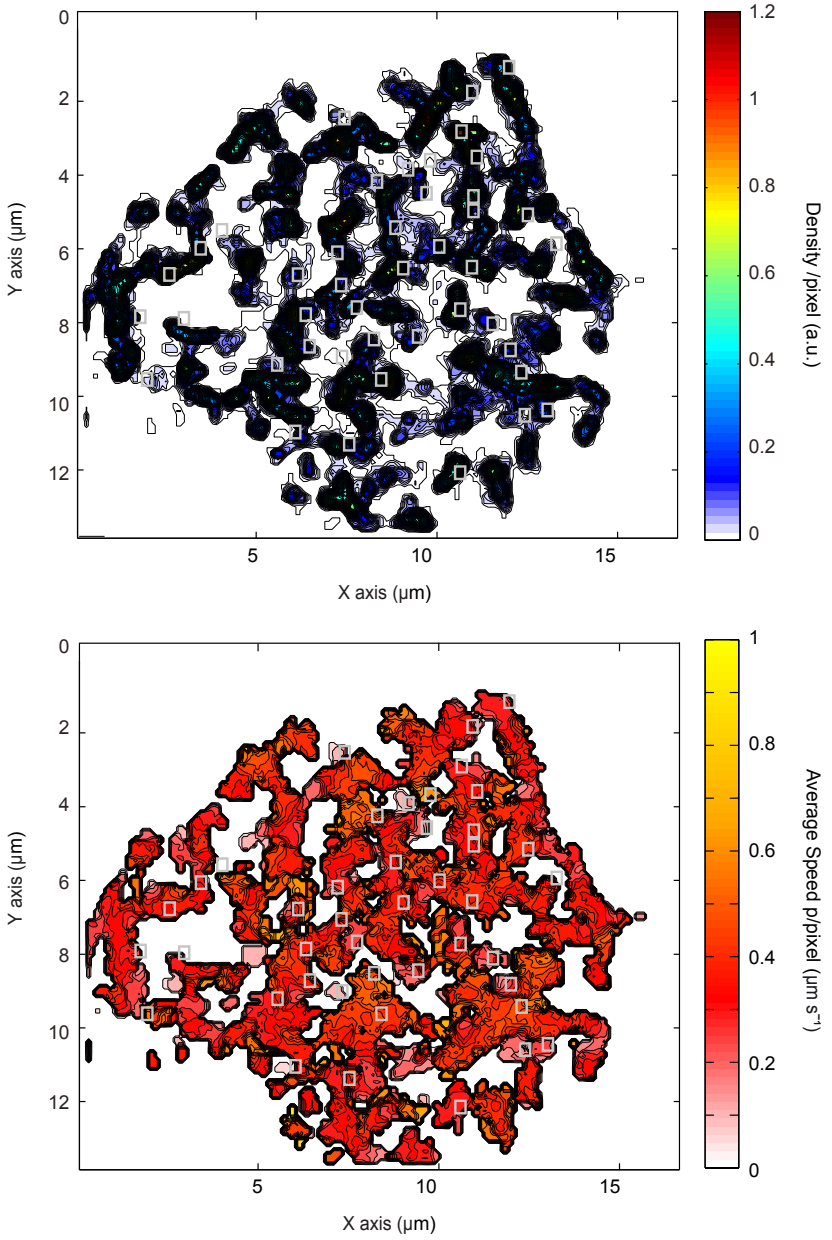

Figure 4.22 Sites of vesicle fusion correlate with regions of high density. Sites of vesicle fusion are depicted as 0.4 µm² white boxes over 'contour' maps of a representative stimulated PC12 cell over a 45 second recording; n= 5,329 tracks. A) Density 'contour' map showing number of tracks within each pixel. B) Speed 'contour' map showing average speed of tracks per pixel in µm s^{-1}.

4.3 Conclusions

This chapter initially aimed to establish the vesicle behaviour at the plasma membrane of unstimulated neuroendocrine cells using an optimum acquisition time and improved accuracy analysis methods. Vesicle tracking in commercial software demonstrated the non-random arrangement of vesicle localisation at the plasma membrane (Figure 4.1). The majority of vesicles appear to be restricted to designated areas across the membrane and there is minimal movement between these punctate regions. Further examination improved on previous tracking methods by using a more sensitive analysis program to provide spatial information on a larger group of vesicles and further demonstrated the preference for selected sites (Figure 4.2). The caged mobility of vesicles has been discussed extensively in past works (Steyer et al., 1997; Oheim and Stühmer, 2000; Johns et al., 2001) and data within this chapter found it to be the predominant type of motion undergone by the vesicles (Figure 4.4). These data provided a more in-depth examination than previously seen as the direction, speed and angle of each step taken by a large number of vesicles was analysed.

As previously mentioned vesicle mobility has been categorised into three groups dependent on mobility and allocated to vesicle pools (Nofal et al., 2007). The data presented within this chapter does not directly agree with this model and instead describes an alternative based on vesicle displacement (Figure 4.7). One set of vesicles do not track outside of their vesicle radius (set 1) and could be tethered to the plasma membrane; however their docked or primed status is not distinguishable. The remaining two groups represent vesicles displacing outside of their vesicle radius within their track. The first move in a caged manner as if attempting to tether to the membrane (set 2). Past works have described a link between vesicle dynamics and fusion-mediating proteins such as the SNAREs and synaptotagmin (De Wit et al., 2009; López et al., 2009) and so it is plausible that vesicles within set 2 are transitioning in and out of protein associations. The final group have markedly higher displacements and move in a directed manner across the membrane, these are rare (set 3). Some vesicles are specific to these groups however there are many vesicles

that transition between them. The speed at which the vesicles travel on average across a track agrees with previous reports that show an average speed of 0.33 μm s^{-} (Steyer and Almers, 2001; Nofal et al., 2007). One view is that the mobility is related to the protein and lipid associations between the vesicle and the plasma membrane however the role of actin must also be considered as an influential factor in how a vesicle behaves. The importance of actin stability in membrane protein localisation and lipid order has been shown recently (Tomatis et al., 2013; Dinic et al., 2013), implicating a possible role in the control of regulated exocytosis.

The implications of depleting cholesterol from the plasma membrane on exocytosis in past works imply that the sterol is required for efficient vesicle fusion. In addition depleted pools of vesicles at the plasma membrane have been observed implying a reduced ability to target to fusion sites and dock (Zhang et al., 2009; Koseoglu et al., 2011). Vesicles tracked in MβCD-treated cells in section 4.2.4 were found to be more mobile, an effect that could be propagated through a number of different pathways. The tethering of vesicles to cortical actin has been described previously (Tomatis et al., 2013) and the role of actin in recruiting vesicles to the plasma membrane is also suggested (Oheim and Stühmer, 2000). By perturbing actin the movement of the vesicles would therefore be affected. Recent studies show that by stabilising actin lipids at the plasma membrane are more ordered (Dinic et al., 2013), the destabilisation of actin through cholesterol depletion could demonstrate a more indirect pathway of plasma membrane disordering. The alteration of the lipid arrangement at the plasma membrane, through indirect and direct reduction of lipid ordering, could disrupt vesicle targeting to specific sites. To more directly investigate the importance of lipid ordering on vesicle mobility across the membrane the two components would ideally be imaged in combination. This is not currently possible as Laurdan emission is not compatible for the dual colour imaging of vesicles and lipids and by imaging two components at once the acquisition time is increased and information on vesicle mobility is reduced.

An increase in vesicle mobility is observed after cell stimulation, with vesicle displacement and maximum displacement showing the most dramatic changes

(Figure 4.12). There is a reduction in the number of vesicles with the shortest displacements (set 1), as these are suggested to represent docked and primed vesicles (Steyer et al., 1997; Oheim et al., 1998) this could be due to the fusion of vesicles from this population. In correspondence with my previous vesicle allocation the number of vesicles moving with a predominantly caged mobility outside of the vesicle radius (set 2) has increased and may represent those vesicles looking for fusion sites upon the secretory signal. These conclusions are mirrored by similar changes in maximum displacements within a vesicle track. In addition the number of vesicles undergoing faster speeds has increased after cell stimulation.

With the aim to identify which vesicle types may be responsible for these changes selected vesicles were isolated and analysed. A type of vesicle seen to scan the plasma membrane and transition between a caged and directed motion were identified within neuroendocrine cells before and after stimulation (Figure 4.13). This vesicle type, termed ‘scanners’, has not been previously reported; however their sampling behaviour at the plasma membrane particularly over sites previously visited by other vesicles provides insight into targeting to exocytotic sites. In unstimulated cells these vesicles display track displacements that fall within set 3, however in stimulated cells these types of vesicles display shorter displacements that fall within set 2. The increase in vesicles undergoing these types of displacements in the histogram may be attributed to an increase in the number of vesicles displaying this type of behaviour after stimulation. Interestingly these vesicles slow down after stimulation and become more caged, which suggests the vesicles are searching more for fusion sites upon secretory signals (Figure 4.15). The reduced speed within these vesicles imply this type do not contribute to the increased speed in vesicle mobility after stimulation.

The isolation and analysis of the newly recruited fusing vesicles appear to contribute to the increase in vesicles moving faster after cell stimulation (Figure 4.18). These vesicles approach the plasma membrane within a recording of a stimulated cell and so represent those coming in from inside the cell; possibly from the reserve pool (Augustine and Nehert, 1992; Steyer et al., 1997). Past works have

described an increase in speed on approach to the plasma membrane followed by a dramatic decrease upon membrane association (Johns et al., 2001; Degtyar et al., 2007); however these measurements were made in the z dimension. Within this chapter and a previous study (Yang et al., 2012a) a similar increase in speed in the final step was observed, however the movement occurred laterally to the plasma membrane. In Figure 4.19 the vesicle dynamics leading up to fusion have been quantified for the resident and newly recruited vesicles separately and demonstrate a dramatic increase in the newly recruited vesicles in the fusion step. In addition the speed leading up to fusion was significantly increased in this vesicle sub-type compared to resident vesicles further demonstrating the increased mobility of those vesicles recruited to the membrane from inside the cell.

Comparison of the speed and displacement of fusing vesicles resident prior to stimulation and those that are newly recruited are informative of vesicle targeting to fusion sites. Those resident prior to stimulation at the membrane do not move far to fuse, which has been previously shown (Oheim et al., 1998), and could suggest they are tethered to fusion-ready sites before secretory signals arrive. The vesicles recruited to the plasma membrane move faster with larger displacements; however their track length is smaller implying the targeting of these vesicles to their fusion sites is tightly controlled with minimal dwell time at the plasma membrane. Although short, the dwell times at the plasma membrane for newly recruited vesicles are varied with immediate, caged and ‘scanning’ fusers; suggesting there is an element of temporal control at these sites, which could be imposed by the protein-lipid or protein-lipid arrangement within the area tracked by the vesicle. This temporal control is also suggested by the selective fusion over certain time periods within the stimulation (Figure 4.20). Figure 4.20 shows the biphasic release of vesicles at the plasma membrane, which has been seen previously and corresponds with the fast and slow burst of exocytosis (Augustine and Neher, 1992; Voets et al., 1999). Previous works have predominantly used high potassium to stimulate cells and observe fusion between 2 – 16 seconds post stimulation with the majority occurring in the first few seconds (Steyer and Almers, 1999; Degtyar et al., 2007). ATP elicits a longer

stimulation response compared to high potassium and has been shown in one report to stimulate cell fusion for ~ 20 seconds post stimulus (Pouli et al., 1998).

Specific sites for exocytosis have been proposed in previous works to be dependent on components of the exocytotic machinery such as; calcium channels (Becherer et al., 2003), SNARE proteins (Lang et al., 2001; Barg et al., 2010) and the lipid environment (Chamberlain et al., 2001; Domanska et al., 2010). Further evidence for these sites has emerged from multiple fusion events in neuroendocrine cells (Oheim et al., 1999; Allersma et al., 2004) and in neurons (Zenisek et al., 2000). This has been observed in PC12 cells within this chapter; strongly supporting the behavioural analysis indicating vesicle localisation over specific sites for fusion. In multiple fusion events the time between the first and subsequent fusion at the same 400 nm square site ranges between 1.5 and 25 seconds. A LDCV contains approximately 1.67 μm^2 of lipids, which are significantly more disordered than those at the plasma membrane; upon fusion this vast number of lipids has to incorporate into the membrane. The short time frame between fusions could imply a 'kiss and run' mechanism (Ceccarelli et al., 1973; Taraska et al., 2003) as it is less disruptive than the incorporation of the lipids from a LDCV membrane if full fusion occurred; however single vesicle fusion events analysed within this chapter underwent full fusion as they fully released their content and were not detected after the event. Studies have shown complete fusion can occur within 10 ms (Wang et al., 2009) and the lipids within the membrane can transition from one phase to another in millisecond time frames (Bacia et al., 2004). Data presented in Figure 4.21 therefore suggests that the membrane is able to relatively rapidly reorganise its lipid membrane and protein components ready for another fusion.

The localisation of vesicle fusion has not previously been related to the surrounding vesicle behaviour. Within this chapter sites of fusion have been merged with contour maps showing density and speed of vesicle tracking. Fusion predominantly occurs within regions of high density, which supports the theory that sites repeatedly visited by vesicles represent sites that contain the correct environment for efficient fusion. There are fusion sites on the periphery of these

‘hotspots’, which demonstrate an exception to this rule. The distance from the ‘hotspots’ is too large to be explained by the ‘jump’ to fuse seen in Figure 4.19 and could instead provide evidence for fusion sites where the t-SNAREs can transition from a non-functional to a functional state (Fasshauer et al., 1997; Weninger et al., 2008; Rickman et al., 2010) (see Chapter Five) in a controlled manner to allow fusion at a site not predetermined prior to stimulation (Oheim et al., 1998; Barg et al., 2010; Yang et al., 2012a).

Within this chapter I have applied alternative analysis approaches to closely examine vesicle dynamics at the plasma membrane of neuroendocrine cells. The existence of vesicle fusion sites is strongly implied within my data, in particular with the examination of a ‘scanning’ vesicle subtype not previously identified. My previous experiments in Chapter Three enabled quantitative analysis of vesicle behaviour after the disruption of lipid order; which strengthen the possible association found between the plasma membrane lipid organisation and the vesicle behaviour. My data is largely in agreement with findings from past works however the use of optimum sampling rates as well as custom tracking software has provided further insight into vesicle dynamics in relation to the fusion event.

Chapter Five:

t-SNARE Organisation at the Plasma Membrane

5.0 Introduction

It is well established that the t-SNAREs colocalise at the plasma membrane of neuroendocrine cells (Lang et al., 2001; Rickman et al., 2004; Halemani et al., 2010), which relates to an overlap in the fluorescence of two fluorescently tagged proteins under diffraction-limited microscopy (Manders et al., 1993). These same works (Lang et al., 2001; Rickman et al., 2004) have described the t-SNAREs as clustered at the plasma membrane with a cluster diameter of 200 nm, which is the resolution limit of the system. The advancements in super-resolution techniques (Patterson and Lippincott-Schwartz, 2002; Betzig et al., 2006; Subach et al., 2009) have allowed a closer inspection of protein clusters; however there are still only a few studies looking at the exocytotic machinery (Willig et al., 2006; Sieber et al., 2006, 2007; Yang et al., 2012). A study using STED on membrane sheets was one of the first to report on a syntaxin-1 cluster diameter smaller than the limit of resolution, these were 50-60 nm (Sieber et al., 2007); however single molecules were not resolved within these clusters. A recent study from our group (Yang et al., 2012) has localised single molecules of syntaxin-1 at the plasma membrane and revealed a more complex arrangement than the homologous clusters previously described (Sieber et al., 2007). The study shows that both endogenous (dSTORM) and exogenous (PALM) syntaxin-1 molecules are heterogeneously arranged with regions of densely formed clusters as well as regions of low density (Yang et al., 2012). The study of single SNAP-25 molecule localisation using super-resolution microscopy has been minimal compared to syntaxin-1 (Sieber et al., 2006; Barg et al., 2010); however this recent study has used single molecule localisation microscopy to reveal SNAP-25 exhibits a similar heterogeneous pattern displayed by single molecules of syntaxin-1 (Yang et al., 2012).

The localisation of the SNARE proteins in relation to their lipid order has been studied *in vitro* and using diffraction-limited imaging approaches. Initial *in vitro* studies found that SNAREs exist in DRMs and allocated these proteins to more ordered regions of plasma membrane (Brown and Rose, 1992; Chamberlain et al., 2001; Foster et al., 2003). This method involves the solubilisation of the membrane

and has been criticised for not being representative of the lipid environment within live cells (Lichtenberg et al., 2005). Other works have focused on microscope techniques to investigate the relationship. One study suggests that syntaxin-1 clustering is cholesterol-dependent (Lang et al., 2001), but these clusters are observed under diffraction-limited microscopy and the concentration of MβCD used to deplete cholesterol is higher than used in other works (Zhang et al., 2009; Rickman et al., 2010) (see 3.1). Conversely there are studies implying that SNAREs prefer to reside in lipid disordered domains; however these experiments used GUVs and not native membranes as a platform (Bacia et al., 2004). SNAP-25 is palmitoylated at the plasma membrane and modification of this process has been suggested to dictate lipid raft localisation (Salaün et al., 2005). It is interesting that this protein has not been the focus for cholesterol depletion experiments, instead syntaxin-1 remains the protein of interest in most works (Lang et al., 2001; Lam et al., 2008; Murray and Tamm, 2009).

Investigations into the t-SNARE binary complex *in vitro* have proven important in establishing the sequential zippering of these proteins and the interactions between each helix (Fasshauer et al., 1997; Fiebig et al., 1999). Studies revealed the existence of an alternative conformation where the second SNARE helix of SNAP-25 is disassociated (Hayashi et al., 1994; Fasshaueret al., 1997; Weninger et al., 2008); however the functional relevance of this configuration is still under debate. Examination of the t-SNARE complex in live cells has predominantly involved the use of intensity-based FRET, where an interaction is reported upon an increase in acceptor fluorescence (An and Almers, 2004; Wang et al., 2008). These works have confirmed the existence of the alternative conformation in reconstituted bilayers and HEK293 cells and suggest a transitioning between the two states. As discussed in Section 2.4.4 FRET is the transfer of energy from a donor fluorophore to an acceptor fluorophore when at intermolecular distances (Stryer, 1978; Förster, 1946; Clegg, 1995). FRET has been measured in the works discussed above using a change in acceptor fluorescence intensity as an indicator of interaction. Measuring interaction using intensity-based FRET does not consider the number of interacting molecules within the imaged sample, this means increase in acceptor fluorescence

could be reported as a change in interaction status when in fact more molecules are undergoing an interaction. In addition the detection of emitted light from a fluorophore can be heavily influenced by bleaching and chromatic aberration, which can lead to unreliable intensity recordings (Lakowicz, 1999). Previous works have used TCSPC-FLIM (see 2.4.4) to accurately quantify the degree of FRET between fluorescently tagged t-SNAREs in cellular trafficking as FLIM is able to provide data unaffected by donor or acceptor concentration (Lakowicz, 1999; Medine et al., 2007).

This chapter aimed to analyse the localisation of single molecules of SNAP-25 at the plasma membrane using single molecule localisation microscopy as well as the interaction between SNAP-25 and syntaxin using TCSPC-FLIM. The effects of cholesterol depletion on both the localisation and interaction status of SNAP-25 were also investigated.

5.1 Materials and Methods

PALM experiments (see 2.4.5) were performed on fixed PC12 cells co-transfected with EGFP-NPY and PA-Cherry-SNAP-25 and imaged at room temperature under TIRFM illumination. In cholesterol-depletion PALM experiments cells were incubated with 10 mM MβCD 30 minutes (previously ascertained to quantifiably disrupt lipid order in Chapter Three, Figure 3.4) immediately prior to fixation. dSTORM experiments were performed on fixed PC12 membrane sheets (see 2.3.4), which were incubated with 5 μM Laurdan for one hour, unroofed and fixed immediately. This was followed by immunostaining with Alexa-647 tagged to SM181 (anti-SNAP-25) (see 2.1.13). Sheets were imaged in dSTORM buffer with 5 μM Laurdan at 37°C. Laurdan emission was collected as described in 2.3.5. Matlab (Mathworks) was used for analysis as described in 2.5.3. TCSPC-FLIM (see 2.4.4) using the CLSM was performed on live N2a cells co expressing EYFP-SNAP-25 and mCer-syntaxin-1. Cerulean fluorescent lifetime was quantified in these experiments

and data was collected from the base of the cell. Cerulean was tagged to the H3 domain of syntaxin-1 and EYFP to the N-terminus of the first SNAP-25 helix. All cells expressing mCer-syntaxin-1 also expressed Munc18-1 (unfused) to ensure trafficking to the plasma membrane. To deplete cholesterol in these experiments 10 mM MβCD was added for 30 minutes to live cells at 37°C (see 2.3.2).

5.2 Results

5.2.1 Clustering of single molecules of SNAP-25 at the plasma membrane

To visualise single molecules of SNAP-25 at the plasma membrane of PC12 cells PALM was performed under TIRFM. Imaging all SNAP-25 molecules present at the plasma membrane at once presents the proteins as being relatively uniform in distribution with some variation in intensity (Figure 5.1). There are some punctate regions within the summed image which correspond with those described in past work as clusters (Lang et al., 2001; Rickman et al., 2004). The PALM data in Figure 5.1 shows that single molecules of the SNAP-25 appear to reside in a heterogeneous pattern with regions of higher density (clusters) surrounded by more sparsely distributed molecules. To statistically appraise the organisation of SNAP-25 at the plasma membrane Ripley's K function (see 2.5.3) was used with its transforming L-function, which determined the cumulative number of molecules, with expanding radii, from each molecule coordinate within a region of interest (Figure 5.2). This calculation provided the average number of molecules surrounding a central molecule at a given distance. Further analysis recalculated these values thousands of times using random repositioning (maintaining the molecular density) and allowed for the identification of a random, regular or clustered formation of points within a designated region (Ripley, 1977). In simulated spatial analysis a random organisation would show L-function values at 0 (Figure 5.2). To take into account the variables within experimental data minimum and maximum envelopes are created by the Matlab algorithm, which represents the range in which a random organisation would fall. A representative region of plasma membrane from PC12 cells expressing PA-Cherry-SNAP-25 (Figure 5.3) was analysed using this algorithm. These data

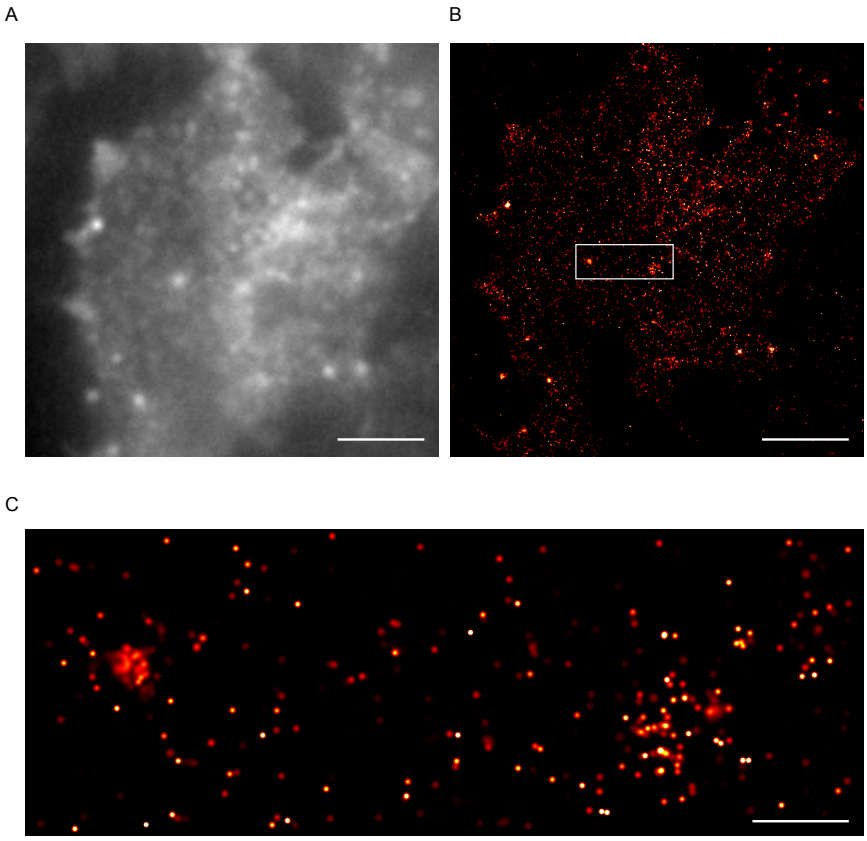

Figure 5.1 Single molecule distribution of SNAP-25 at the plasma membrane. PC12 cells expressing PA-Cherry-SNAP-25 imaged under TIRFM. A) A summed image of all molecules imaged in one recording. Scale bar 4 μm. B) Serial activation and bleaching of PA-cherry-SNAP-25 allows single molecule localisation of SNAP-25. Scale bar 4 μm. C) Single molecules of SNAP-25 within a zoom of a region of interest shown in B. Scale bar 500 nm.

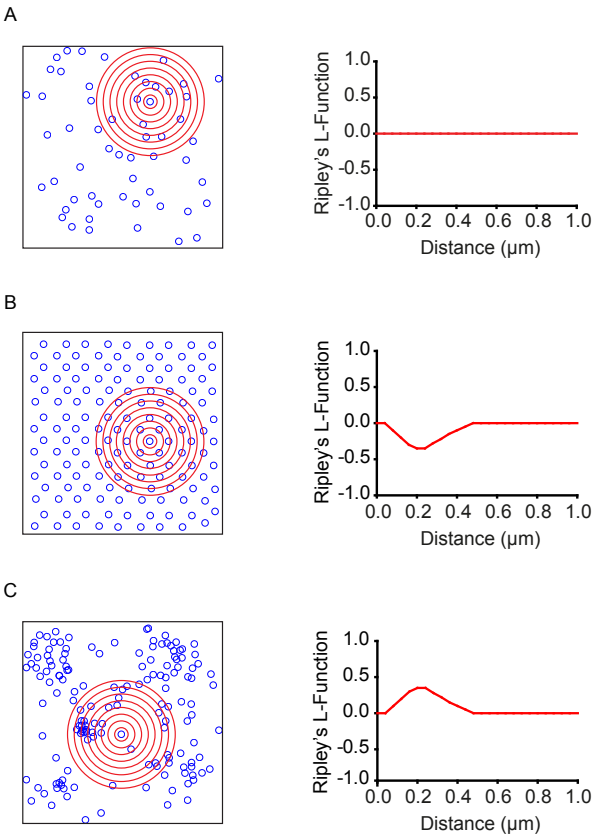

Figure 5.2 Analysis of the spatial organisation of single molecules. Example regions of different molecular arrangements. The number of molecules (blue circles) within an expanding radii (red circles) are recorded for each molecule (left panels) and then randomly processed thousands of times. Representation of each mode on a graph (right panels) shown as a K function transformed using the L-function. A) Complete random distribution B) Ordered distribution C) Clustered distribution.

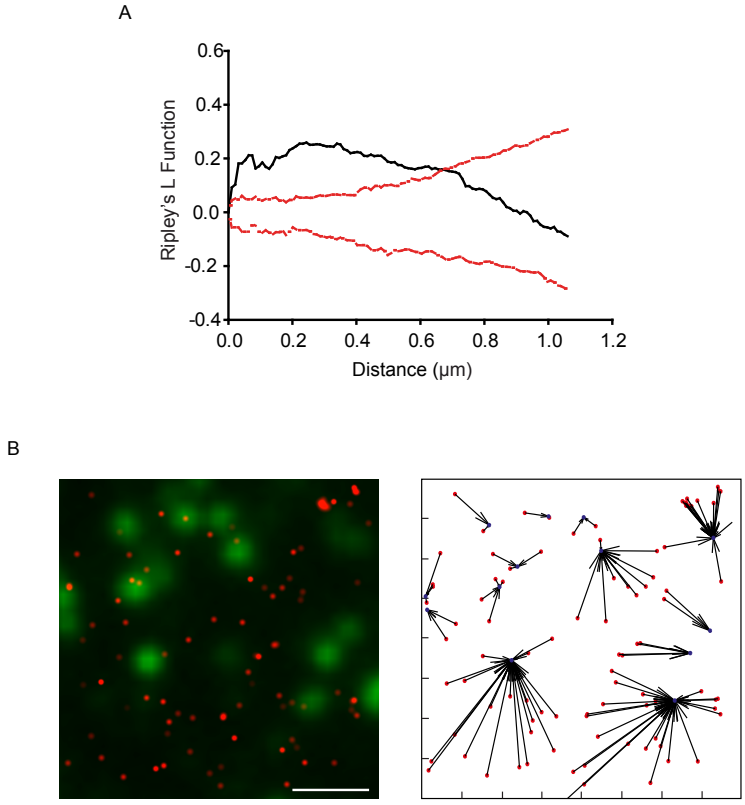

Figure 5.3 SNAP-25 is clustered at the plasma membrane. A) Ripley's plot for molecules within a region of interest shows clustered organisation with L-function values (black line) outside of the minimum and maximum envelopes (red dashed lines) B) A region of interest within a representative PC12 cell expressing PA-Cherry-SNAP-25 (red) and EGFP-NPY (green) vesicles. Scale bar 1 µm (left panel). Quiver plot shows assignment of molecules (red) to nearest vesicle (blue) within 200 nm, corresponding to left panel (right panels). Mean number of molecules under a vesicle = 5.5.

demonstrate a protein clustering organisation as the L-function graph displays values above the envelopes. Similar experiments using syntaxin-1 show a similar distribution to SNAP-25 with clusters of protein surrounded by dispersed single molecules (Rickman et al., 2010; Yang et al., 2012). Prior to photoactivating the SNAP-25 molecules the EGFP-NPY-filled vesicles were imaged for a few seconds for every cell. Upon initial observation these data suggest that the vesicles tend to reside over areas less densely populated by the proteins. To quantifiably examine this the vesicles were localised and their localisation related to SNAP-25 molecules. The algorithm used for this, known as nearest neighbour (Bartlett, 1963; Besag, 1972), assigned each molecule to its nearest vesicle centre and was able to determine the number of molecules proximal to each vesicle in the image within a certain radius. This analysis revealed a relatively small number of SNARE molecules with an average of 5 SNAP-25 molecules within 200 nm from the centre of a vesicle in PC12 cells.

5.2.2 SNAP-25 molecules remain clustered after cholesterol depletion

To investigate the dependence on cholesterol in the clustering of SNAP-25 PALM experiments were performed in cells treated with MβCD (Figure 5.4). The finding consistently seen throughout these treated cells was that the molecules remain clustered at the plasma membrane, as demonstrated by L-function values above the envelopes in the graph. A representative image of the vesicles superimposed with the molecules shows that the vesicles continue to reside in areas less populated with SNAP-25 after cholesterol depletion. The application of the nearest neighbour analysis to these data show a significant decrease in the number of molecules found underneath the vesicles from an average of 5.5 down to 3.5.

To further examine the relationship between lipid order and SNARE protein localisation super-resolution imaging of SNAP-25 was combined with Laurdan imaging on membrane sheets. SNAP-25 molecules imaged using dSTORM were localised in Matlab and the GP values at the x-y coordinates coinciding with these

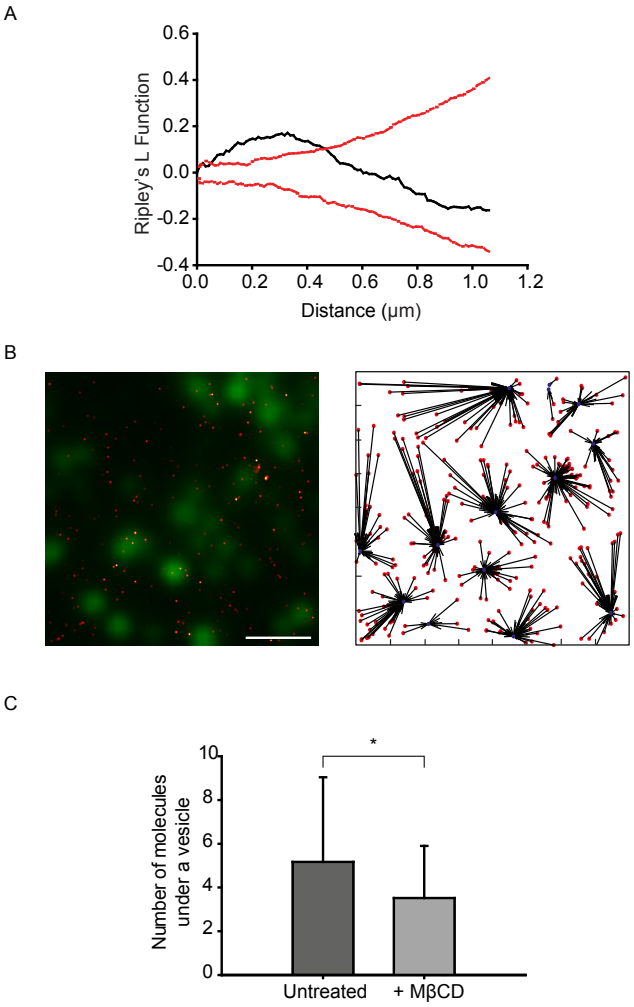

Figure 5.4 SNAP-25 remains clustered at the plasma membrane after cholesterol depletion. A) Ripley's plot for molecules within a region of interest in a MβCD-treated PC12 cell shows clustered organisation with L-function values (black line) outside of the minimum and maximum envelopes (red dashed lines). B) A region of interest within a representative MβCD-treated PC12 cell expressing PA-Cherry-SNAP-25 (red) and EGFP-NPY (green) vesicles. Scale bar 1 μm (left panel). Quiver plot shows assignment of molecules (red) to nearest vesicle (blue) within 200 nm, corresponding to left panel (right panel). C) Number of molecules within 200 nm of a vesicle for untreated and MβCD-treated cells. Mean ± SEM n= 5 cells (untreated), mean ± SEM n= 4 (MβCD-treated cells), Mann Whitney p=0.021.

single molecules were extracted (Figure 5.5). Processing of these data involved using a binary mask, producing a high number of values at 0 GP, this is demonstrated on a logarithm scale; these values were an artefact and so removed for further analysis. Within a region of interest from a membrane sheet the GP values under single molecules of SNAP-25 have been compared to all the GP values within the region and they show similar distributions. These data could suggest that SNAP-25 shows no preference for lipid arrangement but it is more likely that collection of Laurdan emission under diffraction-limited methods lacks the resolution to show lipid arrangement within an area as small as a single molecule.

5.2.3 The t-SNARE interaction at intermolecular distances

Super-resolution imaging allows for the localisation of the t-SNARE proteins at the plasma membrane but is unable to report on their interaction when in complex. To examine this interaction TCSPC FLIM-based FRET experiments were performed in N2A cells. To be able to measure the interaction between mCer-syntaxin-1 and EYFP-SNAP-25 the fluorescent lifetime of mCer-syntaxin-1 was first quantified using TCSPC-FLIM (Figure 5.6). The intensity is compared to the fluorescent lifetime of mCer-syntaxin-1 in a representative cell; demonstrating the additional information provided by using this method. mCer-syntaxin-1 is relatively uniform in its lifetime throughout the cell with a few spots of shortened lifetime; these may relate to intracellular compartments where syntaxin-1 is more mobile. A single fluorescence lifetime of 2288 $\pm$ 40 ps was measured in these cells.

Within a solution of two interacting proteins there will never be 100 % of molecules undergoing interaction; instead equilibrium between interacting and non-interacting states will exist. This has been described in *in vitro* studies for syntaxin-1 and SNAP-25, which also describe the 1:1 molar ratio exhibited by these proteins (Fasshauer and Margittai, 2004; Rickman et al., 2004). This can be applied to studies investigating the t-SNARE interaction in live cells; within one pixel of an image there will be a complement of interacting and non-interacting fluorescent molecules

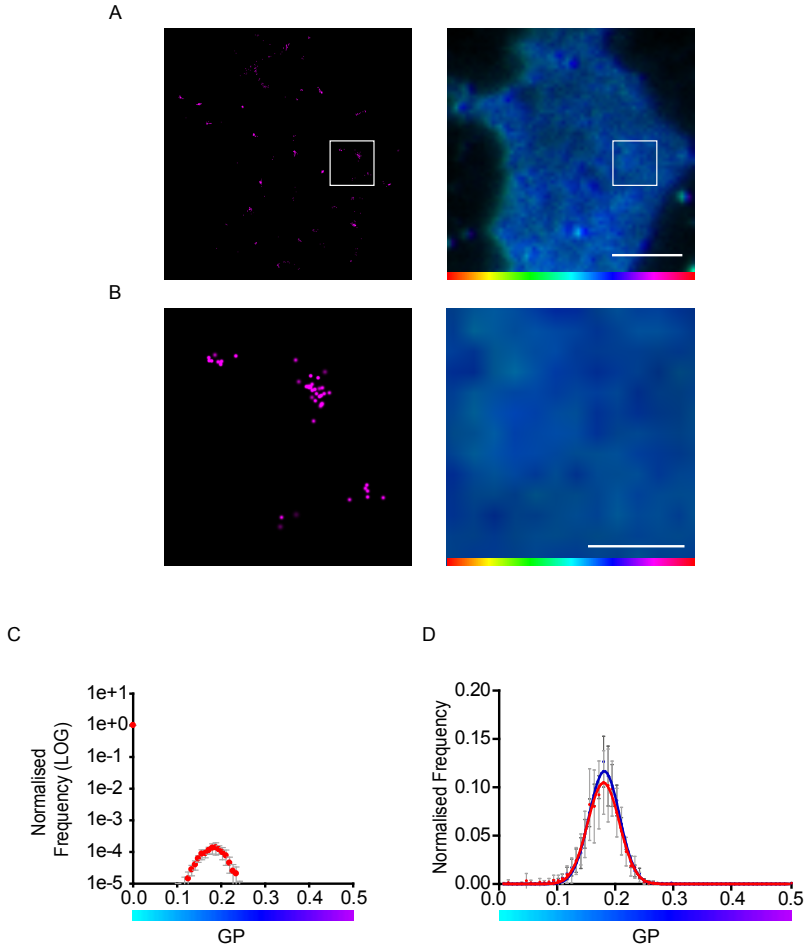

Figure 5.5 Single molecules of SNAP-25 reside proximal to lipids of varying order. A) Single molecules of SNAP-25 stained with Alexa647 in a representative PC12 membrane sheet imaged using STORM (left panel). GP of Laurdan within the same sheet (right panel). Scale bar 2 µm. B) A zoom of a region of interest shown in B showing single molecules of SNAP-25 (left panel) and GP of Laurdan (right panel). Scale bar 500 nm. Colour scale -0.1 - 0.1 GP for A and B. C) Frequency of GP values coinciding with SNAP-25-Alexa647 fluorescence detected by STORM normalised to number of pixels. n= 4 cells. D) Frequency of GP values coinciding with SNAP-25-Alexa647 fluorescence detected by STORM normalised to number of pixels (red), 0 values removed for clarity. All GP values across the membrane normalised to number of pixels (blue). Both fit to a single Gaussian distribution with R^2= 0.99 for both curves. n= 4 cells. Colour scale 0 - 0.5 GP for D and C.

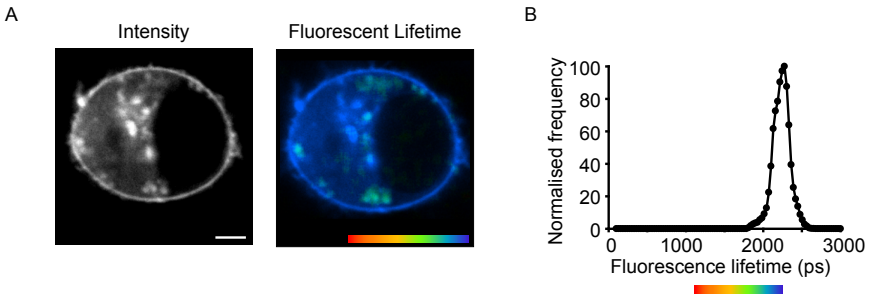

Figure 5.6 mCer-syntaxin-1 at the plasma membrane has a mean fluorescent lifetime of 2288 ± 40 ps. A) A representative N2a cell expressing mCer-syntaxin-1 imaged by TCSPC-FLIM displayed on an intensity scale (left panel) and fluorescent lifetime (right panel). Scale bar 2 µm. Colour scale 1250 - 2250 ps. B) The normalized fluorescent lifetime of mCer-syntaxin-1 within the representative cell (left panel) follows a single Gaussian distribution. Colour scale 1250 - 2250 ps.

and so every pixel will describe an average of these Cerulean lifetimes. When mCer-syntaxin-1 is not interacting with EYFP-SNAP-25 the lifetime of Cerulean remains monoexponential, (ie identical to the non-interacting control); however when the fluorescently tagged t-SNAREs interact the lifetime of Cerulean is markedly shortened (Figure 5.7). It is important to note that non-interacting syntaxin-1 in this case relates to mCer-syntaxin-1 not interacting with EYFP-SNAP25, it is likely that some mCer-syntaxin-1 will interact with endogenous SNAP-25. The mixture of non-interacting and interacting molecules can be quantified by examining the fluorescence decay trace for Cerulean within one pixel over a 12 ns period; this decay is biexponential depicting a population of FRET and non-FRET in each pixel of the image (interacting and non-interacting fluorescent molecules). This was seen consistently throughout experiments and the non-FRET lifetime remained within the range of 2288 ps; this allowed for the non-FRET lifetime to be set at this value for future analysis. The fitting algorithm delivered the lifetimes (t) and exponent amplitudes (a) of FRET and non-FRET values for mCer-syntaxin-1 in the presence of EYFP-SNAP-25 within N2a cells (Figure 5.8). A representative cell shows a higher proportion of non-FRET values compared to FRET and also a marked difference in the lifetime of these values. These values are required to calculate the weighted mean lifetime of mCer-syntaxin-1 within the cell using the displayed equation. The existence of non-FRET lifetimes, at a higher percentage, results in an average lifetime closer to non-FRET values; however the shortening of lifetime is still evident.

5.2.4 Identification of two conformation of t-SNARE interaction at the plasma membrane

Using CLSM it was possible to perform FLIM near the plasma membrane of live cells by adjusting the focal plane. These experiments displayed a heterogeneous array of fluorescent lifetime values for mCer-syntaxin-1 when co-expressed with EYFP-SNAP-25 (Figure 5.9). The weighted mean lifetime from all of the pixels within an image were combined to give the weighted mean lifetime distribution for a

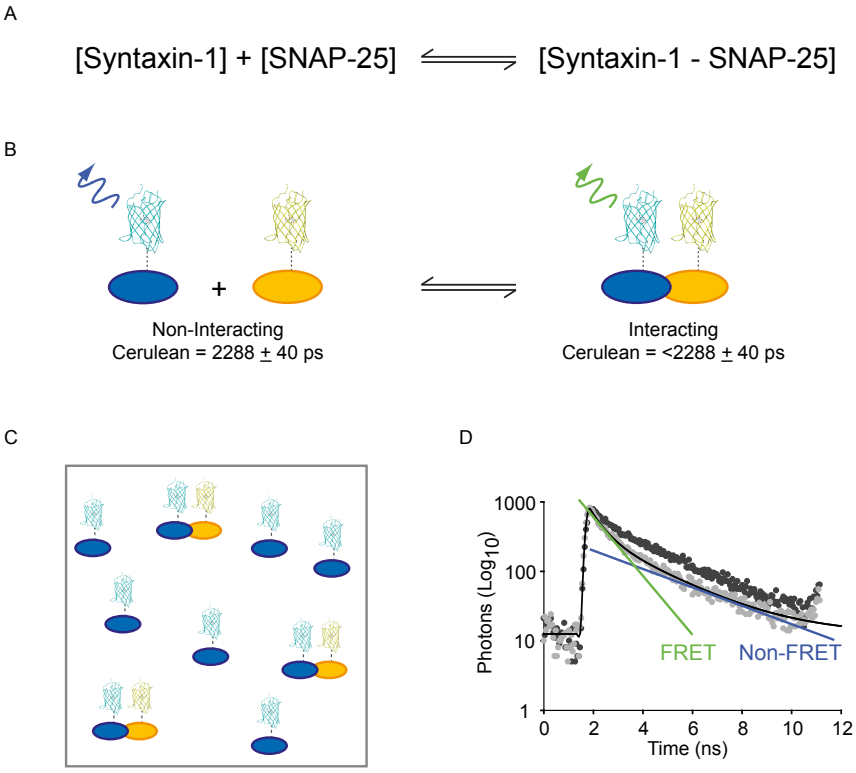

Figure 5.7 SNAP-25 and syntaxin-1 interaction within one pixel of an image. A) The t-SNAREs exist in equilibrium. B) Non-interacting mCer-syntaxin-1 and EYFP-SNAP-25 do not undergo FRET, mCerulean fluorescent lifetime= 2288 ± 40 ps (blue arrow). When in the t-SNARE complex FRET occurs and the fluorescent lifetime of Cerulean shortens to <2288 ± 40 ps (green arrow). C) Within one pixel (grey square) there are non-interacting and interacting molecules of mCer-syntaxin-1 and EYFP-SNAP-25. D) A fluorescence decay trace for Cerulean in one pixel; the detected photons were collected in 256 time bins over a repetitive 12 second period and the accumulated number of photons in each bin is shown. mCer-syntaxin-1 follows a single fluorescence decay (dark grey circles), mCer-syntaxin-1 and EYFP-SNAP-25 display a biexponential decay (light grey circles).

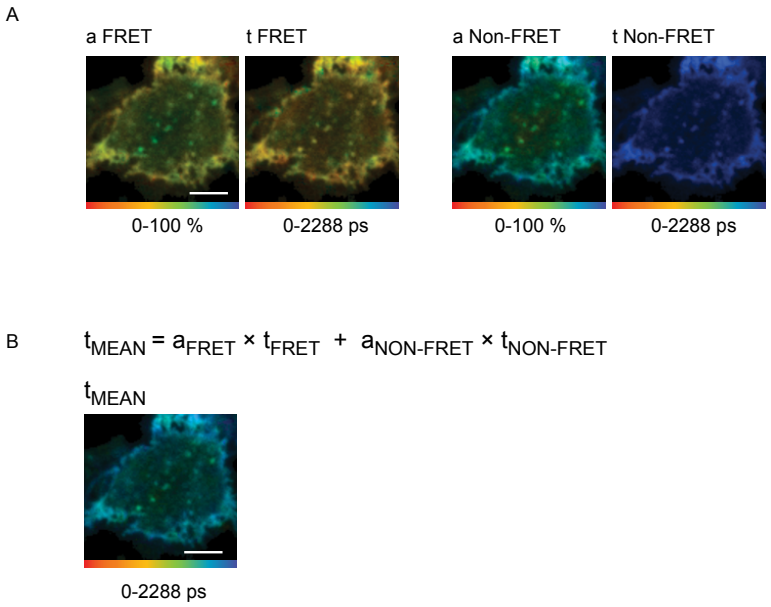

Figure 5.8 Calculating the mean lifetime of mCer-syntaxin-1 at the plasma membrane A) The plasma membrane of a representative N2a cell expressing EYFP-SNAP-25 and mCer-syntaxin-1 imaged using TCSPC-FLIM. Amplitude (a) and lifetime (t) are shown for FRET and Non-FRET values. B) Equation used to calculate the mean fluorescence lifetime. The mean fluorescent lifetime of the representative cell in A. All scale bars 4 µm.

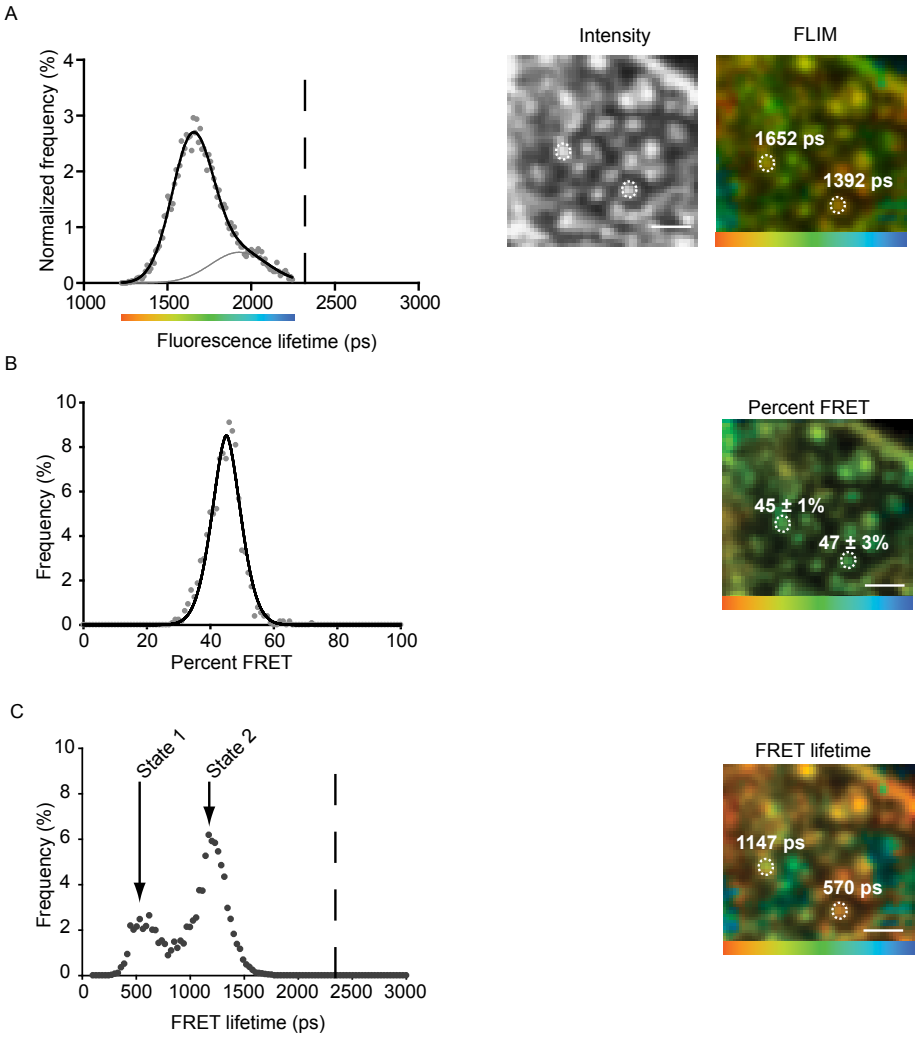

Figure 5.9 Heterogeneous interaction states of syntaxin and SNAP-25 are spatially distinct. The plasma membrane of a representative N2a cell expressing mCer-Syntaxin-1 and EYFP-SNAP-25 is displayed. Colour scale 1250 - 2250 ps. Scale bars 1 µm unless otherwise stated. A) The amplitude weighted mean lifetime of the time constants of both FRET and non-FRET components is best fit by the sum of two Gaussian distributions R^2= 0.99. Dashed line corresponds to mean non-FRET value (2288 ps) (left panel). Intensity and FLIM image of the plasma membrane of the representative cell. FLIM displays spatial segregation of two FRET lifetimes (right panel). B) a-FRET values fit to a single distribution (left panel). The a-FRET shows minimal variance (right panel). Colour scale 0 -100 %. C) t-FRET is bimodal with state 1 and 2 (left panel). The two states are segregated between the two representative clusters.Colour scale: 0 - 2000 ps (right panel).

representative cell. There is a marked shortening of fluorescent lifetime and interestingly there appear to be two different populations as these data are best fit to a sum of two Gaussian distributions. Further to this the examination of the fluorescence lifetimes across the plasma membrane revealed there is a spatial distinction between these populations as they were found within defined punctate regions. To identify the cause of this bimodal distribution the number of interacting molecules was assessed by extracting the FRET amplitude (a-FRET) across the plasma membrane. These data were fit to a single distribution and demonstrate the two populations are not a result of a different number of interacting molecules. In addition the previously identified spots within this cell show no significant change in a-FRET between them. To establish if variations in the degree of FRET between interacting molecules were responsible for the two populations the FRET lifetime (t-FRET) values for the same representative cell were extracted; these fit to a bimodal distribution demonstrating the existence of two interaction states at the plasma membrane of live N2a cells. These were named state 1 (shortest t-FRET) and state 2 (longer t-FRET) and quantification of t-FRET within the same two spots show that these two states are spatially distinct at the plasma membrane.

5.2.5 SNAP-25 engagement is the determining factor in t-SNARE conformation states

The difference in t-FRET between the two conformations is indicative of a change in interaction; however the data are insufficient to establish which helix may be responsible for these populations. To investigate the involvement of the SN2 of SNAP-25 three mutants of EYFP-SNAP-25 were produced: the first was truncated to mimic BoNT/A cleavage with removal of the last 9 amino acids (Δ9) from SN2, the second to mimic BoNT/E cleavage with removal of the last 26 amino acids (Δ26) from SN2 and the third lacked the entire SN2 helix (Δ121) (Figure 5.10). FLIM experiments on the plasma membrane of N2a cells expressing these proteins alongside mCer-syntaxin-1 show a significant change in t-FRET populations (Figure 5.11). The t-FRET values for control mCer-syntaxin-1 with EYFP-SNAP-25 are

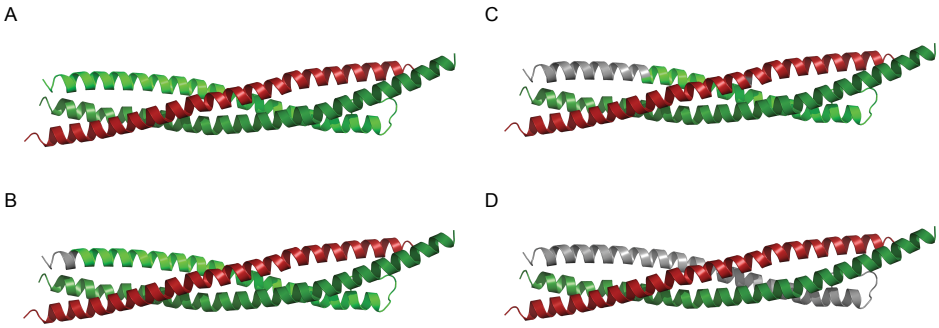

Figure 5.10 SNAP-25 mutations on the second SNARE helix. A) The SNARE helices in the t-SNARE complex (Syntaxin-1 180-262 (red), SNAP-25 (excluding linker) 1-83 (light green) and 120-206 (dark green). B) SNAP-25 Δ9 C) SNAP-25 Δ26. D) SNAP-25 Δ121.

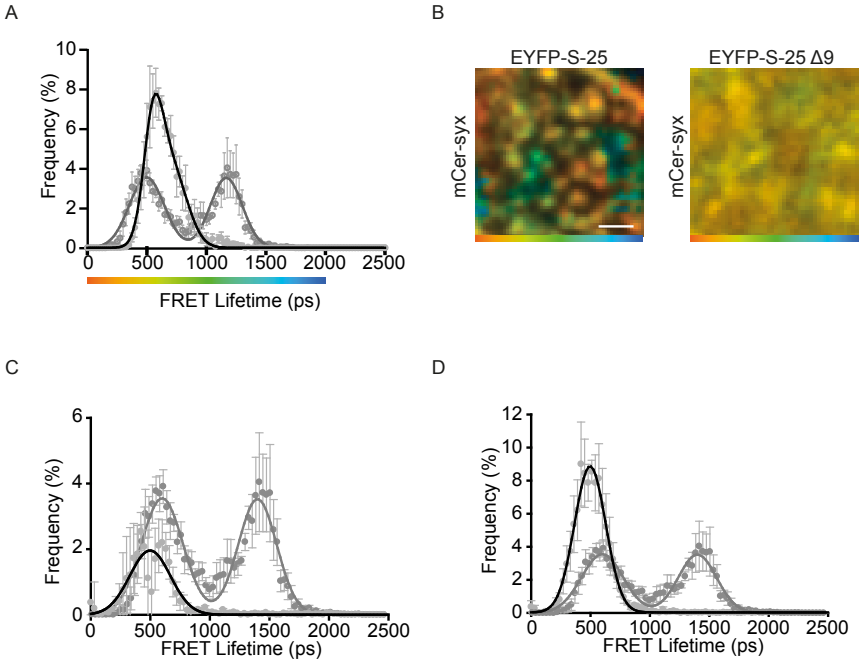

Figure 5.11 Two t-SNARE conformations are a result of differential SNAP-25 engagement. A) Botulinum A-mimicked cleavage (Δ9) of SNAP-25 (black line) gives a shorter lifetime throughout the cell compared to intact SNAP-25 (grey) (mean ± SEM n= 5 cells). Data best fit to a sum of two Gaussians R^2= 0.99. B) The FRET lifetime values within a representative region of plasma membrane of N2a cells coexpressing mCer-syntaxin-1 and EYFP SNAP-25 (left panel) and mCer-syntaxin-1 and EYFP SNAP-25 Δ9 (right panel). Colour scale 0-2000 ps. Scale bar 1 μm. C) Botulinum E-mimicked cleavage (Δ26) of SNAP-25 (black line) gives a shorter lifetime throughout the cell compared to intact SNAP-25 (grey) (mean ± SEM n= 6 cells). Data best fit to a single Gaussian R^2= 1. D) Removal of the entire second SNARE helix (Δ121) of SNAP-25 (black line) gives a shorter lifetime throughout the cell compared to intact SNAP-25 (grey) (mean ± SEM n= 6 cells). Data best fit to a single Gaussian R^2= 0.99.

shown as an average from multiple cells in this figure. The distribution of t-FRET values for mCer-syntaxin-1 in the presence of EYFP-SNAP-25[Δ9] from multiple cells show a significant shortening of fluorescent lifetime toward state 1. This is fit to sum of two Gaussian distributions and the range falls into that of state 2, implying molecules of EYFP-SNAP-25[Δ9] predominantly exist in state 1 but some can form state 2. Images from representative cells further describe the loss of longer lifetimes and a more uniform distribution of lifetimes. In the presence of EYFP-SNAP-25[Δ26] the shortening of t-FRET values is more dramatic with a complete loss of any molecules present in state 2. In addition the frequency of t-FRET is markedly lower, which implies a less stable interaction after this truncation where many molecules of EYFP-SNAP-25[Δ26] cannot interact with mCer-syntaxin-1 at all. Interestingly cleavage of the entire second SNAP-25 helix is more stable than that of EYFP-SNAP-25[Δ26] with a frequency similar to that of EYFP-SNAP-25[Δ9]. This mutation shows the most distinct shortening of t-FRET lifetimes. These data show the second SNARE helix of SNAP-25 is required for state 2 to form whereas state 1 can form when it is either truncated or absent, which implies a functional relevance for state 2.

5.2.6 The interaction status of the t-SNAREs is dependent on lipid order

To investigate the effect of lipid order on the t-SNARE interaction TCSPC-FLIM was performed on MβCD-treated cells (Figure 5.12). The same control data from Figure 5.11 are used here as a comparison. Depleting cholesterol from the plasma membrane of these cells is shown to have a marked effect on the interaction states the t-SNAREs adopt at the plasma membrane. The distribution of t-FRET from treated cells shows a dramatic reduction in state 1; however the range of lifetimes displayed by this conformation has not changed. The second population of molecules within treated cells do not directly correspond with state 2 seen in control cells. There is a reduction in the number of molecules undergoing state 2 and a large proportion of molecules displaying a t-FRET value closer to mCer-syntaxin-1 non-FRET. Representative images of t-FRET fluorescent lifetime within the plasma

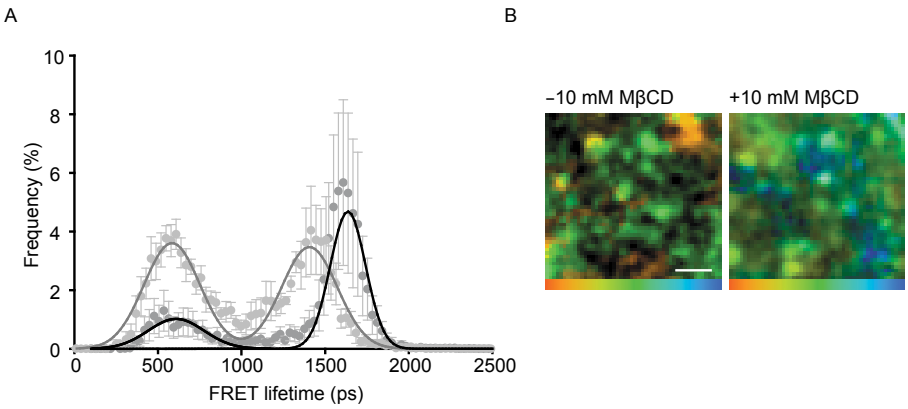

Figure 5.12 Cholesterol depletion influences the t-SNARE interaction. A) The FRET lifetime of mCer-syntaxin-1 in the presence of EYFP-SNAP-25 at the plasma membrane of N2A cells (light grey). The FRET lifetime after 10 mM MβCD treatment (dark grey circles, black line) shows a shift to state 2 (mean ± SEM, n= 5 cells). B) Representative fluorescent lifetime of syntaxin at the plasma membrane before and after MβCD treatment. Colour scale 0 -2000 ps. Scale bar 1 µm.

membrane depict the addition of the longer lifetimes and show that the spatial segregation of these different states still occurs.

5.3 Conclusions

The clustering of syntaxin-1 at the plasma membrane of neuroendocrine cells has been discussed extensively in past works (Lang et al., 2001; Sieber et al., 2007; Barg et al., 2010); however the localisation of SNAP-25 has been over looked in many. These studies assume single molecules of SNAP-25 interact with these syntaxin-1 clusters even though there is a lack of experimental data to validate this hypothesis (Sieber et al., 2006, 2007). Data presented in this chapter show single molecules of SNAP-25 are arranged at the plasma membrane in a similar fashion to syntaxin-1 (Rickman et al., 2010; Yang et al., 2012); residing in microdomains of high or low density in a non-random organisation (Figure 5.1). Past works have described clusters which appear homogeneous across the plasma membrane (Lang et al., 2001); however this work is limited by the diffraction of emitted light within the optical system, which can make a single fluorophore appear much bigger than it is (Lakowicz, 1999). Unfortunately limitations with PALM do not allow for dual imaging of these molecules at sub-resolution at present and so the distribution of the two proteins cannot be directly compared. Despite this the similarity in single molecule arrangement between SNAP-25 and syntaxin-1 at the plasma membrane does suggest an alternative model for t-SNARE interaction: that SNAP-25 and syntaxin-1 exist together in clusters of relatively equal numbers. Furthermore FLIM data presented within this chapter (Rickman et al., 2010) demonstrate clusters are not uniform and show heterogeneity in their interaction status (Figure 5.9).

The theory that the t-SNAREs represent sites for exocytosis is a realistic one as these proteins are membrane bound and known to be essential for vesicle fusion (Schiavo et al., 1992; Söllner et al., 1993; Pevsner et al., 1994). It is interesting therefore that the vesicles shown in Figure 5.3 tend to reside in regions where the proteins are less dense or absent entirely. This localisation has been shown for both

syntaxin-1 and SNAP-25 individually using PALM and STORM to resolve single molecules in our recent work (Yang et al., 2012). The number of SNARE proteins required for vesicle fusion has been under debate recently with some works suggesting 5-8 molecules are required (Han et al., 2004) while others (Knowles et al., 2010) propose larger dense clusters of approximately 60 SNARE molecules that reside immediately underneath vesicles. My data show the number of molecules of SNAP-25 underneath a vesicle (within 200 nm from the centroid position) is small - approximately 5 (Figure 5.4). These data could support the notion that the dense clusters represent a reserve pool of proteins and that vesicle fusion does not occur at that spatial point but at regions of plasma membrane where the SNARE proteins are more dispersed. A recent study in our group applied single particle tracking PALM to both SNAP-25 and syntaxin-1 in PC12 cells to characterise the mobility of single molecules at the plasma membrane (Yang et al., 2012). Computational modelling combining the single molecule dynamics with vesicle mobility revealed the number of molecules resident within 82.5 nm from the centre of each vesicle at any time was between 0 and 7. It is proposed that resident vesicles do not significantly move from where they reside shortly before exocytosis in order to fuse (Chapter Four, Figure 4.17). This suggests that localisation of the vesicles in resting cells can approximate (within a few 100 nm) where fusion will occur and therefore strongly suggests that the number of SNAREs required for fusion is small. These experiments are highly informative and allow for speculation about the number of SNAREs required for fusion based on the number of molecules a vesicle will see. It is important to consider the limitations in these methods as PALM experiments are fixed and fixation (as shown in Chapter Three, Figure 3.5) has an effect on lipid ordering, which may influence vesicle and protein localisation.

The interaction between the t-SNAREs has been of great interest in the past 20 years since it is believed to act as a binding site for synaptobrevin and therefore promotes the merging of the vesicle and plasma membrane in fusion. Studies *in vitro* showing the two proteins undergoing two states of interaction have been supported by further works in live cells, as discussed in Section 5.0 (Fasshauer et al., 1997; An and Almers, 2004; Wang et al., 2008). Within this section the limitations imposed by

the data acquisition in previous works (intensity-based FRET) have been outlined and data shown has applied a more quantifiable approach (TCSPC-FLIM-based FRET). These data support previous findings, with two interaction states existing at the plasma membrane of live cells between SNAP-25 and syntaxin-1. The use of FLIM-based FRET has allowed visualisation of punctate regions of fluorescent lifetime at the plasma membrane and has demonstrated the spatial segregation of the two interaction states within distinct clusters. A possible reason for these two conformations of t-SNARE complex is the presence or absence of synaptobrevin; results presented in (Rickman et al., 2010) demonstrate this is not the case as there is insignificant colocalisation between syntaxin-1 and synaptobrevin at the plasma membrane of neuroendocrine cells.

The functional relevance of the two states was investigated using progressive truncation of the second SNARE helix of SNAP-25 (Figure 5.10). The importance of this helix in the t-SNARE complex formation as well as ternary complex and vesicle fusion has been enforced by botulinum toxin studies (Schiavo et al., 1993; Chapman et al., 1994; Bajohrs et al., 2004). Past works have shown the t-SNARE complex forms in the presence of BoNT/A, whereas BoNT/E cleaved SNAP-25 is rapidly cleared from the plasma membrane (McMahon et al., 1992; Keller and Neale, 2001). Using EYFP-SNAP-25 with truncations mimicking these toxins supplied functional information about the two states (Figure 5.11). The shortening of fluorescent lifetime by all truncations strongly suggests the requirement of the second SNARE helix of SNAP-25 in forming state 2 and implies in this interaction state SN2 is zippered with syntaxin-1. The single distribution of EYFP-SNAP-25[Δ121] molecules with lifetimes similar to state 1 implies that this state is not functional as the ternary complex cannot form when the entire SN2 is missing (Chapman et al., 1994). The small number of EYFP-SNAP-25[Δ9] molecules still undergoing state 2 suggests the loss of the last 9 amino acids can be overcome but still predominantly cause SN2 to become partially zippered. In comparison EYFP-SNAP-25[Δ26] forms an unstable interaction with mCer-syntaxin-1 and implies the amino acids between Ile-180 and Gln-197 (Binz et al., 1994) are required for stable t-SNARE complex formation and efficient zippering of the SNARE complex.

Super-resolution imaging was applied to PC12 cells to reveal single SNAP-25 molecules are heterogeneous in their distribution across the membrane, forming clusters, which are not dispersed by the addition of MβCD (Figure 5.4). These findings are surprising considering past works suggesting a cholesterol dependence on its SNARE partner syntaxin-1 (Lang et al., 2001; Ohara-Imaizumi et al., 2004). Due to the experimental procedure the effect of cholesterol depletion cannot be observed before and after in the same cell and so these data cannot suggest there is no change in the localisation but does confirm that clustering of SNAP-25 is not affected. Additionally the fixation of the plasma membrane is shown to have an effect on lipid ordering (Chapter Three, Figure 3.5) and so it is not possible to distinguish which is a change through cholesterol depletion and which is through the application of PFA. Both procedures cause a shift to the more disordered lipid arrangement however and so these experiments can reliably claim that a decrease in lipid order does not disperse the SNAP-25 clusters. The number of SNAP-25 molecules found under the diameter of a vesicle is shown to be significantly lower after treatment with MβCD; however the possible change in vesicle mobility after MβCD-treatment (Chapter Four, Figure 4.9), the postulated affect on the actin network and the mobility of the proteins themselves may be responsible for this change.

Despite numerous works into the partially zippered state of interaction the t-SNAREs exhibit, none have investigated the effect of cholesterol depletion on this interaction. Using FLIM-based FRET it was possible to observe the change in the distribution of fluorescence lifetimes when the t-SNAREs were interacting (Figure 5.12). These data show that although cholesterol is not required for the clustering of SNAP-25 molecules it is important in the interaction states of the t-SNAREs. The partially unzippered state is dramatically reduced and is replaced with a state exhibiting a fluorescent lifetime closer to that of mCer-syntaxin-1 alone. Whether this proportion of molecules is functional cannot be ascertained from these data as the information only reports on a change in conformation; which in this case is a distancing of the fluorophores. There are studies that describe reduced fusion

efficiency upon MβCD-treatment (Zhang et al., 2009; Koseoglu et al., 2011), which would suggest this longer fluorescent lifetime conformation is not functionally efficient compared to state 2. There are a proportion of molecules undergoing state 2, which could account for the degree of exocytosis that does occur in stimulated cells treated with MβCD.

The data presented in this chapter has revealed a clustered organisation of SNAP-25 at the level of single vesicles and further established the importance of the second SNARE helix in the zippering of the t-SNARE complex. The sites of vesicle fusion have been questioned by the observation of vesicles residing within the gaps molecules leave at the plasma membrane and demonstrates the requirement of combined vesicle and protein imaging in real time to examine this relationship. In addition the clustered organisation of these proteins does not appear to be cholesterol-dependent; however the importance of cholesterol in the interaction of the t-SNAREs is strongly implied.

Chapter Six:

Discussion

6.0 Summary of Results

The data presented within this thesis aimed to provide insight into the influence that plasma membrane proteins and lipids have over the localisation of vesicle fusion at the plasma membrane. To investigate this an assay for quantifying lipid order at the plasma membrane was developed, the localisation of SNAP-25 as single molecules and within t-SNARE complex was examined and the dynamics of vesicles at the plasma membrane were studied. The main findings from this body of work can be categorised as follows: i) SNAP-25 imposes temporal and spatial control over exocytosis through single molecule distribution and the zippering of the second SNARE helix; ii) SNAP-25 clusters are regulated by the cholesterol-induced lipid order at the level of t-SNARE interaction and iii) LDCVs prefer regions of plasma membrane with low SNARE density.

Lipid ordering within neuroendocrine cells has been investigated within Chapter Three, demonstrating the distribution of lipid phases throughout a whole cell (Figure 3.1) and the lipid arrangement at the plasma membrane using unroofing techniques (Figure 3.2). The effect of MβCD on the lipids at the plasma membrane has been demonstrated (Figure 3.4), quantifying a reduction in lipid order that supports experiments investigating vesicle dynamics and protein localisation using this chelating agent. The methods used to examine lipids enabled isolation of the plasma membrane however they were not capable of resolving lipid microdomains, which limited any correlation with single molecule SNARE proteins (Figure 5.5).

In this thesis the tracking of large dense core vesicles under TIRFM has been analysed under resting, stimulated and cholesterol-depleted conditions. Results presented in Chapter Four comprehensively describe the restricted behaviour displayed by vesicles at the plasma membrane; in particular the tendency to reverse and move in a caged motion. Analysis of selected vesicles, termed ‘scanners’, gave functional relevance to this caged behaviour showing an increase upon cell stimulation and furthermore strongly implied the existence of selective fusion sites (Figure 4.14). The data have demonstrated that disruption of membrane cholesterol

causes an increase in vesicle mobility (Figure 4.9); a reaction that implies cholesterol-induced regulation is required for membrane association and regulated movement across the membrane. This regulation may direct through cholesterol depletion from lipid ordered domains or may be propagated indirectly via changes in the actin structure. The fusing vesicles were analysed in isolation to examine vesicle dynamics leading to fusion and have shown that resident vesicles do not change their mobility upon stimulation signals and do not move across the membrane to fuse (Figure 4.17), unlike newly recruited vesicles which are highly mobile with a significant jump to fuse (Figure 4.19). Secretory events in PC12 cells were shown over time to reveal a biphasic pattern: a fast burst of vesicle release followed by a slower more sustained phase (Figure 4.20). Custom spatial analysis was used in combination with the isolation of fusion events in commercial software to demonstrate the fusion events predominantly occur in regions commonly visited by other vesicles at the plasma membrane (Figure 4.22).

The localisation of SNAP-25 using PALM was performed to observe large groups of single molecules of the protein at the plasma membrane of neuroendocrine cells and found a non-random distribution with distinct regions of high and low density (Figure 5.1). In addition data has shown that the vesicles at the plasma membrane of these cells show a preference for domains of low SNARE density (Figure 5.3). A spatial analysis algorithm was used to describe these proteins as clustered at the membrane and demonstrated that this clustering is independent of cholesterol-induced lipid order (Figure 5.4). The localisation of single molecules provided a greater spatial resolution than diffraction-limited techniques were able to; however these super-resolution experiments were performed on fixed samples and the effects of fixation are not fully understood, it is shown to affect lipid ordering (Figure 3.5) and may influence the localisation of these molecules.

The interaction between SNAP-25 and syntaxin-1 was quantified using TCSPC-FLIM at the plasma membrane and spatially distinct clusters were revealed that represent two conformations of t-SNARE complex (Figure 5.9). A mutant version of SNAP-25 which lacked the entire SN2 as well as two that mimicked the

cleavage of BoNT/A and BoNT/E were used in TCSPC-FLIM experiments. These experiments showed that SNAP-25 with SN2 truncated >9 amino acids from its C-terminus could not form state 2 (longer FRET lifetime) and instead all interacting mutant molecules underwent state 1 (short FRET lifetime) (Figure 5.11). t-SNARE imaging was paired with the disruption of membrane cholesterol to show that cholesterol-induced lipid order has a significant effect on the conformation states adopted by the two SNAREs (Figure 5.12).

6.1 Interpretation of Findings

6.1.1 SNAP-25 imposes temporal and spatial control over exocytosis through single molecule distribution and the zippering of the second SNARE helix

Examining the organisation of SNAP-25 at the plasma membrane was highly informative in understanding the localisation of vesicle fusion as this protein is believed to be required for the docking of synaptobrevin to the complexed t-SNAREs (Chapman et al., 1994). SNAP-25 has been shown to form homologous clusters in previous works using diffraction-limited microscopy (Lang et al., 2001). In Chapter Five SNAP-25 was localised using PALM under TIRFM, which enabled single molecules to be resolved at the plasma membrane (Figure 5.1). Quantification of this distribution described a heterogeneous clustered spatial arrangement. The spatial arrangement of both syntaxin-1 and SNAP-25 have been further studied in recent works (Bar-On et al., 2012), including a study from our group (Yang et al., 2012), which described a heterogeneous distribution of these proteins with microdomains containing low or high densities of molecules. These works provide an alternative model of SNAP-25 interaction with syntaxin-1 than that previously proposed using STED microscopy (Sieber et al., 2007). In this study SNAP-25 was suggested to interact with syntaxin-1 in or around the edges of the syntaxin-1 clusters, however recent findings suggest the peripheral single molecules of syntaxin-1 are the more likely sites for t-SNARE interaction (Yang et al., 2012; Bar-On et al., 2012).

The interaction between two proteins can be quantified at intermolecular distances using TCSPC-FLIM to measure FRET, independent of donor concentration. Application of this technique revealed the t-SNAREs can adopt two different conformations at the plasma membrane of live cells, termed state 1 and state 2 (Rickman et al., 2010) (Chapter Five). Previous studies using intensity-based FRET have also described similar findings in cellular membranes (An and Almers, 2004; Wang et al., 2008); however as discussed in 2.4.4 intensity-based FRET may not be a reliable measurement of protein interaction (Lakowicz, 1999). Furthermore these studies lacked spatial information; conversely Figure 5.9 (Rickman et al., 2010) showed that these conformations are within distinct heterogeneous domains at the plasma membrane.

The sequential formation of the t-SNARE complex has been extensively studied in the past (Söllner et al., 1993; Chapman et al., 1994; Hayashi et al., 1994) and a particular *in vitro* study found that the t-SNARE complex can form when the SN2 of SNAP-25 is dissociated (unzippered) (Fasshauer et al., 1997). To determine whether this intermediate conformation accounted for either state observed under TCSPC-FLIM in live cells (Rickman 2010) (Figure 5.9) SN2 truncated mutants of SNAP-25 were used. These data (Figure 5.11) identify SN2 as the determining factor in t-SNARE conformation; either fully or partially associating with syntaxin-1. Truncations of SNAP-25 in these experiments mimicked *Botulinum* toxin cleavage; as these toxins are known to disrupt exocytosis (Binz et al., 1994; Hayashi et al., 1994; Rickman et al., 2004) these data provided a functional relevance to the two spatially distinct conformations; with only state 2 capable of eliciting vesicle fusion.

The functionally segregated domains shown in TCSPC-FLIM experiments are diffraction limited and so these findings paired with single molecule localisation using PALM suggest within a specific region of ~200 nm there is predominantly one type of t-SNARE interaction and these proteins are arranged in a non-random distribution. The control imposed on vesicle fusion is suggested here at two levels: across the plasma membrane there are large fusion capable domains determined by t-

SNARE interaction and within these sites single molecule organisation pinpoints the fusion site on a nanometre scale.

6.1.2 SNAP-25 clusters are regulated by the cholesterol-induced lipid order at the level of t-SNARE interaction

Whole cell imaging using TCSPC-FLIM and Laurdan distinguished the different lipid ordering at the plasma membrane and intracellular compartments (Figure 3.1) demonstrating the importance of particular lipid compositions in specific processes. The importance of lipid composition in exocytosis and localisation of the exocytotic machinery has been extensively researched, cholesterol has been shown to affect fusion pore kinetics (Zhang et al., 2009; Koseoglu et al., 2011) and PIP_2 is believed to facilitate synaptotagmin-dependent vesicle fusion (Schiavo et al., 1996; Bai et al., 2004). The dependence of t-SNARE clustering on cholesterol at the plasma membrane has been accepted for many years despite the minimal number of works supporting this theory (Lang et al., 2001; Ohara-Imaizumi et al., 2004). Findings from our group (Rickman et al., 2010) have demonstrated that concentrations of MβCD used to disperse these clusters (Lang et al., 2001) were lethal to cell viability. Furthermore the complexity of t-SNARE arrangement inside these regions (clusters) of >200 nm is not homogeneous; a number of high density and low density domains reside within these regions as described above (Bar-On et al., 2012; Yang et al., 2012) (Chapter Five). These works highlighted the need for accurate examination of the effect of cholesterol-induced lipid order on the SNARE protein arrangement at the level of single molecules. The use of 10 mM MβCD to create a significant shift to less ordered lipids at the plasma membrane of neuroendocrine cells is extensively characterised in Chapter Three. This concentration of cholesterol, despite its effect on plasma membrane lipids, did not induce dispersion of SNAP-25 clustering at the plasma membrane; single molecules continued to produce regions of high and low molecular density at the plasma membrane (Figure 5.4). These results demonstrate that the ability for SNAP-25 to cluster at the plasma membrane is not cholesterol-dependent; however the importance of the lipid composition on this localisation is not discounted. Studies are

emerging using super-resolution microscopy demonstrating the effect of PIP_2 on syntaxin-1 phosphorylation (Khelashvili et al., 2012) and clustering (Murray and Tamm, 2009); however clustering is still described as cholesterol-dependent in this work. A recent study describes a reduction in PIP_2-dependent clustering of syntaxin-1 when in the t-SNARE complex, which supports the theory that this interaction and possibly fusion occurs in regions of lower molecular density (Murray and Tamm, 2011).

Data presented in Chapter Five strongly suggests that SNAP-25 clusters independent of plasma membrane cholesterol-induced lipid order; however the ability for this protein to interact with syntaxin-1 was shown to be affected (Figure 5.12) (Rickman et al., 2010). As previously discussed two conformations of t-SNARE exist at the plasma membrane and our study shows that incubation with 10 mM MβCD disrupts the prevalence of each state. MβCD-treated cells have been shown to allow exocytosis; although fusion efficiency is reduced (Zhang et al., 2009; Rickman et al., 2010; Koseoglu et al., 2011). State 2 can still form in MβCD-treated cells but it is a diminished population, which may provide an explanation for the reduced fusion efficiency. The t-SNAREs appear less able to form the unzippered state 1 and this is not counteracted by an increase in fully zippered complex, instead a new distribution is seen with proteins undergoing a longer FRET lifetime termed state 3. The association of the t-SNARE helices cannot be ascertained from these data; however the reduced fusion indicates it is not functionally efficient. The effect of lipid composition, including cholesterol, on the polybasic juxtamembrane region of syntaxin-1 has been reported recently (Murray and Tamm, 2011) and could suggest the influence of cholesterol on the t-SNARE interaction is exerted through earlier stages in the sequential helical folding.

The mechanism of morphological docking of a vesicle to the plasma membrane has been heavily debated over the years; the requirement of the SNARE proteins has been questioned although such studies relied on subjective measurements in electron microscopy (Hunt et al., 1994; Broadie et al., 1995). More recent studies describe a docking mechanism where synaptobrevin associates with

the t-SNARE complex and partially zippers awaiting secretory signals (De Wit et al., 2009; Wu et al., 2012; Hernandez et al., 2012). The t-SNARE conformation termed state 2, but not state 1, would permit this interaction as SN2 is known to be required for synaptobrevin association (Chapman et al., 1994). The dynamics of a vesicle at the plasma membrane have been associated with its docked or primed status in past works (Steyer and Almers, 1999; Duncan et al., 2003; Nofal et al., 2007). In Chapter Four the behaviour of vesicles at the plasma membrane in cells where cholesterol has been sequestered show an increase in the displacement and the speed of the vesicles (Figure 4.9). Furthermore single molecule localisation of SNAP-25 molecules show that fewer molecules are found underneath a vesicle (Figure 5.4). These data imply a reduced docking mechanism that can be justified by the reduction in fusion efficient t-SNAREs at the plasma membrane.

6.1.3 LDCVs prefer regions of plasma membrane with low SNARE density

Vesicle dynamics have been thoroughly examined within Chapter Four using high sampling rates and highly accurate tracking analysis and each experiment supports the same conclusion that vesicles are targeted to specific sites at the plasma membrane for fusion. The tendency to reverse that the vesicles demonstrate (Figure 4.4) is indicative of an attempt to tether to the membrane and tracking of a large group of membrane-proximal vesicles has shown that the positioning of these caged vesicles is not random (Figure 4.2). This type of vesicle behaviour has been reported previously (Steyer and Almers, 1999; Oheim and Stühmer, 2000; Johns et al., 2001); however data within this thesis has further validated these hypotheses by applying faster sampling rates and advanced spatial tracking. Vesicles are not always successful in tethering at these sites as is seen by the newly identified ‘scanning’ subset of vesicles, which move between previously visited sites (Figure 4.13). These data imply a highly controlled system that is not only spatially but also temporally controlled where potential fusion sites may be held in an incompetent state until required. The observation of vesicles fusing within the same 400 nm region provides the most significant evidence that specific fusion sites exist (Figure 4.21). Super-

resolution imaging in Chapter Five shows the highly complex and heterogeneous organisation of single SNARE molecules; with this in mind past works which have reported multiple fusion events in 1 μm square regions are not indicative of multiple events at one exocytotic site (Oheim et al., 1999). In vesicle tracking the position of a vesicle from one frame to another is quantified, with a slower sampling rate the time between frames is longer and more information is missed from the recording. The observation of refractory periods of 1.5 seconds between fusions at the same site in my data (Figure 4.21) demonstrate the need for sampling rates faster than those used in past works (Allersma et al., 2004).

Investigation into the protein/lipid environment at sites of exocytosis has questioned the incidence of more ordered (Chamberlain et al., 2001; Lang et al., 2001) or less ordered lipids (Bacia et al., 2004) as well as the exact number of t-SNARE proteins present (Knowles et al., 2010; Karatekin et al., 2010; van den Bogaart et al., 2010). Key findings within Chapter Four have provided a model for vesicle fusion in stimulated cells that can be applied to cells at rest to predict sites for exocytosis with nanometre resolution. One such finding relates to the mobility of a resident fusing vesicle before and after stimulation; there is not a significant change in displacement or speed meaning the vesicles do not move far to fuse (Figure 4.17). Furthermore the localisation of exocytotic events in relation to whole cell vesicle dynamics (Figure 4.22) revealed that vesicles predominantly fuse over areas commonly visited by other vesicles. This collection of data strongly implies that the localisation of vesicles at the plasma membrane of resting cells is an accurate indication of where they will fuse.

Vesicles that appear ‘docked’ to the plasma membrane are believed to be surrounded by an abundance of t-SNARE proteins according to a number of works (Lang et al., 2001; Barg et al., 2010; Knowles et al., 2010); however these results stem from colocalisation and intensity ratio calculations. These methods rely on diffraction-limited systems to describe two objects in the same place; advances in super-resolution microscopy are revealing higher complexity within domains the size of the limit of resolution that contradicts previous findings (Rickman et al., 2010;

Bar-On et al., 2012). The localisation of single molecules of the t-SNARE proteins in relation to the membrane-proximal vesicles is possible through PALM. Data in Figure 5.3 shows that an average of 5 SNAP-25 molecules will reside within the radius of a vesicle in a resting cell and that the vesicles are positioned over lower density SNARE domains. Further to this a recent study from our group (Yang et al., 2012) has examined both endogenous and exogenous SNAP-25 and syntaxin-1 using SMLM and found that within 82.5 nm (the radius predicted to allow t-SNARE and synaptobrevin interaction) only 1 - 2 SNARE proteins reside. Live particle tracking in this study was able to characterise the mobility of the single protein molecules; revealing a restricted mobility and determine that the number of SNARE molecules under a vesicle at any point in time is between 0 – 7. These findings strongly support the hypothesis that vesicles prefer regions of low t-SNARE protein density. As discussed above the positioning of vesicles in unstimulated cells is indicative of where they will fuse and so these data suggests vesicles prefer to fuse at sites with low SNARE density. The number of SNARE proteins required for fusion has been heavily debated recently with some groups suggesting as many as 75 molecules are required (Sieber et al., 2007; Knowles et al., 2010); however my data suggests only a few SNAREs are required for vesicle fusion and this is strongly supported by previous reports *in vitro* (Hua and Scheller, 2001), in reconstituted bilayers (Shi et al., 2012) and using SMLM in fixed and live cells (Bar-On et al., 2012; Yang et al., 2012).

6.2 The Significance of my Findings in Regulated Exocytosis

The data presented within this thesis can be combined to produce a model for the spatial and temporal control the proteins and the lipids exert over vesicle fusion in regulated exocytosis (Figure 6.1).

Areas where vesicles prefer to reside are defined by high density tracking of membrane-proximal vesicles and these areas are where fusion often occurs. Data presented within this thesis and from within our group (Yang et al., 2012) have

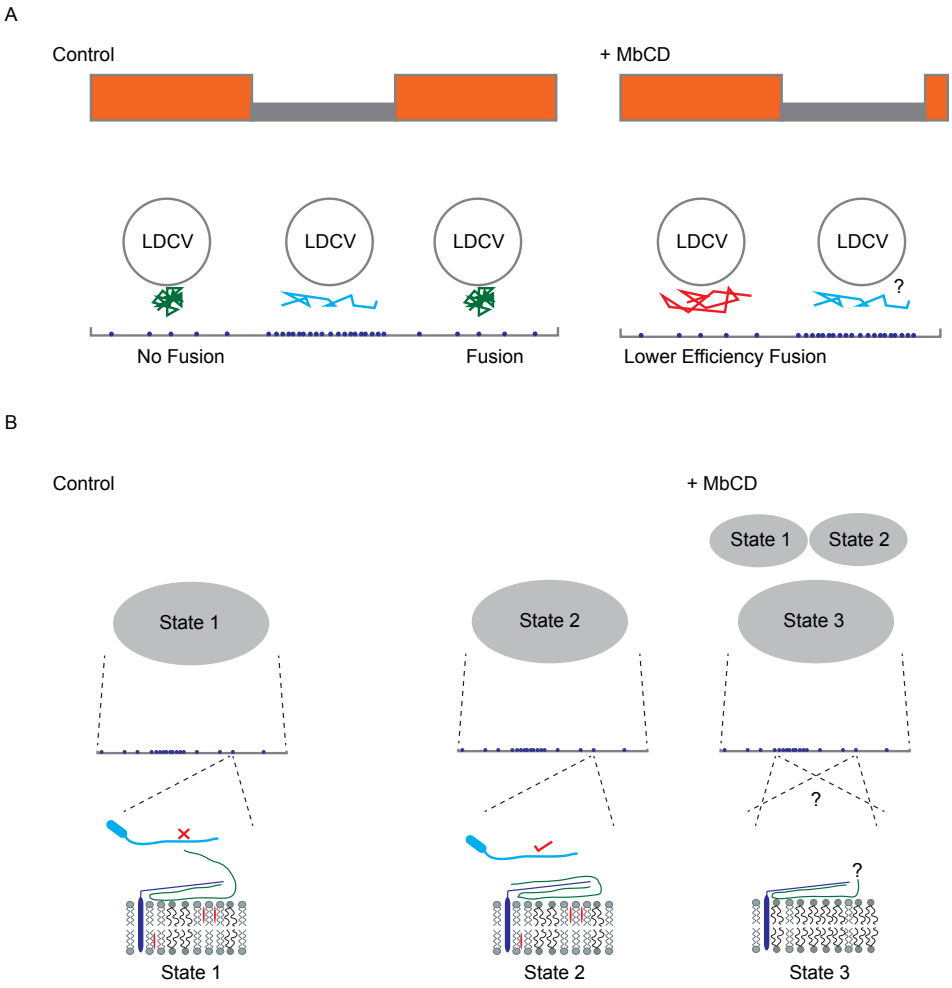

Figure 6.1 Spatial and temporal control of exocytosis. A) In control cells (left column) regions where vesicles tend to reside (orange bar) correspond to low SNAP-25 density (dark blue circles) and less vesicle populated regions (grey bar) correspond to denser SNAP-25 localisation at the plasma membrane (grey line). Data suggests vesicles (LDCV) are caged (green track) over lower molecule denisty and more directed (cyan track) over high molecule density. The modification of membrane-cholesterol leaves SNAP-25 clusters intact (right column) and vesicles still maintain regions of preferred vesicle localisation over low SNAP-25 density but tracks are more displaced (red track). B) In control cells (left column) diffraction-limited clusters (grey filled oval) contain single molecules predominantly undergoing either state 1 or 2. Heterodimers in state 1 (syntaxin: dark blue, SNAP-25: green) at plasma membrane (cholesterol: red) with SN2 not associated; synaptobrevin (cyan) cannot bind. Heterodimers in state 2 with SN2 of SNAP-25 associated; synaptobrevin can bind. In cells with altered membrane-cholesterol (right column) state 1, state 2 and state 3 exist. The association of SN2 in state 3 and whether the vesicle fuses at sites of low or high SNAP-25 density is unknown in these cells.

shown that at these sites both SNAP-25 and syntaxin-1 molecules are less densely crowded; this is shown in both fixed cells (Figure 5.3) and in a model simulating SNARE protein and vesicle mobility (Yang et al., 2012). These data strongly suggest that the number of SNARE proteins required for fusion is <7.

There are distinct regions of plasma membrane patterned by their fusion capability, a cluster (>200 nm) predominantly exhibiting state 1 being less fusion efficient as synaptobrevin cannot bind a t-SNARE complex with the second SNARE helix of SNAP-25 dissociated. A cluster (>200 nm) containing more fully zippered state 2 t-SNARE complex however is capable of binding synaptobrevin and eliciting fusion. The spatial and temporal control of vesicle fusion appears to be imposed at two levels of magnification. The influence of lipid order in this model is less definitive. The loss of efficient docking is strongly implied in vesicle tracking experiments and the vesicles remain over less populated areas; however with no information on the mobility of fusing vesicles after stimulation in MβCD-treated cells the site of vesicle fusion after cholesterol depletion cannot be described. The t-SNARE complex undergoes alternative conformations after lipid order disruption with some state 1, state 2 and a structurally unidentified configuration termed state 3. The reduction in fusion efficiency after membrane cholesterol depletion (Zhang et al., 2009; Rickman et al., 2010) strongly implies that state 3 is not fusion-competent.

6.3 Summary

The process of regulated exocytosis has been examined within this thesis using a range of microscopy techniques and analysis systems. The restricted mobility of the vesicles and the variation in vesicle dynamics dependent on when they fuse are evidence of an extremely regulated process that leads to calcium-triggered exocytosis. Additionally the highly complex single molecule organisation of the t-SNARE proteins and the alternative states of t-SNARE complex describe how the fusion event is controlled to ensure exocytosis occurs at the right time and place. A resounding finding in these data is that diffraction-limited systems are no longer

adequate to solely investigate such processes and that super-resolution microscopy is required to understand the mechanisms behind regulated exocytosis. The data presented in this thesis describes a two tiered regulation with functionally capable complexed proteins segregated in large domains at the plasma membrane and a spatial arrangement within these domains that pinpoint the exact sites of vesicle fusion. How these sites are perturbed by cholesterol modification is not conclusive from these data; however the importance of this sterol in maintaining the natural lipid arrangement as well as efficient regulated exocytosis is clear. Limitations with microscopy remain within the imaging of more than one component as fast sampling rates are problematic in super-resolution techniques; however considering these limitations the data described within this thesis come together to provide a novel model of exocytotic control.

Bibliography:

Abbe, E. (1873). Contributions to the theory of the microscope and microscopic perception. Archive for Microscopic Anatomy *9*, 413–418.

Alberts, B., Johnson, A., Lewis, J., Raff, M., Roberts, K., and Walter, P. (2002). Molecular Biology of the Cell 4th Edition.

Allersma, M. W., Wang, L., Axelrod, D., and Holz, R. W. (2004). Visualization of Regulated Exocytosis with a Granule-Membrane Probe Using Total Internal Reflection Microscopy. Molecular Biology of the Cell *15*, 4658–4668.

Alés, E., Tabares, L., Poyato, J. M., Valero, V., Lindau, M., and Alvarez de Toledo, G. (1999). High calcium concentrations shift the mode of exocytosis to the kiss-and-run mechanism. Nature Cell Biology *1*, 40–44.

An, S. J., and Almers, W. (2004). Tracking SNARE complex formation in live endocrine cells. Science (New York, N.Y.) *306*, 1042–1046.

Ando, R., Mizuno, H., and Miyawaki, A. (2004). Regulated fast nucleocytoplasmic shuttling observed by reversible protein highlighting. Science (New York, N.Y.) *306*, 1370–1373.

Aoki, R., Kitaguchi, T., Oya, M., Yanagihara, Y., Sato, M., Miyawaki, A., and Tsuboi, T. (2010). Duration of fusion pore opening and the amount of hormone released are regulated by myosin II during kiss-and-run exocytosis. The Biochemical Journal *429*, 497–504.

Arunachalam, L., Han, L., Tassew, N. G., He, Y., Wang, L., Xie, L., Fujita, Y., Kwan, E., Davletov, B., Monnier, P. P., et al. (2008). Munc18-1 Is Critical for Plasma Membrane Localization of Syntaxin1 but Not of SNAP-25 in PC12 Cells. Molecular Biology of the Cell *19*, 722–734.

Augustin, I., Rosenmund, C., Südhof, T. C., and Brose, N. (1999). Munc13-1 is essential for fusion competence of glutamatergic synaptic vesicles. Nature *400*, 457–461.

Augustine, B. Y. G. J., and Nehert, E. (1992). Calcium Requirements for secretion in bovine chromaffin cells. Journal of Physiology *450*, 247–271.

Augustine, G. J., and Neher, E. (1992). Neuronal Ca2+ signalling takes the local route. Current opinion in neurobiology *2*, 302–307.

Avery, J., Ellis, D. J., Lang, T., Holroyd, P., Riedel, D., Henderson, R. M., Edwardson, J. M., and Jahn, R. (2000). A cell-free system for regulated exocytosis in PC12 cells. The Journal of Cell Biology *148*, 317–324.

Bacia, K., Scherfeld, D., Kahya, N., and Schwille, P. (2004a). Fluorescence correlation spectroscopy relates rafts in model and native membranes. Biophysical Journal *87*, 1034–1043..

Bacia, K., Schuette, C. G., Kahya, N., Jahn, R., and Schwille, P. (2004b). SNAREs prefer liquid-disordered over "raft" (liquid-ordered) domains when reconstituted into giant unilamellar vesicles. The Journal of Biological Chemistry *279*, 37951–37955.

Bagatolli, L. a (2006). To see or not to see: lateral organization of biological membranes and fluorescence microscopy. Biochimica et biophysica acta *1758*, 1541–1556.

Bagatolli, L. a, and Gratton, E. (1999). Two-photon fluorescence microscopy observation of shape changes at the phase transition in phospholipid giant unilamellar vesicles. Biophysical Journal *77*, 2090–2101.

Bai, J., Tucker, W. C., and Chapman, E. R. (2004). PIP2 increases the speed of response of synaptotagmin and steers its membrane-penetration activity toward the plasma membrane. Nature structural & molecular biology *11*, 36–44.

Bai, L., Wang, Y., Fan, J., Chen, Y., Ji, W., Qu, A., Xu, P., James, D. E., and Xu, T. (2007). Dissecting multiple steps of GLUT4 trafficking and identifying the sites of insulin action. Cell metabolism *5*, 47–57.

Bajohrs, M., Rickman, C., Binz, T., and Davletov, B. (2004). A molecular basis underlying differences in the toxicity of botulinum serotypes A and E. EMBO reports *5*, 1090–1095.

Baltrusch, S., and Lenzen, S. (2008). Monitoring of glucose-regulated single insulin secretory granule movement by selective photoactivation. Diabetologia *51*, 989–996.

Banerjee, a, Kowalchyk, J. a, DasGupta, B. R., and Martin, T. F. (1996). SNAP-25 is required for a late postdocking step in Ca2+-dependent exocytosis. The Journal of Biological Chemistry *271*, 20227–20230.

Bar-On, D., Gutman, M., Mezer, A., Ashery, U., Lang, T., and Nachliel, E. (2009). Evaluation of the heterogeneous reactivity of the syntaxin molecules on the inner leaflet of the plasma membrane. The Journal of Neuroscience : the official Journal of the Society for Neuroscience *29*, 12292–12301.

Bar-On, D., Wolter, S., van de Linde, S., Heilemann, M., Nudelman, G., Nachliel, E., Gutman, M., Sauer, M., and Ashery, U. (2012). Super-resolution imaging reveals the internal architecture of nano-sized syntaxin clusters. The Journal of Biological Chemistry, 1–17.

Barg, S., Knowles, M. K., Chen, X., Midorikawa, M., and Almers, W. (2010). Syntaxin clusters assemble reversibly at sites of secretory granules in live cells. PNAS *107*.

Barlowe, C. (1998). COPII and selective export from the endoplasmic reticulum. Biochimica et Biophysica Acta *1404*, 67–76.

Barnstable, C. J., Hofstein, R., and Akagawa, K. (1985). A marker of early amacrine cell development in rat retina. Brain Research *352*, 286–290.

Bartlett, B. M. S. (1963). The Spectral Analysis of Point Processes. Journal of the Royal Statistical Society *25*, 264–296.

Becherer, U., Moser, T., Stühmer, W., and Oheim, M. (2003). Calcium regulates exocytosis at the level of single vesicles. Nature Neuroscience *6*, 846–853.

Becherer, U., and Rettig, J. (2006). Vesicle pools, docking, priming, and release. Cell and tissue research *326*, 393–407.

Becker, W. (2005). Advanced Time-Correlated Single photon Counting Techniques Springer S. (Springer).

Bennett, M. K., Calakos, N., and Scheller, R. H. (1992). Syntaxin: a synaptic protein implicated in docking of synaptic vesicles at presynaptic active zones. Science (New York, N.Y.) *257*, 255–259.

Bennett, M. K., García-Arrarás, J. E., Elferink, L. a, Peterson, K., Fleming, a M., Hazuka, C. D., and Scheller, R. H. (1993). The syntaxin family of vesicular transport receptors. Cell *74*, 863–873.

Bergmann, J. E., Tokuyasu, K. T., and Singer, S. J. (1981). Passage of an integral membrane protein, the vesicular stomatitis virus glycoprotein, through the Golgi apparatus en route to the plasma membrane. Proceedings of the National Academy of Sciences of the United States of America *78*, 1746–1750.

Besag, J. E. (1972). Nearest-Neighbour Systems and the Auto-Logistic Model for Binary Data. Journal of the Royal Statistical Society *34*, 75–83.

Betzig, E., Patterson, G. H., Sougrat, R., Lindwasser, O. W., Olenych, S., Bonifacino, J. S., Davidson, M. W., Lippincott-Schwartz, J., and Hess, H. F. (2006). Imaging intracellular fluorescent proteins at nanometer resolution. Science (New York, N.Y.) *313*, 1642–1645.

Binz, T., Blasi, J., Yamasaki, S., Baumeister, a, Link, E., Südhof, T. C., Jahn, R., and Niemann, H. (1994). Proteolysis of SNAP-25 by types E and A botulinal neurotoxins. The Journal of Biological Chemistry *269*, 1617–1620.

Blasi, J., Chapman, E. R., Yamasaki, S., Binz, T., Niemann, H., and Jahn, R. (1993). Botulinum neurotoxin C1 blocks neurotransmitter release by means of cleaving HPC-1/syntaxin. The EMBO Journal *12*, 4821–4828.

Block, M. R., Glick, B. S., Wilcox, C. a, Wieland, F. T., and Rothman, J. E. (1988). Purification of an N-ethylmaleimide-sensitive protein catalyzing vesicular transport. Proceedings of the National Academy of Sciences of the United States of America *85*, 7852–7856.

Bock, J. B., Klumperman, J., Davanger, S., and Scheller, R. H. (1997). Syntaxin 6 functions in trans-Golgi network vesicle trafficking. Molecular biology of the cell *8*, 1261–1271.

van den Bogaart, G., Holt, M. G., Bunt, G., Riedel, D., Wouters, F. S., and Jahn, R. (2010). One SNARE complex is sufficient for membrane fusion. Nature structural & molecular biology *17*, 358–364.

Bowen, M., and Brunger, A. T. (2006). Conformation of the synaptobrevin transmembrane domain. Proceedings of the National Academy of Sciences of the United States of America *103*, 8378–8383.

Bowen, M. E., Weninger, K., Brunger, A. T., and Chu, S. (2004). Single molecule observation of liposome-bilayer fusion thermally induced by soluble N-ethyl maleimide sensitive-factor attachment protein receptors (SNAREs). Biophysical Journal *87*, 3569–3584.

Broadie, K., Prokop, a, Bellen, H. J., O'Kane, C. J., Schulze, K. L., and Sweeney, S. T. (1995). Syntaxin and synaptobrevin function downstream of vesicle docking in Drosophila. Neuron *15*, 663–673.

Brown, D. A., and Rose, J. K. (1992). Sorting of GPI-Anchored Proteins to Membrane Subdomains during Transport to the Apical Cell Surface. Cell *66*, 533–544.

Burgess, T. L., and Kelly, R. B. (1987). Constitutive and regulated secretion of proteins. Annual review of Cell Biology *3*, 243–293.

Burgoyne, R. D., and Morgan, A. (1993). Regulated exocytosis. Biochemical Journal *316*, 305–316.

Calakos, N., Bennett, M. K., Peterson, K. E., and Scheller, R. H. (1994). Protein-protein interactions contributing to the specificity of intracellular vesicular trafficking. Science *263*, 1146–1149.

Cao, X., Ballew, N., and Barlowe, C. (1998). Initial docking of ER-derived vesicles requires Uso1p and Ypt1p but is independent of SNARE proteins. The EMBO Journal *17*, 2156–2165.

Carey, K. L., Richards, S. a, Lounsbury, K. M., and Macara, I. G. (1996). Evidence using a green fluorescent protein-glucocorticoid receptor chimera that the Ran/TC4 GTPase mediates an essential function independent of nuclear protein import. The Journal of Cell Biology *133*, 985–996.

Carr, C. M., Grote, E., Munson, M., Hughson, F. M., and Novick, P. J. (1999). Sec1p binds to SNARE complexes and concentrates at sites of secretion. The Journal of Cell Biology *146*, 333–344.

Castillo, B. Y. J. D. E. L., and Katz, B. (1954). Quantal components of the end-plate potential. The Journal of Physiology, 560–573.

Ceccarelli, B., Hurlbut, W. P., and Mauro, a (1973). Turnover of transmitter and synaptic vesicles at the frog neuromuscular junction. The Journal of Cell Biology *57*, 499–524.

Chamberlain, L. H., Burgoyne, R. D., and Gould, G. W. (2001). SNARE proteins are highly enriched in lipid rafts in PC12 cells: implications for the spatial control of exocytosis. Proceedings of the National Academy of Sciences of the United States of America *98*, 5619–5624.

Chapman, E. R., An, S., Barton, N., and Jahn, R. (1994). SNAP-25, a t-SNARE Which Binds to Both Syntaxin and Synaptobrevin via Domains That May Form Coiled Coils. Biochemistry *269*, 27427–27432.

Chapman, E. R., and Davis, a F. (1998). Direct interaction of a Ca2+-binding loop of synaptotagmin with lipid bilayers. The Journal of Biological Chemistry *273*, 13995–14001.

Chapman, E. R., Hanson, P. I., An, S., and Jahn, R. (1995). Calcium Regulates the Interaction between Synaptotagmin and Syntaxin 1. Journal of Biological Chemistry *270*, 23667–23671.

Chattoraj, M., King, B. a, Bublitz, G. U., and Boxer, S. G. (1996). Ultra-fast excited state dynamics in green fluorescent protein: multiple states and proton transfer. Proceedings of the National Academy of Sciences of the United States of America *93*, 8362–8367.

Chen, P., Bruederle, C., Gaisano, H., and Shyng, S. (2011). Syntaxin 1A regulates surface expression of beta-cell ATP-sensitive potassium channels. American Journal of Physiology Cell Physiology *300*, C506–C516.

Chen, X., Tomchick, D. R., Kovrigin, E., Araç, D., Machius, M., Südhof, T. C., and Rizo, J. (2002). Three-dimensional structure of the complexin/SNARE complex. Neuron *33*, 397–409.

Chen, Y. a, Scales, S. J., Jagath, J. R., and Scheller, R. H. (2001a). A discontinuous SNAP-25 C-terminal coil supports exocytosis. The Journal of Biological Chemistry *276*, 28503–28508.

Chen, Y. a, Scales, S. J., and Scheller, R. H. (2001b). Sequential SNARE assembly underlies priming and triggering of exocytosis. Neuron *30*, 161–170.

Chen, Y. a, and Scheller, R. H. (2001). SNARE-mediated membrane fusion. Nature reviews. Molecular Cell Biology *2*, 98–106.

Cheng, L., Fu, J., Tsukamoto, A., and Hawley, R. G. (1996). Use of green fluorescent protein variants to monitor gene transfer and expression in mammalian cels. Nature Biotechnology *14*, 606–609.

Chicka, M. C., and Chapman, E. R. (2009). Concurrent Binding of Complexin and Synaptotagmin to Liposome-Embedded. Biochemistry *48*, 657–659.

Clary, D. O., Griff, I. C., and Rothman, J. E. (1990). SNAPs, a family of NSF attachment proteins involved in intracellular membrane fusion in animals and yeast. Cell *61*, 709–721.

Clegg, R. M. (1995). Fluorescence resonance energy transfer. Current opinion in biotechnology *6*, 103–110.

Cody, C. W., Prasher, D. C., Westler, W. M., Prendergast, F. G., and J, W. W. W. (1993). Chemical Structure of the Hexapeptide Chromophore of the. Biochemistry *32*, 1212–1218.

Cohen, C., and Parry, D. A. D. (1986). Helical coiled coils — a widespread motif in proteins. Trends in Biochemical Sciences *11*, 245–248.

Coons, A. H., Creech, H. J., Jones, N., and Berliner, E. (1942). The demonstration of pneumococcal antigen in tissues by the use of fluorescent antibody. the Journal of Immunology *45*, 159–170.

Cowan, M., Südhof, T. C., and Stevens, C. F. (2001). Synapses (John Hopskins University Press).

Cross, G. A. M. (1987). Eukaryotic Protein Modification and Membrane Attachment via Phosphatidylinisitol. Cell *48*, 179–181.

Dale, H. (1936). Some recent extensions of chemical transmission. Cold Spring Harbor Symposia on Quantitative Biology *4*, 143–149.

Dalton, B. Y. A. J., Ph, D., and Felix, A. M. D. (1956). A Comparative Study of the Golgi Complex. J. Biophysic. and Biochem. Cytol *2*, 79–94.

Dascher, C., Ossig, R., Gallwitz, D., and Schmitt, H. D. (1991). Identification and structure of four yeast genes (SLY) that are able to suppress the functional loss of YPT1, a member of the RAS superfamily. Molecular and cellular biology *11*, 872–885.

Degtyar, V. E., Allersma, M. W., Axelrod, D., and Holz, R. W. (2007). Increased motion and travel, rather than stable docking, characterize the last moments before secretory granule fusion. Proceedings of the National Academy of Sciences of the United States of America *104*, 15929–15934.

Denk, W., Strickler, J. H., and Webb, W. W. (1990). Two-photon laser scanning fluorescence microscopy. Science (New York, N.Y.) *248*, 73–76.

Dietrich, C., Bagatolli, L. a, Volovyk, Z. N., Thompson, N. L., Levi, M., Jacobson, K., and Gratton, E. (2001a). Lipid rafts reconstituted in model membranes. Biophysical Journal *80*, 1417–1428.

Dietrich, C., Volovyk, Z. N., Levi, M., Thompson, N. L., and Jacobson, K. (2001b). Partitioning of Thy-1, GM1, and cross-linked phospholipid analogs into lipid rafts reconstituted in supported model membrane monolayers. PNAS *98*, 10642–10647.

Dinic, J., Ashrafzadeh, P., and Parmryd, I. (2013). Actin filaments attachment at the plasma membrane in live cells cause the formation of ordered lipid domains. Biochimica et Biophysica Acta (BBA) *1828*, 1102–1111.

Domanska, M. K., Kiessling, V., and Tamm, L. K. (2010). Docking and fast fusion of synaptobrevin vesicles depends on the lipid compositions of the vesicle and the acceptor SNARE complex-containing target membrane. Biophysical Journal *99*, 2936–2946.

Dulubova, I., Sugita, S., Hill, S., Hosaka, M., Fernandez, I., Südhof, T. C., and Rizo, J. (1999). A conformational switch in syntaxin during exocytosis: role of munc18. The EMBO Journal *18*, 4372–4382.

Duncan, R. R., Greaves, J., Wiegand, U., Matskevich, I., Bodammer, G., Apps, D. K., Shipston, M. J., and Chow, R. H. (2003). Functional and spatial segregation of secretory vesicle pools according to vesicle age. Nature *422*, 176–180.

Dunn, L. a, and Holz, R. W. (1983). Catecholamine secretion from digitonin-treated adrenal medullary chromaffin cells. The Journal of Biological Chemistry *258*, 4989–4993.

Eccles, J. C. (1948). Conduction and synaptic transmission in the nervous system. Annual review of Physiology *10*, 93–116.

Edidin, M. (1974). Rotational and translational diffusion in membranes. Annual review of biophysics and bioengineering *3*, 179–201.

Eggeling, C., Ringemann, C., Medda, R., Schwarzmann, G., Sandhoff, K., Polyakova, S., Belov, V. N., Hein, B., von Middendorff, C., Schönle, A., et al. (2009). Direct observation of the nanoscale dynamics of membrane lipids in a living cell. Nature *457*, 1159–1162.

Elferink, L. a, Trimble, W. S., and Scheller, R. H. (1989). Two vesicle-associated membrane protein genes are differentially expressed in the rat central nervous system. The Journal of Biological Chemistry *264*, 11061–11064.

Ellena, J. F., Liang, B., Wiktor, M., Stein, A., Cafiso, D. S., Jahn, R., and Tamm, L. K. (2009). Dynamic structure of lipid-bound synaptobrevin suggests a nucleation-propagation mechanism for trans-SNARE complex formation. Proceedings of the National Academy of Sciences of the United States of America *106*, 20306–20311.

Fahey, P. F., Koppel, D. E., Barak, L. S., Wolfe, D. E., Elson, E. L., and Webb, W. W. (1977). Lateral Diffusion in Planar Lipid Bilayers. Science *195*, 305–306.

Farquhar, M. G., and Palade, G. E. (1981). The Golgi apparatus (complex)-(1954-1981)-from artifact to center stage. The Journal of Cell Biology *91*, 77s–103s.

Fasshauer, D., and Margittai, M. (2004). A transient N-terminal interaction of SNAP-25 and syntaxin nucleates SNARE assembly. The Journal of Biological Chemistry *279*, 7613–7621.

Fasshauer, D., Otto, H., Eliason, W. K., Jahn, R., and Brünger, a T. (1997). Structural changes are associated with soluble N-ethylmaleimide-sensitive fusion protein attachment protein receptor complex formation. The Journal of Biological Chemistry *272*, 28036–28041.

Fasshauer, D., Sutton, R. B., Brunger, a T., and Jahn, R. (1998). Conserved structural features of the synaptic fusion complex: SNARE proteins reclassified as Q- and R-SNAREs. Proceedings of the National Academy of Sciences of the United States of America *95*, 15781–15786.

Fasshauer, D, Bruns, D., Shen, B., Jahn, R., and Brunger, A. T. (1997). A Structural Change Occurs upon Binding of Syntaxin to SNAP-25. Journal of Biological Chemistry *272*, 4582–4590.

Fatt, B. P., and Katz, B. (1951). An analysis of the end-plate potential recorded with an intra-cellular electrode. The Journal of Physiology, 320–370.

Fatt, P., and Katz, B. (1950). Membrane potentials at the motor end-plate. The Journal of Physiology *111*, 46–47.

Fernandez, I., Araç, D., Ubach, J., Gerber, S. H., Shin, O., Gao, Y., Anderson, R. G., Südhof, T. C., and Rizo, J. (2001). Three-dimensional structure of the synaptotagmin 1 C2B-domain: synaptotagmin 1 as a phospholipid binding machine. Neuron *32*, 1057–1069.

Fernández-Chacón, R., and Südhof, T. C. (1999). Genetics of synaptic vesicle function: toward the complete functional anatomy of an organelle. Annual review of Physiology *61*, 753–776.

Ferro-Novick, S., and Jahn, R. (1994). Vesicle fusion from yeast to man. Nature *370*, 191–193.

Fiebig, K. M., Rice, L. M., Pollock, E., and Brunger, A. T. (1999). Folding intermediates of SNARE complex assembly. Nature Structural Biology *6*, 117–123.

Fletcher, A. I., Shuang, R., Giovannucci, D. R., Zhang, L., Bittner, M. a, and Stuenkel, E. L. (1999). Regulation of exocytosis by cyclin-dependent kinase 5 via phosphorylation of Munc18. The Journal of Biological Chemistry *274*, 4027–4035.

Foster, L. J., De Hoog, C. L., and Mann, M. (2003). Unbiased quantitative proteomics of lipid rafts reveals high specificity for signaling factors. Proceedings of the National Academy of Sciences of the United States of America *100*, 5813–5818.

Fries, E. (1980). Transport of Vesicular Stomatitis Virus Glycoprotein in a Cell-Free Extract. Proceedings of the National Academy of Sciences *77*, 3870–3874.

Fujita, Y., Shirataki, H., Sakisaka, T., Asakura, T., Ohya, T., Kotani, H., Yokoyama, S., Nishioka, H., Matsuura, Y., Mizoguchi, a, et al. (1998). Tomosyn: a syntaxin-1-binding protein that forms a novel complex in the neurotransmitter release process. Neuron *20*, 905–915.

Fukata, M., Fukata, Y., Adesnik, H., Nicoll, R. A., and Bredt, D. S. (2004). Identification of PSD-95 palmitoylating enzymes. Neuron *44*, 987–996.

Förster, T. (1946). Energiewanderung und Fluoreszenz (Energy migration and fluorescence). Naturwissenschaften *6*, 166–175.

García-Sáez, A. J., Chiantia, S., and Schwille, P. (2007). Effect of line tension on the lateral organization of lipid membranes. The Journal of Biological Chemistry *282*, 33537–33544.

Garden, G. A., and La Spada, A. R. (2012). Intercellular (mis)communication in Neurodegenerative Disease. 2Neuron *73*, 886–901.

Gaus, K., Gratton, E., Kable, E. P. W., Jones, A. S., Gelissen, I., Kritharides, L., and Jessup, W. (2003). Visualizing lipid structure and raft domains in living cells with two-photon microscopy. Proceedings of the National Academy of Sciences of the United States of America *100*, 15554–15559.

Giordano, L., Jovin, T. M., Irie, M., and Jares-Erijman, E. a (2002). Diheteroarylethenes as thermally stable photoswitchable acceptors in photochromic fluorescence resonance energy transfer (pcFRET). Journal of the American Chemical Society *124*, 7481–7489.

Giraudo, C. G., Garcia-Diaz, A., Eng, W. S., Chen, Y., Hendrickson, W. A., Melia, T. J., and Rothman, J. E. (2009). Alternative Zippering as an On-Off Switch for SNARE-Mediated Fusion. Science *512*.

Gladycheva, S. E., Ho, C. S., Lee, Y. Y. F., and Stuenkel, E. L. (2004). Regulation of syntaxin1A-munc18 complex for SNARE pairing in HEK293 cells. The Journal of Physiology *558*, 857–871.

Goda, Y. (1997). SNAREs and regulated vesicle exocytosis. Proceedings of the National Academy of Sciences of the United States of America *94*, 769–772.

Gong, L.-W., Di Paolo, G., Diaz, E., Cestra, G., Diaz, M.-E., Lindau, M., De Camilli, P., and Toomre, D. (2005). Phosphatidylinositol phosphate kinase type I gamma regulates dynamics of large dense-core vesicle fusion. PNAS *102*, 5204–5209.

Gonzalo, S., Greentree, W. K., and Linder, M. E. (1999). SNAP-25 is targeted to the plasma membrane through a novel membrane-binding domain. The Journal of Biological Chemistry *274*, 21313–21318.

Gonzalo, S., and Linder, M. E. (1998). SNAP-25 palmitoylation and plasma membrane targeting require a functional secretory pathway. Molecular biology of the cell *9*, 585–597.

Graham, J., and Gerard, R. W. (1946). Membrane potentials and excitation of impaled single muscle fibres. Journal of Cellular and Comparative Physiology *28*, 99–117.

Graham, M. E., Barclay, J. W., and Burgoyne, R. D. (2004). Syntaxin/Munc18 interactions in the late events during vesicle fusion and release in exocytosis. The Journal of Biological Chemistry *279*, 32751–32760.

Granseth, B., Odermatt, B., Royle, S. J., and Lagnado, L. (2007). Clathrin-mediated endocytosis: the physiological mechanism of vesicle retrieval at hippocampal synapses. The Journal of Physiology *585*, 681–686.

Greaves, J., Gorleku, O. a, Salaun, C., and Chamberlain, L. H. (2010). Palmitoylation of the SNAP25 protein family: specificity and regulation by DHHC palmitoyl transferases. The Journal of Biological Chemistry *285*, 24629–24638.

Greene, L. a, and Tischler, a S. (1976). Establishment of a noradrenergic clonal line of rat adrenal pheochromocytoma cells which respond to nerve growth factor. Proceedings of the National Academy of Sciences of the United States of America *73*, 2424–2428.

Griffiths, G., and Simons, K. A. I. (1986). The trans Golgi Network: Sorting at the exit site of the Golgi complex. Advancement Of Science *234*, 438–443.

Grosshans, B. L., Ortiz, D., and Novick, P. (2006). Rabs and their effectors : Achieving specificity in membrane traffic. PNAS *103*, 11821–11827.

Gschwind, a, Zwick, E., Prenzel, N., Leserer, M., and Ullrich, a (2001). Cell communication networks: epidermal growth factor receptor transactivation as the paradigm for interreceptor signal transmission. Oncogene *20*, 1594–1600.

Gulyás-Kovács, A., de Wit, H., Milosevic, I., Kochubey, O., Toonen, R., Klingauf, J., Verhage, M., and Sørensen, J. B. (2007). Munc18-1: sequential interactions with the fusion machinery stimulate vesicle docking and priming. The Journal of Neuroscience : the official Journal of the Society for Neuroscience *27*, 8676–8686.

Halemani, N. D., Bethani, I., Rizzoli, S. O., and Lang, T. (2010). Structure and Dynamics of a Two-Helix SNARE Complex in Live Cells. Traffic, 394–404.

Hammond, a T., Heberle, F. a, Baumgart, T., Holowka, D., Baird, B., and Feigenson, G. W. (2005). Crosslinking a lipid raft component triggers liquid ordered-liquid disordered phase separation in model plasma membranes. Proceedings of the National Academy of Sciences of the United States of America *102*, 6320–6325.

Han, X., Wang, C., Bai, J., Chapman, E. R., and Jackson, M. B. (2004). Transmembrane segments of syntaxin line the fusion pore of Ca2+-triggered exocytosis. Science (New York, N.Y.) *306*, 289–292.

Hanson, P. I., Otto, H., Barton, N., and Jahn, R. (1995). The N-Ethylmaleimide-sensitive Fusion Protein and alpha-SNAP Induce a Conformational Change in Syntaxin. The Journal of Biological Chemistry *270*, 16955–16961.

Hanson, P. I., Roth, R., Morisaki, H., Jahn, R., and Heuser, J. E. (1997). Structure and conformational changes in NSF and its membrane receptor complexes visualized by quick-freeze/deep-etch electron microscopy. Cell *90*, 523–535.

Hata, Y., Slaughter, C., and Sudhof, T. (1993). Synaptic vesicle fusion complex contains unc-18 homologue bound to syntaxin. Nature *366*, 347–351.

Haverstick, D. M., and Glaser, M. (1987). Visualization of Ca2+-induced phospholipid domains. Proceedings of the National Academy of Sciences of the United States of America *84*, 4475–4479.

Hayashi, T., McMahon, H., Yamasaki, S., Binz, T., Hata, Y., Südhof, T. C., and Niemann, H. (1994). Synaptic vesicle membrane fusion complex: action of clostridial neurotoxins on assembly. The EMBO Journal *13*, 5051–5061.

Hazzard, J., Südhof, T. C., and Rizo, J. (1999). NMR analysis of the structure of synaptobrevin and of its interaction with syntaxin. Journal of biomolecular NMR *14*, 203–207.

Heim, R., Cubitt, A. B., and Tsien, R. Y. (1995). Improved Green Fluorescence. Nature *373*, 663–664.

Heim, R., Prasher, D. C., and Tsien, R. Y. (1994). Wavelength mutations and posttranslational autoxidation of green fluorescent protein. Proceedings of the National Academy of Sciences of the United States of America *91*, 12501–12504.

Heim, R., and Tsien, R. Y. (1996). Engineering green fluorescent protein for improved brightness, longer wavelengths and fluorescence resonance energy transfer. Current biology : CB *6*, 178–182.

Heinemann, C., Riiden, L. V., Chow, R. H., and Neher, E. (1993). A two-step model of secretion control in neuroendocrine cells. European Journal of Physiology *424*, 105–112.

Hell, S. W., and Wichmann, J. (1994). Breaking the diffraction resolution limit by stimulated emission: stimulated-emission-depletion fluorescence microscopy. Optics letters *19*, 780–782.

Hernandez, J. M., Stein, A., Behrmann, E., Riedel, D., Cypionka, A., Farsi, Z., Walla, P. J., Raunser, S., and Jahn, R. (2012). Membrane fusion intermediates via directional and full assembly of the SNARE complex. Science (New York, N.Y.) *336*, 1581–1584..

Hess, S. T., Girirajan, T. P. K., and Mason, M. D. (2006). Ultra-high resolution imaging by fluorescence photoactivation localization microscopy. Biophysical Journal *91*, 4258–4272.

Heuser, J. E., and Reese, T. S. (1973). Evidence for recycling of synaptic vesicle membrane during transmitter release at the frog neuromuscular junction. The Journal of Cell Biology *57*, 315–344.

Holthuis, J. C., Pomorski, T., Raggers, R. J., Sprong, H., and Van Meer, G. (2001). The organizing potential of sphingolipids in intracellular membrane transport. Physiological reviews *81*, 1689–1723.

Hosono, R., Hekimi, S., Kamiya, Y., Sassa, T., Murakami, S., Nishiwaki, K., Miwa, J., Taketo, A., and Kodaira, K. I. (1992). The unc-18 gene encodes a novel protein affecting the kinetics of acetylcholine metabolism in the nematode Caenorhabditis elegans. Journal of Neurochemistry *58*, 1517–1525.

Hu, K., Carroll, J., Fedorovich, S., Rickman, C., Sukhodub, A., and Davletov, B. (2002a). Vesicular restriction of synaptobrevin suggests a role for calcium in membrane fusion. Nature *415*, 646–650.

Hu, K., Carroll, J., Rickman, C., and Davletov, B. (2002b). Action of complexin on SNARE complex. The Journal of Biological Chemistry *277*, 41652–41656.

Hua, Y., and Scheller, R. H. (2001). Three SNARE complexes cooperate to mediate membrane fusion. Proceedings of the National Academy of Sciences of the United States of America *98*, 8065–8070.

Huang, J., and Feigenson, G. W. (1999). A microscopic interaction model of maximum solubility of cholesterol in lipid bilayers. Biophysical Journal *76*, 2142–2157.

Hunt, J. M., Bommert, K., Charlton, M. P., Kistner, a, Habermann, E., Augustine, G. J., and Betz, H. (1994). A post-docking role for synaptobrevin in synaptic vesicle fusion. Neuron *12*, 1269–1279.

Inoue, A., Obata, K., and Akagawa, K. (1992). Cloning and sequence analysis of cDNA for a neuronal cell membrane antigen, HPC-1. The Journal of Biological Chemistry *267*, 10613–10619.

Inoue, K., and Nakazawa, K. (1989). Extracellular adenosine 5'-triphosphate-evoked norepinephrine secretion not relating to voltage-gated Ca channels in pheochromocytoma PC 12 cells. Neuroscience letters *106*, 294–299.

Ipsen, J. H., Mouritsen, O. G., and Zuckermann, M. J. (1989). Theory of thermal anomalies in the specific heat of lipid bilayers containing cholesterol. Biophysical journal *56*, 661–667.

Jafari-Mamaghani, M., Andersson, M., and Krieger, P. (2010). Spatial Point Pattern Analysis of Neurons Using Ripley's K-Function in 3D. Frontiers in neuroinformatics *4*, 9.

Jaiswal, J. K., Fix, M., Takano, T., Nedergaard, M., and Simon, S. M. (2007). Resolving vesicle fusion from lysis to monitor calcium-triggered lysosomal exocytosis in astrocytes. Proceedings of the National Academy of Sciences of the United States of America *104*, 14151–14156.

Jaiswal, J. K., Rivera, V. M., and Simon, S. M. (2009). Exocytosis of post-Golgi vesicles is regulated by components of the endocytic machinery. Cell *137*, 1308–1319.

Jewell, J. L., Oh, E., and Thurmond, D. C. (2010). Exocytosis mechanisms underlying insulin release and glucose uptake: conserved roles for Munc18c and syntaxin 4. American journal of physiology. Regulatory, integrative and comparative physiology *298*, R517–31.

Johns, L. M., Levitan, E. S., Shelden, E. a, Holz, R. W., and Axelrod, D. (2001). Restriction of secretory granule motion near the plasma membrane of chromaffin cells. The Journal of Cell Biology *153*, 177–190.

Kaether, C., and Gerdes, H. H. (1995). Visualization of protein transport along the secretory pathway using green fluorescent protein. FEBS letters *369*, 267–271.

Kahya, N., Scherfeld, D., Bacia, K., Poolman, B., and Schwille, P. (2003). Probing lipid mobility of raft-exhibiting model membranes by fluorescence correlation spectroscopy. The Journal of Biological Chemistry *278*, 28109–28115.

Karatekin, E., Di Giovanni, J., Iborra, C., Coleman, J., O'Shaughnessy, B., Seagar, M., and Rothman, J. E. (2010). A fast, single-vesicle fusion assay mimics physiological SNARE requirements. Proceedings of the National Academy of Sciences of the United States of America *107*, 3517–3521.

Karatekin, E., Tran, V. S., Huet, S., Fanget, I., Cribier, S., and Henry, J.-P. (2008). A 20-nm step toward the cell membrane preceding exocytosis may correspond to docking of tethered granules. Biophysical Journal *94*, 2891–2905.

Katz, B., and Miledi, R. (1965). the Measurement of Synaptic Delay, and the Time Course of Acetylcholine Release At the Neuromuscular Junction. Proceedings of the Royal Society of London. Series B, Containing papers of a Biological character. Royal Society (Great Britain) *161*, 483–495.

Keath, J. R., and Westhead, E. W. (2004). Factors affecting habituation of PC12 cells to ATP. European Journal of biochemistry / FEBS *271*, 4034–4041.

Kee, Y., Lin, R. C., Hsu, S. C., and Scheller, R. H. (1995). Distinct domains of syntaxin are required for synaptic vesicle fusion complex formation and dissociation. Neuron *14*, 991–998.

Kee, Y., Yoo, J. S., Hazuka, C. D., Peterson, K. E., Hsu, S. C., and Scheller, R. H. (1997). Subunit structure of the mammalian exocyst complex. Proceedings of the National Academy of Sciences of the United States of America *94*, 14438–14443.

Keller, J. E., and Neale, E. a (2001). The role of the synaptic protein snap-25 in the potency of botulinum neurotoxin type A. The Journal of Biological Chemistry *276*, 13476–13482.

Khelashvili, G., Galli, A., and Weinstein, H. (2012). Phosphatidylinositol 4,5-Biphosphate (PIP(2)) Lipids Regulate the Phosphorylation of Syntaxin N-Terminus by Modulating Both Its Position and Local Structure. Biochemistry *51*, 7685–7698.

Kim, T., Tao-Cheng, J., Eiden, L., and Loh, Y. P. (2001). Chromogranin A, an "On/Off" Switch Controlling Dense-Core Secretory Granule Biogenesis. Cell *106*, 499–509.

Klemm, R. W., Ejsing, C. S., Surma, M. a, Kaiser, H.-J., Gerl, M. J., Sampaio, J. L., de Robillard, Q., Ferguson, C., Proszynski, T. J., Shevchenko, A., et al. (2009). Segregation of sphingolipids and sterols during formation of secretory vesicles at the trans-Golgi network. The Journal of Cell Biology *185*, 601–612.

Klumperman, J., Kuliawat, R., Griffith, J. M., Geuze, H. J., and Arvan, P. (1998). Mannose 6-phosphate receptors are sorted from immature secretory granules via adaptor protein AP-1, clathrin, and syntaxin 6-positive vesicles. The Journal of Cell Biology *141*, 359–371.

Knowles, M. K., Barg, S., Wan, L., Midorikawa, M., Chen, X., and Almers, W. (2010). Single secretory granules of live cells recruit syntaxin-1 and synaptosomal associated protein 25 (SNAP-25) in large copy numbers. Proceedings of the National Academy of Sciences of the United States of America *107*, 20810–20815.

Korlach, J., Schwille, P., Webb, W. W., and Feigenson, G. W. (1999). Characterization of lipid bilayer phases by confocal microscopy and fluorescence correlation spectroscopy. PNAS *96*, 8461–8466.

Koseoglu, S., Love, S. a, and Haynes, C. L. (2011). Cholesterol effects on vesicle pools in chromaffin cells revealed by carbon-fiber microelectrode amperometry. Analytical and bioanalytical chemistry *400*, 2963–2971.

Kuo, C., and Hochstrasser, R. M. (2011). Super-resolution microscopy of lipid bilayer phases. Journal of the American Chemical Society *133*, 4664–4667.

Kwik, J., Boyle, S., Fooksman, D., Margolis, L., Sheetz, M. P., and Edidin, M. (2003). Membrane cholesterol, lateral mobility, and the phosphatidylinositol 4,5-bisphosphate-dependent organization of cell actin. Proceedings of the National Academy of Sciences of the United States of America *100*, 13964–13969.

Laage, R., Rohde, J., Brosig, B., and Langosch, D. (2000). A conserved membrane-spanning amino acid motif drives homomeric and supports heteromeric assembly of presynaptic SNARE proteins. The Journal of Biological Chemistry *275*, 17481–17487.

Ladinsky, M. S., Mastronarde, D. N., McIntosh, J. R., Howell, K. E., and Staehelin, L. a (1999). Golgi structure in three dimensions: functional insights from the normal rat kidney cell. The Journal of Cell Biology *144*, 1135–1149.

Lakowicz, J. R. (1999). Principles of Fluorescence Spectroscopy 2nd ed. (New York: Plenum Publishing Corporation).

Lam, A. D., Tryoen-toth, P., Tsai, B., Vitale, N., and Stuenkel, E. L. (2008). SNARE-catalyzed Fusion Events Are Regulated by Syntaxin1A – Lipid Interactions. Molecular Biology of the Cell *19*, 485–497.

Lang, T. (2008). Imaging Ca2+-triggered exocytosis of single secretory granules on plasma membrane lawns from neuroendocrine cells. Methods in molecular biology (Clifton, N.J.) *440*, 51–59.

Lang, T. (2007). SNARE proteins and “membrane rafts”. The Journal of Physiology *585*, 693–698.

Lang, T., Bruns, D., Wenzel, D., Riedel, D., Holroyd, P., Thiele, C., and Jahn, R. (2001). SNAREs are concentrated in cholesterol-dependent clusters that define docking and fusion sites for exocytosis. The EMBO Journal *20*, 2202–2213.

Lang, T., Margittai, M., Hölzler, H., and Jahn, R. (2002). SNAREs in native plasma membranes are active and readily form core complexes with endogenous and exogenous SNAREs. The Journal of Cell Biology *158*, 751–760.

Lang, T., and Rizzoli, S. O. (2010). Membrane protein clusters at nanoscale resolution: more than pretty pictures. Physiology (Bethesda, Md.) *25*, 116–124.

Lang, T., Wacker, I., Steyer, J., Kaether, C., Wunderlich, I., Soldati, T., Gerdes, H. H., and Almers, W. (1997). Ca2+-triggered peptide secretion in single cells imaged with green fluorescent protein and evanescent-wave microscopy. Neuron *18*, 857–863.

Letourneur, F., Gaynor, E. C., Hennecke, S., Démollière, C., Duden, R., Emr, S. D., Riezman, H., and Cosson, P. (1994). Coatomer is essential for retrieval of dilysine-tagged proteins to the endoplasmic reticulum. Cell *79*, 1199–1207.

Li, F., Pincet, F., Perez, E., Eng, W. S., Melia, T. J., Rothman, J. E., and Tareste, D. (2007). Energetics and dynamics of SNAREpin folding across lipid bilayers. Nature structural & molecular biology *14*, 890–896.

Li, L., and Chin, L.-S. (2003). The molecular machinery of synaptic vesicle exocytosis. Cellular and molecular life sciences : CMLS *60*, 942–960.

Lichtenberg, D., Goñi, F. M., and Heerklotz, H. (2005). Detergent-resistant membranes should not be identified with membrane rafts. Trends in biochemical sciences *30*, 430–436.

Lin, R. C., and Scheller, R. H. (1997). Structural Organization of the Synaptic Exocytosis Core Complex. Cell *19*, 1087–1094.

van de Linde, S., Löschberger, A., Klein, T., Heidbreder, M., Wolter, S., Heilemann, M., and Sauer, M. (2011). Direct stochastic optical reconstruction microscopy with standard fluorescent probes. Nature protocols *6*, 991–1009.

Lingwood, D., Ries, J., Schwille, P., and Simons, K. (2008). Plasma membranes are poised for activation of raft phase coalescence at physiological temperature. Proceedings of the National Academy of Sciences of the United States of America *105*, 10005–10010.

Lingwood, D., and Simons, K. (2010). Lipid rafts as a membrane-organizing principle. Science (New York, N.Y.) *327*, 46–50.

Liu, T., Tucker, W. C., Bhalla, A., Chapman, E. R., and Weisshaar, J. C. (2005). SNARE-driven, 25-millisecond vesicle fusion in vitro. Biophysical Journal *89*, 2458–2472.

Llopis, J., McCaffery, J. M., Miyawaki, a, Farquhar, M. G., and Tsien, R. Y. (1998). Measurement of cytosolic, mitochondrial, and Golgi pH in single living cells with green fluorescent proteins. Proceedings of the National Academy of Sciences of the United States of America *95*, 6803–6808.

Loranger, S. S., and Linder, M. E. (2002). SNAP-25 traffics to the plasma membrane by a syntaxin-independent mechanism. The Journal of Biological Chemistry *277*, 34303–34309.

Low, S. H., Vasanji, A., Nanduri, J., He, M., Sharma, N., Koo, M., Drazba, J., and Weimbs, T. (2006). Syntaxins 3 and 4 Are Concentrated in Separate Clusters on the Plasma Membrane before the Establishment of Cell Polarity. Molecular Biology of the cell *17*, 977–989.

Lukyanov, K. A., Chudakov, D. M., Lukyanov, S., and Verkhusha, V. V. (2005). Photoactivatable fluorescent proteins. Nature Reviews Molecular Cell Biology *6*, 885–891.

Lévêque, C., el Far, O., Martin-Moutot, N., Sato, K., Kato, R., Takahashi, M., and Seagar, M. J. (1994). Purification of the N-type calcium channel associated with syntaxin and synaptotagmin. A complex implicated in synaptic vesicle exocytosis. The Journal of Biological Chemistry *269*, 6306–6312.

López, I., Ortiz, J. a, Villanueva, J., Torres, V., Torregrosa-Hetland, C. J., del Mar Francés, M., Viniegra, S., and Gutiérrez, L. M. (2009). Vesicle motion and fusion are altered in chromaffin cells with increased SNARE cluster dynamics. Traffic (Copenhagen, Denmark) *10*, 172–185.

Manders, E. M. M., Verbeek, F. J., and Ate, J. A. (1993). Measurement of co-localization of objects in dual-colour confocal images. Journal of microscopy *169*, 375–382.

Manley, S., Gillette, J. M., Patterson, G. H., Shroff, H., Hess, H. F., Betzig, E., and Lippincott-schwartz, J. (2008). High-density mapping of single-molecule trajectories with photoactivated localization microscopy. Nature Methods *5*, 2007–2009.

Mao, S., Javois, L. C., and Kent, U. M. (1999). Overview of antibody use in immunocytochemistry. Methods in molecular biology *115*, 3–10.

Margittai, M., Fasshauer, D., Jahn, R., and Langen, R. (2003). The Habc domain and the SNARE core complex are connected by a highly flexible linker. Biochemistry *42*, 4009–4014.

Marshall, J., Molloy, R., Moss, G. W., Howe, J. R., and Hughes, T. E. (1995). The jellyfish green fluorescent protein: a new tool for studying ion channel expression and function. Neuron *14*, 211–215.

Martens, S., Kozlov, M. M., and McMahon, H. T. (2007). How Synaptotagmin Promotes Membrane Fusion. Science *316*, 1205–1208.

Matlin, K. S., and Simons, K. (1983). Reduced temperature prevents transfer of a membrane glycoprotein to the cell surface but does not prevent terminal glycosylation. Cell *34*, 233–243.

Matthew, W. D., Tsavaler, L., and Reichardt, L. F. (1981). Identification of a Synaptic Vesicle-Specific Membrane Protein with a Wide Distribution in Neuronal and Neurosecretory Tissue Immunohistochemistry Isolation of Hybridoma Secreting Cell Lines. The Journal of Cell Biology *91*, 257–269.

Maximov, A., Tang, J., Yang, X., Pang, Z. P., and Südhof, T. C. (2009). Complexin controls the force transfer from SNARE complexes to membranes in fusion. Science (New York, N.Y.) *323*, 516–521.

McConnell, H. M., and Radhakrishnan, A. (2003). Condensed complexes of cholesterol and phospholipids. Biochimica et biophysica acta *1610*, 159–173.

McMahon, H. T., Foran, P., Dolly, J. O., Verhage, M., Wiegant, V. M., and Nicholls, D. G. (1992). Tetanus toxin and botulinum toxins type A and B inhibit glutamate, gamma-aminobutyric acid, aspartate, and met-enkephalin release from synaptosomes. Clues to the locus of action. The Journal of Biological Chemistry *267*, 21338–21343.

McMahon, H. T., Missler, M., Li, C., and Südhof, T. C. (1995). Complexins: cytosolic proteins that regulate SNAP receptor function. Cell *83*, 111–119.
McNally, J. G., Karpova, T., Cooper, J., and Conchello, J. a (1999). Three-dimensional imaging by deconvolution microscopy. Methods (San Diego, Calif.) *19*, 373–385.

Mckinney, S. A., Murphy, C. S., Hazelwood, K. L., Davidson, M. W., and Looger, L. L. (2009). A bright and photostable photoconvertible fluorescent protein. Nature methods *6*, 131–133.

Medine, C. N., Rickman, C., Chamberlain, L. H., and Duncan, R. R. (2007). Munc18-1 prevents the formation of ectopic SNARE complexes in living cells. Journal of cell science *120*, 4407–4415.

Van Meer, G. (1989). Lipid traffic in animal cells. Annual review of Cell Biology *5*, 247–275.

Van Meer, G., and Simons, K. (1988). Lipid polarity and sorting in epithelial cells. Journal of Cellular Biochemistry *36*, 51–58.

Van Meer, G., Voelker, D. R., and Feigenson, G. W. (2008). Membrane lipids: where they are and how they behave. Nature reviews. Molecular Cell Biology *9*, 112–124.

Melia, T. J., Weber, T., McNew, J. a, Fisher, L. E., Johnston, R. J., Parlati, F., Mahal, L. K., Sollner, T. H., and Rothman, J. E. (2002). Regulation of membrane fusion by the membrane-proximal coil of the t-SNARE during zippering of SNAREpins. The Journal of Cell Biology *158*, 929–940.

Meyer, A. C., Frank, T., Khimich, D., Hoch, G., Riedel, D., Chapochnikov, N. M., Yarin, Y. M., Harke, B., Hell, S. W., Egner, A., et al. (2009). Tuning of synapse number, structure and function in the cochlea. Nature Neuroscience *12*, 444–453.

Miesenbock, G., De Angelis, D. A., and Rothman, J. E. (1998). Visualizing secretion and synaptic transmission with pH-sensitive green fluorescent proteins. Nature *394*, 192–195.

Milosevic, I., Sørensen, J. B., Lang, T., Krauss, M., Nagy, G., Haucke, V., Jahn, R., and Neher, E. (2005). Plasmalemmal phosphatidylinositol-4,5-bisphosphate level regulates the releasable vesicle pool size in chromaffin cells. The Journal of Neuroscience *25*, 2557–2565.

Minta, A., Kao, J. P., and Tsien, R. Y. (1989). Fluorescent Indicators for Cytosolic Calcium Based on Rhodamine and Fluorescein Chromophores. The Journal of Biological Chemistry *264*, 8171–8178.

Misura, K. M., Scheller, R. H., and Weis, W. I. (2000). Three-dimensional structure of the neuronal-Sec1-syntaxin 1a complex. Nature *404*, 355–362.

Miyawaki, A., Llopis, J., Heim, R., Mccaffery, J. M., Adams, J. A., Ikurak, M., and Tsien, R. Y. (1997). Fluorescent indicators for Ca 2 + based on green fluorescent proteins and calmodulin. Letters to Nature *388*, 882–887.

Mohrmann, R., de Wit, H., Verhage, M., Neher, E., and Sørensen, J. B. (2010). Fast vesicle fusion in living cells requires at least three SNARE complexes. Science (New York, N.Y.) *330*, 502–505.

Morise, H., Shimomura, O., Johnson, F. H., and Winant, J. (1974). Intermolecular energy transfer in the bioluminescent system of Aequorea. Biochemistry *13*, 2656–2662.

Murray, D. H., and Tamm, L. K. (2009). Clustering of syntaxin-1A in model membranes is modulated by phosphatidylinositol 4,5-bisphosphate and cholesterol. Biochemistry *48*, 4617–4625.

Murray, D. H., and Tamm, L. K. (2011). Molecular Mechanism of Cholesterol- and Polyphosphoinositide-Mediated Syntaxin Clustering. Biochemistry *50*, 9014–9022.

Nakazawa, K., Fujimori, K., Takanaka, A., and Inoue, K. (1990). Pheochromocytoma cells. Journal of Physiology *428*, 257–272.

Naren, A., Quick, M. W., Collawn, J. F., Nelson, D. J., and Kirk, K. L. (1998). Syntaxin 1A inhibits CFTR chloride channels by means of domain-specific protein – protein interactions. PNAS *95*, 10972–10977.

Niwa, H., Inouye, S., Hirano, T., Matsuno, T., Kojima, S., Kubota, M., Ohashi, M., and Tsuji, F. I. (1996). Chemical nature of the light emitter of the Aequorea

green fluorescent protein. Proceedings of the National Academy of Sciences of the United States of America *93*, 13617–13622.

Nofal, S., Becherer, U., Hof, D., Matti, U., and Rettig, J. (2007). Primed Vesicles Can Be Distinguished from Docked Vesicles by Analyzing Their Mobility. Analysis *27*, 1386–1395.

Novick, P., Ferro, S., and Schekman, R. (1981). Order of Events in the Yeast Secretory Pathway. Cell *25*, 461–469.

Ohara-Imaizumi, M., Nishiwaki, C., Kikuta, T., Kumakura, K., Nakamichi, Y., and Nagamatsu, S. (2004a). Site of docking and fusion of insulin secretory granules in live MIN6 beta cells analyzed by TAT-conjugated anti-syntaxin 1 antibody and total internal reflection fluorescence microscopy. The Journal of Biological Chemistry *279*, 8403–8408.

Ohara-Imaizumi, M., Nishiwaki, C., Kikuta, T., Nagai, S., Nakamichi, Y., and Nagamatsu, S. (2004b). TIRF imaging of docking and fusion of single insulin granule motion in primary rat pancreatic β-cells : different behaviour of granule motion between normal and Goto – Kakizaki diabetic rat β-cells. The Biochemical Journal *38*, 13–18.

Oheim, M., Loerke, D., Stühmer, W., and Chow, R. H. (1999). Multiple stimulation-dependent processes regulate the size of the releasable pool of vesicles. European biophysics Journal : EBJ *28*, 91–101.

Oheim, M., Loerke, D., Stühmer, W., and Chow, R. H. (1998). The last few milliseconds in the life of a secretory granule. European Biophysics Journal, 83–98.

Oheim, M., and Stühmer, W. (2000). Tracking chromaffin granules on their way through the actin cortex. European Biophysics Journal *29*, 67–89.

Ohtani, Y., Irie, T., Uekama, K., Fukunaga, K., and Pitha, J. (1989). Differential effects of alpha-, beta- and gamma-cyclodextrins on human erythrocytes. European Journal of biochemistry / FEBS *186*, 17–22.

Orci, L., Stamnes, M., Ravazzola, M., Perrelet, A., So, T. H., Rothman, J. E., and Geneva, C.- (1997). Bidirectional Transport by Distinct Populations of COPI-Coated Vesicles. Cell *90*, 335–349.

Ormo, M., Cubitt, A. B., Karen, K., Gross, L. A., Tsien, R. Y., and Remington, J. (1996). Crystal Structure of the Aequorea victoria Green Fluorescent Protein. Science *273*.

Ostenson, C.-G., Gaisano, H., Sheu, L., Tibell, A., and Bartfai, T. (2006). Impaired gene and protein expression of exocytotic soluble N-ethylmaleimide attachment protein receptor complex proteins in pancreatic islets of type 2 diabetic patients. Diabetes *55*, 435–440.

Owen, D. M., Lanigan, P. M. P., Dunsby, C., Munro, I., Grant, D., Neil, M. a a, French, P. M. W., and Magee, A. I. (2006). Fluorescence lifetime imaging provides enhanced contrast when imaging the phase-sensitive dye di-4-ANEPPDHQ in model membranes and live cells. Biophysical Journal *90*, L80–2.

Owen, D. M., Neil, M. a a, French, P. M. W., and Magee, A. I. (2007). Optical techniques for imaging membrane lipid microdomains in living cells. Seminars in cell & developmental biology *18*, 591–598.

Oyler, G. A., Higgins, G. A., Hart, R. A., Battenberg, E., Billingsley, M., Bloom, F. E., and Wilson, M. C. (1989). The Identification of a Novel Synaptosomal-associated Protein, SNAP-25, Differentially Expressed by Neuronal Subpopulations. Cell *109*, 3039–3052.

O'Connor, V., Augustine, G. J., and Betz, H. (1994). Synaptic Vesicle Exocytosis: Molecules and Models. Cell *76*, 757–787.

O'Connor, V., Heuss, C., De Bello, W. M., Dresbach, T., Charlton, M. P., Hunt, J. H., Pellegrini, L. L., Hodel, A., Burger, M. M., Betz, H., et al. (1997). Disruption of syntaxin-mediated protein interactions blocks neurotransmitter secretion. PNAS *94*, 12186–12191.

Palade, G. (1975). Intracellular aspects of the process of protein synthesis. Science (New York, N.Y.) *189*, 867.

Palay, S. L., and Palade, G. E. (1955). The Fine Structure of Neurons. The Journal of biophysical and Biochemical Cytology *1*, 69–88.

Palfreyman, M., Hammarlund, M., Watanabe, S., Olsen, S., and Jorgensen, E. (2006). SNAREs and docking: Is syntaxin alone or is docking SNARE complex formation? Neuronal Development Synaptic Function and Behavior Meeting.

Palm, G. J., Zdanov, A., Gaitanaris, G. A., Stauber, R., Pavlakis, G. N., and Wlodawer, A. (1997). The structural basis for the spectral variations in green fluorescent proteins. Nature structural biology *4*, 361–365.

Pang, Z. P., Sun, J., Rizo, J., Maximov, A., and Südhof, T. C. (2006). Genetic analysis of synaptotagmin 2 in spontaneous and Ca2+-triggered neurotransmitter release. The EMBO Journal *25*, 2039–2050.

Parasassi, T., and Gratton, E. (1995). Membrane Lipid Domains and Dynamics as Detected by Laurdan Fluorescence. Journal of Fluorescence *5*.

Parasassi, T., Gratton, E., Yu, W. M., Wilson, P., and Levi, M. (1997). Two-photon fluorescence microscopy of laurdan generalized polarization domains in model and natural membranes. Biophysical Journal *72*, 2413–2429.

Parasassi, T., De Stasio, G., Ravagnan, G., Rusch, R. M., and Gratton, E. (1991). Quantitation of lipid phases in phospholipid vesicles by the generalized polarization of Laurdan fluorescence. Biophysical Journal *60*, 179–189.

Parasassis, T., Conti, F., Glasers, M., and Gratton, E. (1984). Detection of Phospholipid Phase Separation. The Journal of Biological Chemistry *259*, 14011–14017.

Patterson, G. H., Hirschberg, K., Polishchuk, R. S., Gerlich, D., Phair, R. D., and Lippincott-Schwartz, J. (2008). Transport through the Golgi apparatus by rapid partitioning within a two-phase membrane system. Cell *133*, 1055–1067.

Patterson, G. H., Knobel, S. M., Sharif, W. D., Kain, S. R., and Piston, D. W. (1997). Use of the green fluorescent protein and its mutants in quantitative fluorescence microscopy. Biophysical Journal *73*, 2782–2790.

Patterson, G. H., and Lippincott-Schwartz, J. (2002). A photoactivatable GFP for selective photolabeling of proteins and cells. Science (New York, N.Y.) *297*, 1873–1877.

Patterson, G. H., Piston, D. W., and Barisas, B. G. (2000). Förster distances between green fluorescent protein pairs. Analytical biochemistry *284*, 438–440.

Pawley JB (2006) Handbook of Biological Confocal Microscopy.

Pellizzari, R., Rossetto, O., Lozzi, L., Giovedi, S., Johnson, E., Shone, C. C., and Montecucco, C. (1996). Structural Determinants of the Specificity for Synaptic Vesicle-associated Membrane Protein / Synaptobrevin of Tetanus and Botulinum Type B and G Neurotoxins. Biochemistry *271*, 20353–20358.

Peter, M., Ameer-Beg, S. M., Hughes, M. K. Y., Keppler, M. D., Prag, S., Marsh, M., Vojnovic, B., and Ng, T. (2005). Multiphoton-FLIM quantification of the EGFP-mRFP1 FRET pair for localization of membrane receptor-kinase interactions. Biophysical Journal *88*, 1224–1237.

Pevsner, J., Hsu, S., Braun, J. E. A., Calakos, N., Ting, A. E., Bennett, M. K., and Scheller, R. H. (1994). Specificity and Regulation of a Synaptic Vesicle Docking Complex. Cell *13*, 353–361.

Pike, L. J. (2006). Rafts defined: a report on the Keystone Symposium on Lipid Rafts and Cell Function. Journal of lipid research *47*, 1597–1598.

Plattner, H., Artalejo, A. R., and Neher, E. (1997). Ultrastructural Organization of Bovine Chromaffin Cell Cortex—Analysis by Cryofixation and Morphometry of Aspects Pertinent to Exocytosis. Cell *139*, 1709–1717.

Porter, K. R., Claude, A., and Fullam, E. F. (1945). A study of tissue culture cells by electron microscopy: Methods and preliminary observations. Jounral of exploratory medicine *18*, 233–246.

Pouli, A. E., Emmanouilidou, E., Zhao, C., Wasmeier, C., Hutton, J. C., and Rutter, G. A. (1998). Secretory-granule dynamics visualised in vivo with a phogrin-green fluorescent protein chimaera. Biochem. Journal *199*, 193–199.

Presley, J. F., Cole, N. B., Schroer, T. a, Hirschberg, K., Zaal, K. J., and Lippincott-Schwartz, J. (1997). ER-to-Golgi transport visualized in living cells. Nature *389*, 81–85.

Radhakrishnan, A., Stein, A., Jahn, R., and Fasshauer, D. (2009). The Ca2+ affinity of synaptotagmin 1 is markedly increased by a specific interaction of its C2B domain with phosphatidylinositol 4,5-bisphosphate. The Journal of Biological Chemistry *284*, 25749–25760.

Rahamimoff, R., and Yaari, Y. (1973). Delayed release of transmitter at the frog neuromuscular junction. Journal of Physiology *228*, 241–257.

Rettig, J., Heinemann, C., Ashery, U., Sheng, Z., Yokoyama, C. T., William, A., and Neher, E. (1997). Alteration of Calcium Dependence of Neurotransmitter Release by Disruption of Calcium Channel/Syntaxin Interaction. The Journal of Nueroscience *17*, 6647–6656.

Richards, D. a, Bai, J., and Chapman, E. R. (2005). Two modes of exocytosis at hippocampal synapses revealed by rate of FM1-43 efflux from individual vesicles. The Journal of Cell Biology *168*, 929–939.

Rickman, C., and Davletov, B. (2005). Arachidonic Acid Allows SNARE Complex Formation in the Presence of Munc18. *12*, 545–553.

Rickman, C., and Davletov, B. (2003). Mechanism of Calcium- independent Synaptotagmin Binding to Target SNAREs. Biochemistry, 5501–5504.

Rickman, C., and Duncan, R. R. (2010). Munc18/Syntaxin interaction kinetics control secretory vesicle dynamics. The Journal of Biological Chemistry *285*, 3965–3972.

Rickman, C., Hu, K., Carroll, J., and Davletov, B. (2005). Self-assembly of SNARE fusion proteins into star-shaped oligomers. Society *79*, 75–79.

Rickman, C., Medine, C. N., Bergmann, A., and Duncan, R. R. (2007). Functionally and Spatially Distinct Modes of Munc18-Syntaxin 1 Interaction. Biochemistry *282*, 12097–12103.

Rickman, C., Medine, C. N., Dun, A. R., Moulton, D. J., Mandula, O., Halemani, N. D., Rizzoli, S. O., Chamberlain, L. H., and Duncan, R. R. (2010). t-SNARE protein conformations patterned by the lipid microenvironment. The Journal of Biological Chemistry *285*, 13535–13541.

Rickman, C., Meunier, F. a, Binz, T., and Davletov, B. (2004). High affinity interaction of syntaxin and SNAP-25 on the plasma membrane is abolished by botulinum toxin E. The Journal of Biological Chemistry *279*, 644–651.

Ripley, B. D. (1977). Modelling Spatial Patterns. Journal of the Royal Statistical Society *39*, 172–212.

Robinson, J. P. (2001). Principles of confocal microscopy. Methods in Cell Biology *63*, 89–106.

Rohrbach, a (2000). Observing secretory granules with a multiangle evanescent wave microscope. Biophysical Journal *78*, 2641–2654.

Romoser, V. a, Hinkle, P. M., and Persechini, A. (1997). Detection in living cells of Ca2+-dependent changes in the fluorescence emission of an indicator composed of two green fluorescent protein variants linked by a calmodulin-binding sequence. A new class of fluorescent indicators. The Journal of Biological Chemistry *272*, 13270–13274.

Rossetto, O., Deloyeb, F., Poulainb, B., Pellizzari, R., Schiavo, G., and Montecucco, C. (1995). The metallo-proteinase activity of tetanus and botulism neurotoxins. Journal Physiology *89*, 43–50.

Roth, A. F., Wan, J., Bailey, A. O., Sun, B., Kuchar, J. A., Green, N., Phinney, B. S., Iii, J. R. Y., and Davis, N. G. (2006). Global analysis of Protein Palmitoylation in Yeast. Cell *125*, 1003–1013.

Roth, D., and Burgoyne, R. D. (1994). SNAP-25 is present in a SNARE complex in adrenal chromaffin cells. Nature *351*, 207–210.

Rothman, J. E., and Orci, L. (1992). Molecular dissection of the secretory pathway. Nature *355*, 409–415.

Rothman, J. E., and Wieland, F. T. (1996). Protein Sorting by Transport Vesicles. Advancement Of Science *272*, 227–234.

Rowe, J., Corradi, N., Malosio, M. L., Taverna, E., Halban, P., Meldolesi, J., and Rosa, P. (1999). Blockade of membrane transport and disassembly of the Golgi complex by expression of syntaxin 1A in neurosecretion-incompetent cells: prevention by rbSEC1. Journal of cell science *112 (Pt 1*, 1865–1877.

Rust, M. J., Bates, M., and Zhuang, X. (2006). Imaging by stochastic optical reconstruction microscopy (STORM). Nature Methods *3*, 793–795.

Sakaba, T., Stein, A., Jahn, R., and Neher, E. (2005). Distinct kinetic changes in neurotransmitter release after SNARE protein cleavage. Science (New York, N.Y.) *309*, 491–494.

Salaün, C., Gould, G. W., and Chamberlain, L. H. (2005). Lipid raft association of SNARE proteins regulates exocytosis in PC12 cells. The Journal of Biological Chemistry *280*, 19449–19453.

Sasaki, T. (1996). Phosphorylation of Munc-18/n-Sec1/rbSec1 by Protein Kinase C. Journal of Biological Chemistry *271*, 7265–7268.

Schaub, J. R., Lu, X., Doneske, B., Shin, Y.-K., and McNew, J. A. (2006). Hemifusion arrest by complexin is relieved by Ca2+-synaptotagmin I. Nature Structural & Molecular Biology *13*, 748–750.

Schekman, R., and Orci (1996). Coat Proteins and Vesicle Budding. Science *271*, 1526–1533.

Schermelleh, L., Heintzmann, R., and Leonhardt, H. (2010). A guide to super-resolution fluorescence microscopy. The Journal of Cell Biology *190*, 165–175.

Schiavo, G., Benfenati, F., Poulain, B., Rossetto, O., Polverino De Laureto, P., DasGupta, B. R., and Montecucco, C. (1992). Tetanus and botulinum-B neurotoxins block neurotransmitter release by proteolytic cleavage of synaptobrevin. Nature *359*, 832–835.

Schiavo, G., Gu, Q., Prestwich, G. D., Sollner, T. H., and Rothman, J. E. (1996). Calcium-dependent switching of the specificity of phosphoinositide binding to synaptotagmin. PNAS *93*, 13327–13332.

Schiavo, G., Santucci, a, Dasgupta, B. R., Mehta, P. P., Jontes, J., Benfenati, F., Wilson, M. C., and Montecucco, C. (1993). Botulinum neurotoxins serotypes A and E cleave SNAP-25 at distinct COOH-terminal peptide bonds. FEBS letters *335*, 99–103.

Schnell, U., Dijk, F., Sjollema, K. a, and Giepmans, B. N. G. (2012). Immunolabeling artifacts and the need for live-cell imaging. Nature methods *9*, 152–158.

Shafer, T. J., and Atchison, W. D. (1991). Transmitter, ion channel and receptor properties of pheochromocytoma (PC12) cells: a model for neurotoxicological studies. Neurotoxicology *12*, 473–492.

Shaner, N. C., Steinbach, P. A., and Tsien, R. Y. (2005). A guide to choosing fluorescent proteins. Nature Methods *2*, 905–909.

Shi, L., Shen, Q.-T., Kiel, A., Wang, J., Wang, H.-W., Melia, T. J., Rothman, J. E., and Pincet, F. (2012). SNARE proteins: one to fuse and three to keep the nascent fusion pore open. Science (New York, N.Y.) *335*, 1355–1359.

Shimomura, O., Johnson, F. H., and Saiga, Y. O. (1962). Extraction , Purification and Properties of Aequorin , a Bioluminescent Protein from the Luminous. Journal of Cell and Computational Physiology *59*, 223–239.

Shtengel, G., Galbraith, J. A., Galbraith, C. G., Lippincott-schwartz, J., Gillette, J. M., Manley, S., Sougrat, R., Waterman, C. M., Kanchanawong, P., Davidson, M. W., et al. (2009). Interferometric fluorescent super-resolution microscopy resolves 3D cellular ultrastructure. PNAS *106*, 3125–3130.

Sibarita, J.-B. (2005). Deconvolution Microscopy. In Advances in Biochemical Engineering/Biotechnology (Springer), pp. 1288–1291.

Sieber, J. J., Willig, K. I., Heintzmann, R., Hell, S. W., and Lang, T. (2006). The SNARE Motif Is Essential for the Formation of Syntaxin Clusters in the Plasma Membrane. Biophysical Journal *90*, 2843–2851.

Sieber, J. J., Willig, K. I., Kutzner, C., Gerding-Reimers, C., Harke, B., Donnert, G., Rammner, B., Eggeling, C., Hell, S. W., Grubmüller, H., et al. (2007). Anatomy and dynamics of a supramolecular membrane protein cluster. Science (New York, N.Y.) *317*, 1072–1076.

Silvius, J. R., and Nabi, I. R. (2006). Fluorescence-quenching and resonance energy transfer studies of lipid microdomains in model and biological membranes. Molecular membrane biology *23*, 5–16.

Simons, K., and Ikonen, E. (1997). Functional rafts in cell membranes. Nature *387*, 569–572.

Simons, K., and Van Meer, G. (1988). Lipid sorting in epithelial cells. Biochemistry *27*, 6197–6202.

Simons, K., and Van Meers, G. (1988). Lipid Sorting in Epithelial Cells. Perspectives in Biochemistry *27*, 6197–6202.

Simons, K., and Vaz, W. L. C. (2004). Model systems, lipid rafts, and cell membranes. Annual review of biophysics and biomolecular structure *33*, 269–295.

Singer, C. (1914). Notes on the Early History of Microscopy. Proceedings of the Royal Society of Medicine *7*, 247–279.

Singer, S. J., and Nicolson, G. L. (1972). The fluid mosaic model of the structure of cell membranes. Science *175*, 720–731.

Sinha, R., Ahmed, S., Jahn, R., and Klingauf, J. (2011). Two synaptobrevin molecules are sufficient for vesicle fusion in central nervous system synapses. PNAS.

Stevens, D. R., Schirra, C., Becherer, U., and Rettig, J. (2011). Vesicle pools: lessons from adrenal chromaffin cells. Frontiers in synaptic Neuroscience *3*, 2.

Steyer, J. A., and Almers, W. (1999). Tracking Single Secretory Granules in Live Chromaffin Cells by Evanescent-Field Fluorescence Microscopy. Biophysical Journal *76*, 2262–2271.

Steyer, J. a, and Almers, W. (2001). A real-time view of life within 100 nm of the plasma membrane. Nature reviews. Molecular Cell Biology *2*, 268–275.

Steyer, J. a, Horstmann, H., and Almers, W. (1997). Transport, docking and exocytosis of single secretory granules in live chromaffin cells. Nature *388*, 474–478.

Stout, A. L., and Axelrod, D. (1989). Evanescent field excitation of fluorescence by epi-illumination microscopy. Applied Optics *28*, 5237–5242.

Stryer, L. (1978). Fluorescence energy transfer as a spectroscopic ruler. Annual review of biochemistry *47*, 819–846.

Subach, F. V., Patterson, G. H., Manley, S., Gillette, J. M., Lippincott-schwartz, J., and Verkhusha, V. V. (2009). Photoactivatable mCherry for high-resolution two-color fluorescence microscopy. Nature methods *6*, 153–160.

Sutton, R. B., Fasshauer, D., Jahn, R., and Brunger, A. T. (1998). Crystal structure of a SNARE complex involved in synaptic resolution exocytosis at 2 . 4 Å. Nature *395*, 347–353.

Söllner, T., Bennett, M. K., Whiteheart, S. W., Scheller, R. H., and Rothman, J. E. (1993a). A Protein Assembly-Disassembly Pathway In Vitro That May Correspond to Sequential Steps of Synaptic Vesicle Docking , Activation and Fusion. Cell *75*, 409–418.

Söllner, T., Whiteheart, S. W., Brunner, M., Erdjument-Bromage, H., Geromanos, S., Tempst, P., and Rothman, J. E. (1993b). SNAP receptors implicated in vesicle targeting and fusion. Nature *362*, 318–324.

Sørensen, J. B., Wiederhold, K., Müller, E. M., Milosevic, I., Nagy, G., de Groot, B. L., Grubmüller, H., and Fasshauer, D. (2006). Sequential N- to C-terminal SNARE complex assembly drives priming and fusion of secretory vesicles. The EMBO Journal *25*, 955–966.

Tagaya, M., Genma, T., Yamamoto, A., and Kozaki, S. (1996). SNAP-25 is present on chromaffin granules and acts as a S N A P receptor. Neuron *394*, 83–86.

Tang, J., Maximov, A., Shin, O.-H., Dai, H., Rizo, J., and Südhof, T. C. (2006). A complexin/synaptotagmin 1 switch controls fast synaptic vesicle exocytosis. Cell *126*, 1175–1187.

Taraska, J. W., Perrais, D., Ohara-imaizumi, M., Nagamatsu, S., and Almers, W. (2003). Secretory granules are recaptured largely intact after stimulated exocytosis in cultured endocrine cells. PNAS *100*, 2070–2075.

Tellam, J., McIntosh, S., and James, D. E. (1995). Molecular Identification of Two Novel Munc-18 Isoforms Expressed in Non-neuronal Tissues. The Journal of Biological Chemistry *270*, 5857–5863.

Thompson, P. M., Egbufoama, S., and Vawter, M. P. (2003). SNAP-25 reduction in the hippocampus of patients with schizophrenia. Progress in neuro-psychopharmacology & biological psychiatry *27*, 411–417.

Thureson-Klein, A. (1983). Exocytosis from large and small dense-cored vesicles in noradrenergic nerve terminals. Neuroscience *10*, 245–259.

Tomatis, V. M., Papadopulos, A., Malintan, N. T., Martin, S., Wallis, T., Gormal, R. S., Kendrick-Jones, J., Buss, F., and Meunier, F. a (2013). Myosin VI small insert isoform maintains exocytosis by tethering secretory granules to the cortical actin. The Journal of cell biology *200*, 301–320.

Toonen, R. F., Kochubey, O., Wit, H. D., Gulyas-kovacs, A., Konijnenburg, B., Sørensen, J. B., Klingauf, J., and Verhage, M. (2006). Dissecting docking and tethering of secretory vesicles at the target membrane. EMBO Journal, 3725–3737.

Traub, L. M., and Kornfeld, S. (1997). The trans-Golgi network: a late secretory sorting station. Current opinion in Cell Biology *9*, 527–533.

Tsien, R. Y. (1998). The green fluorescent protein. Annual review of biochemistry *67*, 509–544.

Tsuboi, T., Kitaguchi, T., Karasawa, S., Fukuda, M., and Miyawaki, A. (2010). Age-dependent Preferential Dense-Core Vesicle Exocytosis in Neuroendocrine Cells Revealed by Newly Developed Monomeric Fluorescent Timer Protein. Molecular Biology of the Cell *21*, 87–94.

Tsuji, A., Kawasaki, K., Ohnishi, S., Merkle, H., and Kusumi, A. (1988). Regulation of band 3 mobilities in erythrocyte ghost membranes by protein association and cytoskeletal meshwork. Biochemistry *27*, 7447–7452.

Valenstein, E. S. (2002). The discovery of chemical neurotransmitters. Brain and cognition *49*, 73–95.

Varma, R., and Mayor, S. (1998). GPI-anchored proteins are organized in submicron domains at the cell surface. Nature *394*, 798–801.

Verhage, M., Vries, K., Røshol, H., Burbach, J. P. H., Gispen, W. H., and Sudhof, T. C. (1997). DOC2 Proteins in Rat Brain : Complementary Distribution and Proposed Function as Vesicular Adapter Proteins in Early Stages of Secretion. Cell *18*, 453–461.

Voets, T., Moser, T., Lund, P., Chow, R. H., Geppert, M., Su, T. C., and Neher, E. (2001). Intracellular calcium dependence of large dense-core vesicle exocytosis in the absence of synaptotagmin I. PNAS.

Voets, T., Neher, E., and Moser, T. (1999). Mechanisms underlying phasic and sustained secretion in chromaffin cells from mouse adrenal slices. Neuron *23*, 607–615.

Vogel, K., Cabaniols, J., and Roche, P. A. (2000). Targeting of SNAP-25 to Membranes Is Mediated by Its Association with the Target SNARE Syntaxin. *275*, 2959–2965.

Wang, J., and Richards, D. a (2011). Spatial regulation of exocytic site and vesicle mobilization by the actin cytoskeleton. PloS one *6*, e29162.

Wang, L., Bittner, M. A., Axelrod, D., and Holz, R. W. (2008). The Structural and Functional Implications of Linked SNARE Motifs in SNAP25. Molecular Biology of the Cell *19*, 3944–3955.

Wang, T., Smith, E. a, Chapman, E. R., and Weisshaar, J. C. (2009). Lipid mixing and content release in single-vesicle, SNARE-driven fusion assay with 1-5 ms resolution. Biophysical Journal *96*, 4122–4131.

Wang, Y., Thiele, C., and Huttner, W. B. (2000). Cholesterol is required for the formation of regulated and constitutive secretory vesicles from the trans-Golgi network. Traffic *1*, 952–962.

Warashina, a, and Ogura, T. (2004). Modeling of stimulation-secretion coupling in a chromaffin cell. Pflügers Archiv : European Journal of Physiology *448*, 161–174.

Washbourne, P., Cansino, V., Mathews, J. R., Graham, M., Burgoyne, R. D., and Wilson, M. C. (2001). Cysteine residues of SNAP-25 are required for SNARE disassembly and exocytosis, but not for membrane targeting. Biochem. Journal *357*, 625–634.

Weber, G., and Farris, F. J. (1979). Synthesis and spectral properties of a hydrophobic fluorescent probe: 6-propionyl-2-(dimethylamino)naphthalene. Biochemistry *18*, 3075–3078.

Weber, P., Wagner, M., and Schneckenburger, H. (2010). Fluorescence imaging of membrane dynamics in living cells. Journal of biomedical optics *15*, 046017.

Weber, T., Zemelman, B. V., Mcnew, J. A., Westermann, B., Gmachl, M., Parlati, F., So, T. H., and Rothman, J. E. (1998). SNAREpins : Minimal Machinery for Membrane Fusion. Cell *92*, 759–772.

Weimbs, T., Hui Low, S., Chapin, S., Mostov, K., Bucher, P., and Hofman, K. (1997). A conserved domain is present in different families of vesicular fusion proteins : A new superfamily. Cell *94*, 3046–3051.

Wendler, F., Page, L., Urbe, S., and Tooze, S. A. (2001). Homotypic Fusion of Immature Secretory Granules During Maturation Requires Syntaxin 6. Molecular Biology of the Cell *12*, 1699–1709.

Weninger, K., Bowen, M. E., Choi, U. B., Chu, S., and Brunger, A. T. (2008). Accessory Proteins Stabilize the Acceptor Complex for Synaptobrevin , the 1 : 1 Syntaxin / SNAP-25 Complex. Structure, 308–320.

Westerink, R. H. S., and Ewing, G. (2009). The PC12 cell as a model for neurosecretion. Acta Physiology *192*, 273–285.

Westphal, V., Rizzoli, S. O., Lauterbach, M. a, Kamin, D., Jahn, R., and Hell, S. W. (2008). Video-rate far-field optical nanoscopy dissects synaptic vesicle movement. Science (New York, N.Y.) *320*, 246–249.

Whyte, J. R. C., and Munro, S. (2002). Vesicle tethering complexes in membrane traffic. Journal of cell science *115*, 2627–2637.

Wiedenmann, J., Ivanchenko, S., Oswald, F., Schmitt, F., Röcker, C., Salih, A., Spindler, K.-D., and Nienhaus, G. U. (2004). EosFP, a fluorescent marker protein with UV-inducible green-to-red fluorescence conversion. Proceedings of the National Academy of Sciences of the United States of America *101*, 15905–15910.

Willig, K. I., Rizzoli, S. O., Westphal, V., Jahn, R., and Hell, S. W. (2006). STED microscopy reveals that synaptotagmin remains clustered after synaptic vesicle exocytosis. Nature *440*, 935–939.

De Wit, H., Walter, A. M., Milosevic, I., Gulyas-Kovacs, A., Riedel, D., Sorensen, J. B., and Verhage, M. (2009). Synaptotagmin-1 Docks Secretory Vesicles to Syntaxin-1 / SNAP-25 Acceptor Complexes. Cell *138*, 935–946.

de Wit, H. (2010). Morphological docking of secretory vesicles. Histochemistry and Cell Biology *134*, 103–113.

de Wit, H., Cornelisse, L. N., Toonen, R. F. G., and Verhage, M. (2006). Docking of secretory vesicles is syntaxin dependent. PloS one *1*, e126.

Wu, M. N., Schulze, K. L., Lloyd, T. E., and Bellen, H. J. (2001). The ROP-Syntaxin interaction inhibits neurotransmitter release. European Journal of Cell Biology *80*, 196–199.

Wu, Y., Gu, Y., Morphew, M. K., Yao, J., Yeh, F. L., Dong, M., and Chapman, E. R. (2012a). All three components of the neuronal SNARE compelx contribute to secretory vesicle docking. The Journal of Cell Biology *198*, 323–330.

Wu, Y., Gu, Y., Morphew, M. K., Yao, J., Yeh, F. L., Dong, M., and Chapman, E. R. (2012b). All three components of the neuronal SNARE complex contribute to secretory vesicle docking. The Journal of Cell Biology *198*, 323–330.

Xia, S., Xu, L., Bai, L., Xu, Z.-Q. D., and Xu, T. (2004). Labeling and dynamic imaging of synaptic vesicle-like microvesicles in PC12 cells using TIRFM. Brain Research *997*, 159–164.

Xu, T., Binz, T., Niemann, H., and Neher, E. (1998). Multiple kinetic components of exocytosis distinguished by neurotoxin sensitivity. America *1*.

Xu, T., Rammner, B., Margittai, M., Artalejo, a R., Neher, E., and Jahn, R. (1999). Inhibition of SNARE complex assembly differentially affects kinetic components of exocytosis. Cell *99*, 713–722.

Yang, L., Dun, A. R., Martin, K. J., Qiu, Z., Dunn, A., Lord, G. J., Lu, W., Duncan, R. R., and Rickman, C. (2012a). Secretory Vesicles Are Preferentially Targeted to Areas of Low Molecular SNARE Density. PLoS ONE *7*, e49514.

Yang, L., Qiu, Z., Greenaway, A. H., and Lu, W. (2012b). A new framework for particle detection in low-SNR fluorescence live-cell images and its application for improved particle tracking. IEEE transactions on bio-medical engineering *59*, 2040–2050.

Yang, Y., and Gillis, K. D. (2004). A highly Ca2+-sensitive pool of granules is regulated by glucose and protein kinases in insulin-secreting INS-1 cells. The Journal of general Physiology *124*, 641–651.

Yang, Z., Li, H., Chai, Z., Fullerton, M. J., Cao, Y., Toh, B. H., Funder, J. W., and Liu, J. P. (2001). Dynamin II regulates hormone secretion in neuroendocrine cells. The Journal of Biological Chemistry *276*, 4251–4260.

Yu, W., So, P., French, T., and Gratton, E. (1996). Fluorescence generalized polarization of cell membranes: a two-photon scanning microscopy approach. Biophysical Journal *70*, 626–636.

Zacharias, D. a, Violin, J. D., Newton, A. C., and Tsien, R. Y. (2002). Partitioning of lipid-modified monomeric GFPs into membrane microdomains of live cells. Science (New York, N.Y.) *296*, 913–916.

Zenisek, D., Steyer, J. a, and Almers, W. (2000). Transport, capture and exocytosis of single synaptic vesicles at active zones. Nature *406*, 849–854.

Zhang, J., Xue, R., Ong, W.-Y., and Chen, P. (2009a). Roles of cholesterol in vesicle fusion and motion. Biophysical Journal *97*, 1371–1380.

Zhang, J. Z., Davletov, B. A., Sqdhof, T. C., and Anderson, R. G. W. (1994). Synaptotagmin I Is a High Affinity Receptor for Clathrin AP-2 : Implications for Membrane Recycling. Cell *78*, 751–760.

Zhang, Z., Hui, E., Chapman, E. R., and Jackson, M. B. (2009b). Phosphatidylserine Regulation of Calcium -triggered Exocytosis and Fusion Pores in PC12 Cells. Molecular Biology of the Cell *20*, 5086–5095.

Zilly, F. E., Sørensen, J. B., Jahn, R., and Lang, T. (2006). Munc18-Bound Syntaxin Readily Forms SNARE Complexes with Synaptobrevin in Native Plasma Membranes. October *4*.

Zimmer, M. (2002). Green fluorescent protein (GFP): applications, structure, and related photophysical behavior. Chemical reviews *102*, 759–781.

Zucker, R. S. (1996). Exocytosis: a molecular and physiological perspective. Neuron *17*, 1049–1055.

Publications:

⌘ *Author's Choice*

THE JOURNAL OF BIOLOGICAL CHEMISTRY VOL. 285, NO. 18, pp. 13535–13541, April 30, 2010

t-SNARE Protein Conformations Patterned by the Lipid Microenvironment*[S]

Received for publication, December 14, 2009, and in revised form, January 12, 2010 Published, JBC Papers in Press, January 21, 2010, DOI 10.1074/jbc.M109.091058

Colin Rickman[**1], **Claire N. Medine**[‡1], **Alison R. Dun**[‡], **David J. Moulton**[‡], **Ondřej Mandula**[§], **Nagaraj D. Halemani**[¶2], **Silvio O. Rizzoli**[‖], **Luke H. Chamberlain**[‡], **and Rory R. Duncan**[‡3]

From the [‡]*Centre for Integrative Physiology and the* [§]*Institute for Adaptive and Neural Computation, School of Informatics, University of Edinburgh, Edinburgh EH8 9XD, Scotland, United Kingdom, the* [¶]*Department of Neurobiology, Max-Planck-Institute for Biophysical Chemistry, Am Fassberg 11, 37077 Göttingen, Germany, the* [‖]*European Neuroscience Institute, Grisebachstrasse 5, 37077 Göttingen, Germany, and the* [**]*Department of Chemistry, School of Engineering and Physical Sciences, Heriot-Watt University, Edinburgh EH14 4AS, Scotland, United Kingdom*

The spatial distribution of the target (t-)SNARE proteins (syntaxin and SNAP-25) on the plasma membrane has been extensively characterized. However, the protein conformations and interactions of the two t-SNAREs *in situ* remain poorly defined. By using super-resolution optical techniques and fluorescence lifetime imaging microscopy, we observed that within the t-SNARE clusters syntaxin and SNAP-25 molecules interact, forming two distinct conformations of the t-SNARE binary intermediate. These are spatially segregated on the plasma membrane with each cluster exhibiting predominantly one of the two conformations, representing the two- and three-helical forms previously observed *in vitro*. We sought to explain why these two t-SNARE intermediate conformations exist in spatially distinct clusters on the plasma membrane. By disrupting plasma membrane lipid order, we found that all of the t-SNARE clusters now adopted a single conformational state corresponding to the three helical t-SNARE intermediates. Together, our results define spatially distinct t-SNARE intermediate states on the plasma membrane and how the conformation adopted can be patterned by the underlying lipid environment.

The soluble NSF attachment protein receptor (SNARE)[4] proteins form a highly conserved family with a central role in the fusion of lipid membranes in both intracellular trafficking and exocytosis. They are well characterized at the atomic structure, domain organization, interaction stoichiometry, and gross membrane localization levels (1–6). In exocytosis, their function relies on the pairing of t-SNAREs (syntaxin and SNAP-25) on the plasma membrane with a vesicle SNARE (synaptobrevin). The t-SNAREs have been observed to colocalize in clusters on the plasma membrane and have been proposed to define the sites of exocytosis (4, 7, 8). Morphological characterization of these t-SNARE clusters has mirrored the advancements in optical microscopy from the diffraction-limited identification of 200–400-nm t-SNARE clusters (7–9) to the observation of 50-nm assemblies using STED microscopy (10). In addition to observing t-SNARE membrane organization, several studies have sought to uncover the mechanisms driving t-SNARE cluster formation. Lipid order has been shown to play a role in t-SNARE cluster organization using sheets of plasma membrane (7). SNAP-25, which has a palmitoylated cysteine-rich linker region essential for membrane targeting (3), may be directed to ordered cholesterol-rich regions in the plasma membrane (11); however, *in vitro*, the individual t-SNAREs were shown to absolutely prefer disordered lipid domains (12). These findings led to the hypothesis that plasma membrane t-SNARE protein clusters may be maintained by membrane rafts (13) or other cholesterol-dependent domains (7) by either sequestration or exclusion. Recently, however, syntaxin self-association has been proposed as a major factor in membrane protein cluster organization (10, 14), implying that SNARE proteins can self-organize into clusters by virtue of their inherent properties. From these studies, the ability of the t-SNAREs to interact *in vitro* and to form clusters at the plasma membrane is not in doubt, but the protein-protein interactions within these clusters remains elusive.

EXPERIMENTAL PROCEDURES

Cell culture reagents were supplied by Invitrogen. Anti-SNAP-25 (SMI81) was obtained from Sternberger Monoclonals (Lutherville, MD). Anti-syntaxin1a (HPC-1) was supplied by Sigma. The rabbit anti-syntaxin1a was a generous gift from Dr. Bazbek Davletov (Laboratory of Molecular Biology, Cambridge, UK). Anti-mouse IgG and anti-rabbit IgG conjugated to Alexafluor-647 or Alexafluor-488, propidium iodide, and calcein AM were obtained from Invitrogen. Protease inhibitor tablets were from Roche Applied Science. All other reagents were obtained from Sigma.

Cell Culture—Neuroblastoma 2a cells were grown in Dulbecco's modified Eagle's medium supplemented with 10% fetal

* This work was supported by Wellcome Trust grants (to R. R. D. and L. H. C.).
⌘ *Author's Choice*—Final version full access.
[S] The on-line version of this article (available at http://www.jbc.org) contains supplemental Figs. 1–3, Movie 1, and an additional reference.
[1] Both authors contributed equally to this work.
[2] Present address: LIMES-Ins., Lab. of Membrane Biochemistry, University of Bonn, 53115 Bonn, Germany.
[3] To whom correspondence should be addressed: Centre for Integrative Physiology, University of Edinburgh, Hugh Robson Bldg., George Square, Edinburgh EH8 9XD, Scotland, UK. Tel.: 44-131-651-1512; Fax: 44-131-650-3128; E-mail: rory.duncan@ed.ac.uk.
[4] The abbreviations used are: SNARE, soluble NSF attachment protein receptor; t-SNARE, target SNARE; FRET, fluorescence resonance energy transfer; EYFP, enhanced yellow fluorescent protein; MβCD, methyl-β-cyclodextrin; PALM, photoactivatable localization microscopy; STED, stimulated emission depletion; FLIM, fluorescence lifetime imaging microscopy; TCSPC, time correlated single photon counting; GP, generalized polarization; BoNT/E, botulinum neurotoxin serotype E.

bovine serum, 10 mM L-glutamine, 50 units of penicillin, 50 μg/ml streptomycin and maintained at 37 °C in 5% (v/v) CO_2, 95% (v/v) air. Pheochromocytoma (PC-12) cells were grown in RPMI 1640 medium supplemented with 10% horse serum, 5% fetal bovine serum, 10 mM Glutamax (Invitrogen), 50 μg/ml gentamicin and maintained at 37 °C in 7.5% (v/v) CO_2, 92.5% (v/v) air. Transfections were performed using ExGen 500 (Fermentas) or Lipofectamine 2000 (Invitrogen). To deplete cholesterol, cells were incubated with 10 mM methyl-β-cyclodextrin (MβCD) in serum-free medium for 15–30 min at 37 °C. To assess cell viability following cholesterol depletion, both propidium iodide and calcein AM (Invitrogen) were added to a final concentration of 3 μM, incubated for 5 min, and then imaged immediately. Live cells were maintained on a heated stage (37 °C) in a chamber containing 5% (v/v) CO_2, 95% (v/v) air during imaging.

Vectors and Transfection—The vector pEGFP-C2 was obtained from Clontech. An EYFP-SNAP-25 fusion was generated by ligation of SNAP-25-(1–206) into BamHI/EcoRI sites of pEGFP-C, followed by the replacement of enhanced green fluorescent protein with EYFP. SNAP-25-EGFP in pEGFP-N1 was a gift from M. Linder. The plasmid pmCerulean-syntaxin1a-(1–288), was described previously (15). Plasmids encoding PACherry-SNAP-25-(1–206) and PACherry-syntaxin1a-(1–288) were generated from the plasmids above by replacement of DNA encoding EYFP or mCerulean with PACherry using AgeI/BsrGI. All cells were cultured on glass coverslips, and transfections were performed using ExGen500 (Fermentas).

Cellular Labeling Procedures—To label cholesterol, neuroblastoma 2a cells were rinsed in phosphate-buffered saline and fixed with 4% (w/v) paraformaldehyde on ice for 30 min. Following phosphate-buffered saline washes, cells were incubated with filipin (50 μg/ml) with 10% (v/v) fetal bovine serum for 2 h. Filipin fluorescence was excited using a titanium sapphire two-photon laser at 780 nm. The same settings were employed for all samples so that their relative staining intensities could be compared. To quantify lipid order, we used laurdan (6-dodecanoyl-2-dimethylaminonaphthalene; Invitrogen) as described previously (16), except that 780-nm two-photon excitation was used.

Confocal Laser Scanning Microscopy and Image Analysis—All images were acquired on a Zeiss Axiovert 100 M confocal microscope fitted with an LSM510 scanning head. Images were sampled at the Nyquist sampling frequency with the photomultiplier tube detector gain and amplifier offset adjusted so that voxel intensities were spread over the full dynamic range. All three-dimensional image data were deconvolved using Huygens software (Scientific Volume Imaging, Hilversum, The Netherlands), using a theoretical or measured point spread function, prior to further analysis.

Photoactivatable Localization Microscopy (PALM)—PALM data (supplemental Fig. 1) were acquired from fixed cells transfected with constructs expressing either SNAP-25 or syntaxin fused to PACherry. Cycles of brief activation at 405 nm, followed by rapid imaging in total internal reflection fluorescence microscopy mode at 561 nm were performed using an Olympus IX-81 microscope equipped with the Olympus Cell-R acquisition software and an ImageEM EM-CCD 512 × 512 camera (Hamamatsu UK). All PALM imaging used an Olympus 150X UApo 1.45NA oil lens with a resulting pixel size of 106 nm. Activation and bleaching steps in each cycle were optimized to ensure a sparse distribution of single molecules was activated and photo-destroyed during each cycle. PALM data analysis was performed using a Matlab routine written by Dr. Samuel Hess (Maine). Spatial distributions of localized single molecules were analyzed using Ripley's analyses using custom-written algorithms in Matlab (Mathworks, Inc., Cambridge, UK).

Preparation of Plasma Membrane Sheets and Immunostaining for STED Microscopy—For the STED experiments, cells were plated onto polylysine-coated glass coverslips and grown between 36 and 40 h. The plated cells were then incubated with or without 10 mM MβCD (Sigma) in Dulbecco's modified Eagle's medium (Invitrogen) at 37 °C for 15 min. After treatment, the cells were sonicated as described previously (17) using a 100-ms ultrasound pulse in ice-cold KGlu sonication buffer (120 mM potassium glutamate, 20 mM potassium acetate, 10 mM EGTA, and 20 mM HEPES, pH 7.2) and fixed in 4% paraformaldehyde in phosphate-buffered saline for 1 h. Paraformaldehyde was quenched using 50 mM NH_4Cl in phosphate-buffered saline for 20 min and immunostained for endogenous syntaxin1a and synaptobrevin-2 using mouse monoclonal HPC-1 (Sigma) and rabbit polyclonal antiserum (Synaptic Systems). Primary antibodies were detected using goat anti-rabbit Cy3 (Dianova) and Atto647N-labeled sheep anti-mouse (provided by Dept. of Nanobiophotonics, Max-Planck Institute for Biophysical Chemistry, Göttingen, Germany) essentially as described previously (7). The samples were embedded in Mowiol (Merck) before imaging.

STED Microscopy—The samples were imaged using a TCS-STED (Leica Microsystems) super-resolution fluorescence microscope equipped with a 1.4 NA ×100 objective. Multichannel confocal images of immunostained plasma membrane sheets were then obtained simultaneously (at 100-Hz scan speed) for Cy3 (synaptobrevin 2) and Atto647N (syntaxin1a) followed by imaging Atto647N applying STED resolution (at 10-Hz scan speed). Pixel size was 21.6 nm. STED excitation was performed with a 635-nm diode laser, and depletion was achieved via a MaiTai tunable laser (Spectra-Physics) at 750 nm. Emission was collected at 645–720 nm for the Atto647N and at 551–602 nm for Cy3. Confocal imaging was performed using photomultiplier tubes, and an avalanche photodiode was used for STED image acquisition. The system resolution limit was ~70–90 nm, measured by analysis of 20 nm crimson-fluorescent beads (Invitrogen). Metamorph (Universal Imaging) was used for the alignment of confocal and STED images. The Cy3- and STED-resolved channels were aligned using the alignment of the Atto647N STED image to the Atto647N confocal image as reference.

Fluorescence Lifetime Imaging Microscopy and Analysis—Time-correlated single photon counting (TCSPC) measurements were made under 800–820-nm two-photon excitation that efficiently excited cerulean, without any detectable direct excitation or emission from EYFP, using a fast photomultiplier tube (H7422; Hamamatsu Photonics UK) coupled directly to the rear port of the Axiovert microscope (supplemental Figs. 3 and 4). Full frame TCSPC recordings were acquired between 30 and 60 s, with mean photon counts between 10^5 and

10^6 counts/s. Images were recorded at 256 × 256 pixels from a 1024 × 1024 image scan with 256 time bins over a 12-ns period. Off-line FLIM data analysis used pixel-based fitting software (SPCImage, Becker & Hickl). The optimization of the fit parameters was performed by using the Levenberg-Marquardt algorithm, minimizing the weighted χ^2 quantity. As controls for nonspecific FRET, or FRET between green fluorescent proteins that may form dimers spontaneously when overexpressed in cells, we determined the fluorescence lifetimes of cerulean-Syx-(1–288) alone, cerulean alone, or cerulean-Syx-(1–288) cotransfected with EYFP (15). No FRET was detected in any of these experiments.

RESULTS

We first examined the localization of single molecules of SNAP-25 (Fig. 1*a*, *upper panels*) in PC12 cells. Using PALM (18, 19) (supplemental Fig. 1 and supplemental movie 1), allowing nanoscale localization of proteins, we found single molecules of SNAP-25 are not distributed homogeneously across the plasma membrane (Fig. 1*a*). Similarly, syntaxin1a molecules are concentrated into ensembles interspersed with largely single molecules (Fig. 1*a*, *lower panels*). Statistical analysis of the spatial distributions of these molecules was performed. Hopkin's statistics compares the nearest neighbor distances from a random subset of data events to the nearest neighbor distances from points placed at random in the data to be tested (20, 21). We thus compared the *XY* coordinates of single t-SNARE molecules to synthetic data exhibiting complete spatial randomness, finding that single SNARE molecules are subject to higher order organization into clusters (data not shown). Furthermore, Ripley's K and L function analyses (Fig. 1*b*) (22) of these datasets revealed that the molecular spatial organization of SNAP-25 and syntaxin1a is nonrandom. Together, these data demonstrate higher order organization of the t-SNAREs in the living plasma membrane at the molecular level. PALM cannot provide an exact measure of the number of molecules in a region as it can never be known that every molecule has been counted (18); however, it can provide a lower limit for the number of molecules per unit area. Our data provided an estimate of ~30–40 syntaxin molecules in an area covered by a 50-nm diameter spot (over the dense ensembles). This complements a recent study (10), using another super-resolution imaging technique, STED, in combination with molecular modeling that predicted 70 molecules per 50-nm cluster. PALM allows the further localization of single molecules within and between these macromolecular assemblies. To test whether the distributions of these two proteins overlap, we quantified the covariance of SNAP-25 and syntaxin1a, finding a high degree of overlap (>86%; supplemental Fig. 2).

Super-resolution optical approaches lack sufficient resolution to provide insight into protein interactions at the molecular level. Therefore, we quantified the interaction between SNAP-25 and syntaxin using TCSPC-FLIM (for explanation of FLIM analysis and presentation see supplemental Fig. 3), an imaging spectroscopy approach we used previously to measure SNARE protein interactions in living cells (15, 23, 24). FLIM has the advantage that it delivers data unaffected by donor or acceptor concentration, the emission light path, sample scatter,

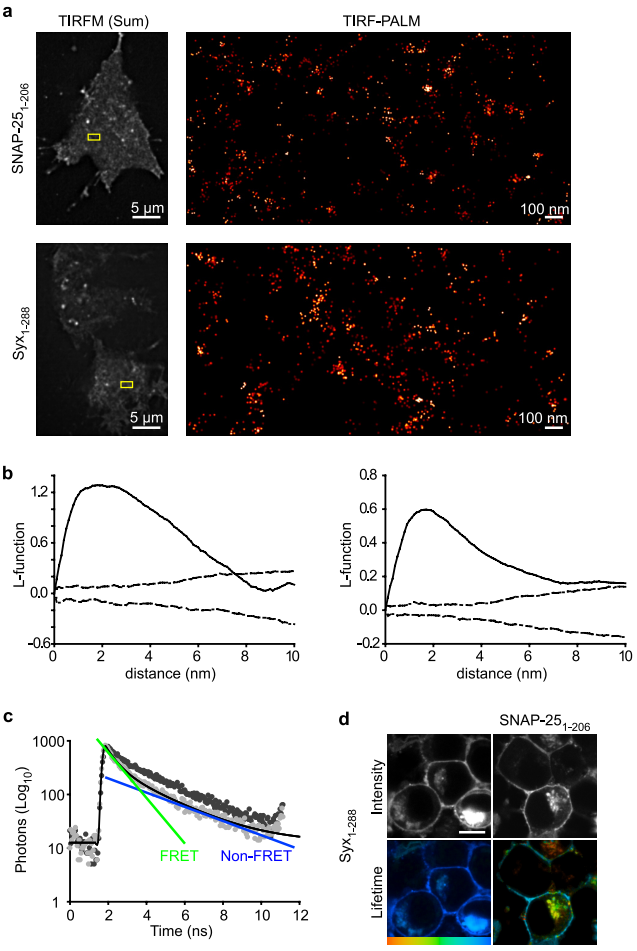

FIGURE 1. **Syntaxin and SNAP-25 molecules interact in clusters on the plasma membrane.** *a,* TIRF-PALM localization map showing single molecules of SNAP-25 and syntaxin (Syx-(1–288)) on the plasma membrane. The *boxed area* highlighted in the summed total internal reflection fluorescence microscopy image (*left panels*) is zoomed in the TIRF-PALM-rendered image (*right panels*), where molecular clustering is clearly visible. *b,* L-function is a commonly used transformation of Ripley's K function and transforms spatially random data into a straight line. Representative L-function plots are shown for syntaxin (*right*) and SNAP-25 (*left*). Each representative dataset, consisting of *XY* coordinates describing the precise localization of individual t-SNARE molecules, was repeatedly randomized, and the L-function was re-derived. Confidence envelopes showing the maximum and minimum L-function values from 1000 randomizations are shown (*dashed line*). This approach thus compares the L-function between experimental data and an identical number and density of random points. Values above the confidence envelopes indicate nonrandom spatial organization. *c,* TCSPC-FLIM analysis confirmed that a syntaxin fluorescent donor (cerulean-syntaxin) followed a single fluorescence decay (*dark gray*). In the presence of a proximal acceptor (EYFP-SNAP-25), this decay was described by a bi-exponential decay (*light gray*). The time constants of the bi-exponential functions correspond to a short FRET lifetime (*green*) and a longer fluorescence lifetime identical to the non-FRET control (*blue*). Both the FRET and non-FRET components are present in every region of the cell in varying proportions. *d,* TCSPC-FLIM of a cell containing cerulean-syntaxin alone (*left panels*) or in the presence of EYFP-SNAP-25 (*right panels*) showing intensity (*gray scale*) and lifetime on a color scale from 1250 to 2250 ps. The lifetime of syntaxin is shortened in the presence of SNAP-25 indicating an interaction. All *scale bars* are 5 μm unless otherwise stated.

or donor/acceptor ratio (25). The donor, mCerulean-Syx-(1–288), in the presence of unfused EYFP, had a single fluorescence lifetime at the plasma membrane (shown in Fig. 1, *c* and *d*) in agreement with our previous findings in neuroblastoma 2a cells (15, 23). FLIM reports protein interactions as a specific quench-

ing of the donor fluorescence lifetime in the presence of a proximal acceptor. To exclude any possibility that high concentrations of donor and acceptor molecules, in clusters at the cell surface, could lead to donor fluorescence lifetime quenching due merely to density, we analyzed cells expressing mCerulean-syntaxin and EYFP-syntaxin. These fluorescent proteins coexisted at the plasma membrane as expected (10), and no donor fluorescence lifetime quenching could be detected (supplemental Fig. 4). However, in the presence of the FRET acceptor EYFP-SNAP-25-(1–206), a change in the donor, mCerulean-syntaxin, fluorescence lifetime was reported, indicating a specific protein-protein interaction (*i.e.* a second fluorescence lifetime component appeared; Fig. 1*b*). TCSPC-FLIM uniquely delivers information describing both interaction (lifetime) and the proportion of donor molecules participating in energy transfer in each pixel of the image. This allows the influence of proximity and number of interacting partners to be dissected. A fuller description of this type of analysis is included in supplemental Fig. 3; in addition, a SNARE-specific FLIM review (26) and a general text (27) on time-correlated single photon counting provides a complete background to this technique.

Spatial Segregation of t-SNARE Heterodimer Conformations—Further analysis at the cell surface measured an interaction between syntaxin and SNAP-25 within the clusters on the plasma membrane (Fig. 2, *a*, *c*, and *d*). Importantly, the weighted mean fluorescence lifetime data (containing both interacting and noninteracting values and their respective amplitudes; supplemental Fig. 3) were bimodal (Fig. 2*a*, *left panel*) due to two spatially segregated types of SNARE cluster containing different FRET "efficiencies" (Fig. 2*a*, *right panels*). The t-SNARE dimer is thought to serve as an acceptor for the vesicular SNARE, synaptobrevin. It was therefore theoretically possible that the two spatially segregated states we observed could be due to the presence, or not, of synaptobrevin. To address this, we employed super-resolution STED imaging (previously used to resolve single SNARE clusters (10)) to ascertain the level of colocalization between synaptobrevin and single t-SNARE clusters on the cell surface (Fig. 2*b*). This showed that the large majority of single syntaxin clusters do not have coincident synaptobrevin. In addition, we found only 9 ± 5% overlap (Mander's overlap coefficient; mean ± S.E., $n = 8$ independent experiments), in immunostained cells using deconvolution microscopy (supplemental Fig. 2). This low level of overlap between the vesicle SNARE and the t-SNAREs is insufficient to account for the observed cluster heterogeneity across the cell surface.

Differences in FRET "efficiency" can be a result of either a change in the number of interacting molecules or differences in the inter-molecular proximity at specific cellular locations. However, FLIM can distinguish between these two possibilities (supplemental Fig. 3), allowing control for any interference from unlabeled SNAREs, which would ordinarily go undetected. First, we quantified the proportion of interacting molecules within every diffraction-limited cluster (containing 30–70 SNARE molecules each) in an image. This is described by a single distribution (Fig. 2*c*, *left panel*) and is further emphasized by an image showing spatial uniformity of this measurement

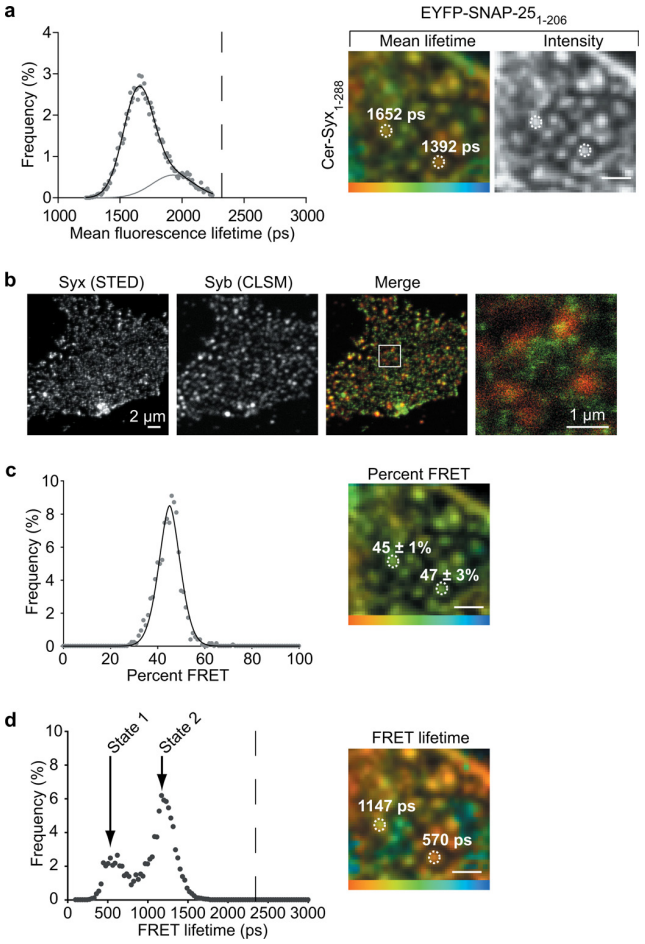

FIGURE 2. **Distinct t-SNARE heterodimer conformations are spatially segregated on the plasma membrane.** *a, histogram* of the amplitude weighted mean lifetime of the time constants of both FRET and non-FRET components measured from the plasma membrane of a cell expressing cerulean-Syx and EYFP-SNAP-25 is best fit by the sum of two Gaussian distributions (*left panel*). The *dashed line* corresponds to the mean non-FRET value. These two fluorescence lifetimes are spatially segregated on the plasma membrane, indicating heterogeneous interaction states (*right panel*). *Color scale,* 1250–2250 ps. *b,* STED and standard confocal laser scanning microscopy demonstrate minimal coincidence between syntaxin and synaptobrevin at the plasma membrane, insufficient to account for the variable t-SNARE interaction status observed. The highlighted region in the *merge panel* is shown enlarged (*right panel*). *c,* heterogeneity between clusters is not due to differences in the proportion of interacting molecules. The amplitude of the FRET lifetime component ("FRET percent," corresponding to the proportion of interacting molecules) is uni-modal as shown in the *histogram* (*left panel*) with clusters exhibiting only a small amount of variance around this mean (*right panel*). *Color scale,* 0–100%. *d,* two spatially segregated populations of t-SNARE heterodimer conformation are the cause of the observed heterogeneity. The FRET lifetime is bi-modal (termed *state 1* and *state 2*) as shown in the histogram (*left panel*); a result of the spatial segregation of FRET lifetimes into different clusters (*right panel*). *Color scale,* 0–2000 ps. All *scale bars* 1 μm unless otherwise stated.

(Fig. 2*c*, *right panel*). Therefore, differences in the number of interacting molecules between clusters cannot account for the observed spatial variations. Next, we analyzed the fluorescence lifetime component derived from only the proportion of interacting molecules within clusters. This revealed two distinct populations, for simplicity here termed state 1 and state 2 (Fig. 2*d*, *left panel*). Importantly, not only do these two states possess different molecular conformations, they are also spatially seg-

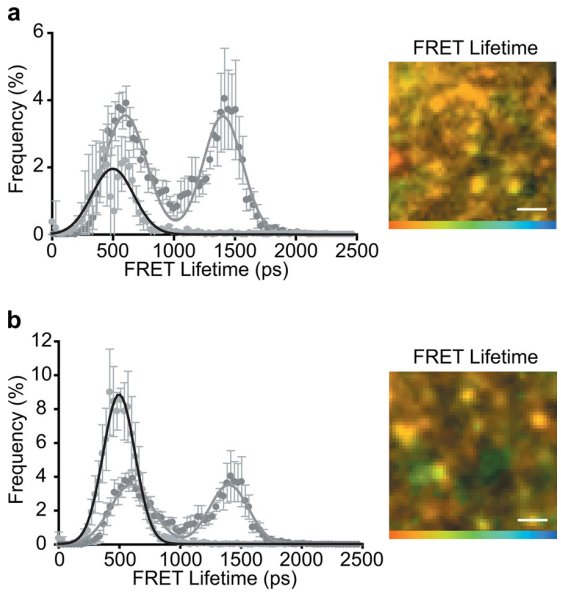

FIGURE 3. **Two t-SNARE conformations are a result of differential SNAP-25 engagement.** *a,* truncation of the C terminus of SNAP-25 to mimic BoNT/E cleavage (SNAP-25-(1–181)) abolished the state 2 conformation as shown in the *histogram* of FRET lifetimes (*left panel*) resulting in a largely uniform spatial distribution of FRET lifetimes (*right panel*) with a lifetime corresponding to the state 1 conformation. *b,* truncation of the entire C-terminal helix of SNAP-25 (SNAP-25-(1–120)) also abolished the state 2 conformation (*left panel*) resulting in a more uniform spatial distribution of FRET lifetimes (*right panel*). All *color scales*: 0–2000 ps. All *scale bars* 1 μm unless otherwise stated. *Graphs* show means ± S.E., n = at least five independent experiments.

regated on the plasma membrane into distinct clusters where one of the two forms predominates (Fig. 2*d, right panel*).

Distinct Heterodimer Conformations Are Due to Differential Engagement of SNAP-25—To gain structural insights into the two observed t-SNARE heterodimer states, we took advantage of the thorough biochemical and structural understanding of SNARE proteins. Recent work suggested that the t-SNAREs can exist in different conformational forms *in vitro* (28), where one form corresponded to a parallel three-helical bundle, whereas a second major form was shown to have the second SNAP-25 helix dissociated. We therefore tested whether these forms could account for the two states we observe in intact cells. We employed another mutant of SNAP-25 to mimic the cleavage product of botulinum neurotoxin serotype E (BoNT/E); this specific cleavage of SNAP-25 (removing the 25 C-terminal amino acids) is known to disrupt t-SNARE interactions (4) and abolish exocytosis (29). This mutant maintained micropatterns morphologically indistinguishable from full-length SNAP-25; however, state 2 (the three helical bundle) was reduced to undetectable levels (Fig. 3*a*). To further understand this, a mutant SNAP-25, where the entire second SNARE helix was deleted (SNAP-25-(1–121)), still formed clusters at the plasma membrane (Fig. 3*b*). Importantly, however, the heterodimer conformation was now uniform across the membrane, with the complete loss of state 2 (Fig. 3*b*). These findings indicate that the first SNARE helix of SNAP-25 is sufficient to initiate the interaction with syntaxin1a but that state 2 relies on the second SNARE helix of SNAP-25 to be present in the heterodimer complex. A previously reported substitution in SNAP-25 (G43D), a mutation in this first helix, was proposed to prevent the formation of a four helical bundle containing two SNARE helices from syntaxin and two N-terminal SNARE helices of SNAP-25 (30). We re-examined the effect of this mutation on the interaction between full-length SNAP-25 with syntaxin *in vitro*; in all assays, we found little or no significant effects (supplemental Fig. 5). We conclude that the heterodimer states we observe represent two different conformations of the t-SNARE heterodimer resulting from a differential engagement of the second SNARE helix of SNAP-25.

Underlying Lipid Order Affects t-SNARE Heterodimer Conformation—How are the two t-SNARE conformations spatially segregated? It has been suggested that these clusters may in some way be affected by the surrounding lipids (7, 13). However, this was at the gross topological or biochemical level and could not examine the interaction status of the proteins *in situ*. Therefore, we addressed the role of lipid order in plasma membrane cluster organization at the molecular level, reasoning that lipid order may play a role in segregating the two conformational states we have defined.

We examined the effect of sublethal (supplemental Fig. 6) cholesterol depletion on the lipid order of the plasma membrane, using laurdan, which reports changes in the packing of surrounding lipids as a spectral shift (31). Generalized polarization scale (GP) values can be calculated, with higher GP values corresponding to more "ordered" lipid environments (16). This revealed two different membrane populations in living neuroendocrine cells, with distinct lipid orders; the first peak (centered at −0.25) corresponds to intracellular membranes and the second peak (centered at 0) to the plasma membrane (Fig. 4*a*). Thus, the plasma membrane, which is normally enriched in cholesterol, typically at levels high enough to induce the liquid ordered phase (30–40 mol % (32)), is more ordered than intracellular membranes, in agreement with previous studies of diverse cell types (16, 33–35). Treatment of the same cells with 10 mM MβCD resulted in a depletion of 21 ± 4% of plasma membrane cholesterol (t test, $p < 0.001$, $n = 12$; see supplemental Fig. 6) leading to the loss of the lipid order in the plasma membrane (Fig. 4*a*, *middle* and *right panels*), while maintaining cell viability. It has been reported extensively that varying cholesterol concentration causes abrupt nonlinear discontinuities in membrane phase properties at 37 °C (36). For this reason, we chose as high a sublethal concentration of MβCD as possible to permit subsequent analyses. This loss of lipid order resulted in no change in the topological arrangement of single clusters as reported by super-resolution STED imaging (Fig. 4*b*) or the colocalization between the t-SNAREs on the plasma membrane (supplemental Fig. 2).

As there was no topological change in the t-SNARE distribution in the disordered plasma membrane, we next examined the effect of lipid order on the two heterodimer conformational states. Combining FLIM datasets confirmed that the FRET data from cells containing mCerulean-syntaxin and EYFP-SNAP-25 followed a bimodal distribution (reporting two conformational states) as before. After lipid order disruption, state 1 (SNAP-25 second helix not fully associated) was significantly reduced (special sum of squares F-test; $p < 0.001$, $n = 5$). The small right shift likely reflects a previous averaging of the data because of the partial overlap of the two peaks, with state 2 now better

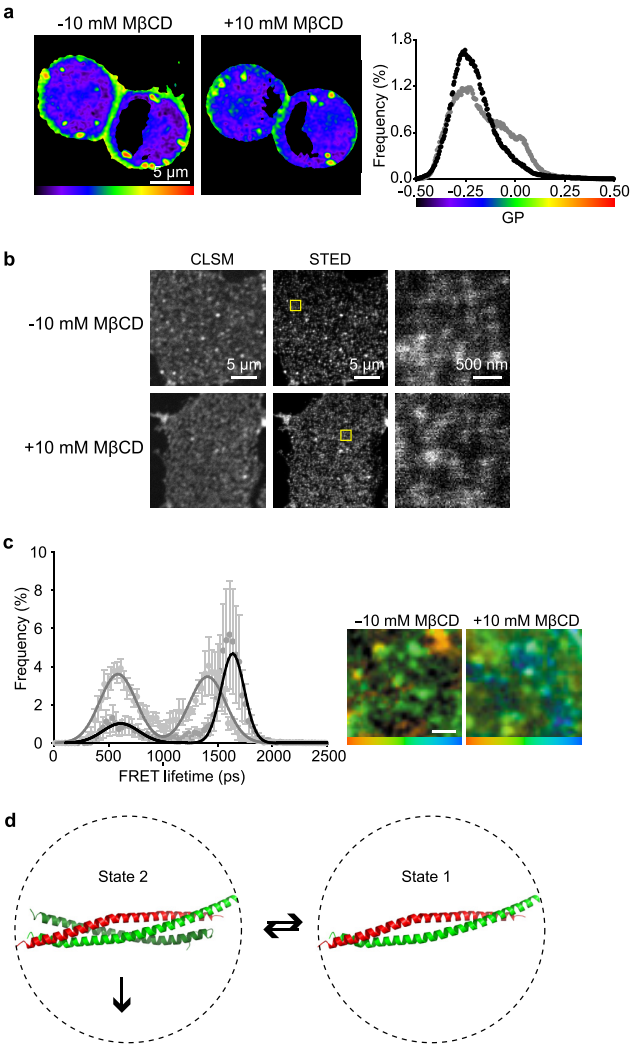

FIGURE 4. **Lipid disordering patterns the conformational states of the t-SNAREs.** *a,* laurdan was used to report lipid packing in cell membranes. The GP values were calculated on a pixel-by-pixel basis and are shown on a color scale before and after treatment with 10 mM MβCD (*left* and *center panels*). *Color scale*, −0.5 (*blue*) to +0.5 (*red*). The *histogram* of GP values is plotted (*right panel*), showing two separate populations (*gray*) corresponding to the plasma membrane (high GP; ordered lipid domains) and intracellular membranes (low GP; disordered domains). After cholesterol depletion with 10 mM MβCD (*black*), the lipid order on the plasma membrane was completely disrupted. *b,* STED microscopy of endogenous syntaxin on the plasma membrane before and after disruption of lipid order with 10 mM MβCD. Endogenous syntaxin clusters remain intact after loss of lipid order in the plasma membrane. Shown for comparison are standard confocal laser scanning microscopy images of the same sample. The highlighted regions in the STED images are shown enlarged (*right panels*). *c,* TCSPC-FLIM analyses of donor mCerulean-syntaxin in the presence of proximal EYFP-SNAP-25, in control (untreated, *gray*), and MβCD-treated (*black*) cells (*left panel*). Upon cholesterol depletion, the state 1 population is reduced, but the SNARE clusters remain intact (*right panel*). *Color scale*, 0–2000 ps. *Scale bar,* 1 μm. *Graphs* show means ± S.E. of donor fluorescence FRET lifetime data, n = at least five independent experiments. *d,* model describing the two molecular conformations of the t-SNAREs (syntaxin, *red*; SNAP-25 N- and C-terminal helices, *light* and *dark green,* respectively) observed on the plasma membrane. These states are spatially segregated in clusters, with the propensity of each form patterned by lipid order. BoNT/E resulted in state 1 predominating which is unable to support ternary SNARE complex formation and fusion.

resolved by the specific decrease in state 1 conformation (the inverse effect can be seen in the minor left shift of the data after BoNT/E treatment). Approximately 30% of the interacting molecules adopted the state 1 conformation (Fig. 4*c*), although after disruption of lipid order, it was reduced to 17%. In contrast, the state 2 population (involving both SNARE helices of SNAP-25) increased in frequency from 70 to 83%. As a control, treatment of mCerulean syntaxin-expressing cells (in the absence of a FRET acceptor) with 10 mM MβCD did not affect the donor fluorescence lifetime data (data not shown). Plasma membrane lipid order thus does not affect t-SNARE cluster morphology at the gross microscopic level; however, the conformational composition of each cluster is patterned by the underlying lipid environment.

DISCUSSION

Our data demonstrate that two distinct t-SNARE heterodimer conformations coexist at the plasma membrane of living neuroendocrine cells, segregated spatially and functionally into macromolecular clusters where one of two conformations predominates. This segregation is organized at least in part by lipid order and results in some clusters (state 1) where the C terminus of SNAP-25 is not engaged with syntaxin. As this protein complex cannot act as an acceptor for synaptobrevin, nor can it support exocytosis, these findings provide a model where proteins can be functionally and spatially patterned on the plasma membrane by the underlying lipid environment, at the level of their protein interactions. In contrast, state 2 can support exocytosis, and these states are spatially segregated. Furthermore, MβCD treatment results in an increased proportion of t-SNAREs adopting the functionally competent state 2 conformation.

We propose that cells could possibly regulate the position of release sites and the magnitude of the exocytotic response by modulating the lipid environment within which t-SNAREs reside. These two conformational t-SNARE heterodimer states may be further stabilized by accessory factors, including munc18-1, as has been observed *in vitro* (28). Further work will be required to determine whether accessory proteins preferentially associate with specific t-SNARE conformational states and their resulting influence.

How do the clusters of interacting t-SNAREs relate to previous findings on the morphological distribution of plasma membrane SNAREs? Syntaxin1 was shown previously to form clusters 50 nm in size, modeled to contain ~70 syntaxin molecules (10). The mechanism for this association was in part attributed to a homotypic interaction utilizing the transmembrane spanning region of syntaxin (37, 38). A proposed model from this work predicted a high degree of molecular crowding of syntaxin in the 50-nm dense clusters, hypothesized to be deleterious for interactions with other protein species. Importantly, however, no evidence for or against this sequestration of syntaxin from t-SNARE interactions has been reported in the literature. As all of the syntaxin clusters we observed reported interactions with SNAP-25, two possibilities exist. First, the presence of syntaxin in clusters does not preclude interaction with other proteins, including SNAP-25. Second, only the syntaxin on the periphery of the cluster is able to interact with SNAP-25. The core of the cluster would thus act as a reserve of syntaxin ready to replenish t-SNARE intermediates consumed in the fusion process. Our findings show a similar number of SNAP-25 molecules (~40–

50) and syntaxin molecules (~30–40) in dense ensembles. This could support the first hypothesis; however, PALM approaches can only provide a lower estimate for the number of molecules in a region, and so this technique cannot exclude either possibility. Recent work examining t-SNARE interactions at the plasma membrane also reported differential t-SNARE intermediate interactions (39), providing further support to our conclusions but no information to distinguish between these two models. As the spatial resolution of the TCSPC-FLIM approach is insufficient to distinguish between t-SNARE interactions throughout the cluster or restricted to the periphery, this question will require the development of single molecule FRET approaches to provide a definitive answer.

Recent work demonstrated that the C-terminal transmembrane domain of syntaxin forms a continuous α-helical structure with the SNARE motif (40). These data suggest that the transmembrane domain of syntaxin may not be long enough if structured to span the plasma membrane bilayer. Therefore, changes in the thickness of the bilayer, due to cholesterol intercalation, may be transduced to alter the conformation of syntaxin depending upon the lipid microenvironment. Furthermore, SNAP-25 is associated with the inner leaflet of the plasma membrane through palmitoylation; it is likely that SNAP-25 targeting, function, and conformation is modulated by cholesterol through differential insertion of palmitate groups into the membrane (41). In addition to cholesterol, phosphatidylinositol 4,5-bisphosphate has been reported to influence both the spatial and functional properties of syntaxin at the plasma membrane (42, 43). In conclusion, it is now becoming clear that the lipids of the plasma membrane play an active role in determining SNARE protein behavior in living cells (44).

Acknowledgments—pEGFP-N1-SNAP-25 was a gift from Maurine Linder (Washington University, St. Louis). A plasmid encoding photoactivatable mCherry was a gift from Vladislav V. Verkhusha (Yeshiva University). PALM data analysis was made possible using a Matlab routine generously gifted by Samuel Hess (Maine).

REFERENCES

1. Sutton, R. B., Fasshauer, D., Jahn, R., and Brunger, A. T. (1998) *Nature* **395,** 347–353
2. Söllner, T., Whiteheart, S. W., Brunner, M., Erdjument-Bromage, H., Geromanos, S., Tempst, P., and Rothman, J. E. (1993) *Nature* **362,** 318–324
3. Gonzalo, S., Greentree, W. K., and Linder, M. E. (1999) *J. Biol. Chem.* **274,** 21313–21318
4. Rickman, C., Meunier, F. A., Binz, T., and Davletov, B. (2004) *J. Biol. Chem.* **279,** 644–651
5. Fasshauer, D., and Margittai, M. (2004) *J. Biol. Chem.* **279,** 7613–7621
6. Fasshauer, D., Sutton, R. B., Brunger, A. T., and Jahn, R. (1998) *Proc. Natl. Acad. Sci. U.S.A.* **95,** 15781–15786
7. Lang, T., Bruns, D., Wenzel, D., Riedel, D., Holroyd, P., Thiele, C., and Jahn, R. (2001) *EMBO J.* **20,** 2202–2213
8. Lang, T., Margittai, M., Holzler, H., and Jahn, R. (2002) *J. Cell Biol.* **158,** 751–760
9. Ohara-Imaizumi, M., Nakamichi, Y., Nishiwaki, C., and Nagamatsu, S. (2002) *J. Biol. Chem.* **277,** 50805–50811
10. Sieber, J. J., Willig, K. I., Kutzner, C., Gerding-Reimers, C., Harke, B., Donnert, G., Rammner, B., Eggeling, C., Hell, S. W., Grubmüller, H., and Lang, T. (2007) *Science* **317,** 1072–1076
11. Melkonian, K. A., Ostermeyer, A. G., Chen, J. Z., Roth, M. G., and Brown, D. A. (1999) *J. Biol. Chem.* **274,** 3910–3917
12. Bacia, K., Schuette, C. G., Kahya, N., Jahn, R., and Schwille, P. (2004) *J. Biol. Chem.* **279,** 37951–37955
13. Chamberlain, L. H., Burgoyne, R. D., and Gould, G. W. (2001) *Proc. Natl. Acad. Sci. U.S.A.* **98,** 5619–5624
14. Laage, R., Rohde, J., Brosig, B., and Langosch, D. (2000) *J. Biol. Chem.* **275,** 17481–17487
15. Rickman, C., Medine, C. N., Bergmann, A., and Duncan, R. R. (2007) *J. Biol. Chem.* **282,** 12097–12103
16. Gaus, K., Gratton, E., Kable, E. P., Jones, A. S., Gelissen, I., Kritharides, L., and Jessup, W. (2003) *Proc. Natl. Acad. Sci. U.S.A.* **100,** 15554–15559
17. Avery, J., Ellis, D. J., Lang, T., Holroyd, P., Riedel, D., Henderson, R. M., Edwardson, J. M., and Jahn, R. (2000) *J. Cell Biol.* **148,** 317–324
18. Betzig, E., Patterson, G. H., Sougrat, R., Lindwasser, O. W., Olenych, S., Bonifacino, J. S., Davidson, M. W., Lippincott-Schwartz, J., and Hess, H. F. (2006) *Science* **313,** 1642–1645
19. Hess, S. T., Girirajan, T. P., and Mason, M. D. (2006) *Biophys. J.* **91,** 4258–4272
20. Numahara, T., Nakagawa, T., and Takaiwa, T. (1992) *J. Dermatol. Sci.* **4,** 202–207
21. Hopkins, B., and Skellam, J. G. (1954) *Ann. Bot.* **18,** 213–226
22. Ripley, B. D. (1977) *J. R. Stat. Soc.* **39,** 172–212
23. Medine, C. N., Rickman, C., Chamberlain, L. H., and Duncan, R. R. (2007) *J. Cell Sci.* **120,** 4407–4415
24. Valkonen, M., Kalkman, E. R., Saloheimo, M., Penttilä, M., Read, N. D., and Duncan, R. R. (2007) *J. Biol. Chem.* **282,** 22775–22785
25. Lakowicz, J. R. (1999) *Principles of Fluorescence Spectroscopy*, 2nd Ed., Plenum Publishing Corp., New York
26. Altenbach, K., Duncan, R. R., and Valkonen, M. (2010) *Fungal Biol. Rev.*, in press
27. Becker, W. (2005) *Advanced Time-correlated Single Photon Counting Techniques*, Springer-Verlag, Berlin
28. Weninger, K., Bowen, M. E., Choi, U. B., Chu, S., and Brunger, A. T. (2008) *Structure* **16,** 308–320
29. Binz, T., Blasi, J., Yamasaki, S., Baumeister, A., Link, E., Südhof, T. C., Jahn, R., and Niemann, H. (1994) *J. Biol. Chem.* **269,** 1617–1620
30. An, S. J., and Almers, W. (2004) *Science* **306,** 1042–1046
31. Parasassi, T., Gratton, E., Yu, W. M., Wilson, P., and Levi, M. (1997) *Biophys. J.* **72,** 2413–2429
32. McMullen, T. P., Lewis, R. N., and McElhaney, R. N. (2004) *Curr. Opin. Colloid Interface Sci.* **8,** 459–468
33. Vieira, O. V., Gaus, K., Verkade, P., Fullekrug, J., Vaz, W. L., and Simons, K. (2006) *Proc. Natl. Acad. Sci. U.S.A.* **103,** 18556–18561
34. Fitzner, D., Schneider, A., Kippert, A., Möbius, W., Willig, K. I., Hell, S. W., Bunt, G., Gaus, K., and Simons, M. (2006) *EMBO J.* **25,** 5037–5048
35. Stetzkowski-Marden, F., Gaus, K., Recouvreur, M., Cartaud, A., and Cartaud, J. (2006) *J. Lipid Res.* **47,** 2121–2133
36. Parasassi, T., Di Stefano, M., Loiero, M., Ravagnan, G., and Gratton, E. (1994) *Biophys. J.* **66,** 120–132
37. Kroch, A. E., and Fleming, K. G. (2006) *J. Mol. Biol.* **357,** 184–194
38. Hofmann, M. W., Peplowska, K., Rohde, J., Poschner, B. C., Ungermann, C., and Langosch, D. (2006) *J. Mol. Biol.* **364,** 1048–1060
39. Halemani, N. D., Bethani, I., Rizzoli, S. O., and Lang, T. (2010) *Traffic* PMID 20002656
40. Stein, A., Weber, G., Wahl, M. C., and Jahn, R. (2009) *Nature* **460,** 525–528
41. Salaün, C., Gould, G. W., and Chamberlain, L. H. (2005) *J. Biol. Chem.* **280,** 19449–19453
42. Murray, D. H., and Tamm, L. K. (2009) *Biochemistry* **48,** 4617–4625
43. Lam, A. D., Tryoen-Toth, P., Tsai, B., Vitale, N., and Stuenkel, E. L. (2008) *Mol. Biol. Cell* **19,** 485–497
44. Lang, T., Halemani, N. D., and Rammner, B. (2008) *Prog. Lipid Res.* **47,** 461–469

Cell Mol Neurobiol (2010) 30:1321–1326
DOI 10.1007/s10571-010-9599-4

REPORT

The t-SNARE Complex: A Close Up

Alison R. Dun · Colin Rickman · Rory R. Duncan

Received: 31 May 2010 / Accepted: 3 September 2010 / Published online: 3 November 2010

Abstract The SNARE proteins, syntaxin, SNAP-25, and synaptobrevin have long been known to provide the driving force for vesicle fusion in the process of regulated exocytosis. Of particular interest is the initial interaction between SNAP-25 and syntaxin to form the t-SNARE heterodimer, an acceptor for subsequent synaptobrevin engagement. In vitro studies have revealed at least two different dynamic conformations of t-SNARE heterodimer defined by the degree of association of the *C*-terminal SNARE motif of SNAP-25 with syntaxin. At the plasma membrane, these proteins are organized into dense clusters of 50–60 nm in diameter. More recently, the t-SNARE interaction within these clusters was investigated in live cells at the molecular level, estimating each cluster to contain 35–70 t-SNARE molecules. This work reported the presence of both partially and fully zippered t-SNARE complex at the plasma membrane in agreement with the earlier in vitro findings. It also revealed a spatial segregation into distinct clusters containing predominantly one conformation apparently patterned by the surrounding lipid environment. The reason for this dynamic t-SNARE complex in exocytosis is uncertain; however, it does take us one step closer to understand the complex sequence of events leading to vesicle fusion, emphasizing the role of both membrane proteins and lipids.

A commentary to this article can be found at doi: 10.1007/s10571-010-9610-0.

A. R. Dun · R. R. Duncan (✉)
Centre for Integrative Physiology, University of Edinburgh Medical School, Hugh Robson Building, George Square, Edinburgh EH8 9XD, UK
e-mail: rory.duncan@ed.ac.uk

C. Rickman
School of Engineering and Physical Sciences, Heriot-Watt University, Edinburgh EH14 4AS, UK

Keywords Exocytosis · SNAP-25 · Syntaxin · FLIM

Abbreviations

SNARE	Soluble *N*-ethylmaleimide-sensitive-factor attachment protein receptor
SNAP-25	Synaptosome-associated protein of 25 kD
FLIM	Fluorescence lifetime imaging microscopy
STED	Stimulated emission depletion microscopy
PALM	Photoactivatable localisation microscopy

Introduction

Investigating the molecular mechanics of vesicle fusion allows us to further understand regulated exocytosis, the process through which a vesicle can release its secretory cargo into the extracellular space in response to a rise in intracellular calcium (Rizo and Sudhof 2002; Sollner et al. 1993b). In both neurons and neuroendocrine cells vesicles are thought to undergo a number of steps before secretion. These vesicles are thought to "dock" at the plasma membrane, mediated by a combination of protein–protein and protein–lipid interactions, where they then undergo a poorly defined molecular priming step before calcium-dependent fusion occurs (Lam et al. 2008; Sollner et al. 1993a; Sudhof 2004).

A vesicle may fuse with the plasma membrane driven by an interaction between three key proteins, synaptobrevin, SNAP-25 and syntaxin-1 (Fig. 1a). These proteins belong to the highly conserved SNARE family and are essential for exocytosis (Hayashi et al. 1994; Jahn and Niemann 1994; Sollner et al. 1993a). Earlier work which leads to the now widely recognised SNARE protein complex configuration

demonstrated that when incubated in vitro, the three SNAREs assemble spontaneously into an SDS resistant core complex (Clary et al. 1990; Hayashi et al. 1994; Sollner et al. 1993a). Further work established that the formation of this complex is strictly sequential and initiated by the association of the target-SNAREs, SNAP-25, and syntaxin1, most likely in a 1:1 stoichiometry at the plasma membrane (Fig. 1b) (Chen et al. 2001; Fasshauer and Margittai 2004; Rickman et al. 2004). The "docking" of vesicles to the plasma membrane relies on other proteins, notably synaptotagmin and munc18 (de Wit et al. 2009). Electrophysiological studies suggested that a poorly defined molecular "maturation" follows, involving the association of priming factors, which act to catalyze the fusion event (Fiebig et al. 1999; James et al. 2009; Sutton et al. 1998; Weber et al. 1998). The t-SNAREs interact with high affinity and so these two proteins are trafficked independently of each other to prevent ectopic interactions occurring prematurely (Arunachalam et al. 2008; Hata et al. 1993; Medine et al. 2007). After formation of the t-SNARE heterodimer acceptor complex, the vesicle-associated synaptobrevin can bind, forming a tight 4-helical ternary SNARE complex.

SNARE proteins are well established as key facilitators of regulated exocytosis and the dissection of their structure and binding partners has been extensively studied. Although the individual components involved have been analyzed in great detail in vitro, how they come together in the cell and the exact site of vesicle fusion in relation to these molecules remains speculative. Here we review one component in particular, the t-SNARE heterodimer complex, to see how this has enhanced our knowledge of regulated exocytosis and how super-resolution imaging techniques may provide a route to finally dissect the role of the SNAREs in regulated exocytosis.

The Sequential Formation of a Core Complex

SNARE proteins are alpha helical in complex and investigation into how the core complex forms has relied upon the in-depth analysis of these structures as well as the identification of the essential binding regions of each of the interacting helices (Chapman et al. 1994; Sollner et al. 1993a; Sutton et al. 1998). Among these are the highly conserved SNARE motifs which are integral to the formation of the core complex. Syntaxin contains one motif within its *C*-terminal SNARE helix whereas SNAP-25 has two, present at the *C*- and *N*-termini, which are separated by a linker region. The SNAP-25 linker region contains multiple cysteine residues at amino acids 84–92, which are known to be sites for attachment to the membrane through thioester linkage to palmitic acid (Oyler et al. 1989; Veit et al. 1996). Conversely, syntaxin1 is associated with the membrane via a transmembrane domain which allows the *C*-terminal alpha helical coil to protrude into the intracellular space where it associates with the *N*-terminal alpha helix of SNAP-25 (Hayashi et al. 1994). Cleavage of the *C*-terminus of SNAP-25 with Botulinum neurotoxin serotype A demonstrates the necessity of this second SNARE helix for synaptobrevin binding and the full zippering of the SNARE complex (Chapman et al. 1994).

The identification of the SNARE motif predicted that the SNARE complex would follow Crick's classic model for the coiled-coil structure (Crick 1953). It is now known that the hydrophobic residues within the SNARE motif pack together in the centre of the four helical ternary SNARE complex (Fasshauer et al. 1998; Sutton et al. 1998) and this is proposed to subsequently provide the required energy for lipid bilayer merger (Hanson et al. 1997; Li et al. 2007; Lin and Scheller 1997). In addition the four SNARE helices

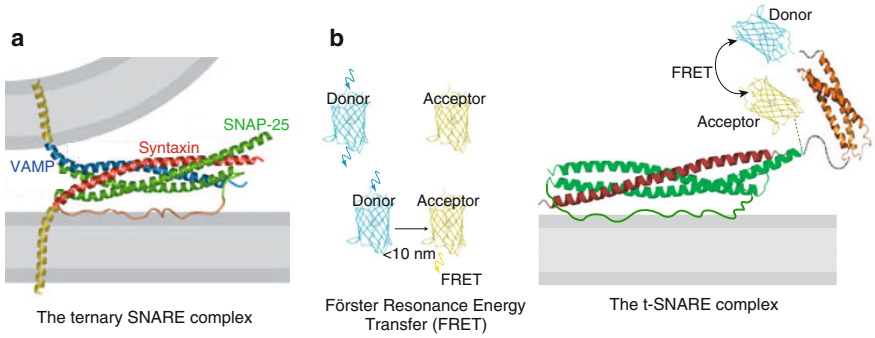

Fig. 1 The examination of SNARE proteins at the plasma membrane. **a** The four SNARE helices interact at the membrane to form a tight 4-helical bundle bringing opposing bilayers close enough for fusion (adapted from Sutton et al. 1998). **b** FRET can occur between two fluorophores, with overlapping excitation and emission spectra, when the inter-fluorophore distance is less than approximately 10 nm. This is therefore indicative of interaction. t-SNAREs in complex allow FRET to occur when the fluorophores are conjugated to the *N*-terminus of syntaxin and *C*-terminus of SNAP-25. A 3-helical complex or one that is only partially zippered (for example, with the SNAP-25 *N*-terminal helix partly dissociated) will report a different FRET "efficiency", because the donor and acceptor fluorophores are further apart. Quantifying FRET in every pixel of an image therefore can report a change in interaction, with spatial resolution

each contribute a number of ionic residues, one arginine, and three glutamine, which are highly conserved across the SNARE family (Sutton et al. 1998). These residues line up within the hydrophobic core of the ternary SNARE complex, forming a hydrogen bonding network, which gives both strength and registration to the interactions.

The alpha-helicity of proteins can be quantified using circular dichroism (CD) spectroscopy (Fersht 1999) which can provide insights into the structure of a complex and its individual parts. Formation of the core complex has been shown to be associated with a dramatic increase in alpha-helicity, supporting the existence of a coiled–coiled secondary structure (Fasshauer et al. 1997). The *C*-terminal helix of SNAP-25 does not seem to be essential in this change, but is not redundant. CD analysis suggested this second SNAP-25 SNARE helix does undergo a structural change upon binding to syntaxin1, and that this could be the rate limiting step in synaptobrevin association (Fasshauer et al. 1997; Fasshauer and Margittai 2004; Hayashi et al. 1994). Interestingly, when isolating only the *N*-terminus of SNAP-25 and the *C*-terminus of syntaxin1 in vitro, an increase in alpha-helicity was also observed. This implies that the t-SNARE structure can begin to form, in a coiled-coil manner, with just two helices and in vitro can exist as an intermediate binary conformation (Fasshauer et al. 1997).

Observing the Membrane from the Inside Out

Although in vitro analyses allow the thorough examination of protein properties and structures, the orientation of such proteins as well as their binding partners may be different when membrane associated. By incubating proteins on a supported lipid bilayer in vitro, it is possible to observe them in their membrane bound state. One such study combined this technique with single molecule Förster resonance energy transfer (smFRET) using fluorescently-conjugated recombinant syntaxin1 and SNAP-25 (Weninger et al. 2008). This technique revealed two distinct sub-populations of t-SNARE heterodimer undergoing varying types of interaction. One population consisted of a "fully zippered" t-SNARE complex with all three helices associated, whereas a second major group appeared to have a partially zippered structure with only two helices in complex. In the latter conformation the second, *C*-terminal, SNARE helix of SNAP-25 was dissociated, similar to the binary complex seen originally in vitro (Fasshauer et al. 1997; Weninger et al. 2008). Interestingly, the t-SNARE proteins were seen to transition between the fully- and partially-zippered states in a reversible manner at the lipid membrane, on a time scale of seconds (Weninger et al. 2008).

Such reconstituted bilayer studies have proven useful for examining the t-SNAREs in their membrane-anchored form. It is also possible to examine endogenous proteins on or in native plasma membrane sheets by "unroofing" cultured neuroendocrine cells (Avery et al. 2000; Lang 2003). Stimulated emission depletion (STED) microscopy of these sheets has revealed homodimers of syntaxin1 residing in 50–60 nm clusters at the plasma membrane (Sieber et al. 2007). This is a different t-SNARE configuration to that described from the in vitro studies discussed so far, and while the exact mechanism required for homodimerization of syntaxin1 molecules remain speculative; this membrane bound complex is highly plausible (Laage et al. 2000; Rickman et al. 2005; Sieber et al. 2006). SNAP-25 is believed to reside within close proximity to these syntaxin1 clusters (Sieber et al. 2006), which would provide a possible interface for heterodimer formation and site for vesicle fusion. The intermediate binary t-SNARE complex could still exist within this model as SNAP-25 is shown to interact with the syntaxin1 clusters, in a short-lived manner, with only its *C*-terminal helices (Halemani et al. 2010).

It is well established that the t-SNAREs form a highly regulated and functional heterodimer complex in plasma membrane clusters, in cultured cells. In addition, similar organization has been observed in a study using adrenal medulla slices and proposed to be the site for exocytosis (Lopez et al. 2007). The observation of different t-SNARE intermediate binary complexes both in vitro, in lipid bilayers, native membrane sheets, and in primary preparations raises the question: are these two configurations present in intact live cells and if so how are the t-SNAREs organized at the plasma membrane?

The t-SNARE Complex at Molecular Resolution

Examining and understanding protein–protein interactions in live cells requires a degree of resolution not possible through conventional optical techniques. However, the quantification of FRET between two fluorescently labeled molecules can provide information by reporting the degree of interaction through a change in fluorescence properties (Fig. 1b).

Studies in live cells using intensity based FRET support previous in vitro findings of alternative t-SNARE complexes, where only the *C*-termini of SNAP-25 is bound with high affinity, to syntaxin1 (An and Almers 2004; Wang et al. 2008). In addition, this conformation was seen to be induced upon calcium influx implying a possible role in the priming step prior to fusion (An and Almers 2004).

The FRET can be estimated either through change in intensity, as mentioned above, or quantified more directly using FLIM (Fig. 2a), a technique which provides data

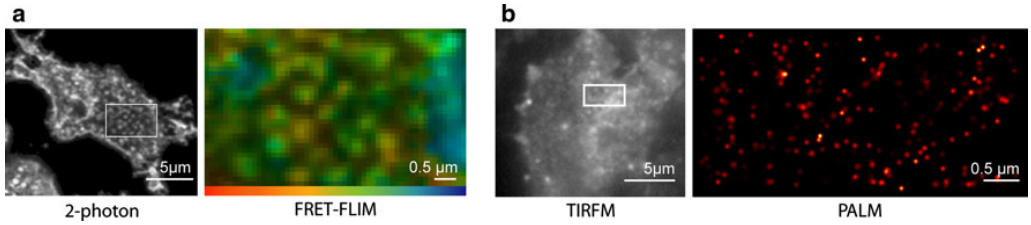

Fig. 2 SNARE protein molecular behavior in living cells. **a** we can see that the 2-photon intensity image clearly shows SNAP-25 as homogeneous puncta on the plasma membrane but that FRET-FLIM imaging is required to reveal heterogeneities between these clusters (Rickman et al. 2010). Different colors represent areas of different donor fluorescent lifetime (see color scale bar) and therefore varying degrees of interaction. Further discussion of FLIM, and its application, can be found in these references (Becker 2005; Altenbach et al. 2010). **b** we demonstrate the ability to visualise single molecules of SNAP-25 at high resolution at the plasma membrane using the super resolution technique photoactivation localization microscopy (PALM; for recent application of this technique to SNARE proteins see (Rickman et al. 2010)). This is displayed in contrast to the same cell imaged through the conventional microscopy technique, TIRFM. PALM allows for the highest possible resolution analysis of the molecular spatial organisation, which in this case demonstrates a non-random pattern. **a** Two-photon intensity image showing clusters of mCerulean-syntaxin1a at the plasma membrane of a PC12 cell, co-expressing EYFP-SNAP-25 (*left panel*). All clusters appear identical. Scale bar: 500 nm. The *boxed area* in the intensity image is enlarged in the TCSPC-FLIM (*right panel*) image. Here, color represents the donor fluorescence lifetime, and brightness the intensity. Differences in color signify altered inter-fluorophore distances and thus "FRET efficiencies". **b** TIRF-PALM localization map showing single molecules of SNAP-25 on the plasma membrane of a PC12 cell. Scale bar: 500 nm. The *boxed area* in the summed TIRFM image (*left panel*) is enlarged in the TIRF-PALM rendered image (*right panel*). Scale bar: 5 nm. A non-random distribution of single SNAP-25 molecules is apparent at the plasma membrane. Scale bar: 5 nm, color scale bar: 1250–2250 ps. Approximate certainty a (*left panel*) 200 nm resolution, (*right panel*) 20 nm localisation, **b** (*left panel*) 200 nm resolution, (*right panel*) <10 nm inter-fluorophore distance reported. This figure is modified from Rickman et al. (2010) (Color figure online)

unaffected by donor/acceptor ratio or concentration (Becker 2005). TCSPC–FLIM uniquely delivers information describing both interaction (lifetime) and the proportion of donor molecules participating in energy transfer in each pixel of the image. This allows the influence of proximity and number of interacting partners to be dissected. A SNARE-specific FLIM review (Altenbach et al. 2010) and a general text (Becker 2005) on TCPSC provide a complete background to this technique.

More recently single molecules of SNAP-25 and syntaxin1 have been visualized at the plasma membrane using the super-resolution technique known as Photoactivatable localisation microscopy (PALM). This work supports the SNARE clustering hypothesis as the single molecule distributions across the membrane are non-random (Rickman et al. 2010) (Fig. 2b).

Whether the t-SNARE molecules interact in these clusters at the cell surface, or what the organizational significance of this molecular arrangement is, has remained elusive until recently. Work using FLIM (Rickman et al. 2010) confirmed that the SNARE clusters at the plasma membrane of live cells consist predominantly of t-SNAREs in a binary complex. It is credible that either SNAP-25 may be bound to the periphery of the syntaxin1 clusters (Sieber et al. 2007), or alternatively, this observation could provide an alternative model for SNARE cluster organization. Importantly, clusters at the cell surface were heterogeneous in their interaction status, with predominantly fully-zippered or partially-zippered complex organized into distinct regions (Fig. 2a). It may be that the two different states observed, one an apparently more fully formed complex than the other, relate to the docked or primed status of the vesicle (Nofal et al. 2007). It has also been suggested that the surrounding lipid environment could play a significant role in the molecular organisation of these proteins at the plasma membrane (Rickman et al. 2010). Thus, although the functional importance of this spatial arrangement and the existence of the alternative binary complex for vesicle fusion are still not well defined; it seems investigating protein, lipid, and vesicle relationships may provide important mechanistic insights.

Summary

The fusion of a secretory vesicle with the cell membrane is a highly regulated process with the formation of t-SNARE complex playing a pivotal role. It is now evident that the t-SNAREs are patterned in an organized manner at the plasma membrane where they form a dynamic complex existing as either a fully or partially zippered heterodimer. Further work is required to dissect the functional significance of this plasma membrane organization, the role, if any, of the underlying lipids, and the impact this may have on vesicle fusion.

Acknowledgments This work was supported by Wellcome Trust and Medical Research Council project grants to RRD and a BBSRC Studentship to AD.

References

Altenbach K, Duncan RR, Valkonen M (2010) In vivo FLIM-FRET measurements of recombinant proteins in filamentous fungi. Fungal Biol Rev 23:67–71

An SJ, Almers W (2004) Tracking SNARE complex formation in live endocrine cells. Science 306:1042–1046

Arunachalam L, Han L, Tassew NG, He Y, Wang L, Xie L, Fujita Y, Kwan E, Davletov B, Monnier PP, Gaisano HY, Sugita S (2008) Munc18–1 is critical for plasma membrane localization of syntaxin1 but not of SNAP-25 in PC12 Cells. Mol Biol Cell 19:722–734

Avery J, Ellis DJ, Lang T, Holroyd P, Riedel D, Henderson RM, Edwardson JM, Jahn R (2000) A cell-free system for regulated exocytosis in PC12 cells. J Cell Biol 148:317–324

Becker W (2005) Advanced time-correlated single photon counting techniques. Springer, Heidelberg

Chapman ER, An S, Barton N, Jahn R (1994) SNAP-25, a t-SNARE which binds to both syntaxin and synaptobrevin via domains that may form coiled coils. J Biol Chem 269: 27427–27432

Chen YA, Scales SJ, Scheller RH (2001) Sequential SNARE assembly underlies priming and triggering of exocytosis. Neuron 30:161–170

Clary DO, Griff IC, Rothman JE (1990) SNAPs, a family of NSF attachment proteins involved in intracellular membrane fusion in animals and yeast. Cell 61:709–721

Crick F (1953) The packing of [alpha]-helices: simple coiled-coils. Acta Crystallogr A 6:689–697

de Wit H, Walter AM, Milosevic I, Gulyas-Kovacs A, Riedel D, Sorensen JB, Verhage M (2009) Synaptotagmin-1 docks secretory vesicles to syntaxin-1/SNAP-25 acceptor complexes. Cell 138:935–946

Fasshauer D, Margittai M (2004) A transient interaction of SNAP-25 and syntaxin nucleates SNARE assembly. J Biol Chem 279: 7613–7621

Fasshauer D, Bruns D, Shen B, Jahn R, Brunger AT (1997) A structural change occurs upon binding of syntaxin to SNAP-25. J Biol Chem 272:4582–4590

Fasshauer D, Sutton RB, Brunger AT, Jahn R (1998) Conserved structural features of the synaptic fusion complex: SNARE proteins reclassified as Q- and R-SNAREs. Proc Natl Acad Sci USA 95:15781–15786

Fersht A (1999) Structure and mechanism in protein science: a guide to enzyme catalysis and protein folding. W.H.Freeman, San Francisco

Fiebig KM, Rice LM, Pollock E, Brunger AT (1999) Folding intermediates of SNARE complex assembly. Nat Struct Biol 6:117–123

Halemani ND, Bethani I, Rizzoli SO, Lang T (2010) Structure and dynamics of a two-helix SNARE complex in live cells. Traffic 11:394–404

Hanson PI, Roth R, Morisaki H, Jahn R, Heuser JE (1997) Structure and conformational changes in NSF and its membrane receptor complexes visualized by quick-freeze/deep-etch electron microscopy. Cell 90:523–535

Hata Y, Slaughter CA, Sudhof TC (1993) Synaptic vesicle fusion complex contains unc-18 homologue bound to syntaxin. Nature 366:347–351

Hayashi T, McMahon H, Yamasaki S, Binz T, Hata Y, Sudhof TC, Niemann H (1994) Synaptic vesicle membrane fusion complex: action of clostridial neurotoxins on assembly. EMBO J 13: 5051–5061

Jahn R, Niemann H (1994) Molecular mechanisms of clostridial neurotoxins. Ann NY Acad Sci 733:245–255

James DJ, Kowalchyk J, Daily N, Petrie M, Martin TF (2009) CAPS drives trans-SNARE complex formation and membrane fusion through syntaxin interactions. Proc Natl Acad Sci USA 106: 17308–17313

Laage R, Rohde J, Brosig B, Langosch D (2000) A conserved membrane-spanning amino acid motif drives homomeric and supports heteromeric assembly of presynaptic SNARE proteins. J Biol Chem 275:17481–17487

Lam AD, Tryoen-Toth P, Tsai B, Vitale N, Stuenkel EL (2008) SNARE-catalyzed fusion events are regulated by Syntaxin1A-lipid interactions. Mol Biol Cell 19:485–497

Lang T (2003) Imaging SNAREs at work in 'unroofed' cells–approaches that may be of general interest for functional studies on membrane proteins. Biochem Soc Trans 31:861–864

Li F, Pincet F, Perez E, Eng WS, Melia TJ, Rothman JE, Tareste D (2007) Energetics and dynamics of SNAREpin folding across lipid bilayers. Nat Struct Mol Biol 14:890–896

Lin RC, Scheller RH (1997) Structural organization of the synaptic exocytosis core complex. Neuron 19:1087–1094

Lopez I, Giner D, Ruiz-Nuno A, Fuentealba J, Viniegra S, Garcia AG, Davletov B, Gutierrez LM (2007) Tight coupling of the t-SNARE and calcium channel microdomains in adrenomedullary slices and not in cultured chromaffin cells. Cell Calcium 41: 547–558

Medine CN, Rickman C, Chamberlain LH, Duncan RR (2007) Munc18–1 prevents the formation of ectopic SNARE complexes in living cells. J Cell Sci 120:4407–4415

Nofal S, Becherer U, Hof D, Matti U, Rettig J (2007) Primed vesicles can be distinguished from docked vesicles by analyzing their mobility. J Neurosci 27:1386–1395

Oyler GA, Higgins GA, Hart RA, Battenberg E, Billingsley M, Bloom FE, Wilson MC (1989) The identification of a novel synaptosomal-associated protein, SNAP-25, differentially expressed by neuronal subpopulations. J Cell Biol 109:3039–3052

Rickman C, Meunier FA, Binz T, Davletov B (2004) High affinity interaction of syntaxin and SNAP-25 on the plasma membrane is abolished by botulinum toxin E. J Biol Chem 279:644–651

Rickman C, Hu K, Carroll J, Davletov B (2005) Self-assembly of SNARE fusion proteins into star-shaped oligomers. Biochem J 388:75–79

Rickman C, Medine CN, Dun AR, Moulton DJ, Mandula O, Halemani ND, Rizzoli SO, Chamberlain LH, Duncan RR (2010) t-SNARE protein conformations patterned by the lipid microenvironment. J Biol Chem 285:13535–13541

Rizo J, Sudhof TC (2002) Snares and Munc18 in synaptic vesicle fusion. Nat Rev Neurosci 3:641–653

Sieber JJ, Willig KI, Heintzmann R, Hell SW, Lang T (2006) The SNARE motif is essential for the formation of syntaxin clusters in the plasma membrane. Biophys J 90:2843–2851

Sieber JJ, Willig KI, Kutzner C, Gerding-Reimers C, Harke B, Donnert G, Rammner B, Eggeling C, Hell SW, Grubmuller H, Lang T (2007) Anatomy and dynamics of a supramolecular membrane protein cluster. Science 317:1072–1076

Sollner T, Bennett MK, Whiteheart SW, Scheller RH, Rothman JE (1993a) A protein assembly-disassembly pathway in vitro that may correspond to sequential steps of synaptic vesicle docking, activation, and fusion. Cell 75:409–418

Sollner T, Whiteheart SW, Brunner M, Erdjument-Bromage H, Geromanos S, Tempst P, Rothman JE (1993b) SNAP receptors implicated in vesicle targeting and fusion. Nature 362:318–324

Sudhof TC (2004) The synaptic vesicle cycle. Annu Rev Neurosci 27:509–547

Sutton RB, Fasshauer D, Jahn R, Brunger AT (1998) Crystal structure of a SNARE complex involved in synaptic exocytosis at 2.4 A resolution. Nature 395:347–353

Veit M, Sollner TH, Rothman JE (1996) Multiple palmitoylation of synaptotagmin and the t-SNARE SNAP-25. FEBS Lett 385: 119–123

Wang L, Bittner MA, Axelrod D, Holz RW (2008) The structural and functional implications of linked SNARE motifs in SNAP25. Mol Biol Cell 19:3944–3955

Weber T, Zemelman BV, McNew JA, Westermann B, Gmachl M, Parlati F, Sollner TH, Rothman JE (1998) SNARE pins: minimal machinery for membrane fusion. Cell 92:759–772

Weninger K, Bowen ME, Choi UB, Chu S, Brunger AT (2008) Accessory proteins stabilize the acceptor complex for synaptobrevin, the 1:1 syntaxin/SNAP-25 complex. Structure 16:308–320

OPEN ACCESS Freely available online

PLOS ONE

Secretory Vesicles Are Preferentially Targeted to Areas of Low Molecular SNARE Density

Lei Yang[1], Alison R. Dun[1], Kirsty J. Martin[1], Zhen Qiu[1], Andrew Dunn[1], Gabriel J. Lord[2], Weiping Lu[1], Rory R. Duncan[1☯], Colin Rickman[1*☯]

1 Institute of Biological Chemistry, Biophysics and Bioengineering, Heriot-Watt University, Edinburgh, United Kingdom, **2** Mathematical and Computer Sciences, Heriot-Watt University, Edinburgh, United Kingdom

Abstract

Intercellular communication is commonly mediated by the regulated fusion, or exocytosis, of vesicles with the cell surface. SNARE (soluble N-ethymaleimide sensitive factor attachment protein receptor) proteins are the catalytic core of the secretory machinery, driving vesicle and plasma membrane merger. Plasma membrane SNAREs (tSNAREs) are proposed to reside in dense clusters containing many molecules, thus providing a concentrated reservoir to promote membrane fusion. However, biophysical experiments suggest that a small number of SNAREs are sufficient to drive a single fusion event. Here we show, using molecular imaging, that the majority of tSNARE molecules are spatially separated from secretory vesicles. Furthermore, the motilities of the individual tSNAREs are constrained in membrane micro-domains, maintaining a non-random molecular distribution and limiting the maximum number of molecules encountered by secretory vesicles. Together our results provide a new model for the molecular mechanism of regulated exocytosis and demonstrate the exquisite organization of the plasma membrane at the level of individual molecular machines.

Citation: Yang L, Dun AR, Martin KJ, Qiu Z, Dunn A, et al. (2012) Secretory Vesicles Are Preferentially Targeted to Areas of Low Molecular SNARE Density. PLoS ONE 7(11): e49514. doi:10.1371/journal.pone.0049514

Editor: Ludger Johannes, Institut Curie, France

Received August 2, 2012; **Accepted** October 10, 2012; **Published** November 15, 2012

Funding: This work was supported by the Medical Research Council (to RRD and CR), the Wellcome Trust (to RRD and CR), the Royal Society (to CR), the Robertson Trust (to RRD and CR) and the Engineering and Physical Sciences Research Council (to WL). The funders had no role in study design, data collection and analysis, decision to publish, or preparation of the manuscript.

Competing Interests: The authors have declared that no competing interests exist.

* E-mail: c.rickman@hw.ac.uk

☯ These authors contributed equally to this work.

Introduction

Neuronal and endocrine communication is achieved through the orchestrated action of a highly conserved protein machinery [1,2]. Neurotransmitter, or hormone, containing secretory vesicles, fuse with the plasma membrane, releasing their signal in to the extracellular milieu. Disruption of this process is observed in a growing number of secretion-deficit diseases [3–5]. The SNARE protein family are known to actively mediate the fusion of the secretory vesicle and plasma membranes by catalyzing the merger of the two opposing bilayers [1,2,6,7]. The vesicular SNARE (vSNARE), synaptobrevin 2, interacts with the plasma membrane SNARE proteins (target SNAREs or tSNAREs), syntaxin 1 and SNAP-25, forming a highly stable helical complex [6,8,9]. The energy liberated through the formation of this complex is thought to provide the driving force for exocytosis. Indeed the SNAREs have been demonstrated to be sufficient to fuse artificial bilayers in vitro, with accessory factors serving to regulate this process [7,10–12].

An emerging theme in membrane biology is the organization of membrane proteins into large scale molecular assemblies [13]. Over the last decade, the spatial organization of the plasma membrane SNAREs has been intensively studied [14–18]. Importantly, syntaxin and SNAP-25 differ in their mode of membrane attachment; a single transmembrane helix in the case of syntaxin and post-translational acylation of cysteines for SNAP-25 [19]. Despite this difference, both tSNAREs have been observed to exist in apparent 'clusters' using fluorescence microscopy, which are hypothesized to be an important functional entity, providing a localized concentrated pool of tSNAREs to facilitate and enhance bilayer fusion [14–17]. However, when interpreting these data it is important to understand the influence of the microscope on the recorded image. Light emitting from a single fluorophore will undergo diffraction through the optics of the microscope, appearing much larger in the recorded image than in the original source. For example the fluorescence signal from a sparse distribution of individual single molecules produces an image that can appear as spots, reminiscent of clusters, with a measured size dependent on the imaging modality used [20]. The size of the recorded signal from a single fluorophore determines the lower limit for the accurate determination of cluster size on a particular microscope. The reported size of the tSNARE clusters has tracked the improvement in resolutions of fluorescence microscopy but has always been observed at the lower limit for accurate size determination. We therefore decided to investigate, with molecular precision, the spatial and dynamic organization of individual SNARE protein molecules, to both increase our understanding of regulated secretion and more generally plasma membrane organization.

Results

Recently developed microscopy techniques, including photoactivation localization microscopy (PALM) and ground state depletion microscopy followed by individual molecule return (GSDIM) [21–24], can localize individual protein molecules in cells with nanometer certainty. Together, these types of imaging approaches have been termed single molecule localization microscopy (SMLM) [24]. PALM and GSDIM differ in their precise experimental methodology of acquisition, however they both aim to observe sparse sub-sets of a large population of molecules, enabling highly precise localization of each single molecule. SMLM techniques were employed here to probe the spatial organization and dynamics of large cohorts (typically many tens of thousands) of tSNARE molecules on the plasma membrane. Previous studies investigating tSNARE spatial distributions primarily used fluorescent immunostaining, observing clusters at the limit of resolution of their respective approach [14,25]. Using GSDIM, the nano-scale spatial arrangement of the endogenous tSNARE proteins, syntaxin1 and SNAP-25, was measured on the plasma membrane of neuroendocrine cells (Figure 1A, 1B). These molecules reside in drifts of higher and lower density in the bilayer plane. Surprisingly, in light of current hypotheses regarding tSNARE clusters and their proposed function [14–18], vesicles, detected by immunostaining for the calcium sensor synaptotagmin, were located in the areas of low tSNARE density. Analysis of GSDIM is confounded by the repeated localization of the same fluorescent molecule, limiting accurate analysis of molecular density and organization [26]. This makes it impossible to count the number of molecules in a region or comment on any observed clustering. In contrast, PALM has the advantage that each molecule follows a simple linear path of activation, emission and irreversible photobleaching [21,22]. PALM analysis, using functional fluorescently labeled syntaxin and SNAP-25 [27,28], reported densities in agreement with previous measures for endogenous tSNAREs [14,29]. These data recapitulated the findings using GSDIM; the segregation of more dense groups of tSNAREs from sites occupied by secretory vesicles (Figure 1C, 1D). The same organization was observed when cargo was used as the label for secretory vesicles (Figure S1A, S1B). Importantly, the molecular arrangement of the tSNAREs is not representative of a random distribution; instead the molecules conform to a non-random ordered model of organization (Figure S2C, S2D). The molecular map derived by GSDIM and PALM can be used to generate an image, of the same region, as observed using a standard fluorescence microscope or under STED illumination (Figure 1 and Figure S1C–E). At these lower resolutions, partial overlap between tSNARE fluorescence signals and secretory vesicles is apparent, in agreement with previous reports [17,25].

In addition to the rendered GSDIM and PALM images, the precise X-Y co-ordinates of every molecule are recorded, with a typical localization accuracy of 4–10 nm and 8–21 nm respectively. Lateral drift of the sample can compound single molecule localization approaches. To negate this an adapted sample holder was utilized resulting in a lateral drift of 5 nm in either dimension over the recording period (Figure S2A, S2B). This is of the order of the inaccuracy in the molecular localization in both PALM and GSDIM and hence has no impact on the observed molecular organization. This allows for the quantitative appraisal of tSNARE molecular organization relative to secretory vesicles (also localized with similar nano-scale precision) using nearest neighbor analysis. Available structural information of SNARE proteins in lipid bilayers [30,31] indicates that the maximum separation over which the plasma membrane and vesicular SNARE proteins could interact is 17.8 nm (Figure 2A). Assuming a zero nanometer distance between the plasma membrane and secretory vesicles (previously used to define 'docked' secretory vesicles by electron microscopy [32]) this would provide a maximum radius of 82.5 nm from the center of the secretory vesicle, over which the SNARE proteins would be predicted to be able to interact and drive membrane fusion. This scenario provides the most stringent criteria for measurement. The lateral coordinate data were thus used to assign each molecule to its nearest secretory vesicle and then the number of detected molecules, within 82.5 nm of each vesicle center, was measured (Figure 2B and 2C). This revealed that the average number of each tSNARE, within a functionally relevant distance of each vesicle was of the order of one or two molecules, in good agreement with the estimates of endogenous SNARE molecular density reported by GSDIM.

The previous experiments provide a snapshot of the spatial molecular distribution of the tSNAREs and secretory vesicles with maximum precision, but require immobilization of the protein molecules through fixation [33]. The plasma membrane of a live cell, however, is a highly dynamic environment [34], and so we decided to employ the PALM approach in live cells with single particle tracking (sptPALM) [35]. The sptPALM approach has the advantage of being able to track sparse numbers of protein molecules repeatedly, providing information at the level of individual molecular motion for the whole population of proteins observed (Figure S3A). Approximately 25,000 individual protein molecules were tracked in the basal plasma membrane of each cell, providing nano-scale information on the molecular motion of proteins in live cells with high temporal resolution (Figure 3). The resulting complex network of molecular tracks can be simplified by the generation of 'contour maps' reporting the parameters of protein movement in a region of the plasma membrane. sptPALM was performed for both SNAP-25 and syntaxin, both of which exhibit a heterogeneous spatial distribution in their movement with regions of high and low density observed on the plasma membrane (Figure 3A and 3B). This is in agreement with the spatial heterogeneity observed for syntaxin and SNAP-25 using GSDIM and PALM in fixed cells. Speed contour maps of the same region show only small variations in the molecular velocity across the plasma membrane with no apparent correlation with track density.

Both tSNAREs exhibit a single component distribution of mean track speed, with syntaxin having an overall lower mean speed distribution than SNAP-25, as may be expected for an integral membrane protein compared to a peripherally associated molecule (Figure 4A). This speed differential was also confirmed using FRAP (Figure S3B–D). It is important to note that both of these approaches are fit by a single diffusion component and do not discriminate between the molecular motions of different oligomeric tSNARE states. Interestingly, comparing total track length to maximum displacement (the longest distance between any two points in the track) showed that despite the presence of long molecular tracks, both syntaxin and SNAP-25 exhibited maximum displacements of less than 1.6 μm (Figure 4B and Figure S4). This could be indicative of the tSNAREs moving with a caged motion through inclusion in, or exclusion from, domains on the plasma membrane [34,36–38]. To understand this, we examined every individual step in every molecular track (approximately 190,000 events from at least three cells for each tSNARE). Taking pairs of consecutive points, labeled 1 and 2 (Figure 4C) to define the direction of travel, we asked the question: where does a molecule choose to go next? We found that, relative to their current trajectory, the molecules exhibit a distinct bias towards reversing

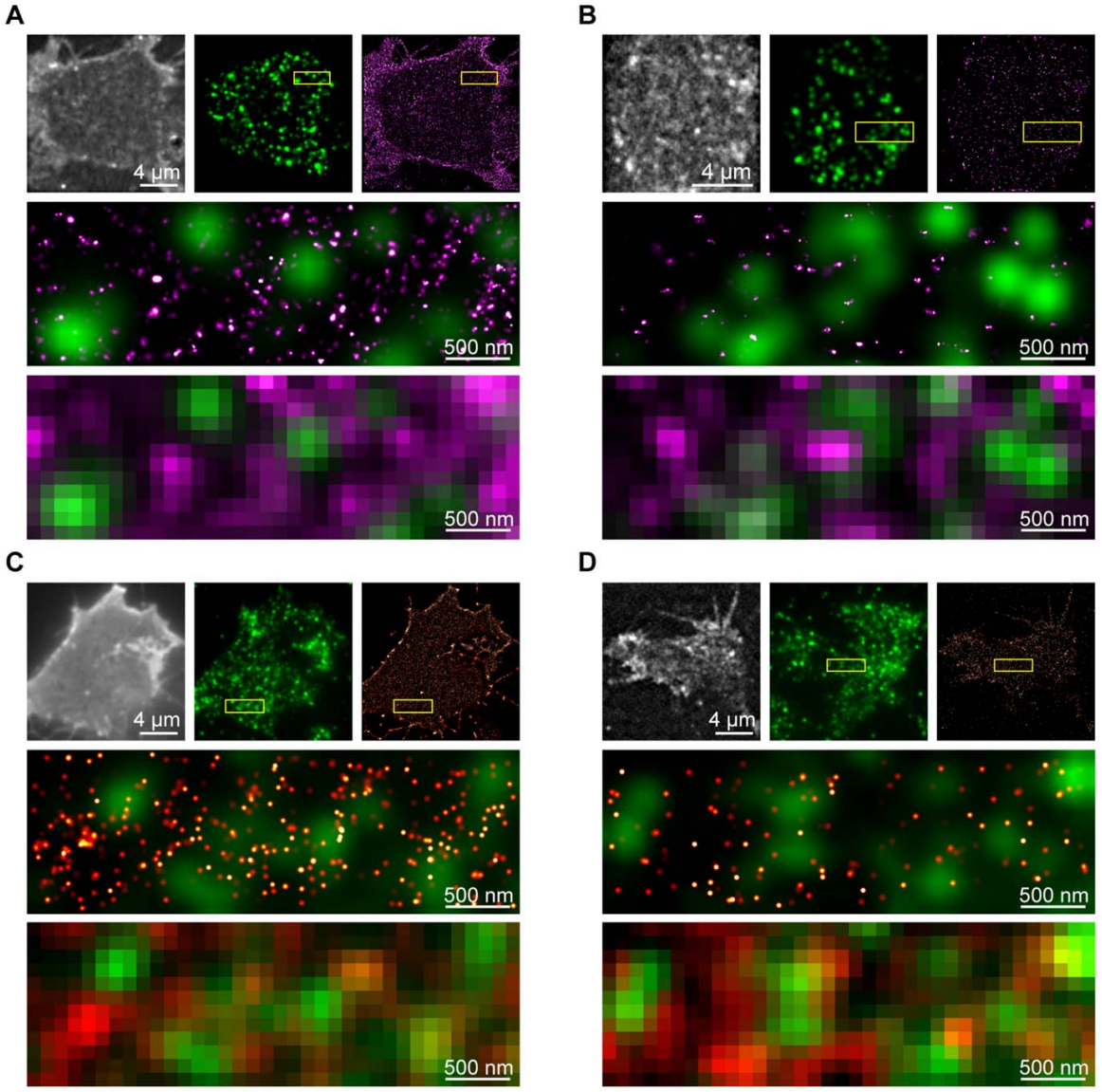

Figure 1. Secretory vesicles preferentially occupy areas of low tSNARE density. (**A**) GSDIM of endogenous SNAP-25. A TIRFM image generated from summation of all detected molecular signals (*upper left*), immunostained vesicles (*upper center*) and rendered GSDIM (*upper right*) are shown for a representative cell. The indicated region (*yellow box*) is shown enlarged (*center*) as an overlay of rendered GSDIM data (*magenta*) and secretory vesicles (*green*). The coordinate data from the GSDIM localization was used to calculate a diffraction-limited resolution TIRFM image of the same field of view (*lower*). (**B**) GSDIM of endogenous syntaxin with panel layout as in (A). (**C**) PALM of SNAP-25. A TIRFM image generated from summation of all detected molecular signals (*upper left*), immunostained vesicles (*upper center*) and rendered PALM (*upper right*) are shown for a representative cell. The indicated region (*yellow box*) is shown enlarged (*center*) as an overlay of rendered PALM data (*red*) and secretory vesicles (*green*). The coordinate data from the PALM localization was used to calculate a diffraction-limited resolution TIRFM image of the same field of view (*lower*). (**D**) PALM of syntaxin with panel layout as in (C).
doi:10.1371/journal.pone.0049514.g001

direction (Figure 4C). This is analogous of a ball ricocheting inside a box and indicates that the tSNARE proteins are contained in micro-domains, constraining their molecular motion, and maintaining a non-random spatial distribution.

In addition to the lateral movement of the tSNAREs in the plasma membrane secretory vesicles are also mobile [39,40]. Electron microscopy (on fixed samples) demonstrated that some secretory vesicles are docked in close apposition to the plasma membrane [32,40]. Under TIRFM illumination, membrane-proximal vesicles exhibit a highly restricted lateral diffusion often referred to as 'morphological docking' [40,41]. To characterize the molecular motion of secretory vesicles, we tracked vesicles up to

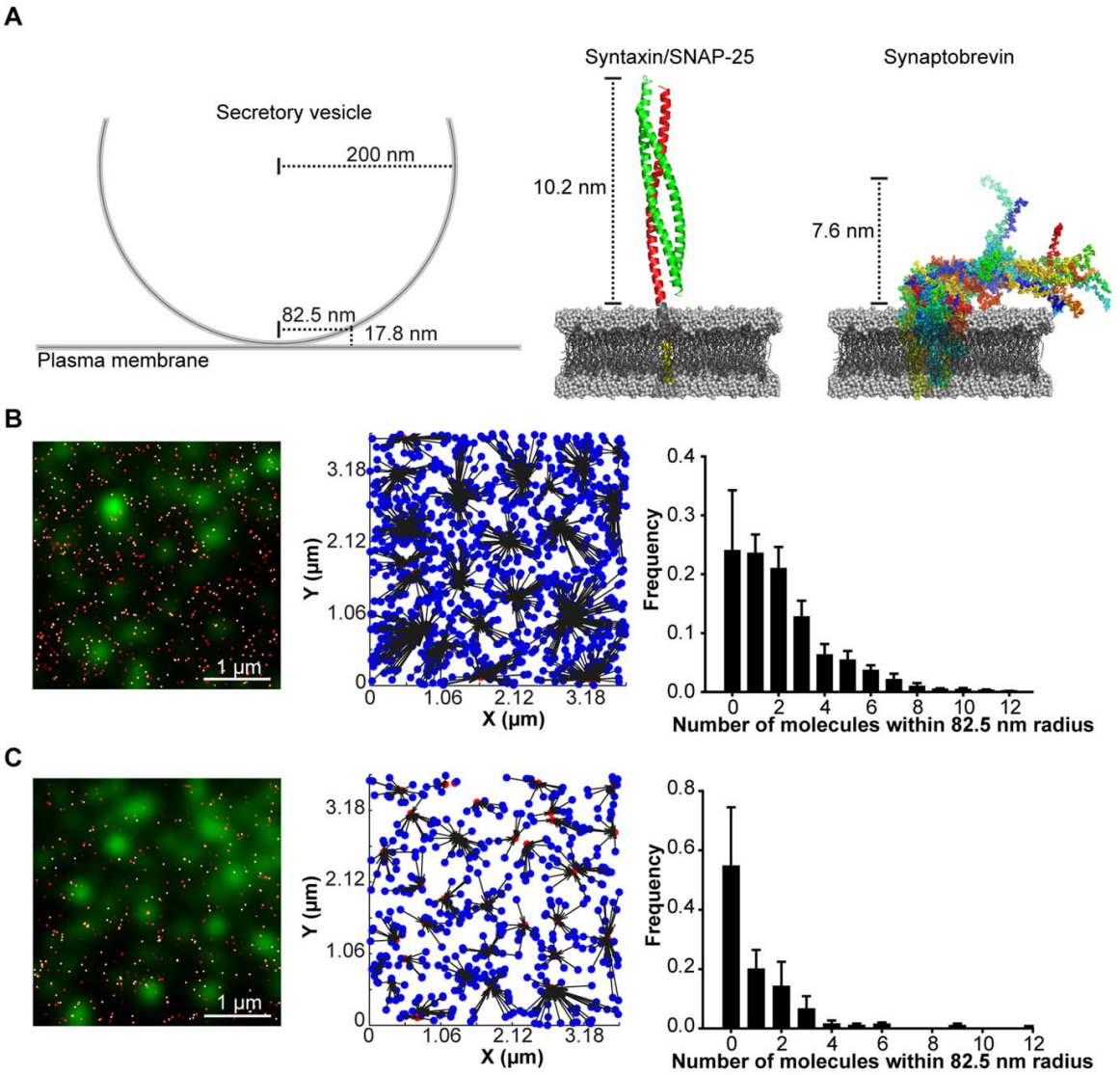

Figure 2. Low numbers of tSNAREs are within a functional distance of secretory vesicles. (**A**) A schematic representation of a secretory vesicle (*left*). A ribbon representation of the complex formed between syntaxin and SNAP-25 (*center*, based on PDB:3IPD [31]) and NMR structures of synaptobrevin (*right*, based on PDB:2KOG [30]) both in synthetic lipid bilayers. The combined maximum reach of these proteins when in opposing bilayers is 17.8 nm. Assuming a distance of 0 nm between opposing bilayers, a chord 17.8 nm from the plasma membrane would have a half-length of 82.5 nm (*left*). This radial distance was used to calculate the number of plasma membrane SNAREs residing under each secretory vesicle. (**B**) A region of plasma membrane showing an overlay of rendered PALM data of SNAP-25 (*red*) and immunostained secretory vesicles (*green*). The center of mass of each secretory vesicle was calculated and used in a nearest neighbor analysis (*center*). The number of SNAP-25 molecules within 82.5 nm of each vesicle was calculated and is shown as a frequency histogram of mean ±SEM (n = 5 cells). (**C**) As in (B) but for PALM localized syntaxin (n = 5 cells).
doi:10.1371/journal.pone.0049514.g002

the point of fusion (Figure S5A–C), finding that these vesicles exhibited a tethered motion with a relatively slow speed. Immediately prior to exocytosis, a nascent fusing vesicle undergoes a brief rapid acceleration in its movement, in agreement with recent studies in chromaffin cells [39].

As it is not possible to record the movement of secretory vesicles and individual tSNARE molecules simultaneously over the same time course, a modeling approach was used to combine the quantified data describing the non-random distribution of the tSNAREs, the molecular dynamics of the individual tSNAREs and the motion of the secretory vesicles into a single unifying simulation. The model was kept as simple as possible, using only parameters derived from sptPALM and vesicle tracking data, along with initial positions for individual tSNAREs and secretory vesicles from fixed cell PALM datasets. A five second simulation was chosen to replicate the maximum period over which a single

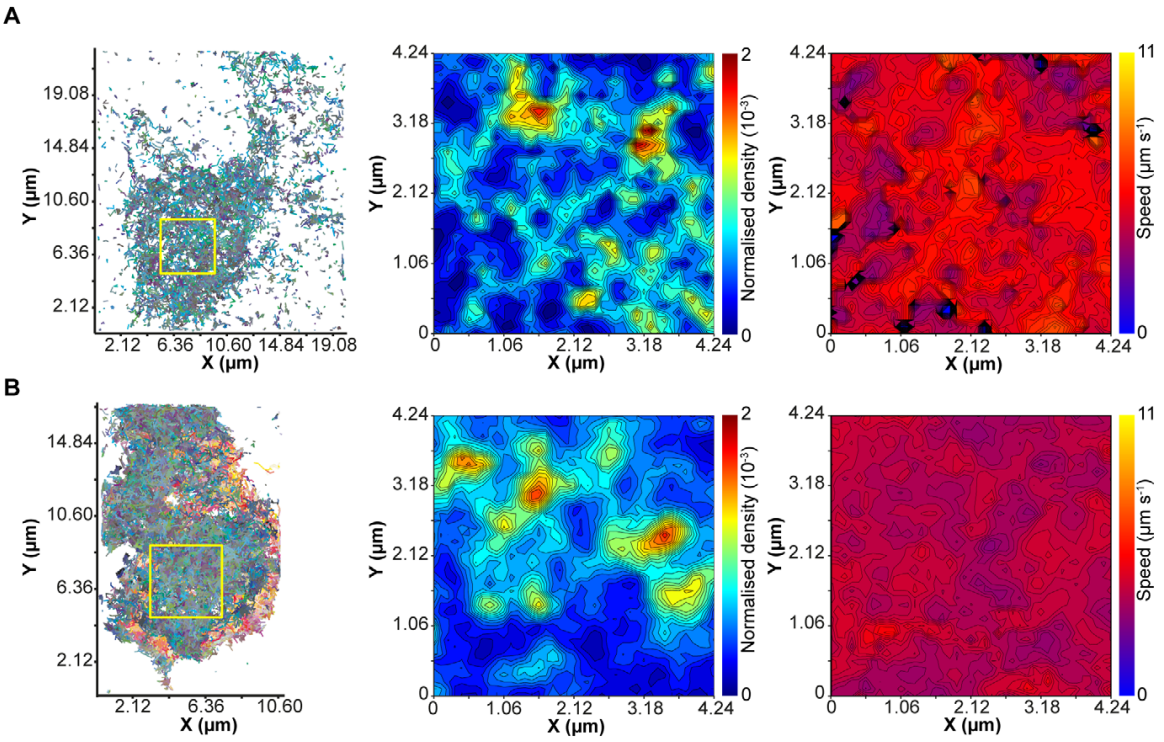

Figure 3. tSNARE molecular dynamics in living membranes. (**A**) Compilation of tracks from individual molecules of SNAP-25 with a temporal resolution of 50 ms(*left*). The indicated region (*yellow box*) was selected and segmented in to an array of 100 nm × 100 nm boxes. The number of tracks passing through each box was measured and is shown as a contour map of normalized density (*center*) such that the sum of all density values is equal to one. The mean speed of all tracks passing through each sampling box was also measured and is displayed as a contour map (*right*). (**B**) As in (A) but for sptPALM of syntaxin.
doi:10.1371/journal.pone.0049514.g003

molecule could be recorded under sptPALM. A single representative simulation for both SNAP-25 and syntaxin is shown (Figure 5A and 5B) along with an enlarged example track. These *in silico* molecules had a resulting speed distribution similar to that measured in sptPALM and produced a comparable distribution for total track length against maximum displacement (Figure S5D, S5E). The simulation allowed the monitoring of the number of mobile tSNAREs within range of interaction with mobile secretory vesicles (Figure 5A, 5B). The numbers of SNARE molecules resident under each secretory vesicle, at any point in time, typically ranged from zero to seven (Figure 5C). This indicates that the tethering and docking of secretory vesicles at the plasma membrane, combined with the restricted freedom of lateral diffusion for the individual SNARE molecules maintains secretory vesicles in a low density SNARE environment.

Discussion

Using super-resolution microscopy techniques with molecular resolution, we demonstrate that tSNARE molecules exist in a non-random spatial distribution, resulting in areas of low and high molecular density, which give rise to the apparent clusters in diffraction-limited microscope data. Our findings show that, at rest, secretory vesicles do not reside over dense clusters of tSNAREs on the plasma membrane. This is in contrast to current models of SNARE-driven membrane fusion where the secretory vesicle is hypothesised to co-locate with the tSNAREs. However, the majority of studies examining tSNARE clustering have observed, at most, only partial colocalisation with secretory vesicles [17,25]. Furthermore these studies have been limited to a supra-molecular resolution. Convolution of our SMLM data, using a theoretical point spread function equivalent to a diffraction limited microscope, or STED illumination, recapitulated these observations of partial colocalisation. The areas of low tSNARE molecular density are favourably targeted by secretory vesicles, as sites of docking, by an as yet undefined mechanism.

The spatial organization of the tSNAREs is maintained, in part, by the restricted mobility of tSNAREs, constrained as though in micro-domains. There are a number of proposed mechanisms for protein sequestration in micro-domains through protein-protein or protein-lipid interactions which serve as generalized principles for membrane organization [36–38]. Our data support and extend current paradigms of membrane organization by providing quantitative data at the level of very large cohorts of individual molecules and organelles in living cells. Interestingly, the SNARE proteins, studied here, have previously been used extensively as model proteins in such studies [14–16]. What is now becoming clear is that the formation and maintenance of the membrane architecture of the tSNAREs is multifactorial, including contributions from both lipidic and protein sources [14–16,25,42].

What implication does this organization of tSNARE molecules and secretory vesicles have for membrane fusion? It is known that secretory vesicles undergo a rapid movement immediately prior to

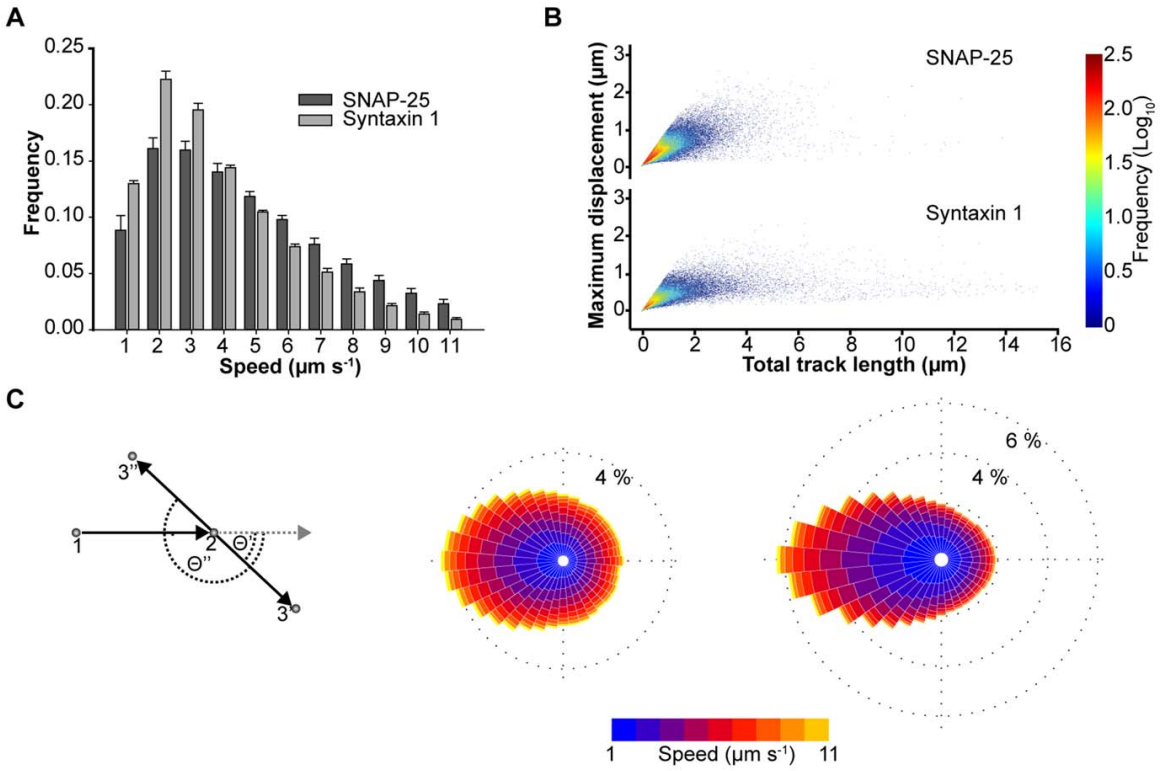

Figure 4. tSNARE molecules exhibit a restricted lateral diffusion in the plasma membrane. (**A**) Combined mean speed for each individual tracks of SNAP-25 and syntaxin shown as a frequency histogram of mean ± SD (n = 3 cells). (**B**) A combined scatter plot of total track length against maximum displacement for SNAP-25 and syntaxin (78641 and 48027 tracks respectively). Maximum displacement has an upper limit of ~1.6 μm regardless of total track length. (**C**) Analysis of individual track movement demonstrates syntaxin and SNAP-25 tend to reverse direction. A schematic of the analysis applied is shown (*left*). Two points of a track are shown (numbered 1 and 2). Deviation of the third point (3′ or 3″) from a forward trajectory (*grey dashed line*) was measured (Θ′ or Θ″ respectively) and angle data combined in to a 'rose diagram' histogram for SNAP-25 (*center, 197,489 data points*) and syntaxin (*right, 188,916 data points*). For the 36 wedges (each corresponding to 10°), the length indicates the normalize frequency of molecular travel in that direction. Color corresponds to speed.
doi:10.1371/journal.pone.0049514.g004

fusion (Figure S5) [39]. This lateral movement of around 50 nm, however, would be insufficient to move the vesicle on to a denser region of tSNAREs from their tSNARE-sparse starting position. Instead this movement may be simply a result of the zippering of SNARE complexes off-center from the axis of the secretory vesicle, resulting in the small rapid translation observed. The low number of tSNAREs close to the secretory vesicle should therefore be sufficient to drive membrane fusion. Indeed the number of tSNAREs observed immediately adjacent to the secretory vesicles falls within the range reported to be sufficient to drive membrane fusion in a variety of biophysical experiments [43–47]. Clearly secretory vesicles residing in a region of the plasma membrane with insufficient numbers of tSNAREs would be unable to fuse. Conversely, above this lower threshold, the probability of vesicle fusion would, in part, be determined by the number of tSNAREs in close proximity to the secretory vesicles. By regulating the tSNARE molecular landscape, through one or more candidate mechanisms [15,16,18,25], the cell could dynamically modulate individual release probabilities and thereby the kinetics of the cellular response.

Materials and Methods

Cell Culture and Immunofluorescence

Plasmids encoding PACherry-SNAP25$_{1–206}$, EGFP-SNAP25$_{1–206}$, PACherry-Syntaxin1a$_{1–288}$, EGFP-Syntaxin1a$_{1–288}$ and NPY-EGFP were described previously [18,48]. PC-12 cells were maintained and propagated as described [18]. For microscopy, coverslips were extensively cleaned in a sonicating waterbath containing 0.1 M sodium hydroxide and 0.1% Decon-90 for 30 seconds followed by washing in deionized water, ethanol and acetone. Coverslips were then coated in 100 μg/ml poly-D-lysine (Sigma) prior to seeding with PC-12 cells (ATCC). Cells were transfected 24 hours after plating using Lipofectamine (Invitrogen) and left for a further 48 hours prior to use in experiments. Immunostaining was performed as described previously with extensive fixation in 4% paraformaldehyde solution for 1 hour at room temperature to ensure maximal immobilization of cellular proteins [33]. For immunostaining, syntaxin-1A was detected using the monoclonal antibody HPC-1 (Sigma), SNAP-25 using the monoclonal antibody SMI81 (Sternberger monoclonals) and secretory vesicles using a polyclonal anti-syntaptotagmin antibody (SySy). Antibodies were detected by immunofluorescence using

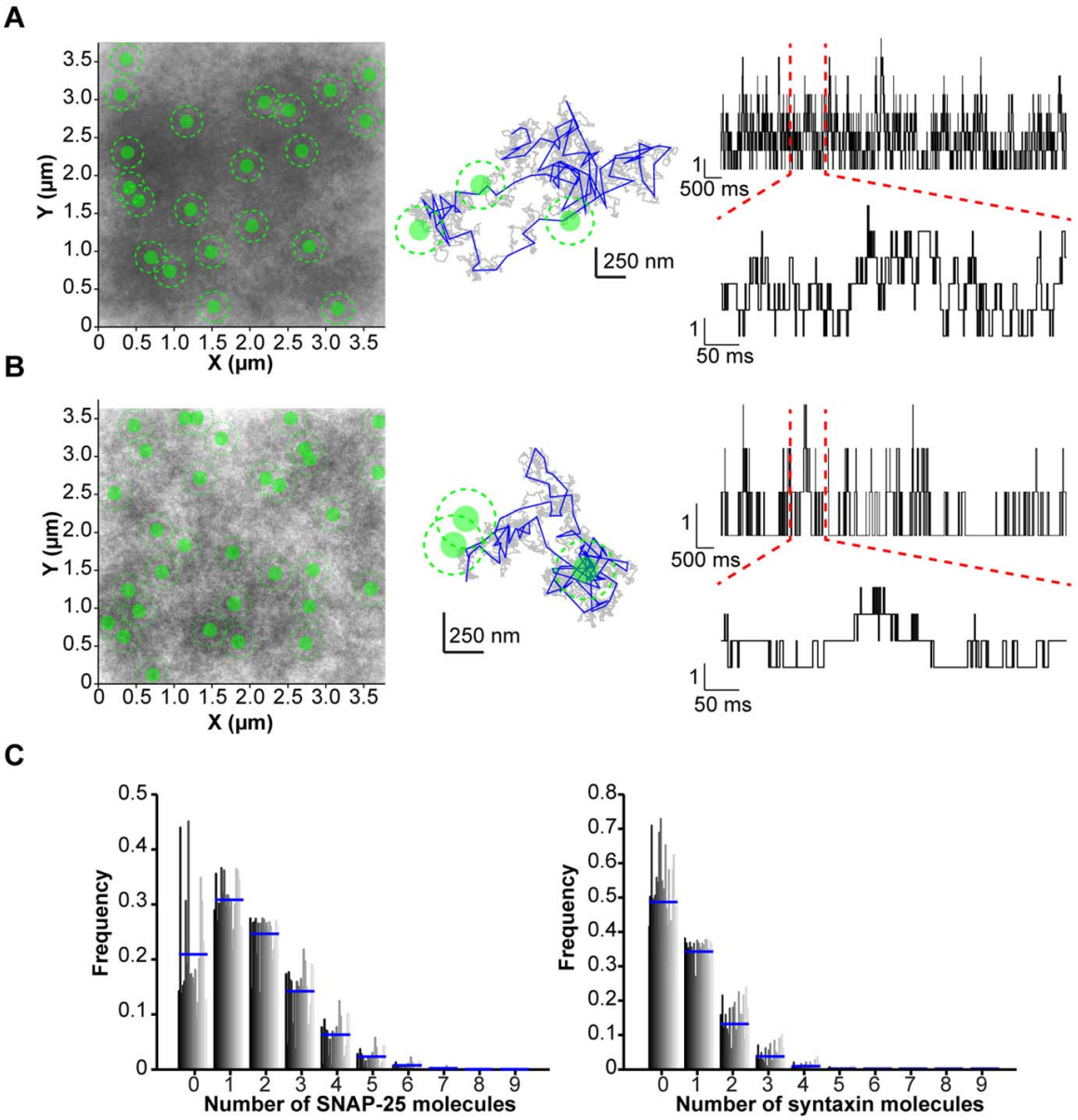

Figure 5. Simulations of the dynamic encounters of secretory vesicles and tSNARE molecules. (**A**) Initial positions of secretory vesicles and SNAP-25 were derived from PALM experiments. Over 5 s molecules and secretory vesicles were allowed to diffuse, bound by the restrictions imposed by the model. A combined image (*left panel*) of all tracks (*grey*) and secretory vesicles (*green, disc signifies sampling window and dashed line circumference of the vesicle*) is shown. A single molecular path is shown (center) with trajectory sampled at 10 μs (*grey*), sampled every 50 ms as in the sptPALM (*blue*) and secretory vesicles (*green*) The number of SNAP-25 molecules within the sampling window is shown over time for a single secretory vesicle over 5 s (*upper right*) and enlarged over 500 ms (*lower right*). (**B**) As in (A) but using initial positions for secretory vesicles and syntaxin derived from PALM experiments (**C**) The probability of each vesicle having a tSNARE within the sampling window at any particular time was calculated using the traces shown in panels a and b. The number of tSNAREs is plotted against frequency for each secretory vesicle in the simulation (*vertical bars, dark grey to light grey*). The mean for all secretory vesicles in each bin is shown (*blue line*). This shows that at any given point in time the majority of vesicles experience three or fewer SNARE molecules.
doi:10.1371/journal.pone.0049514.g005

immunoglobulin Fab' fragments labeled with Alexa 488 or Alexa 647 (Invitrogen).

Microscope Setup

All experiments were performed on an inverted IX81 microscope (Olympus) using a 150 × 1.45 NA objective. Illumination

was provided by a xenon-mercury lamp or a fully motorized four laser TIRF combiner coupled to 405 nm, 491 nm, 561 nm and 540 nm 100 mW lasers. This allowed for rapid switching of penetration depth from widefied to TIRF illumination during experiments. The sample was maintained in an environmental chamber (Okolabs) at 21°C for fixed samples or at 37°C in 5% CO2, 95% Air for live cells. To minimize lateral drift during acquisition a nosepiece stage (Olympus) was employed. Lateral drift using this stage was $\sim\pm 6$ nm over a typical 30 minute acquisition. This meant no correction for drift (e.g. using fiducidal markers) was required post acquisition. This is comparable to the localization accuracy, due to the signal to noise ratio of detected single molecules, of 4–21 nm for PALM or GSDIM datasets. Fluorescence emission was detected using a 512×512 pixels, water-cooled EMCCD camera (Hamamatsu).

Single Molecule Localization Microscopy

GSDIM microscopy was performed based on previously described methods [26]. Cells were fixed and immunostained as above. To ensure efficient switching of Alexa 647, cells were imaged in 0.5 mg/ml glucose oxidase, 40 μg/ml catalase, 10% wt/vol glucose and 50 mM β-mercaptoethylamine. In a typical experiment, cells were initially excited by 491 nm laser light under TIRF illumination to acquire Alexa 488 labeled vesicle fluorescence. The cell was then continuously illuminated with 640 nm laser light under TIRF illumination for 15 to 30 minutes. Emitted fluorescence was detected using an EMCCD camera with an EM Gain of 100–400 and a frame rate of 20 Hz. The resulting image sequences were subsequently analyzed using single molecule identification and localization algorithms described below. The repeated cycling of fluorophores between the excited and dark states results in repetitive localization of the same fluorophore multiple times.

PALM microscopy was performed based on previously described methods [21,22]. Cells, expressing photoactivatable mCherry labeled SNAREs were fixed, and immunostained as required, as detailed above. Cells were imaged in PBS at 21°C. In a typical experiment, cells were initially excited by 491 nm laser light under TIRF illumination to acquire Alexa 488 or GFP labeled vesicle fluorescence. Photoactivatable mCherry was then activated with a brief pulse (1 to 250 ms) of 405 nm laser light under TIRF illumination followed by acquisition of 20 to 40 frames using a 561 nm laser under TIRF illumination and an EMCCD camera with an EM Gain of 400–600 at 5 Hz. This cycle of activation and acquisition was repeated between 150 and 300 times with the activation pulse duration increasing gradually during the experiment.

For static PALM and GSDIM datasets single molecules were detected using a Matlab routine kindly provided by Samuel Hess (Maine) [22]. Long-lived dark states can result in the repeated localization of the same fluorophore in PALM experiments (particularly with mEos2 and Dronpa) [49]. To minimize any influence of dark states in our data, individual frames between activation pulses were summed together using ImageJ before localization. Localized datasets were then used for further analysis in Matlab, or rendered at high resolution. Rendering of localized molecules was performed using the same Matlab algorithms and false colored in ImageJ.

sptPALM

Cells, expressing photoactivatable mCherry labeled SNAREs were imaged in phenol red free culture medium at 37°C and 5% CO_2, 95% air. Photoactivatable mCherry was activated with a brief pulse (1 to 40 ms) of 405 nm laser light under TIRF illumination followed by acquisition of 100 frames using a 561 nm laser under TIRF illumination and an EMCCD camera with an EM Gain of 600–800 at 20 Hz. This cycle of activation and acquisition was repeated between 150 and 300 times with the activation pulse duration increasing gradually during the experiment.

An automated particle detection and tracking system has been developed and applied [50]. The system combines particle detection in each single image frame and frame-to-frame particle correspondence implemented in Matlab. Particle detection in each single frame comprises three components: (1) particle probability image mapping [51], (2) refinement of particle probability image, and (3) particle segmentation. The first component is implemented by three steps: (a) The Haar-like feature for each pixel is measured in the original grayscale image; (b) A weak threshold is applied to the Haar-like feature to coarsely classify each pixel into one of two classes: particle or background; (c) A particle probability concept is defined as the ratio of the number of spatially connected particle pixels to the total number of pixels in a small region of a particle size. Particle features are significantly enhanced in the particle probability image. The second component is implemented by applying a rotationally symmetric Gaussian low pass filter to the newly obtained particle probability image to get more accurate particle probability at each pixel. The third component is implemented by firstly estimating particles existing regions and their corresponding markers of particles from the refined particle probability image, and then using the marker-controlled watershed transform to accurately segment the particle regions from the original grayscale image. Our particle detection algorithm allows for the detection of particle positions at sub-pixel level and accurate estimation of particle topologies such as size and intensity. The robust frame-to-frame particle correspondence is finally implemented by incorporating these particle topologies into the system state vector of an Interacting Multiple Model (IMM) filter to better deal with particle motion modeling and robust data association. Here three motion models, random walk, first order and second order linear extrapolations are used for motion modeling, and a dynamic programming algorithm is used to optimize the particle correspondence by minimizing the association cost function.

Vesicle Tracking and Fusion

For vesicle tracking and stimulation experiments, PC12 cells, expressing NPY-EGFP, were maintained on the microscope at 37°C and 5% CO_2, 95% air. Cells were imaged in KREBs Buffer (115 mM Sodium Chloride, 5 mM Potassium Chloride, 24 mM Sodium Bicarbonate, 2.5 mM Calcium Chloride, 1 mM Magnesium Chloride, 10 mM HEPEs (pH 7.4), 0.1% (w/v) BSA) adjusted to 290 mOsM. For stimulation, ATP was added during the recording to a final concentration of 300 mM. Secretory vesicle movement and fusion were acquired using a 491 nm laser under TIRF illumination and an EMCCD camera with an EM Gain of 200–400 at 20 Hz.

To determine the mobility of secretion competent vesicles, high-speed image sequences were acquired as detailed above. Vesicles undergoing fusion were identified by the characteristic rapid increase in fluorescence upon EGFP un-quenching and then the exponential decay resulting from diffusion of cargo molecules from the site of fusion. Small regions of interest were excised surrounding these fusion events containing the preceding frames. These single vesicle movies were then subjected to particle tracking using Imaris (Bitplane) aligning the maximum intensity frame, equating to fusion, as the final frame to allow the averaging of multiple events.

FRAP

Cells expressing EGFP labeled SNAREs were imaged in phenol red free culture medium at 37°C and 5% CO_2, 95% air. Fluorescence recovery after photobleaching was carried out using the Olympus CellFRAP hardware attachment in conjunction with TIRF illumination. A circular bleach area of radius 0.742 μm was selected and bleached in the camera dead time between frames 5 and 6 of a total image train of 30 acquired at 32 Hz. Membrane sheets were prepared by sonication as described previously [25]. In brief, cells were grown on coverslips as standard. The coverslip was immersed in 100 mL of sheet sonication buffer (120 mM potassium glutamate, 20 mM potassium acetate, 10 mM EGTA, 4 mM $MgCl_2$, 2 mM ATP, 0.5 mM dithiothreitol, and 20 mM HEPES-KOH, pH 7.2) in a 9 cm diameter beaker. A 2 mm sonication probe placed at a height of 1 cm above the coverslip and operated at 40% for 10 s.

Image J was used to extract intensity data from the resulting image files and the software program FRAP_Analyser was used to extract a diffusion coefficient, *D*, from the data gathered from each individual FRAP experiment.

SMLM Spatial Analysis

Following single molecule localization the spatial distribution of individual molecules was analyzed from the coordinate information. Ripley's analyses were performed using custom written Matlab algorithms. To compare the observed spatial distribution to the random state, the same numbers of molecules, in the same spatial area, were redistributed randomly 1000 times. For each simulation the Ripley's K function and L transformation were derived. This is presented as light grey envelopes for the randomized simulations with the test case in black. Deviation of the test case above the envelopes at short radii indicates a non-random morphology with areas of high and low density. Deviation of the test case below the envelopes would indicate some form of minimum distance between adjacent molecules.

To analyze the spatial distribution of secretory vesicles relative to the SNARE molecules, nearest neighbor analysis was performed. Using the PALM coordinates of SNARE proteins and the centroid coordinates of secretory vesicles, SNARE molecules were assigned to their nearest vesicle using a nearest neighbor routine in Matlab. A sampling radii was determined based on the range over which the tSNAREs and vSNARE would be able to interact using available structural information. Following allocation of molecules to their nearest secretory vesicle the number of molecules within 82.5 nm of the centroid of each vesicle was determined.

Molecular Modeling

The motion of the syntaxin and SNAP-25 molecules were both modeled by Brownian motion with the only free parameter being the noise intensity. This parameter was fixed for each molecule by comparison to the experimental data of speeds and track lengths. Brownian motion is consistent with a small molecule moving under random external forcing. For the vesicles the noise intensity for the Ornstein-Uhlenbeck (OU) process was fixed by comparison to experimental data for the speeds and the mean position was fixed from the PALM datasets. The OU process is consistent with a large molecule undergoing random fluctuations with friction. It describes the caged motion observed experimentally and maintains the non-random spatial distribution. These stochastic equations were solved numerically using the standard Euler–Maruyama method with a time step much smaller than the experimental sample rate of 50 ms. For this simple model no interaction was included between any of the molecules. Initial positions of the molecules were taken from experimental PALM datasets. To investigate the number of tSNARE molecules in range of a vesicle we took a computational domain with periodic boundaries.

Supporting Information

Figure S1 Molecular organization of the plasma membrane SNARE machinery. (**A**) PALM of photoactivatable mCherry labeled SNAP-25. A TIRFM image generated from summed individual molecules (*upper left*), NPY-EGFP labeled vesicles (*upper center*) and rendered PALM (*upper right*) are shown for a representative cell. The indicated region (*yellow box*) is shown enlarged (*center*) as an overlay of rendered PALM data (*red*) and secretory vesicles (*green*). (**B**) PALM of photoactivatable mCherry labeled syntaxin with panel layout as in (A). SMLM datasets can reproduce SNARE clusters observed by diffraction limited optical microscopy and STED. (**C**) GSDIM of endogenous SNAP-25. A TIRFM image of immunostained vesicles (*upper left*) and rendered GSDIM (*lower left*) are shown for a representative cell. The indicated region (*yellow box*) is shown enlarged (*right*) as an overlay of rendered GSDIM data (*magenta*) and secretory vesicles (*green*). This region was convolved to show this region under standard and STED resolutions. (**D**) GSDIM convolved with a standard PSF (*upper left*) and immunostained vesicles (*lower left*). The same region is shown overlaid and enlarged (*right*). The pixel size equates to 106 nm (a 150×1.45 NA objective coupled with a 16 μm pixel detector). (**E**) As in (D) but using a calculated PSF under STED illumination. The pixel size is 30 nm as used in previous publications.
(TIF)

Figure S2 Spatial analysis of plasma membrane SNARE distributions observed by PALM. (**A**) To minimize lateral drift a nose-piece stage (Olympus) was employed. The sample chamber was placed on the top plate. The whole microscope was contained within an incubation chamber to minimize air currents and temperature fluctuations. (**B**) 100 nm beads were imaged for 30 minutes at 1 Hz (*upper panel*) and localized by fitting of a 2-dimensional Gaussian distribution to calculate the centroid. The calculated centroid of two beads for each frame in the image train is shown as a scatter plot (*red and green spots*). 99.9% of the points fall within a circle of 6 nm radius. This movement is comparable to the level of accuracy of localization in PALM and GSDIM datasets. (**C**) The coordinates of individual SNAP-25 molecules are plotted (*left panel*, *blue circles*). The region indicated (*red box*) is shown expanded (*center panel*). Ripley's K function followed by transformation to derive the L function is shown (*right panel*, *black line*). The data was randomized 1000 times, maintaining the same area and number of molecules and the L function calculated (*grey lines*). (**D**) As in (C), but using syntaxin PALM coordinate data. Deviation above the random simulations at short sampling distances, as observed in both cases here, indicates a non-random, heterogeneous distribution of areas of higher density reminiscent of clustering.
(TIF)

Figure S3 Measurement of tSNARE mobility on the plasma membrane. (**A**) An automated particle detection and tracking system for sptPALM. A flow diagram representing the individual steps is shown. A raw image (part of a large image series) is subjected to automated particle detection. Individual particles are tracked over 100 individual frames and accumulated. This cycle is then repeated for between 160 and 240 individual activation cycles. FRAP measurement of t-SNARE motion in

intact cells and membrane sheets. (**B**) Representative frames from a single FRAP experiment on a PC12 cell expressing GFP-SNAP25 (*green*). Photobleaching of a circle of radius 0.742 nm was carried out between frames 5 and 6, and frame 6 - the 'bleach moment' - is considered as t = 0. (**C**) Average normalized fluorescence recovery curves from intact cells (*black circles*) and membrane sheets (*grey circles*) for SNAP25 (*left panel*) and syntaxin-1A (*right panel*). Error bars represent standard errors in the mean, n = 3. (**D**) Mean velocities for SNAP25 and syntaxin 1A in intact PC12 cell membranes (*black bars*) and membrane sheets (*grey bars*) extracted from curves fit to normalized FRAP data.
(TIF)

Figure S4 Analysis of individual movement steps demonstrates syntaxin and SNAP-25 move randomly. (**A**) A schematic of the analysis applied is shown (*left*). Two points of a track are shown (numbered 1 and 2). The angle of movement was measured (**Θ**) as shown, and combined in to a rose diagram histogram for SNAP-25 (*center, 287,352 events*) and syntaxin (*right, 257,084 events*). The size of each wedge (corresponding to 10°) indicates the propensity of direction with color corresponding to the speed of the molecule. (**B**) The cumulative number of tracked tSNARE particles against maximum displacement for different total track lengths are shown for SNAP-25 (*left*) and syntaxin (*right*).
(TIF)

Figure S5 Modeling of the secretory machinery. Motion of secretory vesicles prior to exocytosis. (**A**) Single frame from an image sequence of a PC-12 cell expressing NPY-EGFP (*left panel*). Individual vesicles were tracked over time and the path color-coded according to their position during the image sequence (*right panel, color scale blue-red-yellow*). (**B**) Secretory vesicles undergoing fusion were detected and the tracked speed plotted over time with 0 sec corresponding to the fusion event. Mean and error bars representing the SEM are plotted (n = 9 vesicles). (**C**) A representative vesicle showing the track up to the point of fusion (*left, orange*). The dashed line indicates the circumference of the secretory vesicle. The speed and intensity of this vesicle is shown over time (*right panel*). (**D**) A speed histogram of SNAP-25 and syntaxin from ten realizations of the simulation is in good agreement with experimentally measured speeds. (**E**) A combined scatter plot of total track length against maximum displacement for SNAP-25 and syntaxin from ten realizations of the simulation. Maximum displacement was defined as the maximum distance between any two points in a track. The limit of maximum displacement is comparable to that observed for sptPALM.
(TIF)

Author Contributions

Conceived and designed the experiments: CR RRD. Performed the experiments: CR LY ZQ WL ARD AD KJM GL. Analyzed the data: CR LY ZQ WL KJM GL. Wrote the paper: CR LY ZQ WL ARD AD KJM GL RRD.

References

1. Martens S, McMahon HT (2008) Mechanisms of membrane fusion: disparate players and common principles. Nat Rev Mol Cell Biol 9: 543–556. doi:10.1038/nrm2417.
2. Jahn R, Scheller RH (2006) SNAREs–engines for membrane fusion. Nat Rev Mol Cell Biol 7: 631–643.
3. Ostenson CG, Gaisano H, Sheu L, Tibell A, Bartfai T (2006) Impaired gene and protein expression of exocytotic soluble N-ethylmaleimide attachment protein receptor complex proteins in pancreatic islets of type 2 diabetic patients. Diabetes 55: 435–440.
4. Jahn R, Lang T, Sudhof TC (2003) Membrane fusion. Cell 112: 519–533.
5. Jewell JL, Oh E, Thurmond DC (2010) Exocytosis mechanisms underlying insulin release and glucose uptake: conserved roles for Munc18c and syntaxin 4. Am J Physiol Regul Integr Comp Physiol 298: R517–531. doi:10.1152/ajpregu.00597.2009.
6. Sutton RB, Fasshauer D, Jahn R, Brunger AT (1998) Crystal structure of a SNARE complex involved in synaptic exocytosis at 2.4 A resolution. Nature 395: 347–353.
7. Weber T, Zemelman BV, McNew JA, Westermann B, Gmachl M, et al. (1998) SNAREpins: minimal machinery for membrane fusion. Cell 92: 759–772.
8. Fasshauer D, Sutton RB, Brunger AT, Jahn R (1998) Conserved structural features of the synaptic fusion complex: SNARE proteins reclassified as Q- and R-SNAREs. Proc Natl Acad Sci U S A 95: 15781–15786.
9. Sollner T, Bennett MK, Whiteheart SW, Scheller RH, Rothman JE (1993) A protein assembly-disassembly pathway in vitro that may correspond to sequential steps of synaptic vesicle docking, activation, and fusion. Cell 75: 409–418.
10. McNew JA, Weber T, Parlati F, Johnston RJ, Melia TJ, et al. (2000) Close is not enough: SNARE-dependent membrane fusion requires an active mechanism that transduces force to membrane anchors. J Cell Biol 150: 105–117.
11. Shen J, Tareste DC, Paumet F, Rothman JE, Melia TJ (2007) Selective activation of cognate SNAREpins by Sec1/Munc18 proteins. Cell 128: 183–195.
12. van den Bogaart G, Thutupalli S, Risselada JH, Meyenberg K, Holt M, et al. (2011) Synaptotagmin-1 may be a distance regulator acting upstream of SNARE nucleation. Nat Struct Mol biol. doi:10.1038/nsmb.2061.
13. Hartman NC, Groves JT (2011) Signaling clusters in the cell membrane. Current opinion in cell biology 23: 370–376. doi:10.1016/j.ceb.2011.05.003.
14. Sieber JJ, Willig KI, Kutzner C, Gerding-Reimers C, Harke B, et al. (2007) Anatomy and dynamics of a supramolecular membrane protein cluster. Science 317: 1072–1076.
15. Zilly FE, Halemani ND, Walrafen D, Spitta L, Schreiber A, et al. (2011) Ca2+induces clustering of membrane proteins in the plasma membrane via electrostatic interactions. EMBO J 30: 1209–1220.
16. van den Bogaart G, Meyenberg K, Risselada HJ, Amin H, Willig KI, et al. (2011) Membrane protein sequestering by ionic protein–lipid interactions. Nature 479: 552–555.
17. Barg S, Knowles MK, Chen X, Midorikawa M, Almers W (2010) Syntaxin clusters assemble reversibly at sites of secretory granules in live cells. Proc Natl Acad Sci U S A 107: 20804–20809. doi:10.1073/pnas.1014823107.
18. Rickman C, Medine CN, Dun AR, Moulton DJ, Mandula O, et al. (2010) t-SNARE protein conformations patterned by the lipid micro-environment. J Biol Chem 285: 13535–13541. doi:M109.091058 [pii] 10.1074/jbc.M109.091058.
19. Brunger AT (2001) Structure of proteins involved in synaptic vesicle fusion in neurons. Annu Rev Biophys Biomol Struct 30: 157–171.
20. Lakowicz JR, Lackowicz JR (2006) Principles of Fluorescence Spectroscopy. Third. Springer. p.
21. Betzig E, Patterson GH, Sougrat R, Lindwasser OW, Olenych S, et al. (2006) Imaging intracellular fluorescent proteins at nanometer resolution. Science 313: 1642–1645.
22. Hess ST, Girirajan TPK, Mason MD (2006) Ultra-high resolution imaging by fluorescence photoactivation localization microscopy. Biophys J 91: 4258–4272. doi:10.1529/biophysj.106.091116.
23. Fölling J, Bossi M, Bock H, Medda R, Wurm CA, et al. (2008) Fluorescence nanoscopy by ground-state depletion and single-molecule return. Nature methods 5: 943–945. doi:10.1038/nmeth.1257.
24. McEvoy AL, Greenfield D, Bates M, Liphardt J (2010) Q&A: Single-molecule localization microscopy for biological imaging. BMC biology 8. doi:10.1186/1741-7007-8-106.
25. Lang T, Bruns D, Wenzel D, Riedel D, Holroyd P, et al. (2001) SNAREs are concentrated in cholesterol-dependent clusters that define docking and fusion sites for exocytosis. EMBO J 20: 2202–2213.
26. van de Linde S, Löschberger A, Klein T, Heidbreder M, Wolter S, et al. (2011) Direct stochastic optical reconstruction microscopy with standard fluorescent probes. Nature Protocols 6: 991–1009. doi:10.1038/nprot.2011.336.
27. Delgado-Martínez I, Nehring RB, Sørensen JB (2007) Differential abilities of SNAP-25 homologs to support neuronal function. The Journal of neuroscience: the official journal of the Society for Neuroscience 27: 9380–9391. doi:10.1523/JNEUROSCI.5092-06.2007.
28. Lam AD, Tryoen-Toth P, Tsai B, Vitale N, Stuenkel EL (2008) SNARE-catalyzed Fusion Events Are Regulated by Syntaxin1A-Lipid Interactions. Mol Biol Cell 19: 485–497.
29. Knowles MK, Barg S, Wan L, Midorikawa M, Chen X, et al. (2010) Single secretory granules of live cells recruit syntaxin-1 and synaptosomal associated protein 25 (SNAP-25) in large copy numbers. Proc Natl Acad Sci U S A 107: 20810–20815. doi:10.1073/pnas.1014840107.
30. Ellena JF, Liang B, Wiktor M, Stein A, Cafiso DS, et al. (2009) Dynamic structure of lipid-bound synaptobrevin suggests a nucleation-propagation

mechanism for trans-SNARE complex formation. Proc Natl Acad Sci U S A 106: 20306–20311. doi:10.1073/pnas.0908317106.
31. Stein A, Weber G, Wahl MC, Jahn R (2009) Helical extension of the neuronal SNARE complex into the membrane. Nature 460: 525–528. doi:10.1038/nature08156.
32. de Wit H, Walter AM, Milosevic I, Gulyás-Kovács A, Riedel D, et al. (2009) Synaptotagmin-1 docks secretory vesicles to syntaxin-1/SNAP-25 acceptor complexes. Cell 138: 935–946. doi:10.1016/j.cell.2009.07.027.
33. Schnell U, Dijk F, Sjollema KA, Giepmans BNG (2012) Immunolabeling artifacts and the need for live-cell imaging. Nature Methods 9: 152–158. doi:10.1038/nmeth.1855.
34. Vereb G, Szöllosi J, Matkó J, Nagy P, Farkas T, et al. (2003) Dynamic, yet structured: The cell membrane three decades after the Singer-Nicolson model. Proc Natl Acad Sci U S A 100: 8053–8058. doi:10.1073/pnas.1332550100.
35. Manley S, Gillette JM, Patterson GH, Shroff H, Hess HF, et al. (2008) High-density mapping of single-molecule trajectories with photoactivated localization microscopy. Nat Methods 5: 155–157.
36. Simons K, Ikonen E (1997) Functional rafts in cell membranes. Nature 387: 569–572. doi:10.1038/42408.
37. Boiko T (2003) Picket and Other Fences in Biological Membranes. Developmental Cell: 191–192.
38. Singer SJ, Nicolson GL (1972) The fluid mosaic model of the structure of cell membranes. Science 175: 720–731.
39. Degtyar VE, Allersma MW, Axelrod D, Holz RW (2007) Increased motion and travel, rather than stable docking, characterize the last moments before secretory granule fusion. Proc Natl Acad Sci U S A 104: 15929–15934.
40. Steyer JA, Horstmann H, Almers W (1997) Transport, docking and exocytosis of single secretory granules in live chromaffin cells. Nature 388: 474–478. doi:10.1038/41329.
41. Johns LM, Levitan ES, Shelden EA, Holz RW, Axelrod D (2001) Restriction of secretory granule motion near the plasma membrane of chromaffin cells. J Cell Biol 153: 177–190.
42. Laage R, Rohde J, Brosig B, Langosch D (2000) A conserved membrane-spanning amino acid motif drives homomeric and supports heteromeric assembly of presynaptic SNARE proteins. J Biol Chem 275: 17481–17487.
43. Sinha R, Ahmed S, Jahn R, Klingauf J (2011) Two synaptobrevin molecules are sufficient for vesicle fusion in central nervous system synapses. Proc Natl Acad Sci U S A 108: 14318–14323.
44. van den Bogaart G, Holt MG, Bunt G, Riedel D, Wouters FS, et al. (2010) One SNARE complex is sufficient for membrane fusion. Nature structural & molecular biology 17: 358–364. doi:10.1038/nsmb.1748.
45. Domanska MK, Kiessling V, Stein A, Fasshauer D, Tamm LK (2009) Single vesicle millisecond fusion kinetics reveals number of SNARE complexes optimal for fast SNARE-mediated membrane fusion. J Biol Chem 284: 32158–32166. doi:10.1074/jbc.M109.047381.
46. Mohrmann R, de Wit H, Verhage M, Neher E, Sørensen JB (2010) Fast vesicle fusion in living cells requires at least three SNARE complexes. Science 330: 502–505. doi:10.1126/science.1193134.
47. Mohrmann R, Sørensen JB (2012) SNARE Requirements En Route to Exocytosis: from Many to Few. Journal of molecular neuroscience?: MN. doi:10.1007/s12031-012-9744-2.
48. Rickman C, Duncan RR (2010) Munc18/Syntaxin interaction kinetics control secretory vesicle dynamics. J Biol Chem 285: 3965–3972. doi:M109.040402 [pii] 10.1074/jbc.M109.040402.
49. Annibale P, Vanni S, Scarselli M, Rothlisberger U, Radenovic A (2011) Quantitative photo activated localization microscopy: unraveling the effects of photoblinking. PloS one 6: e22678. doi:10.1371/journal.pone.0022678.
50. Yang L, Qiu Z, Greenaway A, Lu W (2012) A New Framework for Particle Detection in Low SNR Fluorescence Live-cell Images and Its Application for Improved Particle Tracking. IEEE transactions on bio-medical engineering. doi:10.1109/TBME.2012.2196798.
51. Yang L, Parton R, Ball G, Qiu Z, Greenaway AH, et al. (2010) An adaptive non-local means filter for denoising live-cell images and improving particle detection. J Struct Biol 172: 233–243.